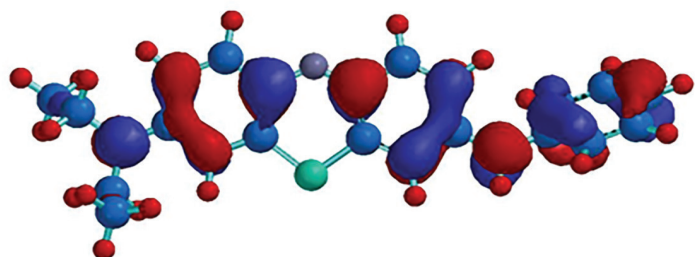
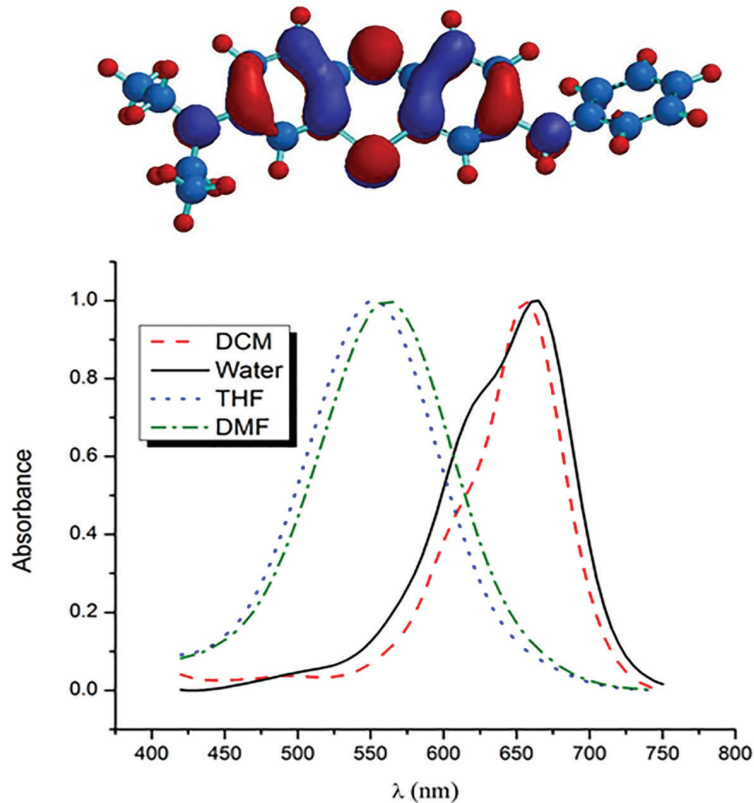




STUDIA UNIVERSITATIS
BABEŞ-BOLYAI



CHEMIA

4/2015

**STUDIA
UNIVERSITATIS BABEŞ-BOLYAI
CHEMIA**

4/2015

**EDITORIAL BOARD OF
STUDIA UNIVERSITATIS BABEŞ-BOLYAI CHEMIA**

ONORARY EDITOR:

IONEL HAIDUC - Member of the Romanian Academy

EDITOR-IN-CHIEF:

LUMINIȚA SILAGHI-DUMITRESCU

EXECUTIVE EDITOR:

CASTELIA CRISTEA

EDITORIAL BOARD:

PAUL ȘERBAN AGACHI, Babeș-Bolyai University, Cluj-Napoca, Romania

LIVAIN BREAU, UQAM University of Quebec, Montreal, Canada

HANS JOACHIM BREUNIG, Institute of Inorganic and Physical Chemistry,
University of Bremen, Bremen, Germany

MIRCEA DIUDEA, Babes-Bolyai University, Cluj-Napoca, Romania

JEAN ESCUDIE, HFA, Paul Sabatier University, Toulouse, France

ION GROSU, Babeș-Bolyai University, Cluj-Napoca, Romania

EVAMARIE HEY-HAWKINS, University of Leipzig, Leipzig, Germany

FLORIN DAN IRIMIE, Babeș-Bolyai University, Cluj-Napoca, Romania

FERENC KILAR, University of Pecs, Pecs, Hungary

BRUCE KING, University of Georgia, Athens, Georgia, USA

ANTONIO LAGUNA, Department of Inorganic Chemistry, ICMA, University of
Zaragoza, Zaragoza, Spain

JURGEN LIEBSCHER, Humboldt University, Berlin, Germany

KIERAN MOLLOY, University of Bath, Bath, UK

IONEL CĂTĂLIN POPESCU, Babeș-Bolyai University, Cluj-Napoca, Romania

CRISTIAN SILVESTRU, Babeș-Bolyai University, Cluj-Napoca, Romania

<http://chem.ubbcluj.ro/~studiachemia/>; studiachemia@chem.ubbcluj.ro

http://www.studia.ubbcluj.ro/serii/chemia/index_en.html

YEAR
MONTH
ISSUE

Volume 60 (LX) 2015
DECEMBER
4

S T U D I A
UNIVERSITATIS BABEŞ-BOLYAI
CHEMIA

4

STUDIA UBB EDITORIAL OFFICE: B.P. Hasdeu no. 51, 400371 Cluj-Napoca, Romania,
Phone + 40 264 405352

CUPRINS – CONTENT – SOMMAIRE – INHALT

ADRIAN PATRUT, STEPHAN WOODBORNE, ROXANA T. PATRUT, GRANT HALL, LASZLO RAKOSY, KARL F. VON REDEN, DANIEL LOWY, DRAGOS MARGINEANU, Radiocarbon Dating of African Baobabs with Two False Cavities: The Investigation of Luna Tree	7
EMŐKE NAGY, MÁRTA GUTTMANN, ZSOLT MOLNÁR-KOVÁCS, RÉKA BARABÁS, Multi-Method Analysis of Bronze Age Ceramics from Satu-Mare County, Romania.....	21
JULIA BARTHA, MARIA GOREA, Ceramic Glazes for Wall Tiles with Different Glass Wastes.....	35
CLAUDIU ACIU, DANIELA LUCIA MANEA, CARMEN PUJA, OANA CADAR, Mortars for the Enhancement of the Indoor Environmental Quality	45
ZAHRA KHALAJ, Influence of Ni Nanoparticles on Growth of DLC Film by PECVD Technique.....	55
ANDREIA CORCIOVĂ, CONSTANTIN CIOBANU, Zinc Quantification in Selected Pharmaceutical Products by Two Analytical Methods ...	67

OANA CADAR, MIRELA MICLEAN, MARIN SENILA, ALEXANDRA HOAGHIA, MANFRED SAGER, Comparative Evaluation of Some Minor- and Major Element Contents in Commercial Yogurts.....	77
ALEXANDRU-FLAVIU TĂBĂRAN, SORIN DANIEL DAN, ALEXANDRA TĂBĂRAN, CONSTANTIN BELE, CORNEL CĂTOI, MIHAI BORZAN, GABRIEL VALASUTEAN, MARIAN MIHAIU, Evaluation of Biochemical Changes Occuring in “Năsal” Cheese During the Ripening Stages	85
ÉVA LASLO, MARA GYÖNGYVÉR, BERNADETT FUNKENHAUZER, EMŐKE DOBRI, ROZÁLIA VERONIKA SALAMON, SZabolcs LÁNYI, BEÁTA ÁBRAHÁM, Isolation and Screening of Lactic Acid Bacteria from Naturally Fermented Sources with High Biotechnological Potential.....	95
ANAMARIA HOSU, CLAUDIA CIMPOIU, A Simple TLC Method for Evaluation of Nicotine in Cigarettes.....	107
MILANA M. ZARIĆ, NENAD M. ZARIĆ, JELENA IVKOVIC, DANIJELA SLAVNIC, BRANKO BUGARSKI, Recent Development of Bioaugmentation Methods for Tobacco Wastewater Treatment	115
ANCA ȘIPOS, PAUL ȘERBAN AGACHI, Direct Sensitivity Analysis of a White Wine Alcoholic Fermentation Process.....	125
ABHILASH NAIR, ALEXANDRINA ZUZA, PAUL-ȘERBAN AGACHI, ARPITA DAS, MARIUS BREHAR, GYŐZŐ FERENCZ BARABÁS, Sensitivity Analysis Using ADM1 Model for Biogas Production.....	143
ANCUȚA ROXANA TRIFOI, AUGUSTIN CRUCEAN, LUCICA STĂNULET, OLIMPIU BLĂJAN, PAUL ȘERBAN AGACHI, Purification of Crude Glycerol by Short Path Evaporation. Theoretical and Practical Analysis of Process Parameters.....	157
MIRCEA LAURENTIU DAN, NICOLAE VASZILCSIN, NARCIS MIHAI DUȚEANU, Electrochemical Behavior of CaBaCO ₂ O _{5±Δ} in Neutral Aqueous Solution	165
IOSIF HULKA, V.A. SERBAN, D. UTU, NARCIS DUTEANU, A. PASCU, I.C. ROATĂ, Corrosion Resistance of Laser Cladded NiCrBSi Composite Coatings	173
SARA ERSALI, MIRCEA V. DIUDEA, QSAR Study on Serotonin Derivatives	185
RALUCA MĂTIEŞ, BEATA SZEFLER, MIRCEA V. DIUDEA, QSAR Study on Dioxins.....	193
BEATA SZEFLER, TEODORA E. HARSA, ALEXANDRA M. HARSA, QSAR and Docking Study on Indolizines	201

GERGELY BÁNÓCZI, CSONGOR SZABÓ, ZSÓFIA BATA, ALINA FILIP, GÁBOR HORNYÁNSZKY, LÁSZLÓ POPPE, Structural Modeling of Phenylalanine Ammonia-Lyases and Related Mio-Containing Enzymes – an Insight into Thermostability and Ionic Interactions.....	213
DIVAMBAL APPAVOO, ROBERT DESCHEAUX, BRUNO THERRIEN, Synthesis and Characterization of Fullerene-Pyridyl Arene Ruthenium Complexes.....	229
CRISTINA NASTASĂ, BRÎNDUŞA TIPERCIUC, LAURIAN VLASE, ADRIAN PÎRNĂU, OVIDIU ONIGA, Synthesis of New 5-(Chromene- 3-YL)Methylene-2,4-Thiazolidinediones	239
ANAMARIA NEGRULESCU, VIORICA PATRULEA, MANUELA MINCEA, CRISTINA MORARU, VASILE OSTAFE, Development of an UPLC Method for Simultaneous Determination of Tartrazine, Congo Red and Methyl Orange	247
DANIELA BENEDEC, IULIA-ELENA POPICA, ILIOARA ONIGA, DANIELA HANGANU, MIHAELA DUMA, RADU SILAGHI-DUMITRESCU, CRISTINA BISCHIN, LAURIAN VLASE, Comparative HPLC-MS Analysis of Phenolics from <i>Achillea Distans</i> and <i>Achillea Millefolium</i> and Their Bioactivity	257
CAMELIA CIOBOTARIU, LUCIAN CORNEL POP, DAN PORUMB, Solvatochromism of Asymmetrical Substituted 3,7-Diamino- phenothiazinium Dye	267
GEORGE LIVIU POPESCU, NICOLAE FILIP, ANDREIA MOLEA, VIOLETA POPESCU, The Effect of Using Pyrolysis Oils from Polyethylene and Diesel on the Pollutant Emissions from a Single Cylinder Diesel Engine	273
CARMEN MÂNZATU, BOLDIZSÁR NAGY, ANAMARIA TÖRÖK, LUMINIȚA SILAGHI-DUMITRESCU, MAJDIK CORNELIA, Crystal Violet Dye Biosorption and Phytoextraction Using Living <i>Salvinia</i> <i>Natans</i> and <i>Salvinia Natans</i> Powder: a Comparative Study.....	289

Studia Universitatis Babes-Bolyai Chemia has been selected for coverage in Thomson Reuters products and custom information services. Beginning with V. 53 (1) 2008, this publication is indexed and abstracted in the following:

- Science Citation Index Expanded (also known as SciSearch®)
- Chemistry Citation Index®
- Journal Citation Reports/Science Edition

RADIOCARBON DATING OF AFRICAN BAOBABS WITH TWO FALSE CAVITIES: THE INVESTIGATION OF LUNA TREE

ADRIAN PATRUT^{a,*}, STEPHAN WOODBORNE^b, ROXANA T. PATRUT^c,
GRANT HALL^d, LASZLO RAKOSY^c, KARL F. VON REDEN^e,
DANIEL LOWY^f, DRAGOS MARGINEANU^a

ABSTRACT. The paper discloses the radiocarbon investigation results of the Luna tree, a representative African baobab from Venetia Limpopo Nature Reserve, South Africa. Several wood samples collected from deep incisions in the trunk were investigated by AMS (accelerator mass spectrometry) radiocarbon dating. The age sequence of segments extracted from the oldest sample demonstrates that ages increase with the distance into the wood up to a point of maximum age, after which ages decrease toward the sample end. This anomaly is typical for multi-stemmed baobabs, having a closed ring-shaped structure with a false cavity inside. Dating results reveal that each of the two large fused units, which build the Luna tree, consist of such a closed ring. The two closed rings include two interconnected false inner cavities. False cavities are empty spaces between fused stems that were never filled with wood. We named this baobab architecture, which has a very high symmetry, double closed ring-shaped structure with two false cavities. The new architecture, which is very uncommon, enables baobabs to reach large sizes and very old ages. The radiocarbon date of the oldest sample segment was 1507 ± 22 BP, which corresponds to a calibrated age of 1405 ± 20 yr. We estimate that the oldest part of Luna tree has an age of 1600 ± 100 yr. By these results, the Luna tree becomes the fourth oldest African baobab with accurate dating results.

Keywords: AMS radiocarbon dating, *Adansonia digitata*, tropical trees, age determination, inner cavity, multiple stems.

^a Babeș-Bolyai University, Faculty of Chemistry and Chemical Engineering, 11 Arany Janos, RO-400028, Cluj-Napoca, Romania.

^b iThemba Laboratories, Box 722 Somerset West, 7129, South Africa.

^c Babeș-Bolyai University, Faculty of Biology and Geology, 44 Gheorghe Bilascu, RO-400015, Cluj-Napoca, Romania.

^d Mammal Research Institute, University of Pretoria, 0001, South Africa.

^e NOSAMS Facility, Dept. of Geology & Geophysics, Woods Hole Oceanographic Institution, Woods Hole, MA 02543, U.S.A.

^f Nova University, 5000 Dawes Ave., Alexandria, VA 22311, U.S.A.

* Corresponding author: apatrut@gmail.com

INTRODUCTION

The genus *Adansonia* which belongs to the Bombacoideae, a subfamily of Malvaceae, consists of nine species. The African baobab (*Adansonia digitata* L.), which is the biggest and best-known of the *Adansonia* species, has a natural distribution in mainland Africa between the latitudes 16° N and 26° S, especially in savanna regions. It can also be found outside Africa, in areas throughout the tropics, where it was introduced [1-7].

Large baobabs are considered living natural monuments. Based on the impressive size of several specimens, certain tree experts considered that the baobab lives to an old age, possibly over 1,000 years. The age of the oldest baobab specimens has remained, however, a controversial topic. Dating accurately large baobabs has proven to be a very difficult task, due to their wide trunk, the presence of hollow parts and the rather faint growth rings [1,4-13].

The baobab produces faint growth rings, considered by many researchers to be annual rings. Nevertheless, for large and old baobabs, a hypothetically accurate ring counting is not possible, as growth rings may no longer be observed in certain areas of the trunk and they are also missing in the area of large cavities [1,5,6]. In addition, for several large baobab stems we identified the growth stop phenomenon, which is due to old age or to prolonged stress conditions. We also found that for several baobab architectures, when considering a given wood segment, the number of counted rings is typically lower than the calendar age determined by radiocarbon dating; this difference increases with the age of the segment. That is why ring counting and ring width analysis are not effective for evaluating the age of big baobabs. Therefore, radiocarbon dating represents the sole accurate method for determining the age of large and old baobabs [5,12-20].

In 2005, we started an in-depth research project to elucidate several controversial or poorly understood aspects regarding the architecture, growth and age of the African baobab. This research is based on our new approach which enables investigation of standing live specimens. Our approach consists of AMS (accelerator mass spectrometry) radiocarbon dating of small wood samples collected especially from inner cavities, but also from deep incisions/entrances in the stems, fractured/broken stems and from the outer part/exterior of large baobabs [16,20]. This methodology involves a very careful analysis and interpretation of the AMS radiocarbon dating results.

The dating results have revealed that all large baobabs are typically multi-stemmed. The radiocarbon investigation of large African baobabs has demonstrated that their architecture is much more complex than previously believed. We identified the so-called open and closed ring-shaped structures, which are the most important architectures that enable African baobabs to reach old ages and large sizes. We also described the false cavities, which are large

natural empty spaces between fused stems disposed in a closed ring-shaped structure. The oldest dated *A. digitata* specimens were found to have ages up to 2000 years. According to these values, the African baobab becomes the angiosperm with the longest life span [5,12,13,15-17,20].

Here we describe a new variation of the closed ring-shaped structure, namely baobabs with two fused closed rings and two false cavities. We identified this new architecture in the investigation of Luna tree, a large and old baobab from South Africa.

RESULTS AND DISCUSSION

The Luna tree and its area. The Luna tree is located within the Venetia Limpopo Nature Reserve, Limpopo Province, South Africa. The Venetia Reserve is positioned in the most northern part of South Africa, slightly south of the meeting point with Botswana and Zimbabwe. It is a private fenced park, with an extent of 345 km², owned by De Beers Diamond Mining Company. The Luna tree is situated in the former Luna farm, close to the Venetia Diamond Mine, the largest producer of diamonds in South Africa. Its GPS coordinates are 22°22.830' S, 029°22.065' E and the altitude is 682 m. Mean annual rainfall in the area is 366 mm (Pontdrift station).



Figure 1. General view of Luna tree taken from the west, during the dry season.



Figure 2. General view of Luna tree taken from the east, during the wet season.
The sampling point 4 is also shown.

The Luna tree has a maximum height of 17.2 m, the circumference at breast height (cbh; at 1.30 m above ground level) is 20.02 m and the overall wood volume (trunk and branches) is around 170 m³. The big trunk consists of two large units (A and B), which are almost completely fused up to a height of ca. 3-4 m and has a prominent buttressed base (**Figures 1 and 2**).

The two units have distinct canopies. On the western side, over the buttress, there are two deep scars in both units, which originate from severe damages in the past, probably including fire episodes. The scar in the northern unit (A) is considerably larger than that in the southern unit (B). Between the two scars, at a height of 1.48 m above ground, there is a narrow elliptical opening into a large central cavity (**Figure 3**). The opening is accessible only for bats and small animals; it is, however, large enough for taking photographs and laser measurements inside. The cavity consists of two connected rooms. The quasi-conical northern cavity room (in unit A) has an ellipsoidal basis, with the axes of 1.98 x 1.35 m and a height of 5.32 m to the ceiling; the corresponding dimensions of the southern cavity room (in unit B) are of 2.41 x 1.70 x 6.69 m. The inner cavity walls are completely covered by bark.

Wood samples. Four wood samples were collected from the outer part of the two units which build the trunk of Luna tree. Two samples (labelled 1 and 2) originate from the large scar in unit A (located on the western side),

while one sample (labelled 3) was extracted from the scar in unit B (also, on the western side) and another (labelled 4) from an incision on the opposite part (eastern side).

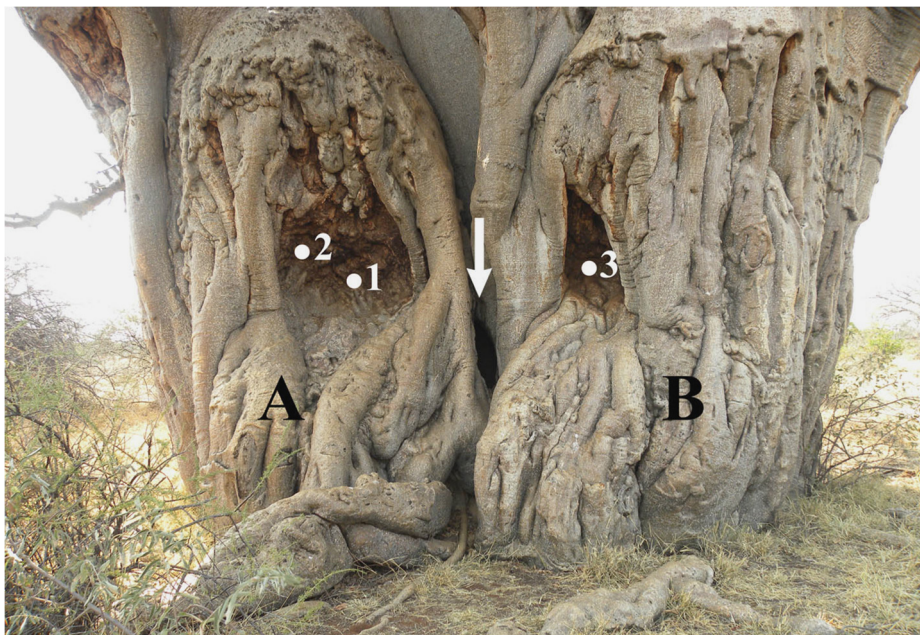


Figure 3. Detail of the western side of Luna tree showing the two units of its trunk (A, B), the two large scars, three sampling points (1, 2, 3) and the opening into the cavity (marked by an arrow).

Given the buttressed trunk, the samples were collected at greater heights than usually, i.e., 2.35, 2.60, 2.40 and 2.60 m. Even if the penetration of the borer in the wood was quasi-complete in all cases, the four samples are relatively short, namely 0.175, 0.22, 0.22 and 0.265 m; this reveals the presence of hollow parts inside the two units. The sampling positions are shown in **Figures 2, 3 and 4**. Thirteen small pieces/segments, each of the length of 0.001 m (marked as a, b, c, d), were extracted from determined positions of the four samples. The segments were processed and investigated by AMS radiocarbon dating.

AMS results and calibrated ages. Radiocarbon dates of the 13 segments extracted from the four samples are listed in Table 1. Radiocarbon dates and errors were rounded to the nearest year. The radiocarbon dates are expressed in ^{14}C yr BP (radiocarbon years before present, i.e., before the reference year AD 1950).

Calibrated (cal) ages, expressed in calendar years, are also shown in Table 1. The $1-\sigma$ probability distribution was selected to derive calibrated age ranges. For four sample segments, the $1-\sigma$ distribution is consistent with only one calibrated age range, while for other five segments the $1-\sigma$ distribution corresponds to two age ranges. For these segments, the confidence interval of one range is, with one exception, considerably greater than that of the others; therefore, it was selected as the cal AD range of the segment for the purpose of this discussion. For segment 4b, the two confidence intervals have close values, both being selected as cal AD ranges.

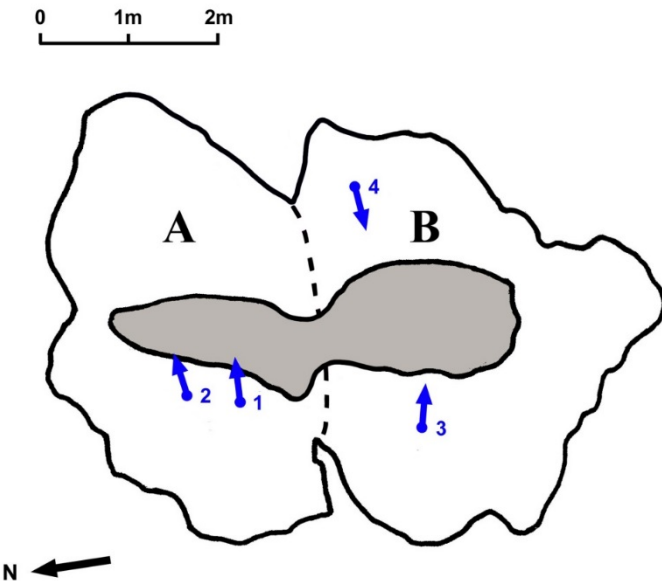


Figure 4. Transversal section of the trunk of Luna tree at 1.3 m above ground. The two units (A, B) and the projection of sampling points (1-4) are marked. The false cavity inside the two units is displayed in grey.

To obtain single age values of sample segments, we derived a mean calendar age of each segment from the selected range (marked in bold). Ages of segments represent the difference between AD 2015 and the mean value of the selected range, with the corresponding error. Ages and errors were rounded to the nearest 5 yr.

For four sample segments, ages fall after AD 1950 (0 BP), namely the ^{14}C activity, expressed by the ratio $^{14}\text{C}/^{12}\text{C}$, is greater than the standard activity in the reference year 1950. Such values, which correspond to negative radiocarbon dates, are termed greater than Modern (>Modern). In these cases, the dated wood is young, being formed after AD 1950.

Table 1. AMS Radiocarbon dating results and calibrated calendar ages of samples/segments collected from the Luna tree.

Sample (Segment)	Depth ¹ [height ²] (10 ⁻² m)	Radiocarbon date [error] (¹⁴ C yr BP)	Cal AD range 1- σ [confidence interval]	Sample age [error] (yr)
1a	5.5 [235]	880 [\pm 24]	1181-1226 [68.2%]	810 [\pm 20]
1b	11.5 [235]	1507 [\pm 22]	590-632 [68.2%]	1405 [\pm 20]
1c	14.5 [235]	1280 [\pm 25]	766-860 [68.2%]	1200 [\pm 45]
1d	17.5 [235]	870 [\pm 25]	1185-1230 [59.3%] 1251-1260 [8.9%]	810 [\pm 20]
2a	5 [260]	–	–	>Modern
2b	17 [260]	75 [\pm 26]	1816-1832 [24.6%] 1892-1922 [43.6%]	110 [\pm 15]
2c	21.5 [260]	–	–	>Modern
3a	5 [240]	909 [\pm 24]	1162-1211 [68.2%]	830 [\pm 25]
3b	15.5 [240]	–	–	>Modern
3c	21.5 [240]	–	–	>Modern
4a	7.5 [260]	64 [\pm 29]	1816-1832 [24.8%] 1892-1923 [43.4%]	110 [\pm 15]
4b	18.5 [260]	709 [\pm 28]	1292-1316 [33.2%] 1356-1381 [35.0%]	710 [\pm 10] or 645 [\pm 15]
4c	25.5 [260]	975 [\pm 30]	1045-1094 [37.8%] 1106-1153 [30.4%]	945 [\pm 25]

¹ Depth in the wood from the sampling point.² Height above ground level.

Dating results of samples (segments). The most interesting dated sample is 1, out of which we investigated four segments. Two segments, 1b and 1c, were found to have radiocarbon dates considerably greater than 1000 BP. The oldest segment 1b originates from a distance of 0.12 m in the wood from the sampling point; the latter is located at a depth of ca. 0.85 m in the

large incision/scar in unit I. Its radiocarbon date of 1507 ± 22 BP corresponds to a calibrated calendar age of 1405 ± 20 yr. The second oldest segment 1c, which originates from a depth of 0.15 m into the wood, was found to have a radiocarbon date of 1280 ± 25 BP and an age of 1200 ± 45 yr. The dating results of the four segments extracted from sample 1 show that the age values increase with the distance/depth into the wood up to a point of maximum age, i.e., segment 1b, after which they decrease toward the cavity.

The ages of two segments of sample 2, i.e., 2a and 2c, fall after AD 1950, being unexpectedly young. The age of the middle segment 2b is also young, around 110 yr. Such values demonstrate that the three dated segments consist of recent regrowth layers and not of the original old wood. Baobabs exhibit an unusual self-healing ability deep within the stem and also in their larger or smaller cavities. The new growth layers are due to repairing the interior xylem after significant wood damage, likely triggered by fire [16]. The ages of segments extracted from sample 2 evince at least two significant damages in this area of Luna tree, which occurred around AD 1900 and after AD 1950. The last fire damage after AD 1950, which triggered the youngest regrowth layer, affected not only the outer part, but also the cavity inside unit I.

For sample 3, only the first segment 3a consists of the original old wood. Its radiocarbon date of 909 ± 24 BP corresponds to a calibrated age of 830 ± 25 yr. The ages of the deeper segments 3b and 3c, which are very close to the cavity inside unit B, fall after AD 1950 and consist of regrowth. These results show that the last fire affected to a certain extent both rooms of the cavity.

For sample 4, the only one collected from the eastern side of unit B, we dated three segments. As expected, their ages exhibit a continuous increase with the depth into the wood. The oldest segment 4c was dated to 975 ± 30 BP and is 945 ± 25 yr old.

Architecture of Luna tree. Our long term research, based extensively on AMS radiocarbon dating, has revealed that all big African baobabs are multi-stemmed. The majority of baobabs start growing as single-stemmed trees. Over time, single-stemmed individuals become multi-stemmed owing to the baobabs' ability to produce periodically new stems, as other tree species produce branches. Typically, new stems shoot from the roots or emerge from fallen stems. Over time, the new stems may fuse with older stems or among them [17].

With a few exceptions, we investigated and dated the 50 largest known African baobab specimens, which are distributed in mainland Africa, African islands and Asia. In this respect, the Luna tree, with its very complex structure, was probably the most difficult to investigate and interpret of all big baobabs. The Luna tree consists of two fused units, each with a heavily buttressed base.

It has a large inner cavity with two rooms, which are inaccessible for people; the tree also has two big scars, one in each unit, due to severe damages in the past. There are several hollow parts in the wood of each unit and also several regrowth layers triggered by successive fire damage. There are buttressed roots all around the trunk and several “ornamental features” for a better anchorage. Consequently, it was difficult to find adequate sampling points in the trunk of Luna tree and, in addition, the collected wood samples were short.

It was, however, possible to determine the general architecture of Luna tree from the ages of the four segments extracted from sample 1, which originate from unit A (Table 1). The age sequence shows that the ages increase with the distance into the wood from the sampling point up to a point of maximum age (1b), after which they decrease toward the end of the sample, in the direction of the cavity. We identified and disclosed this anomaly, which is specific only to the closed ring-shaped structure, the most enigmatic architecture of the African baobab and of other baobab species. We also described the closed ring-shaped structure, which consists of several fused stems disposed in a ring, with an empty space inside. We termed this natural empty space between the fused stems as false cavity [17,19].

The Luna tree consists of two distinct units (A and B), which are fused up to a height of 3-4 m. The two units, which are very similar, have the same architecture, i.e., a closed ring-shaped structure. Consequently, in the case of Luna tree, we identified for the first time baobabs with two closed rings. We called this new architecture double closed ring-shaped structure.

Our research on baobabs evinced that the number of fused stems, which build the closed ring, varies between three and eight [17]. In principle, the number of stems can be determined from the analysis of radiocarbon dates of many samples collected from different areas of the tree, combined with a careful visual inspection of the false cavity, the trunk and the canopy for identifying stems and possible fusion lines [17,19]. In the case of Luna tree, due to the very high buttress and to the presence of hollow parts inside its trunk, the sampling was difficult, the samples were too short and their number was insufficient for an accurate determination of the number of stems which build each closed ring. However, after analysing the photographs of the Luna tree, taken from all directions, we can conclude that each unit is composed of four fused stems.

False cavities of Luna tree. In previous work, we described the false cavities and how they differ from normal/true cavities. Large normal cavities occur by wood removal, due to fungi decay, fire, animal or human damage; the pith/centre of the stem is located inside the cavity. False cavities are natural empty spaces between fused stems disposed in a closed ring-shaped structure. These empty spaces were never filled with wood. The oldest part of the fused

stems is positioned between the false cavity walls and the outer part/exterior of each stem, always closer to the cavity. Normal cavities usually have irregular shapes and are not very tall (1.0–2.7 m). By contrast, false cavities are much larger and taller (3.0–8.3 m), have more regular shapes and their lower part is located at ground level. The first noticeable difference between false and normal cavities is the presence or absence of the bark inside the cavity. While normal cavities become larger over time due to continuous decay, false cavities become smaller because of stem growth [17,19]. The false cavities are associated with the presence of closed ring-shaped structures.

The described characteristics of false cavities fit very well the large inner cavity of Luna tree. The lower part is located at ground level (**Figure 5a**), its ceiling is very high (**Figure 5b**) and the cavity walls are covered by bark. As already mentioned, the Luna tree consists of two units, having each a ring-shaped structure. Each ring-shaped structure includes mandatory a false cavity between the fused stems. Consequently, the Luna tree includes two interconnected false cavities, rather than a false cavity with two connected rooms.

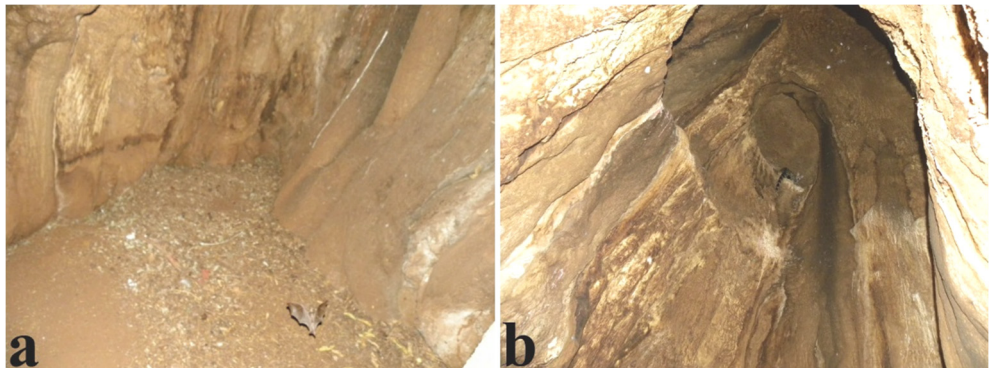


Figure 5. The images show the lower part of the inner false cavity in unit B (a) and the typical ceiling of the false cavity in unit A (b). One can notice that the walls of both cavities are covered by bark.

Age of Luna tree. One can state beyond any doubts that the age of the oldest part of Luna tree exceeds the age of the oldest dated sample segment 1b, i.e., 1405 ± 20 yr. This value corresponds to the point of maximum age of sample 1, which was collected from the large scar in unit A, located on the western side. However, the two rings are not yet completely closed, the still open part being the connection area of the two false cavities (**Figure 4**). We consider that the parent stem of the ring in unit A is located in the opposite

direction to the still open part of the rings/false cavities, namely on the northern side. Because sample ages demonstrate that the growth of Luna tree was extremely slow over its life cycle, we estimate that the parent stem of the ring in unit A started growing at least 200 yr prior to the stem from which sample 1 originates. In this estimate, the Luna tree has an age of 1600 ± 100 yr. Thus, this baobab has started growing around AD 400.

The oldest dated sample segments collected from unit B are considerably younger, up to 945 ± 25 yr. This is probably a consequence of collecting short samples, given the presence of hollow parts in the wood; therefore, the points of maximum age were not reached. By considering that the two units and their canopies are quasi-similar, we consider that both units of Luna tree may have comparable ages.

CONCLUSIONS

Our research reports the results of the AMS radiocarbon investigation of Luna tree, a large African baobab from Venetia Limpopo Nature Reserve, South Africa. The research was performed for determining the architecture and age of the baobab. A number of four wood samples were collected from deep incisions in the trunk of Luna tree, which consists of two units and has a large inner cavity with two rooms. The age sequence of the dated segments from the oldest sample shows that ages increase with the distance into the wood up to a point of maximum age, after which they decrease toward the sample end. This anomalous age sequence is specific only to baobabs which have a multi-stemmed closed ring-shaped structure with a false cavity inside. In the case of Luna tree, each unit possesses such a closed ring. We also learned that the inner cavity with two rooms consists, in fact, of two interconnected false cavities. Consequently, for Luna tree, we identified for the first time a new architecture of the baobab, namely the double closed ring-shaped structure with two false cavities.

The radiocarbon date of the oldest sample segment was found to be 1507 ± 22 BP, which corresponds to a calibrated age of 1405 ± 20 yr. By considering the architecture of the baobab, we conclude that the oldest part of Luna tree has an age of 1600 ± 100 yr. By these values, the Luna tree becomes the fourth oldest African baobab with accurate dating results.

According to our research, the closed ring-shaped structure with a false cavity inside is seldom among African baobabs. Typically, this architecture enables baobabs to reach large sizes and old ages. We determined that the oldest dated specimen with single closed ring-shaped structure is the Lebombo Eco Trail baobab from Mozambique, with an age of 1400 yr [17].

In the current research, we identified a new architecture, that we named double closed ring-shaped structure with two false cavities. This architecture is exceptionally rare for baobabs and enables them to reach even older ages than the single ring-shaped structure, namely up to 1600 yr for Luna tree and 1750 yr for Holboom, a very large baobab from Namibia.

EXPERIMENTAL SECTION

Sample collection. The four wood samples were collected with a Haglöf CH 600 increment borer (60 cm long, 0.54 cm inner diameter). A number of small pieces/segments of the length of 0.1 cm were extracted from determined positions of the original four samples. These segments were processed and investigated by AMS radiocarbon dating.

Sample preparation. The standard acid-base-acid pretreatment method [21] was used for removing soluble and mobile organic components. The obtained samples were combusted to CO₂, via the closed tube combustion method [22]. Then, CO₂ was reduced to graphite on iron catalyst, under hydrogen atmosphere [23]. Finally, the resulting graphite samples were analysed by AMS.

AMS measurements. AMS radiocarbon measurements were performed at the NOSAMS Facility of the Woods Hole Oceanographic Institution (Woods Hole, MA, U.S.A.) by using the Pelletron ® Tandem 500 kV AMS system [24]. The obtained fraction modern values, corrected for isotopic fractionation with the normalized $\delta^{13}\text{C}$ value of -25‰, were ultimately converted to a radiocarbon date.

Calibration. Radiocarbon dates were calibrated and converted into calendar ages with the OxCal v4.2 for Windows [25], by using the SHCal13 atmospheric data set [26].

ACKNOWLEDGMENTS

Authors thank De Beers Diamond Mining Company, Duncan MacFayden Research Centre and The South African National Parks for granting access in the reserve and for authorising the investigation of Luna tree. Authors also thank Diana Mayne, Thomas Huffman and Sarah Venter for support in the investigation and sampling of the baobab. The research was funded by the Romanian Ministry of National Education CNCS-UEFISCDI under grant PN-II-ID-PCE-2013-76.

REFERENCES

- [1]. G.E. Wickens, P. Lowe, "The Baobabs: Pachycauls of Africa, Madagascar and Australia", Springer, Dordrecht, **2008**, pp. 232–234, 256–257, 295–296.
- [2]. D.A. Baum, *Annals of the Missouri Botanical Garden*, **1995**, 82, 440–471.
- [3]. J.D. Pettigrew, L.K. Bell, A. Bhagwandin, E. Grinan, N. Jillani, J. Meyer, E. Wabuyele, C.E. Vickers, *Taxon*, **2013**, 61, 1240–1250.
- [4]. G.E. Wickens, *Kew Bulletin*, **1983**, 47, 173–209.
- [5]. A. Patrut, K.F. von Reden, D.A. Lowy, A.H. Alberts, J.W. Pohlman, R. Wittmann, D. Gerlach, L. Xu, C.S. Mitchell, *Tree Physiology*, **2007**, 27, 1569–1574.
- [6]. F. von Breitenbach, *Journal of Dendrology*, **1985**, 5, 1–21.
- [7]. J.G. Adam, *Notes Africaines*, **1962**, 94, 33–44.
- [8]. S. Woodborne, G. Hall, I. Robertson, A. Patrut, M. Rouault, N.J. Loader, M. Hofmeyr, *PLoS ONE*, **2015**, 10(5), e0124202, doi: 10.1371/journal.pone.0124202.
- [9]. T. Pakenham, "The Remarkable Baobab", Weidenfeld & Nicholson, London, **2004**.
- [10]. R. Watson, "The African Baobab", Struik, Cape Town, **2007**.
- [11]. J. Robertson, N.J. Loader, C.A. Froyd, N. Zambatis, I. Whyte I, *Applied Geochemistry*, **2006**, 21, 1674–1680.
- [12]. A. Patrut, D.H. Mayne, K.F. von Reden, D.A. Lowy, S. Venter, A.P. McNichol, M.L. Roberts, D. Margineanu, *Radiocarbon*, **2010**, 52, 727–734.
- [13]. A. Patrut, K.F. von Reden, D.H. Mayne, D.A. Lowy, R.T. Patrut, *Nuclear Instruments and Methods in Physics Research Section B*, **2013**, 294, 622–626.
- [14]. E.R. Swart, *Nature*, **1963**, 198, 708–709.
- [15]. A. Patrut, K.F. von Reden, D.A. Lowy, D.H. Mayne, K.E. Elder, M.L. Roberts, A.P. McNichol, *Nuclear Instruments and Methods in Physics Research Section B*, **2010**, 268, 910–913.
- [16]. A. Patrut, D.H. Mayne, K.F. von Reden, D.A. Lowy, R. Van Pelt, A.P. McNichol, M.L. Roberts, D. Margineanu, *Radiocarbon*, **2010**, 52, 717–726.
- [17]. A. Patrut, S. Woodborne, K.F. von Reden, G. Hall, M. Hofmeyr, D.A. Lowy, R.T. Patrut, *PLoS ONE*, **2015**, 10(1), e0117193, doi: 10.1371/journal.pone.0117193.
- [18]. A. Patrut, K.F. von Reden, P. Danthu, J.-M. Leong Pock-Tsy, R.T. Patrut, D.A. Lowy, *PLoS ONE*, **2015**, 10(3), e0121170, doi: 10.1371/journal.pone.0121170.
- [19]. A. Patrut, K.F. von Reden, P. Danthu, J-M. Leong Pock-Tsy, L. Rakosy, R.T. Patrut, D.A. Lowy, D. Margineanu, *Nuclear Instruments and Methods in Physics Research Section B*, **2015**, 361, 591–598.
- [20]. A. Patrut, K.F. von Reden, R. Van Pelt, D.H. Mayne, D.A. Lowy, D. Margineanu, *Annals of Forest Science*, **2011**, 68, 993–1003.
- [21]. I.U. Olsson, Radiometric Methods. In: B. Berglung, editor "Handbook of Holocene palaeoecology and palaeohydrology", Wiley, Chichester, **1986**, pp. 273–312.
- [22]. Z. Sofer, *Analytical Chemistry*, **1980**, 52, 1389–1391.

- [23]. J.S. Vogel, J.R. Southon, D.E. Nelson, T.A. Brown, *Nuclear Instruments and Methods in Physics Research Section B*, **1984**, 5, 289-293.
- [24]. M.L. Roberts, J.R. Burton, K.L. Elder, B.E. Longworth, C.P. McIntyre, K.F. von Reden, B.X. Han, B.E. Rosenheim, W.J. Jenkins, E. Galutschek, A.P. McNichol, **2010**, 52, 228-235.
- [25]. C. Bronk Ramsey, *Radiocarbon*, **2009**, 51, 337-360.
- [26]. A.G. Hogg, Q. Hua, P.G. Blackwell, M. Niu, C.E. Buck, T.P. Guilderson, T.J. Heaton, J.G. Palmer, P.J. Reimer, R.W. Reimer, C.S.M. Turney, R.H. Zimmerman, *Radiocarbon*, **2013**, 55, 1889-1903.

MULTI-METHOD ANALYSIS OF BRONZE AGE CERAMICS FROM SATU-MARE COUNTY, ROMANIA

EMŐKE NAGY^a, MÁRTA GUTTMANN^{b,c}, ZSOLT MOLNÁR-KOVÁCS^d,
RÉKA BARABÁS^{a,*}

ABSTRACT Bronze Age settlements have been discovered in the region of river Eriu, Satu Mare County, Romania. This study includes the archaeometric examination of eight ceramic artifacts dated from Early to Middle Bronze Age, representing the Otomani culture. The used methods were petrography, scanning electron microscopy (SEM) equipped with energy-dispersive X-ray spectroscopy (EDX), X-ray powder diffraction (XRD), Fourier-transform infrared spectroscopy (FT-IR) and thermal analysis (thermal gravimetric analysis - TGA and differential scanning calorimetry - DSC). The study of archaeological ceramics needs an interdisciplinary approach, where the scientific research can have an important role in supporting the archaeological study. Our aim was to support by scientific methods the archaeological assumptions, which describe the culture, their knowledge and opportunities. For this purpose we wanted to select the most appropriate measuring methods and how can the measuring results complete each other for a complex description of the culture. Therefore, the evaluation methodology of the measurement data was given an increased importance. The selection of the samples depended on archaeological background, therefore the samples allowed a case study for the testing of the measuring methods. The mineral-petrographic analysis included the approximation of firing temperature, identification of potential raw material sources, similarity between samples and the determination of the technology used. Additional objective was the establishment of usability for the testing methods to have accurate measurements. Loam from the region was also analyzed and compared with the results of the ceramic samples.

Keywords: ancient ceramics, physical and mineralogical analyses, reference loam, Bronze Age, Otomani culture, Romania

^a Babeş-Bolyai University, Department of Chemical Engineering of the Hungarian Line of Study, Arany János no. 11, 400028 Cluj-Napoca, Romania.

^b National History Museum of Transylvania, Head of Conservation Department, Constantin Daicoviciu no. 2, 400020 Cluj-Napoca, Romania.

^c Lucian Blaga University of Sibiu, Faculty of Social and Human Sciences, Conservation Department, B-dul Victoriei no.10, 550024 Sibiu, Romania.

^d Babeş-Bolyai University, Department of History, Mihail Kogălniceanu no. 1, 400084 Cluj-Napoca, Romania.

* Corresponding author: breka@chem.ubbcluj.ro

INTRODUCTION

The excavated ceramic artifacts represent the culture of Carei in the second millennium B.C. The settlement concatenation named Bobald established a culturally varied society which entailed numerous finding collections. In this North-Romanian region could evolve an unified ceramic direction.

The first human settling on the plain of Carei was in the late neolithic. Later in the third part of the early Bronze Age the Sanislau group dominated the region. In the middle Bronze Age the settlement concatenation of Bobald developed its own culture without seceding from the Otomani culture. The middle Bronze Age can be divided into three parts, each of them note another developing stage in the Otomani culture (*Fig. 1*).

The existing settlement concatenations had a central and more, smaller settlements which were located in form of a satellite ring. In case of Carei-Bobald five ancient settlements together with the central settlement created a concatenation with representative pottery and bronze culture.

The characteristics of the artifacts can be determined by proper evaluation of the measurement results, but these are not always precise, depending on the method used or on the fact that the properties of the clay depend on several factors between the moment of manufacturing and measuring, like usage, burial, excavation, cleaning and storage, which appear as critical effects.

Due to this fact it is important to reduce the available measuring methods for more accurate results. It is also important the comparative study of the local, reference loam with the artefacts, since they can form the basis for the determination of composition and helps also in the reconstruction of the technology used. This permits the closer examination of the culture from Bronze Age.



Figure 1. The map of excavation locations in Satu Mare County (Berveni, Capleni, Carei, Tiream, Andrid and Pir). The settlement Sanislau represents source the cultural influence in this region besides the Otomani culture.

RESULTS AND DISCUSSION

The aim of the study was to use the results of different measuring methods to scientifically describe the given culture from Bronze Age. This means a wider data set but in the same time more valid information. The information received from one of the measurements complete or form the basis of evaluation in case of another measured data.

Besides the supplement of the archaeological background we also wanted to test the usability of the methods to find the necessary and sufficient information amount for future measurements.

Petrography

A significant similarity was observed in the color of the samples varying shades of gray to black, referring to reductive firing conditions. The only exception was represented by sample no. 12 with a sandwich structure of black interior and lighter outer layers. This layered texture suggested a short-term firing, where the oxygen diffusion was insufficient to unify the color.

The matrix is considered relatively homogenous, however iron aggregates can be also found in some cases. It can be also observed the presence of ceramoclasts in each sample, which makes up 2-3 % of the matrix. The 1 mm thin layer on the outer wall indicates subsequent modification, not an alteration-taking place during firing process.

According to the granulometry, samples can be divided in two categories, medium-fine-grained and coarse-grained ceramics with the maximum particle of 1-2 mm. Based on the ratio between crystalline vs. amorphous phases in the matrix, two fabric types can be defined: microcrystalline and microcrystalline to microcrystalline - amorphous. The characteristic of the matrix and also the dominant presence of illite, kaolinite and montmorillonite confirmed a lower firing temperature than 900°C.

The crystalloclasts are represented by quartz, micas (muscovite and biotite) [1], iron oxide (hematite) and plagioclase as part of the feldspar group (albite, anorthite), epidote, garnet and zircon [2], [3], [4]. The calcite, which is present on the fissures, also suggests that the firing temperature didn't exceed 850-900°C.

The porosity had limited values varying between the pore size of 0.5 x 1.5 and 2.0 x 3.0 mm. This could be observed in case of long, elongated pores, which extended parallel with one another, as in the case of the secondary, irregular pores.

The oval shape of the pores and the parallel position of the mica also reflected the production technology, which in this case was plastic squeezing. The specific properties of the samples can be seen on *Table 1*.

Table 1. The results of the SEM, XRD and petrography analysis:

Sample No.	Estimated Firing Temperature (°C)		Composition Petrography
	SEM	XRD	
1.	700-900	700-850	Crystalloclasts (quartz, micas) Ceramoclasts in a microcrystalline matrix Microcrystalline matrix with carbonate and quartzite
2.	~ 900	700-850	litoclasts Crystalloclasts (garnets, zircon, micas) Microcrystalline matrix with ceramoclasts
3.	~ 700	750-850	Aggregates of iron oxides-hydroxides Crystalloclasts (feldspar, quartz, micas) Microcrystalline matrix with ceramoclasts
4.	700-900	700-850	Carbonatic litoclast Crystalloclasts (quartz, micas)
5.	< 900	700-900	Crystalloclasts (quartz) Ceramoclasts Microcrystalline matrix
6.	700-900	700-900	Secondary calcite on the wall Carbonatic litoclast Crystalloclasts (quartz, micas)
11.	700-900	750-900	Crystalloclasts (quartz) Ceramoclasts
12.	700-900	750-900	Microcrystalline matrix with iron oxide-hydroxide aggregates Crystalloclasts (feldspars, quartz, micas)

SEM/EDX

EDX analysis

Due to the examination it was ascertained the composition of the reference loam and all of the artifacts.

The composition varied from sample to sample; even so the main chemical elements were silicon, aluminum and oxygen. The additional components also didn't show significant variety, which increased the probability of raw materials from the same region.

The composition of the reference loam was compared with the ceramic artifacts. The widest similarity showed sample no. 3 which refers not only to the components but also to the weight percentage values. This result sustained the usage of similar raw materials in this case. Due to this where only one measurement was possible sample no. 3 was analyzed.

SEM analysis

The first case is the reference loam fired at 300°C (*Fig. 2; letter a*) the rough grains, sharp particles such as lumpy texture was representative and no sign of softening appeared.

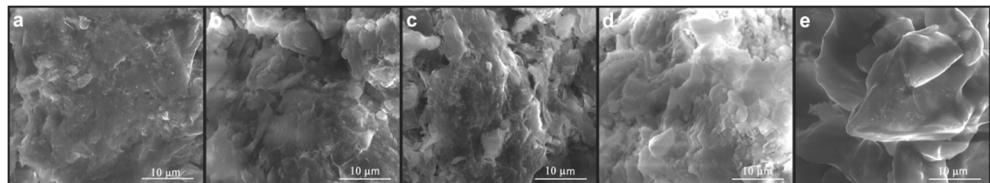


Figure 2. The SEM images of reference loam fired at 300°C (a), 500°C (b), 700°C (c), 900°C (d) and 1100°C (e).

Firing the reference loam at 500°C (*Fig. 2; letter b*) no considerable external changes appeared similar as above.

Firing the loam at 700 (*Fig. 2; letter c*) and 900°C (*Fig. 2; letter d*) it could be seen that the increase of the temperature still didn't affect significantly the surface of the particles, however, the grains started to stick together and the individual particles started to form larger ones.

The most remarkable change was observed by firing the reference loam at 1100°C (*Fig. 2; letter e*): it could be seen that the interface was completely changed, the particles were merged and the surface was softened.

The firing temperature estimation was based on the 2000- and 4000-fold magnification images, which were compared to the images made on the reference loam. The samples no. 1, 4, 6, 11 and 12 the estimated firing temperature range was 700-900°C. In case of sample no. 2 and 5 the temperature trends to 900°C while at sample no. 3 this value is 700°C [5].

As an overview: the determination of the firing temperature was difficult in the interval 300-900°C which can be attributed to several factors like the point wise analysis and the powdered form of the artifacts.

On the other hand, the morphological changes were hardly detectable under 1100°C as it was in case of reference loam. Although the effect of increasing firing temperature was plain, the estimation of firing temperature was difficult; therefore the interval was wider, which can be seen in *Table 1*.

XRD analysis

XRD analysis of reference loam

Through the XRD analysis the phase transitions during firing and the representative stability intervals for the components were studied.

The evaluation of the diffractograms was made by program Match 1.9a. Therefore it was detected the mineralogical composition, in addition, the program enabled the weight percent proportion of the samples by a semi-quantitative analysis based on the ratio of intensities.

Quantitatively the most relevant mineral was quartz, which appears as α -quartz and turns into β -quartz at 573°C [6], respectively appears as α -cristobalite. As a component of feldspars anorthite is also present in significant quantities. As part of the same mineral group microcline and albite appeared as well. Kaolinite and illite, the representatives of the clay mineral group were present in varying degrees. In addition the presence of many other minerals was detected despite their low intensities or due to the concurrence of peaks.

The possible components confirmed the presence of the elements presented by EDX analysis. The main elements were oxygen, aluminum, carbon and calcium, which appear as the spectra's main components forming quartz and anorthite.

Changes can be observed during the rising of temperature by the disappearance or formation of phases depending on temperature.

At 300°C and 500°C due to the low temperature the main component was α -quartz marked in the black part of the columns on *Fig. 3*. As the firing temperature was higher the rate of the quartz increased as well, which could be attributed to the decomposition of other phases at lower temperatures.

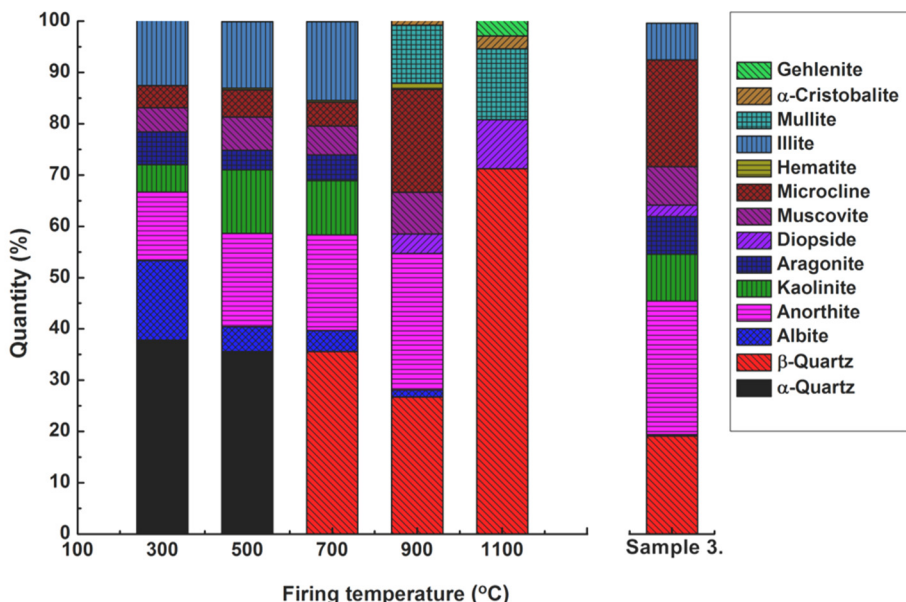


Figure 3. The mineralogical composition of reference loam fired at different temperatures by the semi-quantitative analysis of the program used.

The representatives of the plagioclase group, namely anorthite, and albite, microcline were also present at all firing temperatures, excluding 1100°C. In this wide temperature range these phases were stable [7], [8], [9]. Moreover their proportion was still growing compared to the other phases [10], [11], [12], [13]. Mica was thermally stable up to 500°C [14], but its presence was demonstrated in case of 700 and 900°C as well which could be attributed to a form of muscovite which was stable below 1100°C. The aragonite belonging to the carbonates group it wasn't stable at higher temperatures: it started its decomposition into CaO and CO₂. The studies revealed the presence of aragonite up to 700°C, above this temperature it wasn't demonstrable. The presence of the feldspars and carbonates increases the plasticity of the material, resulting the decreasing of the sintering temperature and a compact product below 1100°C [15]. The kaolinite decomposes to meta-kaolinite around 550°C and forms Al-Si spinel above 925°C, at 1100°C forms mullite and cristobalite. This phase transition can be followed on *Fig. 3*. The kaolinite appeared above 550°C due to the fact that the presence of kaolinite and meta-kaolinite couldn't be distinguished. Since the temperature scale was wide, it couldn't be observed the transformation of meta-kaolinite into spinel.

In addition the participation of the mullite and α -cristobalite denoted the phase transition.

Illite was stable until 750°C, at higher temperature starts its decomposition and ends around 950-1000°C in oxidizing atmosphere, it ends around 850°C in reductive atmosphere, which may result new phases like diopside, anorthite. The formation of new phases brings in the decrease of the amount of illite and the increase of the amount of new phases at higher temperatures [7], [15]. The presence of gehlenite and diopside was observed at 900 and 1100°C, with an increasing proportion. The larger the quantity of CaO is, the higher is the amount of minerals with calcium content, meaning diopside, anorthite and gehlenite [15].

Minerals diopside and mullite are able to take in Fe³⁺ ions due to their crystal structure. Therefore the formation of free iron-oxide (hematite in our case) is not necessary [15]. Nevertheless hematite appeared in small amount at 900 and at 1100°C, which can be attributed to the former fact.

XRD analysis of the artifacts

The estimation of firing temperature of the ceramic artifacts was based on searching for discontinuities in any physical property that can be linked to a specific temperature interval. The description of the culture was performed by more measuring methods. The firing temperature was deduced from XRD results and mineralogical analysis [16].

The type of the clay mineral and the structural changes due to firing were studied by FT-IR and also by SEM as methods for the confirmation of firing temperature. The XRD was used basically for the identification of minerals [17].

The X-ray patterns of the samples were evaluated similarly to the case of reference loam. Based on the weight percentage by the program Match 1.9a and mineral stability it was made a comparison between the reference loam and sample results to estimate their firing temperature.

The mineralogical composition of the samples is presented in *Table 2*. The main components of the ceramic artifacts belong to the silicates group and it was also significant the presence of oxides and carbonates [18]. The representatives of the silicate group were the clay minerals (mainly illite and kaolinite), micas and feldspars.

Table 2. The mineralogical composition of samples according to the interpretation of the X-ray patterns

Sample No.	1.	2.	3.	4.	5.	6.	11.	12.
Illite	x	x	x	x	x	x	x	x
Kaolinite	x	x	x	x	x	x		x
Montmorillonite	x	x	x	x			x	x
Muscovite			x	x	x	x	x	x
Biotite				x		x	x	x
Anorthite	x	x	x	x	x	x	x	x
Microcline	x	x	x	x	x	x	x	x
Albite			x	x	x	x	x	x
Mullite								
Diopside			x	x	x	x		x
Epidote					x			
Zircon					x	x		x
Quartz	x	x	x	x	x	x	x	x
Hematite	x	x		x	x			
Aragonite	x	x	x	x	x	x		x

Considering the weight percent proportion of the appeared elements, no wide variation was observed. The slight variations in the composition of ceramics can be attributed to the slight difference in raw materials or due to the prolonged or repeated exposure to heat, in addition could have differed in the speed of heating.

Compared to the artifacts in case of reference loam couldn't be detected more of the minerals, like epidote, zircon, biotite and montmorillonite. Due to their absence they weren't used for the estimation of firing temperature.

Sample no. 1 contained anorthite and microcline, whom presence supported the firing temperature below 1000°C.

The large amount of illite suggested that this temperature could not exceed immoderately 750°C and it was less than 900°C. The absence of mullite and the amount of carbonates alluded to the firing temperature less than 850-900°C.

Similarly to the latter case, sample no. 2 contained anorthite and microcline indicating the firing temperature below 1000°C. The presence of illite, kaolinite (meta-kaolinite) and the absence of mullite, diopside also suggested 900°C as upper limit. The dominance of anorthite compared to illite marked the beginning of decomposition at 700-750°C.

In case of sample no. 3 the reappearance of anorthite, microcline and muscovite meant a firing temperature below 1000°C. This value was changed to 850-900°C by the presence of illite, kaolinite (meta-kaolinite) and carbonates because at this level it started their decomposition.

The diopside in samples no. 4, 5 and 6 indicated a firing temperature above 750°C. The upper limit was 850-900°C shown by the feldspars, muscovite, carbonates, illite and kaolinite.

In the sample no. 11 the illite and anorthite suggested a firing temperature at 700-750°C, the upper limit marked by the illite, feldspar and muscovite as 900°C.

In case of sample no. 12 the absence of illite and mullite, the appearance of diopside, anorthite, feldspar and muscovite clearly assumed a temperature above 750°C and below 900°C.

FT-IR analysis

The FT-IR spectroscopy was used in case of reference loam fired at different temperatures and also on sample no. 3.

The appeared bands sustained the presence of silicates, carbonates and oxides (mainly quartz and iron-oxide). The broadening of the spectral lines can be attributed to the overlapping of the peaks.

The dominant mineral was quartz, which made an appearance at 796-798 cm⁻¹, 778-780 cm⁻¹ and 692-694 cm⁻¹ wave number values [19], [20]. The clay minerals were identified and differentiated from each other at 3432 cm⁻¹ (montmorillonite) and 1033-1038 cm⁻¹ (kaolinite) [20], [21]. The peak at 3432 cm⁻¹ can be also attributed to absorbed water molecules derived from the measurements or the burial of the samples [22].

The presence of iron-oxides (hematite) was indicated by the peaks at wave numbers between 519-527 cm⁻¹ and 469-472 cm⁻¹ which also supports the conception of firing temperature above 600°C [20]. Several bands indicated

the feldspars in the samples, the shoulder at 552-563 cm⁻¹ (microcline), the peaks at 479 cm⁻¹ and between 429-435 cm⁻¹ (anorthite and albite) wave numbers [20].

The strong peaks of the silicates (kaolinite) could be easily identified being centered between 1033 and 1038 cm⁻¹ wave numbers due to the Si-O bond vibrations [20].

Organic matter was detected by a shoulder at 2957-2958 cm⁻¹ and the wave numbers 2923-2924 cm⁻¹ and 2848-2853 cm⁻¹, whom presence could be attributed to subsequent burial or rehydratation during use. This theory was based on their showing in case of samples fired above 800°C where the organic materials aren't supposed to be present [19].

The carbonates were present by the wave numbers at 875 and 712 cm⁻¹, which implied to a lower firing temperature or to a post-burial of the samples [20].

The Si-O-Al deformation vibrations at 519-527 cm⁻¹ were attributable to the aluminum remained in the octahedral sheet [20]. This bond indicated the iron-oxides (hematite) which were formed by the substitution of aluminium with iron during the firing process around 600°C [18], [21], [22], [23].

DSC and TGA analysis

The thermal gravimetric analysis and differential scanning calorimetry are basic methods for monitoring the physical and chemical transformations in ceramics. The method can be used in the estimation of thermal- and decomposition properties. In addition it is useful to follow the changes in weight of samples.

The evaluation of the TGA and DSC curves of the sample no. 3 showed the loss of adsorbed water in the interval 40-140°C by two endothermic peaks, which could be also identified on the TGA curve by a significant weight loss.

The next endothermic peak around 280°C was attributed to the organic matters remained in the samples. The endothermic peak between temperatures 400-600°C denoted the dehydroxilation of clay minerals by the loss of hydroxyl groups in kaolinite and illite. While illite retained its distorted structure, kaolinite decomposed into meta-kaolinite.

Calcium-carbonates decomposed into calcium-oxide and carbon-dioxide in the range of 600-800°C, which indicated a remarkable weight loss on the TGA curves. In the same time appeared a strong endothermic peak on the DSC curve.

Subsequently, around 900°C it started the shrinkage of the ceramic body. In addition at this temperature level other processes may also occur resulting by the crystallization of other minerals.

The reference clay measured in natural form was characterized by less clear curves. The place of the peaks was similar to the case of sample no.3, the peaks were in the same temperature range only slight differences appeared [24].

It is a question whether the exothermic peaks in both cases around 950°C are the signs of the crystallization of new minerals or just simply measuring failures [25]. The answer needs the repetition of the measurements, which is now a future plan.

CONCLUSIONS

The comparison of the ceramic samples with the reference loam denoted a large advantage not only in the definition of the simple properties but also in the estimation of firing temperatures resulting in more accurate assessment. By firing the reference loam at different temperatures the physical and chemical changes and transformations could be detected.

As a first conclusion, the chemical composition of the reference loam was similar to those used by ancient potters, which was not only confirmed by EDX but also by XRD analysis. Due to the similarity the loam could be used as reference in further evaluations.

As a second result of our investigation we concluded that XRD was the most convenient method for estimating the firing temperature. With the proper evaluation of the diffractograms the phase composition could be detected, which referred to the temperature of the furnace. In each case a firing temperature interval was given according to the phase composition.

The further conclusions were that the SEM investigations as an auxiliary measuring method confirmed the firing temperature intervals from the XRD analysis, although the method was less reliable by detecting only visually the changes in morphology.

Also DSC and TGA measurements provided simple and reliable complementary results referring to the study of the physical and chemical processes, which occur at firing, the most relevant changes were the transformations like the decomposition of hydroxyls or the carbonate decomposition.

As a supplementary method, FT-IR was used to confirm the presence of minerals by the corresponding bonds on the spectra. By this method the peaks of the silicates (mainly clay minerals), carbonates and quartz were identified.

The petrographic studies not only made it possible the analysis of texture but also provided information about mineral composition to complement the firing temperature and technology estimation and also the comparison of samples.

EXPERIMENTAL SECTION

Sample preparation and analytical techniques

For the purpose of archaeological study eight ceramic fragments were selected from the excavations in Satu Mare County, three of them stem from Carei and the rest from surrounding settlements, which can be seen on *Fig. 1*. Loam from the excavation deposit founded in Carei was also analyzed.

The sample preparation of the ceramic depended on the method used. The reference loam was fired at different temperatures, 300, 500, 700, 900 and 1100°C for two hours. This permitted to follow the compositional changes in the material during firing. The upper limit of the firing temperature was 1100°C, although Bronze Age technology might not reach such high temperatures, but it was representative regarding the phase transitions in the material.

The petrographic study consisted of two parts, the macroscopic examination made by Nikon SMZ 645 stereo microscope and the type used for microscopic study was Nikon Eclipse E200.

Scanning electron microscopy was coupled with energy-dispersive X-ray analyzer (spot size of 10 µm). This method allowed the analysis of the ceramic powder.

Scanning electron microscopy was performed by Philips XL30 ESEM-FEG device. The SEM images of the reference loam fired at different temperatures were used to reveal the changes in morphology. These were studied on the 2000-fold, 4000-fold and also on the 8000-fold enlarged surface.

X-ray powder diffraction patterns were measured by diffractometer Shimadzu XRD 600 with Cu-K α radiation.

Fourier-transformed infrared spectroscopy was carried out by Jasco FT-IR 615, the samples were measured in form of KBr pellets (300 mg KBr mixed with fine powder of 1-1.2 mg sample). The spectra were obtained in the range of 4000–400 cm $^{-1}$.

The thermal gravimetric analyses were performed on a SDT Q600 (V20.9 Build 20) instrument.

ACKNOWLEDGMENTS

We are grateful to Marcel Benea from the Babeş-Bolyai University, Department of Geology providing the petrographic study.

REFERENCES

- [1]. C. Ionescu, L. Ghergari, M. Horga, G. Rădulescu, *Studia UBB, Geologia*, **2008**, 52, 29-35.
- [2]. C. Ionescu, V. Hoeck, *European Journal of Mineralogy*, **2011**, 23, 937-958.
- [3]. L.M. Ghergari, C. Stâncel, *Studia UBB, Geologia*, **2012**, 57, 13-21.
- [4]. V. Hoeck, C. Ionescu, L. Ghergari, C. Precup, *Studia UBB, Geologia*, **2009**, 54, 41-51.
- [5]. C. Ionescu, L. Ghergari, "Modeling and firing technology - Reflected in the textural features and the mineralogy of the ceramics from neolithic sites in Transylvania (Romania)", **2002**.
- [6]. V.A. Drebushchak, L.N. Mylnikova, T.N. Drebushchak, V.V. Boldyrev, *Journal of Thermal Analysis and Calorimetry*, **2005**, 82, 617-626.
- [7]. M. Riccardi, *Applied Clay Science*, **1999**, 15, 393-409.
- [8]. E. Nemecz, "Agyagásványok", Akadémiai Kiadó, **1973**.
- [9]. G.W. Brindley, G. Brown, "Crystal Structures of Clay Minerals and Their X-ray Identification", Mineralogical Society, **1980**.
- [10]. O.S. Rye, "Pottery technology: principles and reconstruction", Taraxacum, **1981**.
- [11]. M. Maggetti, "Phase analysis and its significance for technology and origin", in: Archaeological ceramics, Smithsonian Institution Press, **1982**, 121-133.
- [12]. M. Maggetti, "Mineralogical and petrographical methods for the study of ancient pottery", Università degli studi di Roma "La Sapienza", **1994**.
- [13]. G. Cultrone, C. Rodriguez-Navarro, E. Sebastian, O. Cazalla, M.J. De La Torre, *European Journal of Mineralogy*, **2001**, 13, 621-634.
- [14]. G. Survey, "Minerals Yearbook, 2008, V. 1, Metals and Minerals", U.S. Government Printing Office, **2011**.
- [15]. R.B. Heimann, "Classic and advanced ceramics: from fundamentals to applications", John Wiley & Sons, **2010**.
- [16]. M.S. Tite, *Archaeometry*, **2008**, 50, 216-231.
- [17]. H. Mommsen, *Archaeometry*, **2004**, 46, 267-271.
- [18]. E. Lugwisha, "Identification of Clay Minerals of the Eastern Southern Region of Lake Victoria by Ethylene Glycol and Heat: Xray Diffraction and Infrared Spectroscopy Studies", *Tanzania Journal of Science*, **2011**, 37.
- [19]. J. Bertaux, F. Frohlich, P. Ildefonse, "Multicomponent analysis of FTIR spectra: quantification of amorphous and crystallized mineral phases in synthetic and natural sediments", *Journal of Sedimentary Research*, **1998**, 68.
- [20]. G. De Benedetto, R. Laviano, L. Sabbatini, P. Zambonin, *Journal of Cultural Heritage*, **2002**, 3, 177-186.
- [21]. R. Ravisankar, S. Kiruba, C. Shamira, A. Naseerutheen, P.D. Balaji, M. Seran, *Microchemical Journal*, **2011**, 99, 370-375.
- [22]. J. Madejová, P. Komadel, *Clays and clay minerals*, **2001**, 49, 410-432.

- [23]. R. Ravisankar, S. Kiruba, A. Naseerutheen, A. Chandrasekaran, G.R. Annamalai, M. Seran, P. Balaji, *Archives of Physics Research*, **2011**, 2, 108-114.
- [24]. P. Ptáček, J. Brandštetr, F. Šoukal, T. Opravil, “Investigation of Subterranean Termites Nest Material Composition, Structure and Properties”, **2013**.
- [25]. S. Salem, A. Salem, “Mechanisms of Momentum Transport in Viscous Flow Sintering”, **2013**.

CERAMIC GLAZES FOR WALL TILES WITH DIFFERENT GLASS WASTES

JULIA BARTHA^a, MARIA GOREA^{a*}

ABSTRACT. Ceramic glazes are thin coatings which enhance the aesthetical aspect, increase the mechanical strength and chemical stability, and waterproof of the support. The glaze composition contains an important quantity of frit for decreasing the melting point. In this study, the frit is replaced by the different glass wastes and the properties of resulted glazes were evidenced. Various compositions of glazes were formulated. The oxide compositions, the particle size distribution of glass wastes were determined. The glazes were prepared and applied on wall tiles biscuit and thermal treated at 1100°C for three hours. Using optical and scanning electron microscopy the glazes microstructure and the intermediate layer between the glaze and ceramic support were analysed. The linear thermal expansion coefficient of the glazes and chemical stability in acid/alkaline solutions were determined.

Keywords: *ceramic glaze, waste glass, composition, microstructure*

INTRODUCTION

Ceramic wall tiles are porous products made from clay mixed with sand, limestone and other raw materials. Due to their high porosity, the tiles are not used as such, the ceramic support being covered by a thin coating of glaze. As a result, the porous tile becomes waterproofed, the mechanical strength and chemical stability increase, and last but not least a higher possibility of cleaning is obtained.

Research into exploitation and recycling of industrial wastes for the manufacturing more value-added materials is very important and necessary for an eco-friendly environment [1]. Waste electronic and electronical equipment (WEEE) contains a high amount of reusable materials such as plastics, metals and glass, which can be used as secondary raw materials [2].

^a Babeş-Bolyai University, Faculty of Chemistry and Chemical Engineering, 11 Arany Janos Str., RO-400028, Cluj-Napoca, Romania.

* Corresponding author: mgorea@chem.ubbcluj.ro

In the past years the recycling process of WEEE has become an alternative to reduce the cost of materials mainly oxide materials by replacing some expensive raw materials with these wastes. Another advantage resulted by using the glass wastes is to minimize energy consumption in obtaining the fluxes (frit for glazes) and to diminish environmental impact (avoid the landfill disposing of cathode ray-tubes - CRT, due to hazardous elements in composition) [1].

Different studies showed that a wide variety of industrial wastes can be used, in different types of ceramic products like glass and glass-ceramics [2,12], roof tiles [3], floor tiles [4], porcelain stoneware tiles [5], for substitution of non-plastics materials.

A great practical interest, due to their compositions, represents end of life (EOL) CRT panels presents several options for reuse [1,6].

CRT's constitutes approximately 65% of the weight of the television or computer monitor. CRT's are composed of glass components, each of different composition: the panel (65%) – barium-strontium glass, the funnel (35%) – lead glass, the frit – lead glaze, and the neck (5%) a reach lead glass [7, 8]. Several toxicity studies showed that the funnel and neck are hazardous wastes, and the panel shows very little toxicity [9, 10].

Also due to the fact that the recycling of WEEE is not yet fully automated, it remains labor intensive, and requires efforts to make the process profitable, to increase the consumption of WEEE instead of natural raw materials [11].

Because CRT panel composition is similar to glazes, the reuse of these wastes is appropriate for ceramic glazes production, particularly as substitute for ceramic frits (fluxing agent) [7, 13]. A great variety of glazes can be obtained by varying the content of waste in the composition.

The aim of this study is to develop and characterize several compositions of glazes made of different glass wastes, frit and natural raw materials.

RESULTS AND DISCUSSION

Raw materials characterization

Chemical composition

The chemical composition determined by wet chemistry analyses on the frit and glass wastes are presented in Table 1.

The usual frit for wall tiles is mainly consisting of silica, aluminum oxide, calcium oxides besides of alkali and small quantity of ZnO. The CRT glass waste has a similar content in silica, small quantity of alumina and calcium oxide but an increased content in barium oxide and alkalis. The green

and transparent glass wastes are very similar in composition having a higher content in silica than frit and CRT glass, high content in calcium oxide and alkalis.

The chemical composition of the glass wastes and the other raw materials is very important for the formulation of a proper glaze, depending on use of the glaze.

Table 1. Oxide composition of frit and glass wastes

Sample / Oxide [%]	Frit	CRT glass	Green glass (bottle)	Transparent glass (jar)
SiO ₂	58,2	60.73	71.10	69.98
Al ₂ O ₃	10,30	4.23	3.26	2.80
Fe ₂ O ₃	0,08	0.01	0.03	0.04
CaO	6,86	3.01	8.23	10.97
MgO	1,27	0.98	2.66	2.94
Na ₂ O	5,00	8.00	14.00	12.00
K ₂ O	1,00	7.00	0.50	0.50
BaO	-	15.05	-	-
ZnO	3,44	-	-	-

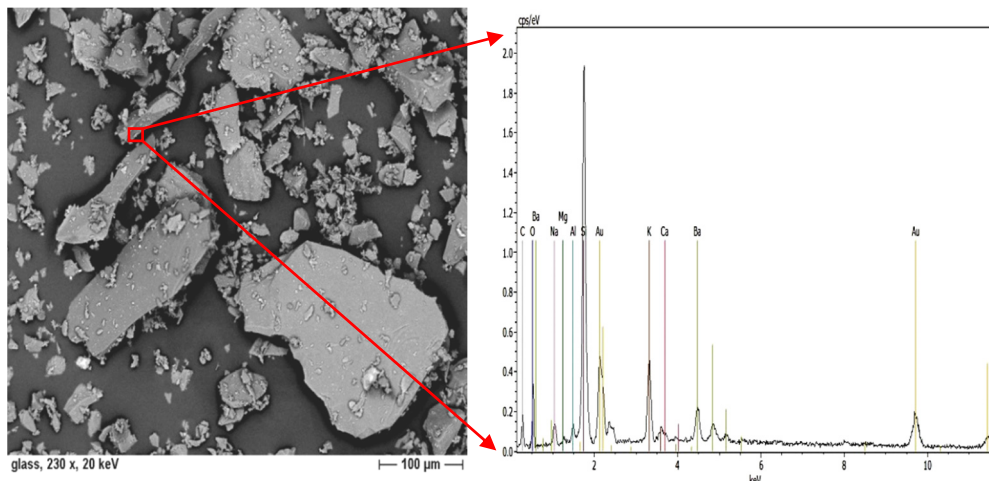


Figure 1. SEM image with EDS spectra of CRT glass

CRT glass wastes come from scrap computer monitors, which were previously separated from plastic/wooden enclosure, and after divided into two parts: - the front (the panel - part without lead), and - the back (the cone – part

which contains lead). The CRT glass used in this study was the panel, glass without lead. In the Figure 1 is presented an image of crushed CRT glass wastes with EDS spectra for a small pieces. The elements identified by EDS spectra are similarly with those from chemical oxide analyses.

The green and the transparent waste glasses are selected from households. Their composition being very similar with a ceramic frit they are frequently used in low temperature glazes.

Particle size distribution of the glass wastes

The melting temperature of the raw glaze depends of the type of ceramic support mainly of its sintering temperature. The wall tiles have the firing temperature about 1000 °C, so at this temperature the glaze mixture has to be completely melted. Therefore, the grain sizes of the compounds is recommended to be very small, mainly micrometer sizes, under 60 µm. The tested glass wastes were milled in a laboratory ball mill and their grain size distributions are presented in Figure 2.

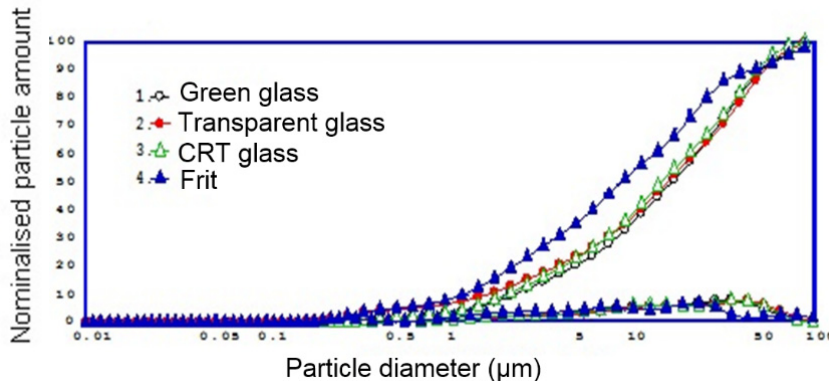


Figure 2. Grain size distribution of studied glass wastes and frit

For all the samples the size range is between 179 nm and 90 µm. In the case of the frit, 92 % grains have a size smaller than 55 µm; the CRT glass waste has about 95 % grains below 58 µm; the sizes of grains for transparent and green glass wastes are very similarly, majority smaller than 58 µm (about 93 %).

Bentonite

Clay and kaolins are usually used in slurry composition for maintaining the solid phase in suspension. In experiments the Romanian bentonite with composition presented in table 2 was tested.

Table 2. Oxide composition of bentonite

Oxide	SiO ₂	TiO ₂	Al ₂ O ₃	Fe ₂ O ₃	CaO	MgO	Na ₂ O	K ₂ O	LOI
[%]	70,92	0,18	12,66	1,32	3,5	1,4	0,45	1,27	8,4

In all experimented compositions the zirconium silicate, ZrSiO₄, having micrometer sizes (1-5 µm) was used as opacifier.

For coloring the glazes a ceramic pigment based on cobalt oxide was used.

Characterization of the glaze slurry

Density of the slurries

For obtaining an adequate raw layer on the ceramic support the density of the slurry is necessary to be around the 1400 g/l. The slurries prepared with water in the laboratory are the density between 1380 g/l and 1450 g/l.

Characterization of the fired glazes

Thermal expansion coefficient, acidity index and surface tension

A ceramic glaze can be considered a glass on a porous support and its thermal expansion coefficient has to be closely to the ceramic support. If these values are very different on the glaze surface appear defects like crazing or peeling. For a good compatibility of the glaze with ceramic support the glaze thermal expansion coefficient should be slightly below the ceramic body.

The calculated acidity index (AI) of the glazes must be between 2 and 3. In the case of index AI smaller than 2 the glaze cannot be formed on the surface of the ceramic body due to the lack of glass forming oxides (SiO₂). An index AI bigger than 3 induces crystallization of some oxides from glaze composition.

The surface tension of a glaze is very important for obtaining an uniform coating on the ceramic body and its value should be around 300 dyne/cm². The thermal expansion coefficients α, in the temperature range 20 – 600 °C, acidity index AI and surface tension of the studied glazes are presented in Table 3. From this point of view all glazes are suitable, except glaze 1.1 which has an acidity index AI smaller than 2. The experimented thermal expansion coefficient for the ceramic support is 8.8x10⁻⁶ C⁻¹.

It can be noted some differences between calculated and experimented thermal expansion coefficient which is attributed to the manufacturing of the samples. The highest value of thermal expansion coefficient is for glaze 1.1 with 90 % CRT glass waste followed by glaze 1.2 and 1.3. By partially replacing of the frit with glass wastes (60 %), the thermal expansion coefficient is decreasing. The value of glaze 2.2 is slightly under the one of ceramic body and the glaze 3 which contains only ceramic frit (90%).

Table 3. Thermal expansion coefficients, acidity index and surface tensions of studied glazes

Sample	Thermal expansion coefficient [C^{-1}] $\alpha \cdot 10^6$		Acidity index AI	Surface tension [dyne/cm ²]
	calculated	experimented		
Glaze 1.1	9.66	13.6	1.71	319.24
Glaze 1.2	8.88	12.1	2.09	334.08
Glaze 1.3	8.45	10.9	2.12	341.57
Glaze 2.1	7.27	10.6	2.00	326.48
Glaze 2.2	7.03	7.8	2.19	333.90
Glaze 2.3	8.82	9.9	2.20	337.65
Glaze 3.0	4.94	9.9	2.25	333.72

It can be concluded that glass wastes can be used as flux in the wall tiles glazes partially replacing the usual frit.

Glazes microstructure

The optical study in polarized light realized on the thin sections of glazed wall tiles allows evidencing some structural-textural characteristics.

The fine texture of the glazed wall tiles is illustrated in polarizing optical microscopy images (Figure 3). A high amount of quartz of various sizes and shapes and closed pores within a relatively homogeneous vitreous matrix in the ceramic support can be noticed.

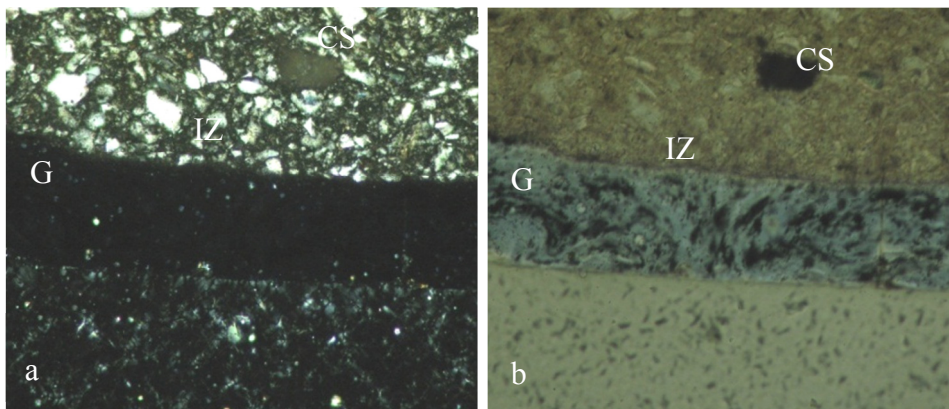


Figure 3. Optical microscopy images of glaze 1.1, (a) N+ (45x); (b) 1N (45x); (CS - ceramic support; G - glaze; IZ - intermediary zone)

Also only partly solubilized large quartz grains, as well as an incomplete homogenization of the blue ceramic pigment in the glaze are visible.

Scanning electron microscopy (SEM)

The SEM image (Figure 4) of the glazed wall tiles evidences a well intermediary layer between ceramic body and glaze. It can be seen that the glaze entered into the pores of the ceramic support, making a very strong glass-ceramic bond.

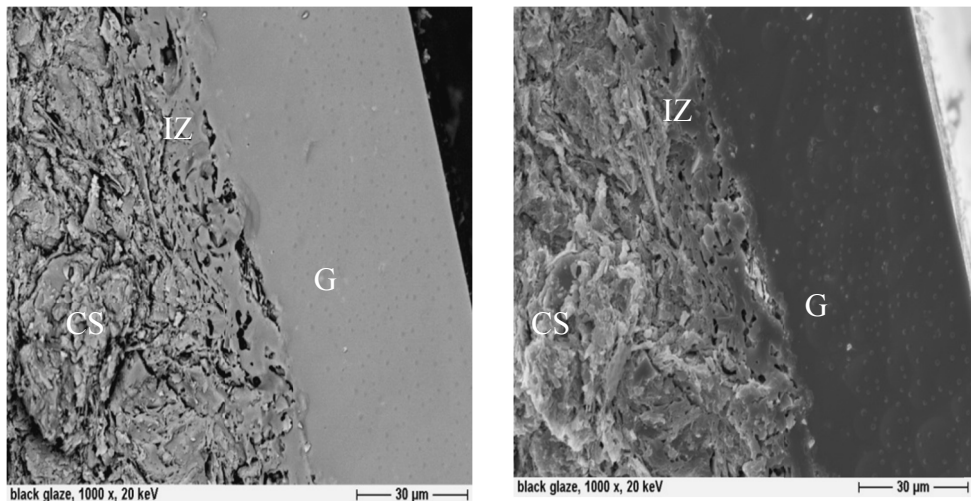


Figure 4. SEM images of glaze 1.1 with 90% CRT (CS- ceramic support; G-glaze; IZ-intermediary zone)

Also small ceramic pigment spots can be observed in the glaze layer.

Chemical stability in acid/alkaline solutions

The glazes presented a very good chemical stability to acid and alkaline corrosion. The weight losses in solutions of 3 % hydrochloric acid respectively sodium hydroxide after 96 hours are presented in Table 4. It can be noted that the weight losses of the glazes are almost insignificant.

This good behavior of the glazes can be attributed to a well-balanced composition of the glazes.

Table 4. Weight losses during the acid/alkaline attack

Attack Solution	Glaze	Weight before attack [g]	Weight after attack [g]	Weight losses [%]
HCl 3%	1.1	18,6841	18,6835	0,003211
	1.2	17,2675	17,2627	0,027806
	1.3	16,0848	16,0808	0,024874
	2.1	18,0898	18,0840	0,032073
	2.2	17,0259	17,0176	0,048773
	2.3	19,4195	19,4150	0,023178
	3	16,6697	16,6626	0,042610
NaOH 3%	1.1	18,3778	18,3778	0
	1.2	18,5901	18,5779	0,065669
	1.3	16,9851	16,9808	0,025323
	2.1	16,8766	16,8733	0,019558
	2.2	17,5218	17,5187	0,017695
	2.3	20,1967	20,1879	0,043590
	3	16,6039	16,5989	0,030122

CONCLUSIONS

Glazes with CRT, and household glass wastes can be obtained by combining the glass wastes with frit, and natural raw materials in various proportions. Also, even if the recycling of CRT glass is not simple because of the varying composition, glazes with CRT show an excellent glaze-ceramic compatibility, with an excellent chemical resistance.

The glaze-ceramic thermal compatibility is very well revealed with the SEM and optical microscopy. A continue intermediary layer between glaze and ceramic support are formed. No defects in glazes were evidenced.

In conclusion, the green and transparent glass wastes and CRT wastes can partially replace the usual frit in the wall tiles glaze compositions.

EXPERIMENTAL SECTION

The glaze suspensions are formed of different raw materials, which can be divided into: non-plastics (frits, oxides, pigments), plastics (clays) and additives (opacifiers, binders).

The experimented compositions are presented in Table 5.

Table 5. The experimented ceramic glaze compositions

Raw materials [%] / sample	CRT glass waste	Transparent glass waste	Green glass waste	Frit	Ceramic pigment	ZrSiO ₄	Bentonite
1.1	90	-	-	-	4	2	4
1.2	-	90	-	-	4	2	4
1.3	-	-	90	-	4	2	4
2.1	60	-	-	30	4	2	4
2.2	-	60	-	30	4	2	4
2.3	-	-	60	30	4	2	4
3	-	-	-	90	4	2	4

The first group of glazes is formed from the compositions 1.1, 1.2 and 1.3 in which the frit is totally replaced by de CRT glass waste, transparent glass waste and green glass waste. In the second group formed from the compositions 2.1, 2.2 and 2.3 the wall tile frit was partially replaced (60 %) by the above mentioned wastes. For comparing the results, the composition with 90 % frit usually used in manufacturing of wall tiles was formulated.

The raw materials weighed according to the recipe were milled in a laboratory mill (type Pulverisette 6) for 45 minutes, at a rotation speed of 250 rpm.

The glaze, kept under continuous stirring in order to avoid sedimentation, was deposited on the moistened ceramic tile, by dipping into the glaze slurry.

After a short drying time the samples were thermal treated in a Nabertherm laboratory kiln. The firing rate was of 10°C/min up to maximum temperature (1100°C), for 30 minutes at this temperature.

The grain size distribution of the frit and glass wastes were studied by using a Counter Coulter WING-SALD 7101 granulometer and the thermal expansion coefficient with a Linseis Horizontal dilatometer L75Hx1400.

From the fired ceramic glaze R 1.1 it has obtained 25-30 micrometers thin sections that were used for the optical study with polarized light under a Nikon Eclipse E200 microscope.

Chemical stability was tested by immersing the glazed samples in solutions of 3 % hydrochloric acid respectively sodium hydroxide.

ACKNOWLEDGMENTS

Many thanks to the Laboratory for Advanced Studies of Geomaterials (Department of Geology, Babes-Bolyai University) for the polarized microscopy studies.

REFERENCES

- [1].R.C. da Silva, S.A. Pianaro, S.M. Tebcherani, *Ceramics International*, **2012**, 38, 2725.
- [2].L.M. Schabbach, F. Andreola, I. Lancelotti, L. Barbieri, *Ceramics International*, **2011**, 37, 1367.
- [3].A. Demir, *Waste Management & Research*, **2009**, 27, 572.
- [4].A.M. Segadeas, M.A. Carvalho, M.A. Carvalho, W. Acchar, *Applied Clay Science*, **2005**, 30, 42.
- [5].F. Andreola, L. Barbieri, E. Karamanova, I. Lancellotti, *Ceramics International*, **2008**, 34, 1289.
- [6].P. Yot, F. Mear, *Journal of Hazardous Materials*, **2011**, 185, 236.
- [7].F. Andreola, L. Barbieri, A. Corradi, I. Lancellotti, *Journal of the European Ceramic Society*, **2007**, 27, 1623.
- [8].F. Mear, P. Yot, M. Cambon, M. Ribes, *Waste management*, **2006**, 26, 1468.
- [9].Y.C. Jang, T.G. Townsend, *Environmental Science & Technology*, **2003**, 37, 4778.
- [10].F. Andreola, L. Barbieri, A. Corradi, A.M. Ferrari, I. Lancellotti, P. Neri, *International Journal of Life Cycle Assessment*, **2007**, 12 (6), 448.
- [11].J Mueller, M Boehm, C Drummond, *Waste Management*, **2012**, 32, 1560.
- [12].A.V. Gorokhovsky, V.A. Gorokhovsky, D.V. Mescheryakov, J. Mendez-Nonell, J.I. Escalante-Garcia, M.I. Pech-Canul, G. Vargas-Gutierrez, *Materials Letter*, **2001**, 51, 281.
- [13].C. Mengjun, Z. Fu-Shu, Z. Jianxin, *Journal of Hazardous Materials*, **2009**, 165, 980.

MORTARS FOR THE ENHANCEMENT OF THE INDOOR ENVIRONMENTAL QUALITY

CLAUDIU ACIU^a, DANIELA LUCIA MANEA^a, CARMEN PUIA^b,
OANA CADAR^{c*}

ABSTRACT. Achieving a healthy indoor environment is an important concern in the construction and building materials industry. This study fits in the context of these concerns and demonstrates the possibility of developing mortars that contain colloidal silver nanoparticles with good antibacterial properties. The optimal recipe was established by replacing 50% of the amount of water in the mortar recipe with a commercial 25 mg/L colloidal silver solution. The obtained mortars have superior physical and mechanical characteristics and excellent antibacterial properties against various Gram-positive and Gram-negative bacteria compared to standard mortar.

Keywords: *mortar, colloidal silver nanoparticles, mechanical properties, antibacterial activity*

INTRODUCTION

The indoor air quality is a determining factor of health due to the fact that people spend most of their lives inside buildings. It has been observed that microbes and allergens, the lack of oxygen, inadequate temperature and humidity, mould, dust, inadequate lighting and ventilation, noise, the presence of building materials that contain noxious substances and generate toxic emissions, the functioning of equipment, etc. can seriously affect a person's health [1].

^a Technical University of Cluj-Napoca, 28 Memorandumului Street, 400114, Cluj-Napoca, Romania.

^b University of Agricultural Sciences and Veterinary Medicine, Faculty of Agriculture, 3-5 Manastur Street, 400372 Cluj-Napoca, Romania.

^c INCDO-INOE 2000, Research Institute for Analytical Instrumentation, 67 Donath Street, 400293, Cluj-Napoca, Romania.

* Corresponding author: oana.cadar@icia.ro

Infections with pathogenic microorganisms are combated with antimicrobial agents, to the action of which these are vulnerable. The use of antimicrobial agents in decorative and building materials, including paints and coatings, has intensified considerably in recent years and their possible effects on human health or the environment have been increasingly studied [2]. Noble metal nanoparticles have attracted great interest due to their different characteristics from those of the macroscopic phase, which allow attractive applications in various fields, such as medicine, biotechnology, optoelectronics, biosensors, catalysis, information storage, energy conversion, and as antimicrobials [3-5].

Silver nanoparticles, an ecological alternative to organic biocides, have a high surface area, a very small size (<20 nm) and high dispersion [6]. Silver nanoparticles can be used in the form of colloidal suspensions or doping agents for a lot of composite materials with polymer matrix. Colloidal silver solutions (CSSs) arouse increased interest due to their antimicrobial properties with different applications (pharmacology, food, industry, human and veterinary medicine, etc.). The interaction of silver nanoparticles with microorganisms, such as viruses, mould, bacteria and fungi, is an expanding field of research [7, 8]. While the mechanism underlying the antibacterial actions of silver is still not fully understood, some previous studies have shown that silver ions penetrate the bacteria and interact with thiol groups of vital enzymes and inactivate them, leading to cell death [9].

Furthermore, colloidal silver solutions can be taken indefinitely because they have no side effects, the body develops no tolerance, and one cannot overdose. Unlike pharmaceutical antibiotics, which kill beneficial enzymes, colloidal silver leaves these tissue-cell enzymes intact. Therefore, colloidal silver is completely safe for humans, plants and all multicellular living organisms [10].

The purpose of this work was the development of a plastering mortar with antibacterial properties using a commercial 25 mg/L Ag solution as an additive. The study focuses on obtaining a plastering mortar with good adhesion to the substrate, low water absorption by capillarity, good mechanical and antibacterial properties.

RESULTS AND DISCUSSION

Physical-mechanical properties

The results for the physical-mechanical properties (apparent density of hardened mortar, flexural and compressive strengths, water absorption by capillarity and adhesion to the substrate) are shown in Table 1.

Table 1. Technical characteristics of the mortars

Recipe	Apparent density [kg/m ³]	Adhesion to the support layer [N/mm ²]	Flexural strength [N/mm ²]	Compressive strength [N/mm ²]	Water absorption by capillarity [Kg/(m ² ·min ^{0.5})]
R I	2210	0.211	6.93	42.7	0.161
R II	2223	0.191	7.31	43.2	0.133
R III	2233	0.193	7.53	43.3	0.121
R IV	2237	0.211	7.61	43.7	0.135
R V	2190	0.189	7.26	42.9	0.191

Table 2 shows the influence of the commercial 25 mg/L Ag solution on the technical characteristics of plastering mortar.

The *apparent density* of the hardened mortars is little influenced by the concentration of the commercial 25 mg/L Ag solution, the values varying by approximately $\pm 1\%$ compared to the apparent density of standard mortar. The greatest variation is noted in the case of recipe IV, in which 50% of water has been replaced with the commercial 25 mg/L Ag solution (density is 1.18% higher compared to the density of the standard recipe). From the point of view of apparent density, all mortars belong to the category of heavy mortars.

Regarding *adhesion to the substrate*, recipe R IV mortar is the best, its adhesion being similar to that of standard mortar.

The *flexural strength* value of mortars developed with the commercial 25 mg/L Ag solution increases compared to that of standard mortar. The increase manifests with the increase in the amount of colloidal water in recipes with up to 50% commercial 25 mg/L Ag solution, in which the flexural strength is the highest, i.e. 7.8 N/mm² compared to 6.9 N/mm² for standard mortar. In the case of the 70% commercial 25 mg/L Ag solution, there is a decrease in flexural strength compared to the mentioned recipes, but this remains higher than the flexural strength of standard mortar.

The same phenomenon is seen in the case of compressive strength. The best compressive strength is that of mortar with a 50% addition of commercial 25 mg/L Ag solution, having a value of 43.7 N/mm², higher than that of the standard recipe, which is 42.7 N/mm².

The determination of *water absorption by capillarity* highlights the following observations: (i) the coefficient of water absorption by capillarity of standard mortar is 0.16 Kg/(m²·min^{0.5}), which places this mortar in class W2; (ii) in the case of recipes II, III and IV, with the increase in the proportion of water replaced by the commercial 25 mg/L Ag solution, the value of the coefficient of water absorption by capillarity decreases compared to standard mortar; these

mortars fall in class W2; and (iii) the coefficient of water absorption by capillarity in the case of recipe V increases compared to the coefficient of recipes II, III and IV, but this fits in class W2.

Given that the studied mortars have less than 1% by mass or volume of homogeneously distributed organic material, they are classified as fire reaction class A1, without requiring testing.

Antibacterial effect of mortar specimens

The antibacterial efficacy of standard mortar (without colloidal silver) and mortars containing colloidal silver in various concentrations according to Table 3 is presented in Table 2.

Table 2. Effect of colloidal silver in mortars on the survival of four bacteria after 24h incubation at 37°C

	<i>Escherichia coli</i>	<i>Pseudomonas aeruginosa</i>	<i>Enterococcus faecalis</i>	<i>Staphylococcus aureus</i>
R I	100	100	100	100
R II	0	80	85	25
R III	0	25	35	0
R IV	0	5	15	0
R V	0	0	0	0

As expected, the standard mortar R I has no inhibitory effect on the investigated bacteria. Already after 24 h, the lowest concentration of colloidal silver in the mortar (R II) was effective against *Escherichia coli* bacteria. In all cases, a higher colloidal silver content (R V) caused 100% inhibition of bacterial growth. The antibacterial efficacy of colloidal silver in mortars demonstrated in our study is consistent with previous studies demonstrating the antimicrobial effect of silver ions [11, 12], which makes them promising for combating the growth of bacteria on interior or exterior walls.

However, these results have to be tested under the specific conditions (moisture, temperature, surface, etc.) to which these materials would be exposed in practical use (hospitals, nursing homes, schools, food preparation and storage areas, etc.); probably a mixture with various organic biocides could show some utility and interesting results.

Silver release

The study of silver release was performed in 1 culture medium, DMEM, and ultrapure water at different time intervals (1, 3, 6, 24 and 48 h). The amounts of silver released at 48 h were comparable to those measured at 24 h and consequently only the values obtained at 24 h were taken into account for this study. The obtained results (Figure 1) are in agreement with published literature data: the leaching solution has a significant effect on the level of leaching [12, 13]. As expected, for the mortar specimen R I, no silver release was observed (<0.01 mg/l). The level of leaching was much higher for specimens that were immersed in Dulbecco's modified eagle's medium (DMEM) compared to specimens immersed in ultrapure water (UW). Furthermore, in both releasing solutions, higher amounts of colloidal silver in the mortar specimens resulted in increased releasing ions: R I > R II > R III > R IV > R V.

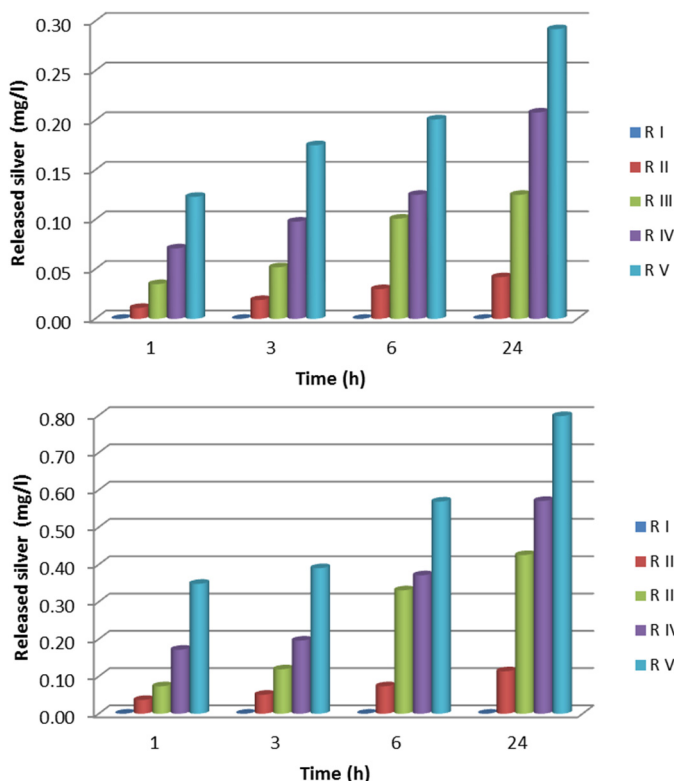


Figure 1. Silver released (mg/L) into UW (above) and DMEM (below) from mortar specimens containing colloidal silver

CONCLUSIONS

The study demonstrates the possibility to develop plastering mortars with good antibacterial properties by introducing colloidal silver instead of the water of mortar recipes. At 28 days, all mortars with colloidal silver solution addition have superior physical-mechanical characteristics and good antibacterial properties compared to the standard recipe.

It can be seen that there is an upper limit of the commercial 25 mg/L Ag solution concentration up to which these characteristics increase, after which a slight decrease occurs. From the point of view of physical-mechanical characteristics, the optimal recipe is that of mortar with 50% commercial 25 mg/L Ag solution, *i.e.* recipe R IV. According to standards in force, depending on compressive strength at 28 days, mortar falls in class CSIV and class W2 in terms of water absorption by capillarity. Under this framework, the obtained mortars can be used for the improvement of hygiene and sanitary conditions in a variety of environments such as hospitals, nursing homes, schools, food preparation and storage areas, etc.

EXPERIMENTAL SECTION

Preparation of mortar specimens

The starting materials used in this work were ordinary Portland cement 42.5, commercial silver colloidal solution (25 mg/L) introduced in various percentages in the water of the standard recipe, and (0-2) mm sand composed of four fractions [(0-0.16) mm – 150 g; (0.16-0.50) mm – 300 g; (0.5-1.00) mm – 450 g and (1.00-2.00) mm – 450 g]. The aqueous Ag colloidal solution was purchased from a local pharmacy.

The study was performed on 5 plastering mortar recipes (Table 3). For standard mortar (recipe 1), a 1:3 binder-sand ratio was chosen, with the recipe composed of 450 g Portland cement 42.5, 1350 g sand and 225 cm³ water. For the silver solution test samples (recipes 2-5), water in the standard mortar recipe was replaced in a 10%, 30%, 50% and 70% proportion with a commercial 25 mg/L Ag solution.

Table 3. Mortar recipes

Recipe	Cement	Water	Commercial 25 mg/L Ag solution		Sand 0-2 mm
	[g]	[mL]	[%]	[mL]	[g]
R I	450	225	-	-	1350
R II	450	202.5	10	22.5	1350
R III	450	157.5	30	67.5	1350
R IV	450	112.5	50	112.5	1350
R V	450	67.5	70	157.5	1350

Physical-mechanical properties of mortar specimens

The mortars (Figure 2) were prepared according to SR EN 1015-2:2001 [14], the raw materials were weighed, homogenized in dry state and then mixed with water (R I) or with water and the commercial 25 mg/L Ag solution (R II – R V) in the mixer.



Figure 2. Mortar test samples (recipes I–V)

The consistency of standard mortar was determined with the flow table (Tecnotest, Italy), in conformity with SR EN 1015-3:2001 [15]. According to SR EN 1015-2:2001 [16], for fresh mortar with an apparent density higher than 1200 kg/m³, the flow value is 175 ± 10 mm.

On the 16 cm x 4 cm x 4 cm prismatic test samples, cast and stored for 28 days according to standards SR EN 998-1:2011 [17], SR EN 1015-2:2001 [18], SR EN 1015-11:2002 [19], the following physical-mechanical determinations were performed:

- *the apparent density of hardened mortar* according to SR EN 1015-10:2002 [18];
- *the mechanical flexural and compressive strengths* according to SR EN 1015-11:2002 [17]. The flexural strength was tested with the automatic flexural tensile tester (Controls, Italy), and the compressive strength with the 250 KN hydraulic press (Tecnotest, Italy).

- the water absorption coefficient due to capillary action according to SR EN 1015-18:2003 [19].
- the adhesion of hardened mortar to the substrate according to SR EN 1015-12:2001 [20], with the pull-off tester 58-C0215/T (Controls, Italy).

Evaluation of antibacterial activity

The 28-day-old-mortar samples R1-R5 were cut into small 20 x 20 x 1 mm³ prisms and dried at 80°C until a constant weight was obtained. All manipulations for this study were performed in a laminar flow hood.

Two Gram-negative bacteria strains (G⁺): *Escherichia coli* ATCC 25922 and *Pseudomonas aeruginosa* ATCC 27853, and 2 Gram-positive bacteria strains (G⁻): *Enterococcus faecalis* ATCC 29212 and *Staphylococcus aureus* ATCC 29213 were used. The bacteria were used at a density of 10⁶ CFU/mL, grown in nutrient agar no. 2 (Sigma-Aldrich, Germany) and incubated for 24-48 h at 37°C, in darkness. The tested specimens were placed on Petri dishes with the culture medium and inoculated with 100 µL bacterial suspension, using a sterile pipette. The inhibition zones around the wells were measured (in mm) with a millimeter ruler. The Petri dishes were incubated again and measured after 48 h. Since the diameters of the microbial growth inhibition zones was comparable to that measured at 24 h, only the values obtained at 24 h were considered for this study. These experiments were repeated at least four times with similar results.

Measurements of silver release

The mortar prisms (~15 g) were submerged in 50 mL sterile centrifuge tubes containing 20 mL sterile DMEM D5796 (Sigma-Aldrich, Germany) or ultrapure water for 1, 3, 6, 24 and 48 h. At each point, the solid part was separated from the rest of the solution through centrifugation at 4000 rpm for 30 min. Solutions were collected and digested with 4 mL HNO₃ and 2 mL H₂O₂ in a closed-vessel microwave system Berghof MWS-3+ with temperature control mode (Berghof, Germany). Samples were digested according to the following 5-step program: (i) 5 min at 180°C and 80% power, ramp 3 min; (ii) 10 min at 220°C and 90% power, ramp 5 min; (iii-v) 5 min at 100°C and 10% power, ramp 1 min. After cooling down to room temperature, the resulting colorless solutions were diluted to 25 mL with deionized water. The silver content was determined by ICP-OES (OPTIMA 5300 DV, Perkin Elmer, USA). Three independent replicates were analyzed for each sample.

Calibration standards were prepared by dilution, with 2% (v/v) HNO₃, of the stock ICP multielement standard solution IV (Merck, Darmstadt, Germany) 1000 mg/L. All reagents (HNO₃ 65%, H₂O₂ 30%) were of analytical grade and were purchased from Merck, Darmstadt, Germany. All dilutions were prepared

using deionized water (18.2 MΩ/cm) obtained from a Millipore Direct-Q3 UV Ultrapure water system (Millipore, Molsheim, France). All PTFE and glass vessels were soaked in 10% (v/v) HNO₃ overnight or longer and rinsed with Milli-Q water prior to use.

ACKNOWLEDGMENTS

This paper was supported by the Post-Doctoral Programme POSDRU/159/1.5/S/137516, a project co-funded from the European Social Fund through the Human Resources Sectorial Operational Programme 2007-2013.

REFERENCES

- [1]. U. Makala, L. Wood, *Biomaterials*, **2006**, 27, 1316.
- [2]. K. Sterflinger, G. Pinar, *Applied Microbiology and Biotechnology*, **2013**, 97, 9637.
- [3]. V. Thomas Mathew, K. Sunny, *Colloids and Surfaces B: Biointerfaces*, **2013**, 101, 14.
- [4]. Y. Sun, Y. Xia, *Science*, **2002**, 298, 2176.
- [5]. S. Priyadarshini, V. Gopinath, N.M. Priyadharshini, D. MubarakAli, P. Velusamy, *Colloids and Surfaces B: Biointerfaces*, **2013**, 102, 232.
- [6]. T. Künniger, A.C. Gerecke, A. Ulrich, A. Huch, R. Vonbank, M. Heeb, A. Wichser, R. Haag, P. Kunz, M. Faller, *Environmental Pollution*, **2014**, 184, 464.
- [7]. J.L. Elechiguerra, J.L. Burt, J.R. Morones, A. Camacho-Bragado, X. Gao, H.H. Lara, M.J. Yacaman, *Journal of Nanobiotechnology*, **2005**, 3, 1.
- [8]. A. Muñoz-Bonilla, M. Fernández-García, *Progress in Polymer Science*, **2012**, 37, 281.
- [9]. J.R. Morones, J.L. Elechiguerra, A. Camacho, K. Holt, J.B. Kouri, J.T. Ramirez, M.J. Yacaman, *Nanotechnology*, **2005**, 16, 2346.
- [10]. L. Suber, I. Sondi, E. Matijevic, D.V. Goia, *Journal of Colloid and Interface Science*, **2005**, 288, 489.
- [11]. M. Rai, A. Yadav, A. Gade, *Biotechnology Advances*, **2009**, 27, 76.
- [12]. K. Kawahara, K. Tsuruda, M. Morishita, M.Uchida, *Dental Materials*, **2000**, 16, 452.
- [13]. W. De Muynck, N. De Belie, W. Verstraete, *Journal of Applied Microbiology*, **2010**, 108, 62.
- [14]. xxx SR EN 1015-2:2001 Methods of test for mortar for masonry - Part 2: Bulk sampling of mortars and preparation of test mortars.
- [15]. xxx SR EN 1015-3:2001 Methods of test for mortar for masonry - Part 3: Determination of consistence of fresh mortar (by flow table).

- [16]. xxx SR EN 998-1:2011 Specification for mortar for masonry - Part 1: Rendering and plastering mortar.
- [17]. xxx SR EN 1015-11:2002 Methods of test for mortar for masonry - Part 11: Determination of flexural and compressive strength of hardened mortar.
- [18]. xxx SR EN 1015-10:2002 Methods of test for mortar for masonry - Part 10: Determination of dry bulk density of hardened mortar.
- [19]. xxx SR EN 1015-18:2003 Methods of test for mortar for masonry- Part 18: Determination of water absorption coefficient due to capillary action of hardened mortar.
- [20]. xxx SR EN 1015-12:2001 Methods of test for mortar for masonry - Part 12: Determination of adhesive strength of hardened rendering and plastering mortars on substrates.

INFLUENCE OF NI NANOPARTICLES ON GROWTH OF DLC FILM BY PECVD TECHNIQUE

ZAHRA KHALAJ^a

ABSTRACT. Plasma enhanced chemical vapor deposition (PECVD) technique is mostly used to fabricate diamond-like carbon (DLC) films on different type of substrate. Research on DLC films has been devoted to find both optimized conditions and characteristics of the deposited films on coated areas. In this work, the DLC films deposition on silicon coated Nickel layer were studied. Aluminum was used as a buffer layer, deposited directly on silicon at the room temperature. Atomic Force Microscopy was used to characterize the surface roughness and distribution function of the nickel nanoparticles. The DLC films quality was studied using Raman spectroscopy and Fourier transform infra-red spectroscopy (FTIR). The results show a lower intensity ratio of I_D/I_G for DLC films by increasing the Ni deposition time on the Si/Al/Ni substrates, providing a good quality of the DLC growth by increasing the nickel content and reducing the average roughness of the surface to less than 4 nm.

Key words: *DLC, AFM, Nickel nanoparticles*

INTRODUCTION

Diamond-Like Carbon (DLC) is a material of interest to scientists owing to its attractive properties and performances including: high hardness, smooth surface morphology, low friction coefficient, chemical inertness, biocompatibility, high optical transparency and ability to absorb photons selectivity [1-4]. Function of the existence of hydrogen atoms in their structure, DLC are categorized in two forms: hydrogenated amorphous carbon (a-C:H) and non-hydrogenated amorphous carbon (a-C). Usually, its structure is a network of sp^2 and sp^3 coordinated carbon and hydrogen atoms in different proportions. For depositing DLC coatings, the PECVD methods are available such as DC-bias, RF sputtering and pulsed-DC [4-8].

^a Young Researchers and Elite Club, Science and Research Branch, Islamic Azad University, Tehran, Iran. Corresponding author: khalaj.z@gmail.com

There are a number of advantages associated with PECVD technique, making it a very attractive method for depositing DLC films, such as low deposition temperature, high deposition rate, and good control over stoichiometry, cleanliness and low particulate levels [9]. For DLC deposition, there are several problems and limitations about the substrate type. Therefore, using a suitable interlayer may help to improve the growth rate and DLC quality by increasing the rate of nucleation and adhesion to the substrate.

In the present study, DLC films were deposited on Si/Al/Ni thin films using DC-plasma of C₂H₂ and H₂ gas mixture by PECVD system. The thickness of Al and the growth conditions for DLC were kept constant in all samples. The Ni content is varied in different samples and the influence of these changes on quality of DLC was investigated. The film characterization was performed by Dektak profilometer, Atomic Force Microscopy (AFM), Raman Scattering Spectroscopy, Fourier Transform Spectroscopy (FTIR) and Scanning Electron Microscopy (SEM).

RESULTS AND DISCUSSION

AFM was typically performed on Si/Al coated thin films in contact mode on 3μm x 3μm area. Figure 1 shows 2D and 3D images of the A₁, A₃ and A₄ samples. Three dimensional images in all samples show different topography, proving different average roughness. All the experimental conditions were same for all the samples, as referred in the last part, except the deposition time for Nickel Nano Particles (NiNPs). The duration of the experiments was 40 minutes for A₁ which increases to 160 minutes at the same temperature for A₄. Therefore, as can be seen in Figure 1, the size distribution of NiNPs is nearly homogeneous for all the samples. In addition, by increasing the sputtering time, the influence of temperature results in smaller nanoparticles, which might be related to changes in the kinetic energy of the particles. Figure 2 shows the histogram of distribution of NiNP size on the surface of Si/Al substrates, calculated using WSxM 5.0 software. The maximum of number of events estimates the average of particles number and its width gives the variance of the particles diameter. Although the distribution of the particle size is sharp for A₄ and less sharp for A₃ and A₁, the full width at the half maximum of particle size distribution is not large for all of them (less than 10nm) which means the size distribution in NiNPs is of a limited range. As the Gaussian diagram shows for all samples, the distribution of the nickel nanoparticles on Si/Al substrates is nearly homogenous, but the homogeneity varies due to the effect of time duration and temperature on nickel coating. The histogram of nanoparticle distribution may be used to interpret the distribution function of particles size.

The 2D AFM image (Fig.1) and diagrams in Fig. 2 show that, by increasing the time duration in the experiments, the particle size becomes smaller and the size homogeneity increases. Using the Gaussian diagram, one can observe that the particle size of the samples is less than 10nm.

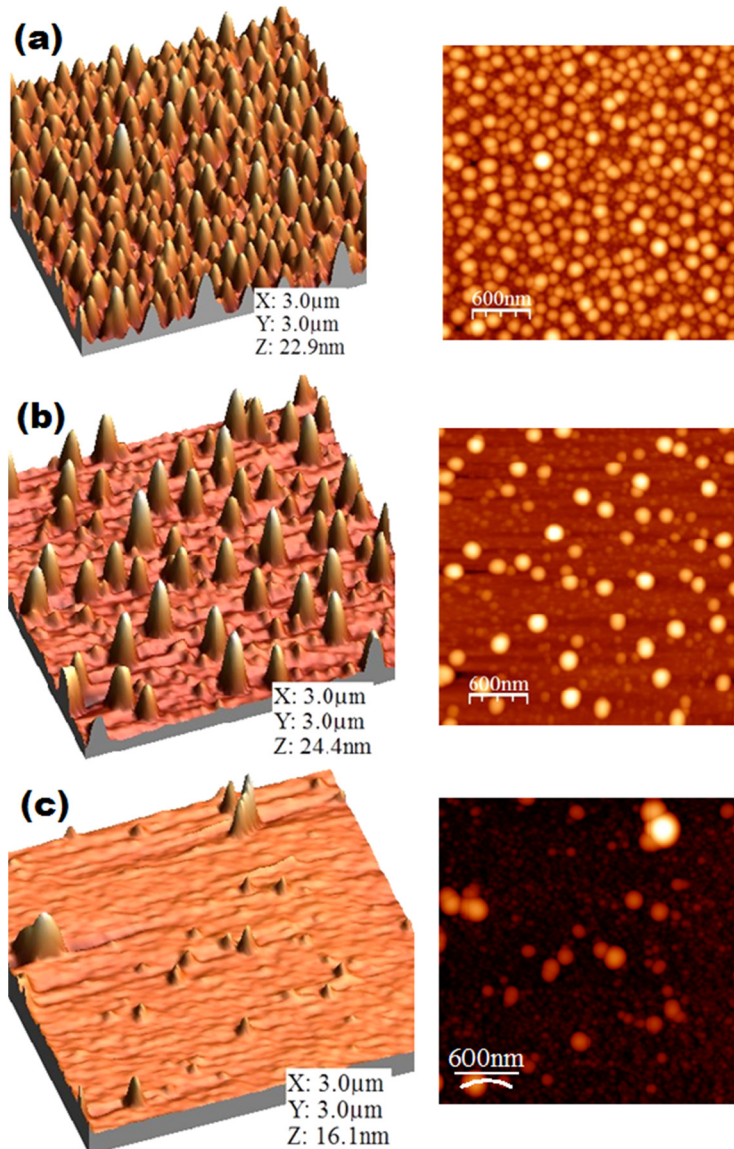


Figure 1. Two and three dimensional AFM images: (a) A₁, (b) A₃ and (c) A₄

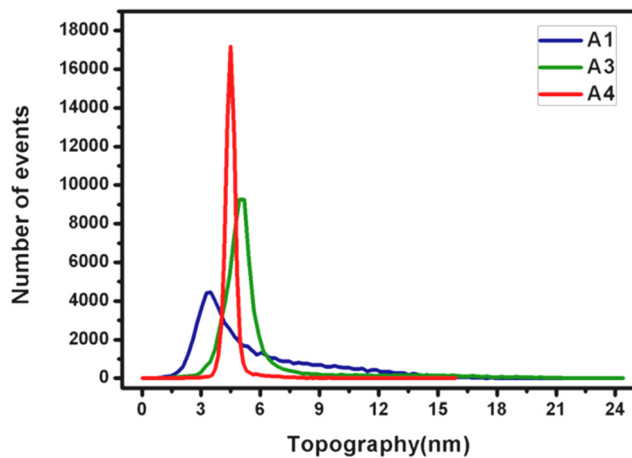


Figure 2. Histogram of NiNPs distribution on Si/Al substrates

The results of surface analysis are listed in Figure 3. The average roughness and RMS roughness of the surface decrease by increasing the Ni sputtering time duration [4]. In addition, the height changes, obtained from the 3D AFM images of Fig.1 using WsXM software are shown here.

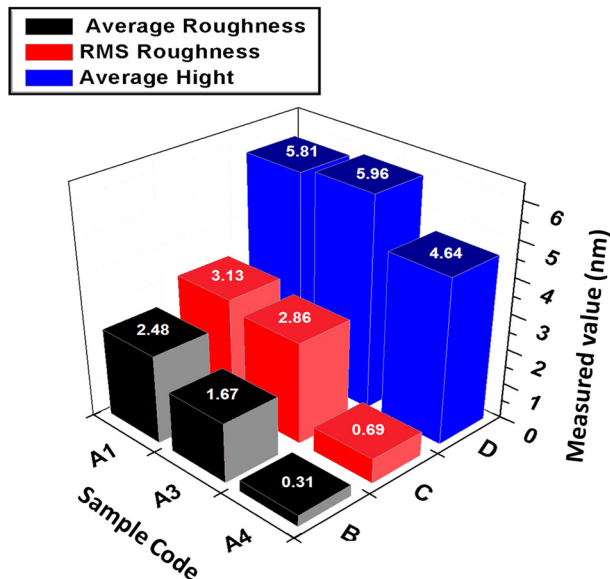


Figure 3. Histogram of the roughness of Ni coating on Si/Al substrates for different sputtering time durations and its height changes

In our previous work [4], the mechanism of adhesion is categorized into mechanical interlocking and chemical bonding, respectively. Mechanical interlocking can be seen as locking by friction and locking by dovetailing [4, 10]. As our group reported elsewhere [4], by decreasing the roughness, the surface becomes smoother. Due to the high degree of chemical bonding and good friction coefficient of Ni nanoparticles layer in this case, there is more adherence to the substrate surface and Nickel nanoparticles [4]. The AFM images show that, by increasing the deposition duration, the NiNPs size was reduced, therefore the surface becomes smoother, which can increase the possibility of mechanical interlocking and also the solubility of carbon atoms in NiNPs. The model of mechanical interlocking was described elsewhere [4].

Raman spectroscopy [11] is a standard nondestructive technique used to evaluate the quality and structural properties of DLC coatings. Fig.4 (a)-(d) shows the Raman spectra of our grown DLC films. These spectra contain typical two broad peaks (see Fig. 4), the so-called G (labeled 'G' for graphite) and D (labeled 'D' for disorder) peaks [12]. The G peak is attributed to the graphite-like layers of sp^2 micro domains, while the D peak is due to the bond-angle disorder in the sp^2 graphite-like micro domains induced by the linking with sp^3 -C atoms as well as the finite crystalline sizes of sp^2 micro domains [13-15]. The results of the Raman study are listed in Table 1.

Table 1. Results of the Raman study for all substrates

Sample Code	D Band (cm^{-1})	G Band (cm^{-1})	I_D/I_G
A ₁	1455	1564.49	1.43
A ₂	1455.11	1562.44	1.25
A ₃	1451/05	1550.94	0.59
A ₄	1459.68	1563.67	0.52

The position of G lines and the intensity ratio of D peak and G peak, I_D/I_G , can be correlated with the sp^2/sp^3 bonding ratio, graphite cluster size, and disorder in these threefold coordinated islands [14]. The Raman analysis shows the ratio $I(D)/I(G)$ values for the DLC coatings in the range 1.43 for A₁ and 0.52 for A₄ substrates. A lower intensity ratio I_D/I_G is connected with higher overall sp^3 content. Therefore, we can infer that the DLC films deposited on A₄ substrate have a more sp^3 content [15-17].

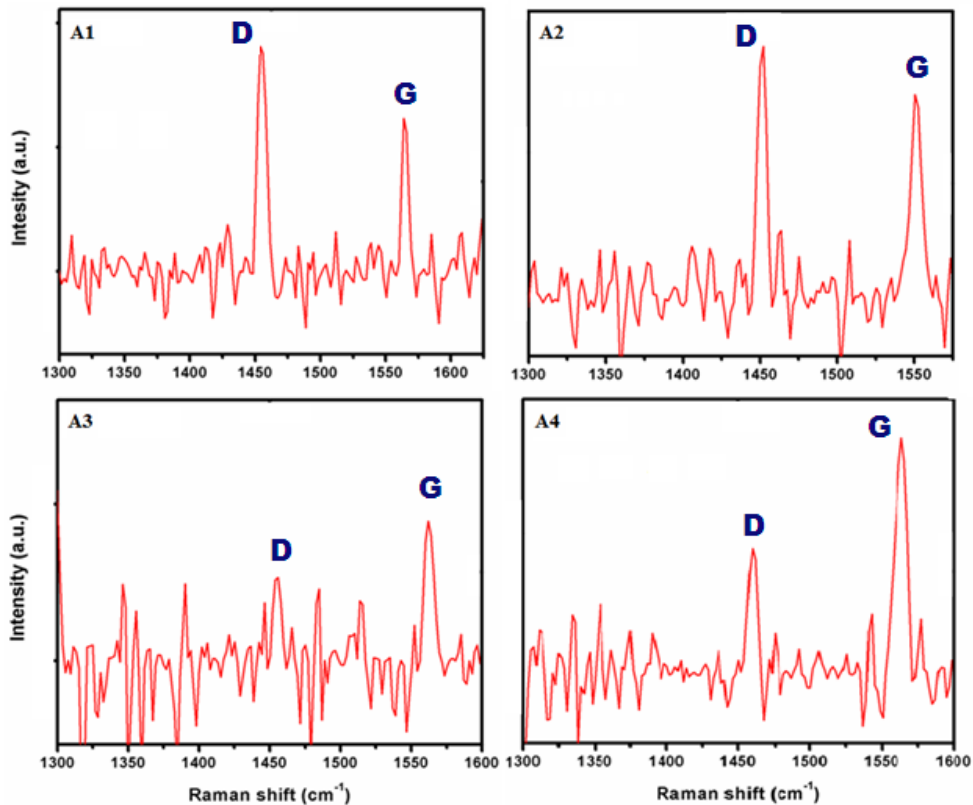
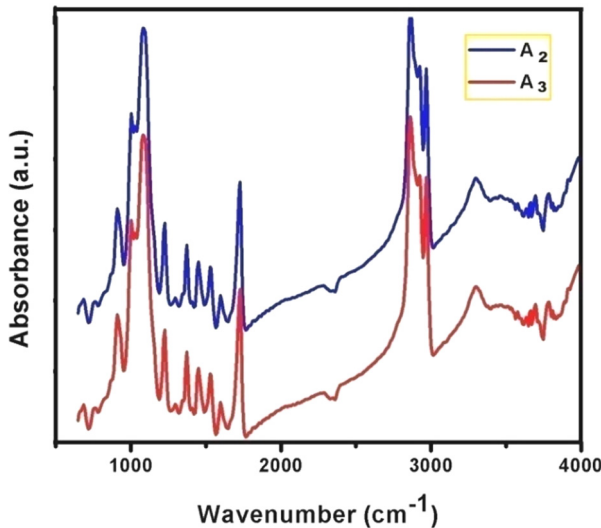


Figure 4. The Raman spectra of DLC films deposited on A₁, A₂, A₃ and A₄ substrates

Fourier Transform Infrared Spectroscopy (FTIR) is a widely used technique to analyze the bonding states of DLC films. Typical FTIR absorption spectra of DLC coatings deposited on our substrates are shown in Figure 5. The band appearing at 905.03 cm⁻¹ is assigned to sp² CH₂ olefinic bonds. The peak near 1231.12 cm⁻¹ could be related to sp²/sp³ C-C bonds and the weak peak near 1295.19 cm⁻¹ may arise due to CH (olefinic) bond in sp²-type carbon. The other absorption peaks are listed in Table 2. The C-H stretching vibration region, observed at 2800-3200 cm⁻¹ in the FTIR spectra of DLC films, is very important to explain the electrical and nano-mechanical properties of these films [4,16]. The peak located at around 2862.70 cm⁻¹ is attributed to sp³-CH_n (n=1, 2, 3) symmetric stretching vibration modes, while the peaks at approximately 2966.80 cm⁻¹ are associated with asymmetric stretching modes. The peak originated at 3292.90 cm⁻¹ represents sp¹ CH bonds.

Table 2. Characteristic $\text{sp}^n \text{CH}_m$ (n and m=1, 2, 3) vibration modes of DLCs grown on Si/Al/Ni: A₂ and A₃

Sample	Wave numbers (cm^{-1})	Bond type
A ₂ , A ₃	905.03	(olef) SP ² CH ₂
	1231.12	SP ² /SP ³ C-C
	1295.19	(olef) SP ² CH
	1375.28	SP ³ CH ₃
	1440.50	SP ³ CH ₂
	2862.70	SP ³ CH _n (n=1,2,3)
	2966.80	SP ³ CH ₂ (asymmetric)
	3292.90	SP ³ CH ₃ (asymmetric)

**Figure 5.** FTIR absorbance spectra of DLC films deposited on Si/Al/Ni substrates

These results suggest the films grown on Ni coated silicon substrates have a DLC structure, in good agreement with the Raman analysis. Typical scanning Electron Microscopy (SEM) of the surface coating for A₄ is shown in Figure 6. The DLC layer of the sample were segregated in order to measure the thickness which was done typically, using Microstructure Measurement software (See Fig.6 (II)).

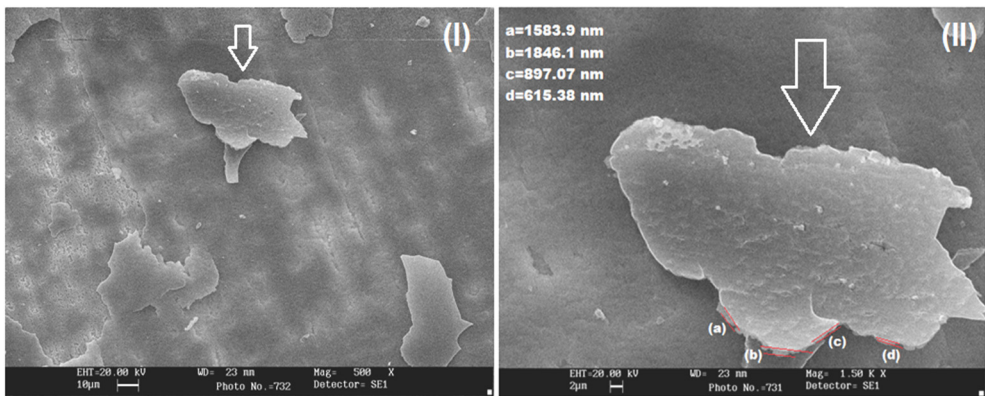


Figure 6. Typical SEM images of DLC deposited on Si/Al/Ni (A₄)

CONCLUSIONS

In this study, DLC films were deposited on Si/Al/Ni substrates. The Al thickness and DLC experimental conditions have been kept constant for all samples but the Ni deposition time was increased from 40 min to 160min. The AFM results show that the particle size distribution of NiNPs was nearly homogeneous for all the samples. In addition, by increasing the sputtering time, the influence of temperature on the nanoparticles growth resulted in smaller size, which might be related to changing in the kinetic energy of the particles; as a consequence, the reduction of average roughness of the substrate surface was observed. The RMS roughness of the surface decreased and the surfaces become smoother with increasing the NiNPs deposition time.

Raman analysis enabled evaluation of the intensity ratio I_D/I_G for the DLC coating on the realized substrates A₁ to A₄. The results have shown that by reducing the surface roughness a lower intensity ratio I_D/I_G can be obtained, in connection with a higher overall sp³ content and the sp² phase organized rather in chain structures. As a result, high quality DLC films have been obtained.

EXPERIMENTAL SECTION

The multilayer was synthesized on P-type silicon wafers (100) in the size of 5×5 mm. The substrates were cleaned in acetone and rinsed with ethanol prior to deposition. Two methods were used for deposition of multilayer:

DC magnetron sputtering and planar DC sputtering. DC magnetron sputtering was performed with Argon gas for Al deposition at 2×10^{-2} Torr for 1 minute at room temperature. The system consists of two coaxial cylinders, used as the cathode (inner one) and anode (outer one) [17]. The plasma current was obtained at 200mA and 600V, respectively. A nearly uniform magnetic field, parallel to the axis of the cylinders, was generated by a coil around the outer cylinder [17]. Fig. 7 shows the thickness measurement of the Al thin film by Dektak3 profilometer. The thickness of the as-deposited Al layer was about 540nm.

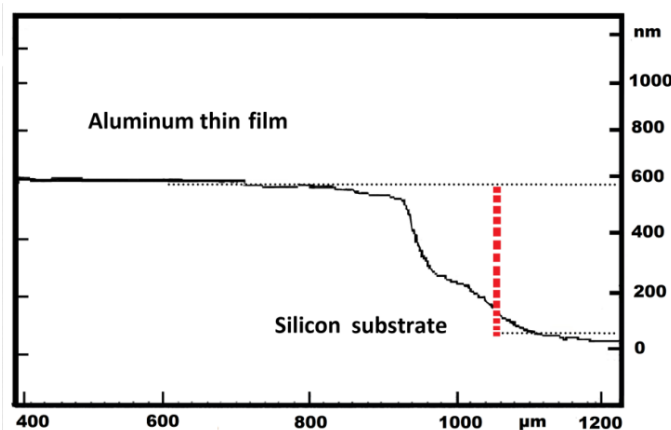


Figure 7. DEKTAK profilometer result, showing the thickness of Al nanolayer

A planner DC sputtering was applied for Nickel sputtering on Si/Al substrates using Ar gas. The temperature does not exceed 200°C during the experiment. The experimental conditions for nickel sputtering were listed in Table 3.

Table 3. Experimental conditions for nickel sputtering on Si/Al substrates

No.	Sample	Temperature (°C)	Ni Deposition time (min)
A ₁	Si/Al/Ni	200	40
A ₂	Si/Al/Ni	200	80
A ₃	Si/Al/Ni	200	120
A ₄	Si/Al/Ni	200	160

Diamond-like Carbon films were produced in a DC-PECVD system. Figure 8 shows the schematic diagram of the PECVD system.

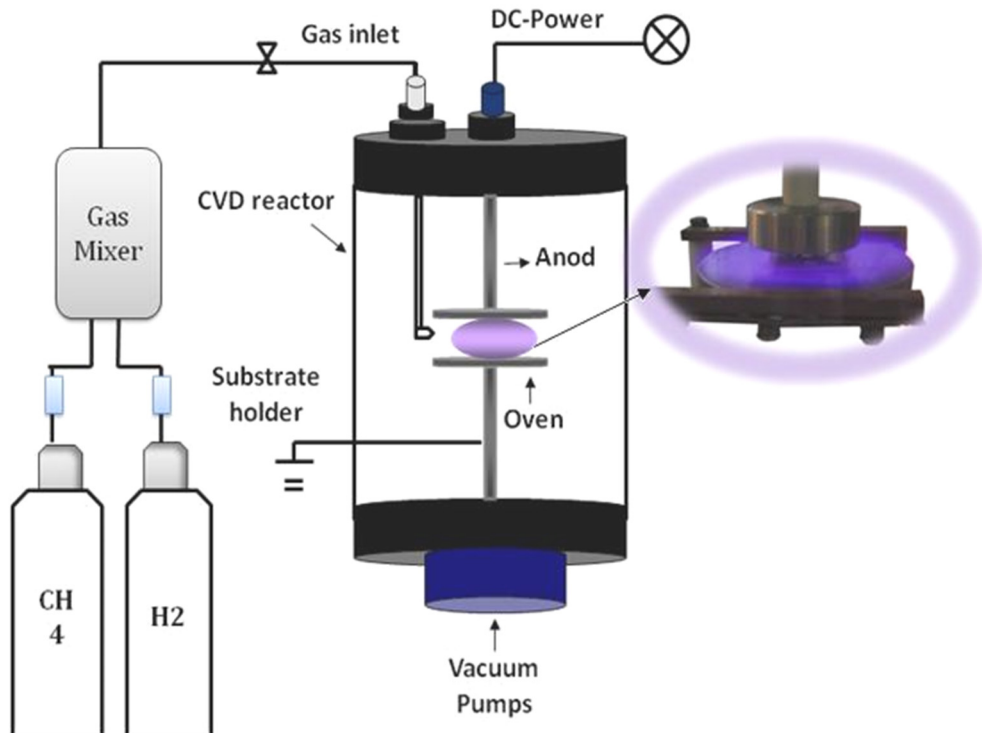


Figure 8. Schematic diagram of the PECVD system

The pretreated substrates were mounted into an oven in the center of PECVD chamber. The cathode was fed by a DC power supply. The DLC films started to be deposited using acetylene for 50 minute (80 sccm gas flow at 10 Torr and a discharge voltage of 100 V). After, the experiment was continued with the C₂H₂/H₂ mixture plasma with 15% flow ratio, during 120 minutes. The voltage was kept constant at 450V and the pressure inside the chamber was 12 Torr. Temperature was reached to 300°C. The schematic form of the deposited layers was shown by a model in Figure 9.

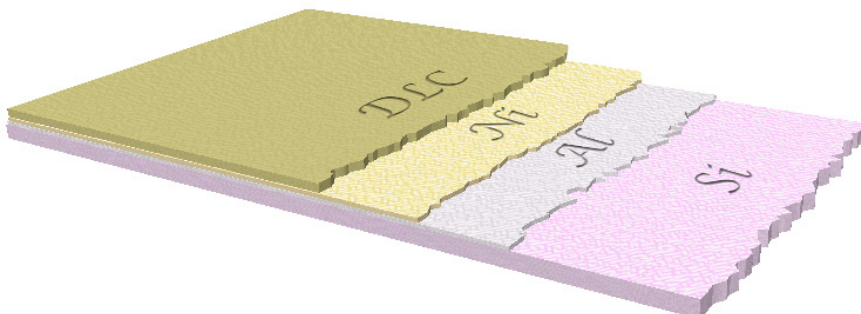


Figure 9. A schematic image of the DLC coated on Si/Al/Ni substrate

ACKNOWLEDGEMENT

Many thanks are addressed to Elnaz Vaghri and Amir Saghaleyni for their technical support on CVD and PVD systems.

REFERENCES

- [1] P.D. Maguirea, J.A. McLaughlina, T.I.T. Okpalugoa, P. Lemoinea, P. Papakonstantinoua, E.T. McAdamsa, M. Needhama, A.A. Ogwub, M. Ballc, G.A. Abbas, *Diamond Relat. Mater.*, **2005**, 14, 1277.
- [2] C. Casiraghi, J. Robertson, A.C. Ferrari, *Mater. Today*, **2007**, 10, 44.
- [3] E. Vaghri, Z. Khalaj, M. Ghoranneviss, M. Borghei, *J. Fusion Energ.*, **2011**, 30, 447–452.
- [4] Z. Khalaj, M. Ghoranneviss, E. Vaghri, A. Saghaleini, M.V. Diudea, *Acta Chim. Slov.*, **2012**, 59, 338–343.
- [5] D.K. Rai, Debjit Datta, Sanjay K. Ramc, Surajit Sarkar, Rajeev Gupta, Satyendra Kumar, *Solid State Sciences*, **2010**, 12, 1449–1454.
- [6] W.S. Choi, J. Heo, I. Chung, B. Hong, *Thin Solid Films*, **2005**, 475, 287.
- [7] G. Reisel, A.D. Reisel, *Diam. Relat. Mater.*, **2007**, 16, 1370.
- [8] S. Kumar, P.N. Dixit, R. Bhattacharyya, *J. Appl. Phys.*, **1999**, 85, 3866.
- [9] D. Tither, W. Ahmed, E. Ahmed, *Materials Science*, **1997**, 32, 1931–1936.
- [10] Kenneth Holmberg, Allan Matthews, *Elsevier*, **2009**, pp.185–297.
- [11] Ruchita S. Das, Y.K. Agrawal, *Vibrational Spectroscopy*, **2011**, 57, 163–176.
- [12] G.E. Stan, D.A. Marcov, A.C. Popa, M.A. Husanu, *Nanomaterials and Biostructures*, **2010**, 5, 705–718.

- [13] F. Tuinstra and J.L. Koenig, *Chem. Phys.*, **1970**, 53, 1126.
- [14] P. Yanga, N. Huang, Y.X. Leng, J.Y. Chen, R.K.Y. Fu, S.C.H. Kwok, Y. Leng, P.K. Chu, *Biomaterials*, **2003**, 24, 2821.
- [15] A.C. Ferrari, J. Robertson, *Philos. Trans. R., Soc. Lond. Ser. A*, **2004**, 362, 2477.
- [16] A.C. Ferrari, J. Robertson, *Phys. Rev. B*, **2000**, 61, 14095.
- [17] Mahmoud Ghoranneviss, Kiomars Yasserian, Abbas Anvari, Hamidreza Pourbalasi, Alireza Hojabri, Homa Hosseini, *J. Plasma Fusion Res.*, **2005**, 7, 1-2.

ZINC QUANTIFICATION IN SELECTED PHARMACEUTICAL PRODUCTS BY TWO ANALYTICAL METHODS

ANDREIA CORCIOVĂ^a, CONSTANTIN CIOBANU^{a,*}

ABSTRACT. The aim of this study was to develop two methods that can be used to determine the concentrations of zinc in some pharmaceutical formulations. The first proposed method follows the formation of a red complex between dithizone and zinc which can be spectrophotometrically determined at 516 nm. The second method is based on the detection of zinc through atomic absorption spectrometry, at 213.857 nm, after wet digestion of the samples. The wet ashing method was performed using a mixture of concentrated nitric acid and 30 % hydrogen peroxide (8:2). Both methods were evaluated in terms of linearity, precision (repeatability and intermediate precision), recovery, limit of detection and limit of quantification. The obtained RSD values for the analyzed performance parameters were smaller than the maximum limits recommended by the international standards, therefore the proposed methods can be successfully applied for the determination of zinc in pharmaceutical formulations.

Keywords: *UV-Vis spectrophotometry, FAAS, zinc-dithizone complex, method validation*

INTRODUCTION

Nowadays, the use of dietary supplements based on vitamins, micro and macro elements is widespread. Both young and older people use these preparations in order to compensate for deficiencies in their diet. They are recommended both in some treatments and prophylactically. The use of these supplements has grown in recent years and continues to grow according to a study conducted in 2007 [1].

Zinc is the second transition metal after iron in terms of importance therefore its level in the human body is essential to a healthy growth and development [2, 3]. This metal is an essential constituent for many biological processes catalysed by metalloenzymes (over 300 enzymes), zinc being involved in lipid, protein and carbohydrate metabolisms [4]. So maintaining

^a “Grigore T. Popa” University of Medicine and Pharmacy Iasi, Faculty of Pharmacy, Drug Analysis Department, 16 Universitatii Street, RO-700115, Iasi, Romania.

* Corresponding author constantin.ciobanu@umfiasi.ro

an optimal level of zinc in the body is very important. For this purpose, continuous monitoring of the concentration of zinc in dietary supplements is of great importance. This can be achieved through the development of simple methods for rapid and accurate determination of this metal. Numerous analytical methods have been used for this purpose and among them we mention: spectrophotometry [5], spectrofluorimetry [6], voltammetry [7], chromatography [8], chemiluminescence [9], capillary electrophoresis [10], atomic absorption spectrometry [11], inductively coupled plasma mass spectrometry [12]. Although some of these methods offer very good precision and accuracy, they require expensive and demanding instruments. Therefore, in this study we used UV-Vis spectrophotometry (Method 1) and Flame Atomic Absorption Spectrometry (FAAS) (Method 2) because they are simple, rapid and their use involves minimal resources. The FAAS method relies on a specific light wavelength which is absorbed by the zinc atoms whereas the spectrophotometric method makes use of ligands which bind to zinc in order to produce a coloured complex [12-14].

This paper presents the determination of zinc content in 3 pharmaceutical preparations from Romanian market. The proposed methods were compared in terms of sensitivity, accuracy and applicability.

RESULTS AND DISCUSSION

The reaction between zinc and alkaline dithizone is presented in figure 1, when a red complex (soluble in chloroform) is formed. In order to optimize the spectrophotometric method, different volumes of 0.01% dithizone were used (0.5 - 2 ml). It was observed that at levels higher than 1 ml, the colour of the complex is masked by the colour of dithizone.

Therefore, different amounts of alkaline ammonium citrate solution were used, establishing the optimum volume at 2 ml.

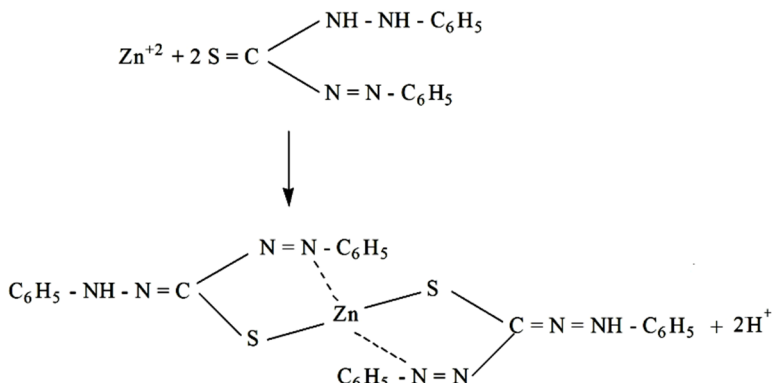


Figure 1. Reaction of zinc with dithizone [15]

Analytical validation

The methods proposed by us were validated according to the ICH recommendations for validation of analytical procedures [16].

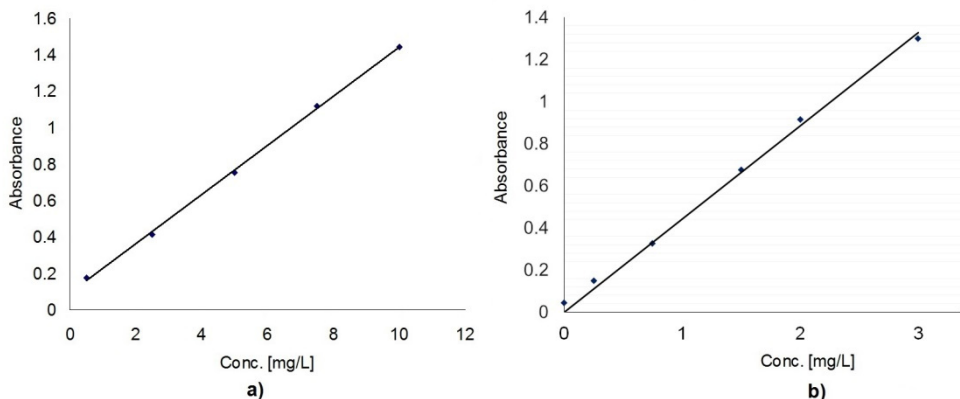


Figure 2. Calibration curves for the spectrophotometric method (a) and for the AAS method (b)

Linearity: for method 1, the results showed good relationship over the concentration range 0.5 - 10 mg/L and for method 2, the analytic response was linear in the range of 0.25 – 3 mg/L. The linear regression equations were found to be $y = 1.3502x + 0.09274$ for method 1 and $y = 0.40915x + 0.09947$ for method 2. Figure 2 presents the obtained calibration curves and Table 1 shows the statistical data regarding zinc determinations.

Table 1. Statistical data and validation parameters for zinc determination

Parameter	Method 1	Method 2
<i>Regression analysis</i>		
Slope	1.3502	0.4091
Intercept	0.0927	0.0994
Standard error	0.0174	0.0041
Regression coefficient (r^2)	0.9991	0.9938
<i>Validation parameters</i>		
Linearity (mg/L)	0.5 - 10	0.25 – 3
Limit of detection (mg/L)	0.4257	0.0078
Limit of quantification (mg/L)	1.2901	0.0238

Accuracy: this parameter represents the closeness of the obtained results to the true theoretical value [17]. The accuracy and reliability of the proposed methods were evaluated by recovery studies of standard addition method (Table 2). The lowest average recovery for all analyzed samples was 98.62 % and the highest 103.1 %, therefore, any change in the active substance concentration can be accurately determined using the proposed methods.

Table 2. Accuracy data for the proposed methods (n = 9)

Method 1			
Added conc. (mg/L)	Absorbance ± SD*	Recovered conc. (mg/L) ± SD*	% Recovery ± SD*
-	0.0015 ± 0.0001	-	-
2.500	0.4303 ± 0.0019	2.499 ± 0.100	100.0 ± 0.57
5.000	0.7631 ± 0.0033	4.976 ± 0.030	99.52 ± 0.64
7.500	1.1090 ± 0.0014	7.526 ± 0.070	100.3 ± 1.00
Method 2			
Added conc. (mg/L)	Absorbance ± SD*	Recovered conc. (mg/L) ± SD*	% Recovery ± SD*
-	0.0456 ± 0.0006	-	-
0.850	0.4424 ± 0.0070	0.838 ± 0.017	98.59 ± 2.03
1.600	0.7748 ± 0.0081	1.650 ± 0.019	103.12 ± 1.23
2.400	1.0864 ± 0.0146	2.412 ± 0.035	100.5 ± 1.48

* Standard deviation of the mean

Precision: the precision of the proposed methods was determined by studying repeatability and intermediate precision. Table 3 presents the repeatability values (expressed as % RSD), which were less than 2 for both methods [18]. These results indicate the precision under the same operating conditions over a short period of time. Intermediate precision presented in Table 4, expresses the results obtained in the same laboratory in different days. With respect to the intermediate precision study, the values for RSD were within the acceptable limits recommended by the international guidelines.

LD (Limit of detection) and LQ (Limit of Quantitation): for method 1 LD and LQ were found to be 0.4257 mg/L and 1.2901 mg/L, respectively, and for method 2, LD and LQ were found to be 0.0078 mg/L and 0.0238 mg/L, respectively.

Table 3. Results of repeatability study (n = 6)

No	Absorbance	
	Method 1	Method 2
1.	0.7519	0.7713
2.	0.7498	0.7718
3.	0.7510	0.7716
4.	0.7508	0.7696
5.	0.7522	0.7856
6.	0.7518	0.7771
Average	0.751	0.774
SD*	0.001	0.006
% RSD**	0.119	0.775

* Standard deviation of the mean

** Relative standard deviation

Table 4. Intermediate precision study (n = 3)

	Concentration (mg/L)			Mean (mg/L) ± SD*	% RSD**
	Day 1	Day 2	Day 3		
Method 1	2.50	2.49	2.48	2.49 ± 0.00	0.33
	4.95	4.96	4.96	4.96 ± 0.00	0.10
	7.59	7.55	7.43	7.52 ± 0.07	0.90
Method 2	0.86	0.85	0.82	0.84 ± 0.02	2.02
	1.61	1.59	1.67	1.62 ± 0.03	2.09
	2.41	2.37	2.42	2.40 ± 0.02	0.90

* Standard deviation of the mean

** Relative standard deviation

Application of the proposed methods for pharmaceutical formulations

Both methods have been applied for the determination of zinc in 3 dietary supplements containing just zinc as an active principle (tablets). Table 5 shows the average of 3 determinations for each analyzed sample, expressed in mg zinc/tablet and their recovery values. The samples were analyzed daily for three consecutive days.

Table 5. Zinc concentrations found in analyzed samples

		Method 1		Method 2	
Sample		mg found/ tablet ± SD*	% Recovery	mg found/ tablet ± SD*	% Recovery
Sample 1 15 mg zinc/tablet	Day 1	14.86 ± 0.72	99.06	14.94 ± 0.13	99.60
	Day 2	15.20 ± 0.22	101.33	14.77 ± 0.19	98.46
	Day 3	14.92 ± 0.68	99.46	14.90 ± 0.19	99.33
Sample 2 10 mg zinc/tablet	Day 1	9.92 ± 0.82	99.20	9.92 ± 0.04	99.20
	Day 2	9.97 ± 0.75	99.70	9.92 ± 0.08	99.20
	Day 3	10.11 ± 0.90	101.1	9.51 ± 0.13	95.10
Sample 1 5 mg zinc/tablet	Day 1	5.09 ± 0.54	101.8	5.12 ± 0.05	102.4
	Day 2	5.01 ± 0.39	100.2	5.04 ± 0.07	100.8
	Day 3	4.98 ± 0.61	99.60	5.09 ± 0.09	101.8

* Standard deviation of the mean

The obtained results are in accordance with the limits imposed by the British Pharmacopoeia ed. 2013, Tablets Monograph [19] and the European Pharmacopoeia 8.0 [20].

CONCLUSIONS

A possible element of originality presented in this paper could be represented by the development, validation and application of a HR-CS-AAS method for the determination of zinc in dietary supplements which contain only zinc as an active principle.

Both methods are precise, simple, however each has its advantages and disadvantages. While the used spectrophotometric method is time consuming and needs more reagents, the FAAS is more sensitive, faster and uses smaller quantities of reagents. On the other hand, the UV-Vis method is cheaper and doesn't require sophisticated equipment. In conclusion, it has been demonstrated that the proposed methods can be successfully used for the determination of zinc in pharmaceutical preparations containing zinc as an active substance.

EXPERIMENTAL SECTION

Reagents

Zinc sulphate ($\text{ZnSO}_4 \cdot 7\text{H}_2\text{O}$) and dibasic ammonium citrate were purchased from Chimopar SA, Romania; Dithizone was supplied by Sigma Aldrich and Chloroform, 65% Nitric acid, 30% Hydrogen peroxide were purchased

from Chemical Company, Romania. The calibration curve for Method 2 was prepared using an ICP multi-element standard solution VIII (0.1 mg/ml) which was supplied by Merck, Germany. All used reagents were of analytical grade. Double distilled water (DDW) was used throughout the experiment.

The analyzed pharmaceutical products were purchased from the local pharmacies in city of Iasi, Romania, between January and March 2014. The samples consisted of 3 types of tablets containing 15 mg zinc/tablet, 10 mg zinc/tablet and 5 mg zinc/tablet.

Preparation of reagent solutions

Dithizone solution 0.1 %: 0.1 g dithizone were dissolved in 100 ml chloroform and kept in brown bottles for one week;

Dithizone solution 0.01 %: 10 ml dithizone solution 0.1 % were mixed with 50 ml ammoniac 250 g/l in a separating funnel and stirred. The chloroformic layer was removed and the extraction was repeated 4 times, each time with 10 ml chloroform. The aqueous layer was filtered and introduced in another separating funnel along with 100 ml chloroform and hydrochloric acid 1/1 until pH = 1. The mixture was vigorously shaken after which the chloroformic layer was separated, washed with DDW several times and filtered through anhydrous sodium sulphate. This solution was prepared when needed.

Alkaline ammonium citrate solution: 25 g of dibasic ammonium citrate were dissolved in 50 ml DDW after which 50 ml of 28 % ammonium hydroxide were added.

Stock solution: zinc sulphate is highly soluble in water, but for a greater stability of the solution, HCl 0.1 M was used. 0.0879 g of ZnSO₄ 7H₂O were dissolved in 100 ml HCl 0.1 mol/L in order to obtain a concentration of 200 mg/L. After preparation, the stock solution was stored at low temperature.

Apparatus

For the UV-Vis spectrophotometric method a Jasco V 530 double beam UV-Vis spectrophotometer was used. All the measurements were made in 1.0 cm quartz cells at a scan speed of 1000 nm min⁻¹ and a scan range of 400-800 nm, fixed slit width of 2 nm.

For the FAAS method a high resolution continuum source flame atomic absorption spectrometer (ContrAA 300, Analytic Jena, Germany) was used. The working conditions consisted of: a mixture of air and acetylene as fuel with a flow of 50 L/h, the burner height was 6 mm and the flame burner was 100 mm in length. The device is equipped with a detector CCD (Charge Coupled Device). In HR-CS-AAS, the background correction is carried out based on various algorithms that are implemented in the software of the atomic absorption spectrometer [21]. The instrumental parameters were optimized in accordance with manufacturer's recommendations.

The procedure of the methods

Method 1: from each prepared solution, a volume of 1 ml was brought to a separating funnel. 2 ml of alkaline ammonium citrate solution and 1 ml of 0.01% dithizone were added and repeated extractions with 5 mL chloroform were performed until the colour of the formed complex disappeared. The absorbance was determined at 516 nm against a blank containing dithizone.

Method 2: the mixture was treated with 8 ml 65% nitric acid and 2 ml 30% hydrogen peroxide in Erlenmeyer flasks. The mixture was subjected to reflux boiling for 4 hours at 140°C using a heating plate. After cooling, the content of the beakers were quantitatively transferred into 100 ml volumetric flasks. The volumes were made up with DDW and filtered. The obtained solutions were analyzed for zinc at 213.857 nm using a flame atomic absorption spectrometer.

Method validation

The method was validated in terms of linearity, accuracy, precision (repeatability and intermediate precision), limit of detection, limit of quantitation.

Linearity: to establish the linearity of the proposed methods, five dilutions were prepared from the stock solution (0.5 mg/L, 2.5 mg/L, 5.0 mg/L, 7.5 mg/L and 10 mg/L for Method 1). For Method 2, another five dilutions were prepared from the ICP multi-element standard solution (0.25 mg/L, 0.75 mg/L, 1.5 mg/L, 2 mg/L and 3 mg/L). The calibration curves were constructed as concentration vs. absorbance (Figs. 2 and 3).

Accuracy: the standard addition method was performed. To determine the accuracy of the spectrophotometric method, 3 concentration levels were used (2.5 mg/L, 5.0 mg/L and 7.5 mg/L) and for each level 3 determinations were performed; the concentrations were calculated using the calibration curve equation. In order to check if the FAAS method is accurate, the samples were spiked with known concentrations of analyte (0.85 mg/L, 1.6 mg/L, 2.4 mg/L) and then wet digested and analyzed.

Precision: precision of the method was evaluated as repeatability (intraday variation) and intermediate precision (interday variation). The repeatability studies were carried out by analyzing samples containing 5 mg/L concentration (method 1) and 1.6 mg/L concentration (method 2) for six times in the same day. Intermediate precision was determined by analyzing three concentrations (2.5 mg/L, 5.0 mg/L and 7.5 mg/L) for method 1 and (0.85 mg/L, 1.6 mg/L, 2.4 mg/L) for method 2, daily for three days.

Detection limit and quantitation limit: the limit of detection and limit of quantitation for zinc by method 1 was calculated using the calibration curves. LD and LQ were calculated as $3.3 \cdot \sigma/S$ and $10 \cdot \sigma/S$, respectively, where σ is the standard deviation of y-intercept of the regression equation and S is the slope

of the calibration curve. For method 2, LD and LQ were calculated as $3.3 \cdot \sigma/S$ and $10 \cdot \sigma/S$, where σ represents the standard deviation of 11 blank determinations and S is the slope of the calibration curve.

Application of the proposed method for pharmaceutical formulations

Prior to analysis, 20 tablets were weighed, their average mass was calculated, after which they were manually grinded using a mortar and pestle, homogenized and sieved through a 1 mm pore diameter plastic sieve.

Quantities of homogenized powder equivalent to 15, 10, 5 mg zinc/tablet were weighed and analyzed according to the proposed methods. For method 1, the mixed powder was quantitatively transferred with HCl 0.1 mol/L in 100 ml volumetric flasks, stirred on a magnetic stirrer for 20 minutes, filtered through Whatman paper and then filled to 100 ml with DDW. Samples were labeled: sample 1 (15 mg zinc/tablet), sample 2 (10 mg zinc/tablet), sample 3 (5 mg zinc/tablet). The concentrations of zinc were determined in solution after suitable dilutions to fit the linear ranges.

REFERENCES

- [1]. C.L. Rock, *American Journal of Clinical Nutrition*, **2007**, 85, 277S.
- [2]. C.J. Frederickson, J.Y. Koh, A.I. Bush, *Nature Reviews Neuroscience*, **2005**, 6, 449.
- [3]. M. Hambidge, *Journal of Nutrition*, **2000**, 130, 1344S.
- [4]. K.A. McCall, C. Huang, C.A. Fierke, *Journal of Nutrition*, **2000**, 130, 1437S.
- [5]. J. Karpiska, M. Kulikowska, *Journal of Pharmaceutical and Biomedical Analysis*, **2002**, 29, 153-158.
- [6]. R. Maties, F. Jimenez, J.J. Arias, M. Roman, *Analytical Letters*, **1997**, 30, 2059.
- [7]. A. Lutka, Z. Kokot, H. Powidzka, *Acta Poloniae Pharmaceutica*, **2004**, 6, 243.
- [8]. K. Nakajima, M. Ohta, H. Yazaki, H. Nakazawa, *Journal of Liquid Chromatography*, **1993**, 16, 487.
- [9]. J.L. Burguera, M. Burguera, *Analytica Chimica Acta*, **1981**, 127, 199.
- [10]. F.S. David, J.S. Michael, *Analytical Chemistry*, **1991**, 63, 179.
- [11]. I.G. Tănase, I.L. Popescu, A. Pană, *Analele Universității din Bucuresti – Chimie*, **2006**, XV, 45.
- [12]. K. Soltyk, A. Lozak, M. Warowna-Greskiewicz, Z. Fijalek, *Acta Poloniae Pharmaceutica*, **2000**, 57, 261.
- [13]. Q. Cheng, H. Dong, *Microchimica Acta*, **2005**, 150, 59.
- [14]. S.P. Mehta, V.B. Patel, *International Journal of Pharmaceutical research & analysis*, **2012**, 2, 87.

- [15]. G.A. Shar, M.I. Bhanger, *Journal of Chemical Society of Pakistan*, **2001**, 23, 74.
- [16]. ICH, ICH Harmonised Tripartite Guideline – Validation of Analytical Procedures: Text and Methodology Q2(R1), London, **2005**, Current Step 4 version.
- [17]. J. Ronowicz, B. Kupcewicz, L. Palkowski, P. Bilski, T. Siodmiak, M.P. Marszall, J. Krysinski, *Chemical Papers*, **2014**, 68, 861.
- [18]. G. Pavalache, V. Dorneanu, *Farmacia*, **2011**, 59, 200.
- [19]. British Pharmacopoeia, General notices and monographs: Tablets, **2013**, 2464.
- [20]. European Pharmacopoeia 8.0, Chapter 2.9.6 Uniformity of content of single-dose preparations, **2014**, 298.
- [21]. B. Welz, H. Becker-Ross, S. Florek, U. Heitmann, “High-Resolution Continuum Source AAS”, Wiley-VCH Verlag GmbH & Co., Weinheim, **2005**, chapter 3.

COMPARATIVE EVALUATION OF SOME MINOR- AND MAJOR ELEMENT CONTENTS IN COMMERCIAL YOGURTS

OANA CADAR^{a*}, MIRELA MICLEAN^a, MARIN SENILA^a,
ALEXANDRA HOAGHIA^a, MANFRED SAGER^b

ABSTRACT. The content of 10 minor and major elements (Cr, Cu, Fe, Mn, Zn, Na, K, Ca, Mg and P) was quantified by inductively coupled plasma optical emission spectrometry (ICP-OES) in 15 commercial plain and fruit mixed yogurts, purchased in supermarkets from Romania. Results of both minor and major elements were found mostly similar in all varieties of yogurt studied. The concentrations in mg/kg fresh weight were: Cr (<0.25), Cu (0.30-0.56), Fe (0.53-1.23), Mn (0.42-0.83), Zn (2.56-3.69), Na (325-522), K (999-1356), Ca (932-1206), Mg (82-113) and P (924-1001). Some of the essential elements were found to have good and healthy contribution to daily nutrition of consumers in accordance to Recommended Dietary Allowance (RDA).

Keywords: *yogurt, minor elements, major elements*

INTRODUCTION

Milk and dairy products are important components of human nutrition. Fresh fermented dairy products such as yoghurt are widely consumed foods in many countries due to their potential health benefits for humans and nutritional properties [1-3]. Compared with milk, the mineral concentrations (K, Ca, Mg, P and Zn) are higher in yogurt by nearly 50% [4]. Yogurt is a fermented milk product obtained by fermentation of milk with bacterial cultures *Lactobacillus bulgaricus* and *Streptococcus thermophiles*. Large numbers of these bacteria remain viable in the product until the time of consumption [5, 6]. Yoghurt is one

^a INCDO-INOE 2000, Research Institute for Analytical Instrumentation, 67 Donath, 400293 Cluj-Napoca, Romania.

^b Competence Centre of Elements, Austrian Agency for Health and Food Safety, 191 Spargelfeldstrasse, A-1220 Vienna, Austria.

* Corresponding author: oana.cadar@icia.ro

of the dairy products whose sales continues to increase due to the diversification of the range available including different flavors (plain, sweetened with fruits or dried fruits, flavored), textures and consistencies (firm, liquid, shakes, smooth, frozen) [7-9].

Yogurt and other fermented dairy products are a good source of nutrients, such as: proteins, fat, important vitamins, major minerals, enzymes and probiotic bacteria [10-12]. The mineral content yogurt is variable due to the factors such as differences between animal species, geographical origin of milk, manufacturing practices and possible contamination from the equipment during the processing. Beside calcium, considered the most important nutrient for bone health, yogurts are a good dietary source of essential and very important elements (like copper, chromium, manganese and zinc) for normal metabolism, growth and development [13].

Although, there are numerous bibliographic references on the major and minor element levels in bovine milk, only several studies have been reported for dairy products, such as yogurt. For the determination of minor and major elements, several analytical techniques have been used: graphite furnace atomic absorption spectrometry, GF-AAS [14], flame atomic absorption spectrometry, FAAS [15-17], inductively coupled plasma optical emission spectrometry, ICP-OES [10, 18], inductively coupled plasma-mass spectrometry, ICP-MS [19, 20], X-ray fluorescence spectrometry, XRF [5] Also, sample preparation is an important step in elemental analysis; microwave digestion has many advantages in comparison with open vessel digestion: short experimental time, low reagent consumption, good recoveries and enhanced operator safety [21].

The objective of this study was the determination of the minor and major element compositions in 15 commercial yogurts (plain and fruit mixed). The study is focused on those essential elements which can be easily determined by ICP-OES, namely Cr, Cu, Fe, Mn, Zn, Na, K, Ca and Mg. The obtained results were used to assess their daily intake and contribution to the recommended dietary allowance (RDA) values.

RESULTS AND DISCUSSION

In order to check the accuracy of the method, CRM (NIST-1549 Non-fat milk powder) was analyzed for the determination of Na, K, Ca, Mg, P, Al, Cu, Fe and Zn (Table 1). The recovery value means of all the investigated elements were found to be in the range of 97.4-103%.

Table 1. Analysis of certified reference material (NIST 1549)

Element	Certified value^a (mg/kg)	Obtained value^a (mg/kg)	Recovery (%)
Na	0.497 ± 0.010 ^b	0.514 ± 0.043	103
K	1.69 ± 0.03 ^b	1.70 ± 0.08	101
Ca	1.30 ± 0.05 ^b	1.28 ± 0.03	98.7
Mg	0.120 ± 0.003 ^b	0.119 ± 0.006	98.9
P	1.06 ± 0.02 ^b	1.08 ± 0.08	102
Cu	0.700 ± 0.100	0.694 ± 0.051	99.1
Fe	1.78 ± 0.10	1.80 ± 0.17	101
Mn	0.26 ± 0.06	0.253 ± 0.031	97.4
Zn	46.1 ± 2.2	46.6 ± 1.1	101

^a Mean±standard deviation^b Concentration in mass fraction (%)

The obtained mean concentrations and standard deviations of analyzed elements in both evaluated type of yogurt (plain vs fruit mixed) are presented in Table 2. The elements were categorized into major elements (concentration more than 100 mg/kg) and minor elements (concentration below 100 mg/kg and decreasing order: Zn>Fe>Mn>Cu>Cr). In general terms, the concentrations of most analyzed elements were quite uniform and without relevant differences between brands. Furthermore, there were no significant differences in concentrations between investigated plain and fruit mixed yogurt samples.

Table 2. Concentrations of minor and major elements (mg/kg fresh weight) in yogurt samples

Element / wavelength (nm)	Plain yogurt^a (n=10)	Fruit mixed yogurt^a (n=5)
<i>Minor elements</i>		
Cr / 267.7	<0.25	<0.25
Cu / 327.4	0.38 ± 0.10	0.32 ± 0.10
Fe / 238.2	0.74 ± 0.20	0.92 ± 0.27
Mn / 257.6	0.64 ± 0.12	0.58 ± 0.11
Zn / 213.9	3.05 ± 0.76	2.78 ± 0.56
<i>Major elements</i>		
Na / 589.6	424 ± 54	401 ± 48.0
K / 769.9	1234 ± 89	1102 ± 101
Ca / 317.9	1045 ± 102	945 ± 76.0
Mg / 279.1	123 ± 24.0	98.0 ± 18.0
P / 213.6	975 ± 10.0	940 ± 11.0

^a Values are mean ± standard deviations of three (n=3) measurements.

Major elements. In all cases, plain yogurt got the highest major element contents. K was found to be the quantitatively most outstanding of the investigated elements with levels between 1234 mg/kg in plain and 1102 mg/kg in fruit mixed yogurt, respectively. The other major elements follow the descending order: Ca>P>Na>Mg in terms of their content. There were no statistically significant differences between the concentrations of plain and fruit mixed yogurts ($p < 0.05$).

The levels of major elements found in dairy yogurt were comparable with those reported in other studies: Na (356-732), K (946-1630), Ca (796-1405 mg/kg) and Mg (78.5-158) mg/kg fresh weight [3, 10, 22]. The obtained concentrations for P were higher than those found in the most consumed trademarks of yogurt in Spain (627-858 mg/kg fresh weight) [3].

Minor elements. Zn was the most abundant minor element in both types of yogurt (3.05 in plain and 2.78 mg/kg in fruit mixed yogurt) followed by the other minor elements, ranked in descending order, Fe>Mn>Cu>Cr in plain yogurt and Fe>Mn>Cu>Cr in fruit mixed yogurt, respectively. The considerable amount of Fe and Mn may be due to the contamination during manufacturing, packaging processes and transport [14].

The obtained values of minor elements were lower than those reported for Turkish yogurt (1.73 mg/kg Fe, 0.71 mg/kg Cu and 4.51 mg/kg Zn) [18]. In comparison with Korean yogurt determined by Khan et al. 2014 [19], the obtained values for Zn and Cr were lower (Zn - 4.7 mg/kg and Cr - 0.271 mg/kg) while those obtained for Cu and Mn were higher (Cu - 0.158 mg/kg and Mn - 0.080 mg/kg). The higher levels of Fe could be attributed to addition of fruit pieces which cause an increase in the concentration of mineral, but also to the existence of enriched yogurts with minerals (Na, K, Ca, Zn or elements which are deficient in the milk: Fe and Mn) [15]. The minor element contents of the yogurt samples from this work were within the concentration ranges in yogurts consumed in Spain, Cr (0.01-0.06), Cu (0.035-0.46), Fe (0.2-3.6), Mn (0.02-0.04) and Zn (2.09-4.65) mg/kg fresh weight, reported by Luis et al. 2015 [10] and Llorent-Martinez et al., 2012 [20]. Several authors have shown that yogurt and milk (the raw material of this product) have similar mineral composition. Milk composition may vary according to factors such as breed, age, mammary gland health, genetic background, lactation stage, feeding and season) [12, 14, 22].

Table 3 present the obtained results for investigated major and minor nutritional elements (the percentage of contribution to RDA is calculated for each element, considering the intake of one yogurt/day). The RDA data (the levels of intake of essential nutrients considered to be adequate to meet the needs of practically all healthy persons) use in this study, are those provided by the Commission of the European Communities, 2008 and World Health Organization (WHO), 2012 [23, 24]. The concentration of Cr in all yogurt samples was below the limits of quantification (0.25 mg/kg). Thus no conclusion can be

drawn regarding the coverage of RDA for Cr. Furthermore, no harmful impacts caused by this element through high consumption of yogurt are to be expected. As a result, the investigated minor and major elements were found to have good nutritional contribution in accordance to RDA. However, it must be considered that yogurts are not the only sources of major and minor elements.

Table 3. Mean daily and percentage of contribution to RDA for investigated nutritional elements in yogurts

Element / yogurt	Level ^a (mg/kg)	Mean daily intake ^b (mg)	RDA ^c (mg)	%RDA
Na	plain	424	200 ^d	26.5
	fruit	401		25.1
K	plain	1234	2000	7.71
	fruit	1102		6.89
Ca	plain	1045	800	16.3
	fruit	945		14.8
Mg	plain	123	375	4.10
	fruit	98.0		3.27
P	plain	975	700	17.4
	fruit	940		16.8
Cu	plain	0.38	1	4.75
	fruit	0.32		4.00
Fe	plain	0.74	14	0.66
	fruit	0.92		0.82
Mn	plain	0.64	2	4.00
	fruit	0.58		3.63
Zn	plain	3.05	10	3.81
	fruit	2.78		3.48

^a Mean concentrations (Table 2);

^b Calculated on the basis of the intake of one yogurt (approx. 125 g);

^c EC Commission directive, 2008;

^d World Health Organization (WHO), 2012.

CONCLUSIONS

In this paper, the determination of macro and trace elements in plain and fruit mixed commercial yogurts has been carried out using microwave digestion with nitric acid and hydrogen peroxide, followed by ICP-OES analysis. Results of both minor and major elements were found mostly similar in all studied yogurt. The levels of investigated essential elements in commercial yogurts were appropriate and thus yogurt having a positive contribution to daily

nutrition of consumers in accordance to Recommended Dietary Allowance (RDA). Metal concentrations in yogurt are conditioned by the composition of the initial milk and the technological procedures used in dairy product processing.

EXPERIMENTAL SECTION

Reagents, standard solutions and CRMs

The calibration standards were prepared by appropriate dilution of the ICP multielement standard solution IV (Merck, Darmstadt, Germany) 1000 mg/l of Cr, Cu, Fe, Mg, Zn, Na, K, Ca, Mg and Phosphorous ICP Standard 1000 mg/l P in 2% (v/v) HNO₃. All reagents (HNO₃ 65%, H₂O₂ 30%) were of analytical grade and were purchased from Merck, Darmstadt, Germany. The certified reference material (NIST-SRM 1549 Whole milk powder) was obtained from LGC Promochem GmbH, Wessel, Germany. For all dilutions, ultrapure water (resistibility 18.2 MΩ/cm) obtained from a Millipore Direct-Q3 UV system (Millipore, France) was used. All PTFE and glass vessels were soaked in 10% HNO₃ for at least 24 h and rinsed extensively with Milli-Q water prior to use.

Sampling

A total of 15 samples of yogurts (10 plain and 5 fruit mixed) from the five major producers were bought from local supermarkets in NW Romania. The samples were purchased in triplicate at different times during September to December, 2014. The selected brands cover more than 75% of the yogurt market in this region, a rate that can also be applied to Romania, where these brands are also distributed. After transport to the laboratory, the yogurt samples were kept in their original packages and stored at 4°C until analysis.

Sample preparation

0.5 g of each sample was weighted and carefully transferred to a Teflon reaction vessel and 5 ml HNO₃ 65% and 2 ml H₂O₂ 30% were added. Samples were left on the bench to pre-digest overnight at room temperature. The vessels were closed and the samples were digested in a closed-vessel microwave system Berghof MWS-3+ with temperature control mode (Berghof, Germany), according to Ayar et al. [14]. After cooling down to room temperature, the completely clear and colorless solutions were quantitatively transferred to 25 mL volumetric flasks and diluted to the mark with double deionized water. Certified reference material NIST 1549 and blank, consisting of deionized water and reagents, were prepared in the same way as the sample. All determinations were carried out in triplicate.

Instrumentation

The major and minor element contents were determined by ICP-OES (OPTIMA 5300 DV, Perkin Elmer, USA) equipped with an ultrasonic nebulizer CETAC U-6000AT+ with heater/condenser (CETAC Technologies, USA). The working conditions were: approximate RF power, 1.3 kW; nebulizer gas, 0.8 L/min; plasma gas, 15 L/min; auxiliary gas, 2.0 L/min; sample flow, 1.1 L/min; axial viewing; background correction, 2-point. The analytical emission lines were selected as the most sensitive ones. The calibration range for all evaluated elements was made from 0.005 to 5 mg/l.

ACKNOWLEDGMENTS

This work was supported by Executive Unit for Financing Higher Education, Research, Development and Innovation (UEFISCDI), Capacities, Bilateral cooperation Programme Romania-Austria, project number 757/2014.

REFERENCES

- [1]. H. Wang, K.A. Livingston, C.S. Fox, J.B. Meigs, P.F. Jacques, *Nutrition Research*, **2013**, 33, 18.
- [2]. H. Kimoto-Nira, Y.Nagakura, C. Kodama, T. Shimizu, M. Okuta, K. Sasaki, N. Koikawa, K. Sakuraba, C. Suzuki, Y.Suzuki, *Journal of Dairy Science*, **2014**, 97, 5898.
- [3]. G. Cano-Sancho, G. Perello, M. Nadal, J.L. Domingo, *Journal of Food Composition and Analysis*, **2015**, 42, 71.
- [4]. A. Germani, R. Luneia, F. Nigro, V. Vitiello, L.M. Donini, V. del Balzo, *Annali di Igieni*, **2014**, 26, 205.
- [5]. S.N. Meydani, W.K. Ha, Immunologic effects of yogurt, *American Journal of Clinical Nutrition*, **2000**, 71, 861.
- [6]. J.M. El-Bakri, I.E.M. El-Zubeir, *International Journal of Dairy Science*, **2009**, 4, 1.
- [7]. S.M. Fiszman, M.A. Liluch, A. Salvador, *International Dairy Journal*, **1999**, 9, 895.
- [8]. M.A. De la Fuente, F. Montes, G. Guerrero, M. Juarez, *Food Chemistry*, **2003**, 80, 573.
- [9]. A.N. Rinaldoni, M.E.Campderros, A.Perez Padilla, E. Perino, J.E. Fernandez, *Latin American Applied Research*, **2009**, 39, 113.
- [10]. G. Luis, C. Rubio, C. Revert, A. Espinosa, D. Gonzalez-Weller, A.J. Gutierrez, A. Hardisson, *Journal of Food Composition and Analysis*, **2015**, 39, 48.
- [11]. A.Y. Tamine, R.K. Robinson, *Yoghurt Science and Technology* (3rd ed.), Boca Raton: CRC Press, **2007**.

- [12]. F. Rey-Crespo, Miranda M., Lopez-Alonso M., *Food and Chemical Toxicology*, **2013**, 55, 513.
- [13]. World Health Organization, WHO, *Evaluation of Certain Food Additives and Contaminants*, Geneva, Switzerland: WHO Technical Report Series 930, **2006**.
- [14]. A. Ayar, D. Sert, N. Akin, *Environmental Monitoring and Assessment*, **2009**, 152, 1.
- [15]. P.J. Sanchez-Segarra, M. Garcia-Martinez, M.J. GordilloOtero, A. Diaz-Valverde, M.A. Amaro-Lopez, R. Moreno-Rojas, *Food Chemistry*, **2000**, 70, 85.
- [16]. M. Yaman, M. Durak, S. Bakirdere, *Spectroscopy Letters*, **2005**, 38, 405.
- [17]. G. Kaya, I. Akdeniz, M. Yaman, *Atomic Spectroscopy*, **2008**, 29, 99.
- [18]. Z. Tarakci, B. Dag, *International Journal of Physical Sciences*, **2013**, 8, 963.
- [19]. N. Khan, I.S. Jeaong, I.M. Hwang, J.S. Kim, S.H. Choi, E.Y. Nho, J.Y. Choi, K.S. Park, K.S. Kim, *Food Chemistry*, **2014**, 147, 220.
- [20]. E.J. Llorent-Martínez, M.L. Fernández de Córdova, A. Ruiz-Medina, P. Ortega-Barrales, *Microchemical Journal*, **2012**, 102, 23.
- [21]. B. Bocca, M.E. Conti, A. Pino, D. Mattei, G. Forte, A. Alimonti, *International Journal of Environmental Analytical Chemistry*, **2007**, 87, 1111.
- [22]. Y.W. Park, *Small Ruminant Research*, **2000**, 37, 115.
- [23]. World Health Organization, WHO Guideline, *Sodium intake for adults and children*, Geneva, **2012**.
- [24]. Commission of the European Communities, Directive 2008/100/EC on nutrition labelling for foodstuffs as regards recommended daily allowances, energy conversion factors and definitions, *Official Journal of the European Union*, **2008**, L285, 9.

EVALUATION OF BIOCHEMICAL CHANGES OCCURRING IN “NĀSAL” CHEESE DURING THE RIPENING STAGES

ALEXANDRU-FLAVIU TĂBĂRAN^a, SORIN DANIEL DAN^a,
ALEXANDRA TĂBĂRAN^{a*}, CONSTANTIN BELE^a, CORNEL CĂTOI^a,
MIHAI BORZAN^a, GABRIEL VALASUTEAN^a, MARIAN MIHAIU^a

ABSTRACT. “Nāsal” cheese is the only sort of Romanian cheese with mould, being unique also by its processing technology and sensorial characteristics. This study is the first complex investigation which focuses on the biochemical changes occurring during the ripening stages of this cheese pointing out its nutritional value. This type of cheese is characterized by a high total solids (45.92%), fat (40.3%) and protein (19.3%) contents at the end of the ripening process. All these biochemical compounds increased during the ripening process, starting from day 20 until day 60, the values being statistically different ($p<0.05$). The increase in values was noticed also in the fatty acids profiles, the most abundant saturated fatty acids being C14:0, C16:0 and C18:0. The most statistically significant increase ($p<0.001$) in quantity during the three stages of ripening analysed, was noticed in case of C4:0, C8:0, C14:0. The ripening applied influences significantly the concentrations of unsaturated fatty acids, favouring the increase in C16:1, C18:1, C18:2, C18:3n3. We concluded that “Nāsal” cheese holds a great nutritional value, the ripening period having a strong influence on the amounts of biochemical compounds. Compared to other type of not-ripened cheese, this type stands out by its higher amount of unsaturated fatty acids, essential in human diet.

Keywords: fatty acids, ripen, unsaturated, protein, total solids.

INTRODUCTION

Along the years, cheese processing has evolved from traditional art to science. A lot of cheese varieties have been developed and tested for different environmental conditions in order to meet the highly pretentious

^a University of Agricultural Sciences and Veterinary Medicine, 3-5 Mănăstur Str., RO-400372, Cluj-Napoca, Romania.

* Corresponding author: alexandra.lapusan@usamvcluj.ro

requests of the consumers. It is estimated that currently there are over 2000 cheese varieties [1], and this list is in continuous growing. Each of these sorts of cheese has a specific particularity, either due to the milk used, processing technology or ingredients.

The uniqueness of cheese sorts develop especially during the ripening stages, being influenced by the starter cultures used [2; 3]. One of the most complex biochemical events that take place during ripening is proteolysis. Researches concerning the pathways for the catabolism of free amino acids during ripening have been published in previous years [4; 5; 6; 7] but still it has not been fully elucidated [8]. Lipolysis is another process that occurs during the ripening process. The free fatty acids released during lipolysis along with the volatile compounds and the proteolysis products contribute directly to cheese flavour [4, 9]. Cheese flavour is one of the most important criteria determining consumer choice and acceptance [10].

In Romania, the ripened dairy products originate from various areas of production, each having their characteristics and nutritional qualities. "Telemea" cheese represents 60% of all kinds of cheeses produced in Romania, having particular nutritional characteristic influenced by the milk, processing technology and area of production. For that matter there are a number of researches that have studied the dynamics of biochemical compounds during the ripening stages.

"Năsal" cheese is part of this category of fermented cheeses, soft content, made from cow milk. On its surface there is a bacteria substrate due to the development of *Brevibacterium linens*, which gives the particularity of this product. This bacterium transforms the cheese components offering its specific taste and consistency, not being necessary the artificial adding of mould spores which often are needed in specific French cheeses. This cheese holds an important value to the traditional production of cheese in Romania, given the fact that it is the only one with this particular technology of processing. The ripening is made in a special environment (Țaga cave) that favours the development of *Brevibacterium linens*. In this cave, the temperature and air humidity are constant during the entire year, ensuring the production of characteristic cheese, appreciated of having exquisite sensorial features [11].

Given the particularities of "Năsal" cheese, the aim of our study was to evaluate the changes in the biochemical composition during the ripening stages and to assess its nutritional value compared to another type of cheese.

RESULTS AND DISCUSSION

The biochemical analysis of the „Näsal” cheese has revealed that the fat percentage shows a consistent upper trend during the ripening stages, from 28.4 ± 0.76 g% within day 20 of ripening to 40.3 ± 1.37 in the last stage (day 60). The differences noticed were statistically different ($p<0.05$) when comparing the three stages of „Näsal” cheese ripening.

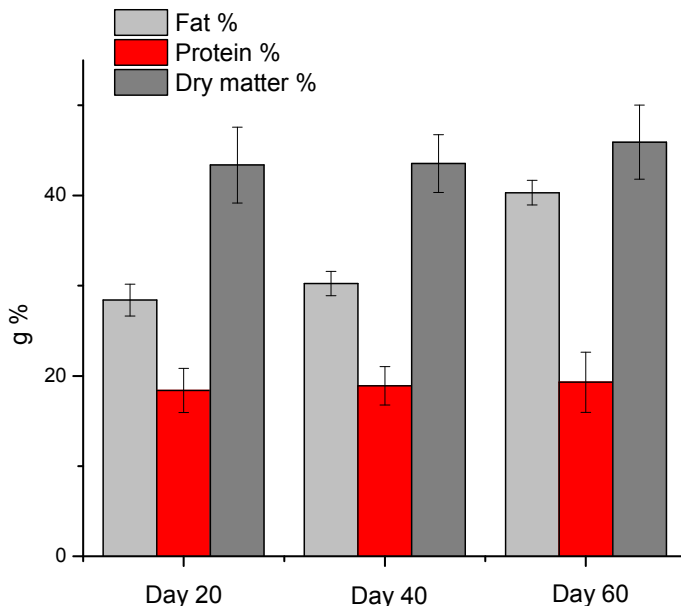


Figure 1. The compositional parameters percentage values according to the ripening stages

The protein values showed also a slight increase from day 20 of ripening (18.39 ± 0.45) compared to day 60 (19.3 ± 0.34), possibly due to the specific environmental conditions of Taga cave which has a specific humidity. Our results are in conformity with the ones found by Pappa et al. (2007) [12], which noticed that in the first day of „Telemea” cheese ripening, the average value of proteins was 15.03 ± 0.52 % and in two months of ripening increased to 16.74 ± 0.13 %. Not all studies obtained the same results, some of them showing a decrease in values during the ripening stages of cheese. Hui and Evranuz (2012) [13] showed a decrease in the content of protein during the ripening stages, explaining that this process is a consequence of various humidity values and the loss of protein components in the brine. We noticed that due to the environmental ripening condition particularities of „Näsal” cheese (higher humidity) the protein content is affected, the caseins being prevented from fragmenting.

The dry matter increased during the ripening stages from 43.38 ± 1.40 g% to 45.92 ± 1.68 g%. During the ripening process, it was noticed that in the first stage of ripening, 5.49% from the total amount of samples, showed lower values compared to the limits imposed by the legislation ((minimum 42%) [11]. In the second stage (day 40), only 2.19% showed lower values than the standards, and at the end of the ripening stages, all samples were in conformity.

From the statistical evaluation, the fat/dry matter fraction presented a uniform trend during the entire ripening stage, from 47.13 ± 0.80 in the first stage of ripening to 47.03 ± 2.79 in the last stage (day 60). From the total amount of examined samples, only 1.1% were in between the minimum admissible limits for this type of cheese (fat/dry matter > 50). This is a concerning fact given that almost all samples examined were not in conformity with this parameter. Pappa et al. (2007) [12] showed higher values regarding this parameter (54%). The same upper trend was noticed by Pappa (2006) [14], the value increasing from 43.2% in the first day of ripening to 55.4% after two months of ripening.

The processing technology of this particular type of cheese allows the maintaining of a high proportion of fatty acids. However, as seen in table 1, there are a series of significant changes statistically interpreted ($p < 0.05$) between the values obtained before ripening (day 0) and after ripening (day 60).

Table 1. Values of fatty acids in Năsal cheese during the ripening period

Free fatty acid	Symbol	Ripening stage (%)			
		Day 0	Day 20	Day 40	Day 60
Butyric	C4:0	0.69	0.75	0.82	1.12
Caproic	C6:0	1.74	1.68	1.79	1.97
Caprylic	C8:0	1.68	1.57	1.67	1.82
Capric	C10:0	5.20	5.45	5.55	5.45
Lauric	C12:0	1.64	1.72	1.75	1.55
Miristic	C14:0	11.73	11.64	11.94	12.15
Miristoleic	C14:1	0.32	0.22	0.24	0.34
Palmitic	C16:0	31.60	32.10	32.50	32.60
Palmitoleic	C16:1	1.13	1.23	1.43	1.53
Stearic	C18:0	12.15	12.22	12.62	12.64
Oleic	C18:1	13.78	13.82	13.84	13.86
Linoleic	C18:2	2.10	2.23	2.13	2.16
Linolenic	C18:3n3	1.03	1.13	1.23	1.53

The fatty acid profile in "Näsal" cheese samples taken before ripening (day 0) revealed essential concentrations of stearic, palmitic and oleic acids and lower values of linoleic, capric, butyric and linolenic acids. After only 20 days of ripening significant changes ($p<0.05$) were noticed. The C18:1, C16:0, C18:0 and C4:0 increased in values while the concentrations of C14:0, C8:0 and C6:0 decreased; these changes were similar during the entire period studied, no matter the season of sampling. After 40 days of ripening, statistically significant changes were revealed in case of C6:0, C10:0, C16:0, C16:1, C18:1 and C18:3n3 ($p<0.05$) which increased in values compared to day 0 of ripening. The period of ripening changes significantly the concentrations of fatty acids, favouring the increase in C16:1, C18:1, C18:2, C18:3n3 as seen from the results obtained after 60 days of ripening.

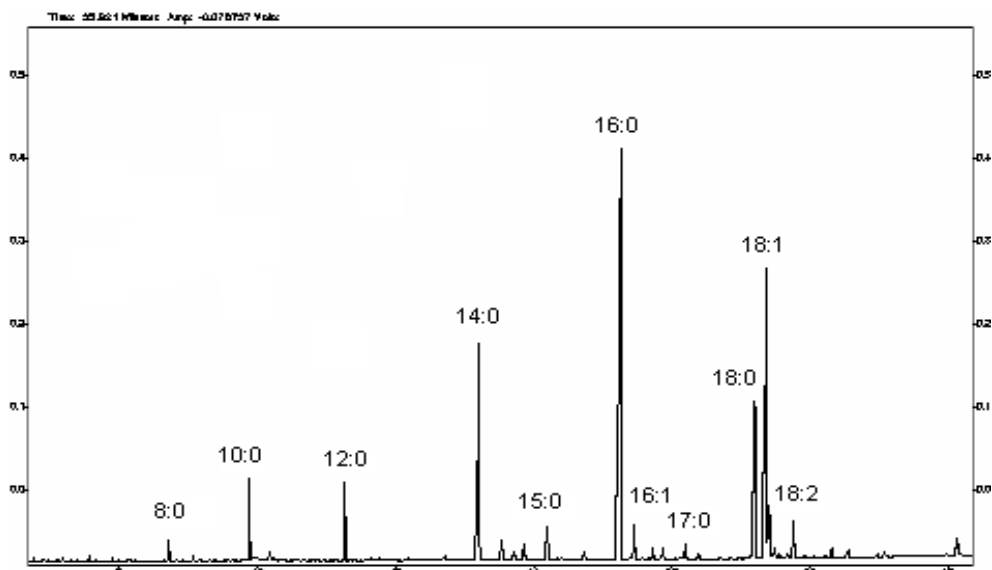


Figure 2. Chromatogram of fatty acids methyl esters in "Näsal" samples after 20 days of ripening

The most statistically significant increase ($p<0.001$) in quantity was noticed in case of C4:0, C8:0, C14:0. This increase can be explained by the fact that the lipases (originated mainly in milk and microorganisms) involved in cheese ripening, hydrolase preferentially the short and medium chain fatty acids [15,16].

Table 2. The averages fatty acids values in “Năsal” cheese ripened 60 days compared to not ripened fresh cheese

<i>Trait</i>	<i>Symbol</i>	“Năsal” cheese (g/100g)				Fresh cheese (g/100g)				P value
		Min.	Max.	Mean	SD	Min.	Max.	Mean	SD	
Butyric	C4:0	0.5	1.33	1.12	0.14	0.2	0.96	0.82	0.11	*
Caproic	C6:0	2.30	3.11	1.97	0.31	1.47	2.75	1.74	0.40	*
Caprylic	C8:0	1.72	1.96	1.82	0.25	1.87	2.43	1.38	0.43	*
Capric	C10:0	4.71	6.43	5.45	1.31	3.18	6.55	5.40	0.41	NS
Lauryc	C12:0	1.3	1.78	1.55	0.31	0.87	1.94	1.44	0.05	NS
Miristic	C14:0	9.56	14.07	12.15	0.12	9.51	13.26	11.53	1.21	*
Miristoleic	C14:1	0.09	0.53	0.34	0.01	0.16	0.45	0.52	0.52	NS
Palmitic	C16:0	22.3	36.3	32.60	0.61	26.75	36.75	31.40	0.10	*
Palmitoleic	C16:1	0.23	1.87	1.53	0.30	0.93	1.27	1.13	0.21	**
Stearic	C18:0	11.23	13.62	12.64	1.28	11.46	13.31	12.55	0.34	NS
Oleic	C18:1	11.83	15.84	13.86	0.34	10.74	15.16	13.48	0.20	*
Linoleic	C18:2	1.38	3.81	2.16	0.37	1.33	3.45	2.20	0.05	NS
Linolenic	C18:3n3	0.70	1.95	1.53	0.21	0.37	1.51	0.53	0.51	***
SFA		60.25	72.34	69.3	0.23	60.11	62.95	66.26	1.90	**
MUFA		31.13	32.45	15.73	0.43	30.36	31.96	14.61	0.59	*
PUFA		3.14	4.11	3.69	0.52	6.21	8.67	2.73	0.18	***

SD = standard deviation; NS = not significant P > 0.05,
 * Significant : P < 0.05; ** P < 0.01; *** P < 0.001

Our results are similar with the ones found by Olmedo and Coll-Hellin (1976) [17] at the traditional ripened sheep cheese and those revealed by Gattuso and Fazio (1980) [18] in the Italian ripened cheese.

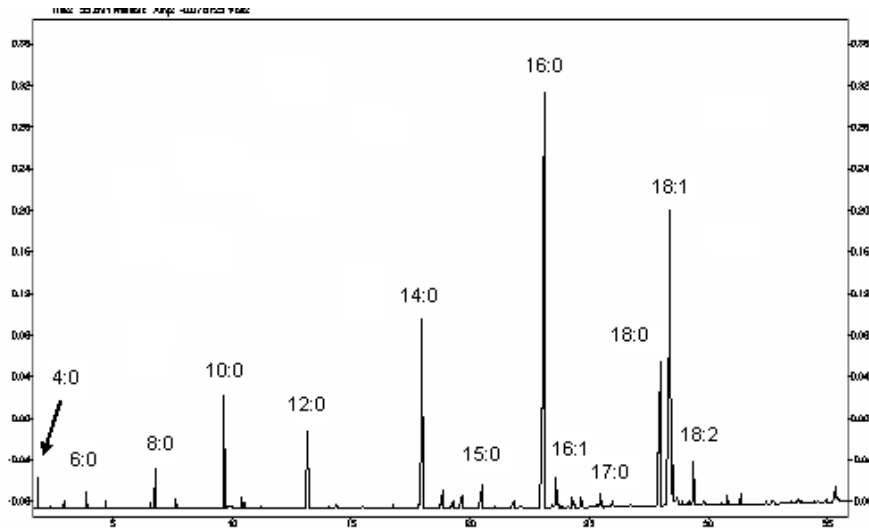


Figure 3. Chromatogram of fatty acids in "Näsal" cheese sampled after 60 days of ripening

After applying the Fisher test on the fatty acids values obtained we noticed that the concentrations of butyric, caprylic, lauric and miristic acids remain approximately constant within the 20 days of ripening but increase significantly until day 60; the concentration of caproic, capric, linoleic and linolein did not increase in values significantly only starting from the second half of the ripening process (day 40).

The concentrations of C12:0 increased significantly within the first period of ripening but by the end the values lowered; although not in a very significant way, the concentrations of C18:1 increased slowly and constantly within the entire ripening period. As seen in table 2, there were significant differences between the fatty acids profile from "Näsal" cheese compared to the not ripened type of cheese (fresh cow cheese).

Although the lactic microflora has a relatively low lipolysis activity, it can hydrolyse milk fat in a significant way during the ripening period, especially if the bacterial level is high [19; 20]. The significant load of *Brevibacterium linens* in „Näsal” cheese gives the particular taste and consistency of this product; also, it might explain the high levels of fatty acids at the end of ripening stage.

The release of C16:0, C18:0, C18:1 was considerable starting from day 20 of ripening probably due to the indigenous lipases from ruminant's milk (not sufficiently characterized until now). Normally, the research concerning the lipolysis in cheese are focused on actual measured fatty acids during a certain period of ripening (which represents an indicator of lipolysis extend); however, supplementary information on the activity of lipases can be extracted from the effective rate of fatty acids release (estimated as being the rapport between the quantity of fatty acids in a certain period of time and the effective period).

CONCLUSIONS

We concluded that "Năsal" cheese has a high nutritional value mainly due to its unique processing technology. The ripening period applied influences the majority of the compounds in a positive way, increasing in quantities. This fact lead us to the idea that the ripening process determines a higher lipolytic and proteolytic activity and that not only the actual process holds importance but also the extent of it.

EXPERIMENTAL SECTION

Sample collection

The study focused on 20 samples of "Năsal" cheese taken from various stages of the ripening process as follows: day 0 meaning before the curd is prepared for ripening; day 20 (stage I) of ripening; day 40 (stage II) of ripening; day 60 (stage III) of ripening. The sample gathering started in the month of February and ended in May. They were kept at refrigeration temperatures (0...+4°C) until their further analysis. For comparison 10 samples of fresh cow cheese (not processed through ripening) were analysed for compositional analysis through the same methods as "Năsal" cheese samples.

The analysis of compositional parameters

All the compositional parameters analysed, such as fat %, protein %, dry matter %, were measured by Infrared Spectrometry using the FoodScan™ (Foss, Germany) apparatus. The instructions given by the producer were followed accordingly.

Dairy product fat extraction

Dairy fat was extracted by using the following protocol: About 0.5g of dairy product were mixed in a separator funnel with 50 ml chloroform and 25 ml of methanol and then agitated for 2-3 min. After this process the lower layer was discarded. Following this step the mixture was passed through a cellulose filter with Na_2SO_4 and then brought to dryness.

Transesterification

Fatty acids were converted to methyl esters by reaction with boron trifluoride/methanol at 80°C for two hours in a closed Pyrex glass tube. The content was transferred into a separator funnel.

The methyl ester extraction

The extraction was made using 10 ml hexane. The hexanic fractions collected were dried using anhydrous sodium sulfate, filtered, concentrated under a nitrogen stream and finally re-eluted in 1 mL hexane. Fatty acids were analysed by gas chromatography (GC) with flame ionization detection (FID). A 1 μL sample was injected into the Shimadzu GC-17A series gas-chromatograph, equipped with a 30m polyethylene glycol coated column (Alltech AT-WAX, 0.25mm I.D., 0.25 μm film thickness). Helium was used as the carrier gas at a pressure of 147 kPa. The injector and detector temperatures were set at 260°C. For the oven temperature the following program was used: 70°C for 2 min. then raised to 150°C at 10°C/min. rate and held at 150°C for 3min., then further raised up to 235°C at a 4°C/min.

ACKNOWLEDGMENTS

This paper was published under the frame of European Social Found, Human Resources Development Operational Programme 2007-2013, project no. POSDRU/159/1.5/S/136893.

REFERENCES

- [1]. N.F. Olson, “Cheese in Biotechnology”, Vol: 9, Edn. H.J. Rehm, G. Reed, Weinheim, Germany: Verlag Chemie, 1995, pp. 355-384.
- [2]. P.F. Fox, “Cheese: Chemistry, Physics, and Microbiology” Chapman & Hall Press, London, 1993, Vol. 1, pp. 1–36.

- [3]. S.U. Rehman, P.L.H., McSweeney, J.M. Banks, E.Y. Brechany, D.D. Muir, P.F. Fox, *Int. Dairy J.*, **2000**, 10, 33.
- [4]. P.L.H. McSweeney, M.J. Sousa, *Le Lait*, **2000**, 80, 293.
- [5]. M. Yvon, L. Rijken, *I. Dairy J.*, **2001**, 11, 185.
- [6]. G. Smit, J.E.T. van Hylckama Vlieg, B.A. Smit, E.H.E. Ayad, W.J.M. Engels, *Aust. J. of Dairy Techn.*, **2002**, 7, 61.
- [7]. Å.C. Curtin, P.L.H. McSweeney, Catabolism of amino acids in cheese during ripening. In P.F. Fox, P.L.H. McSweeney, T.M. Cogan, T.P. Guinee: Cheese - Chemistry, Physics and Microbiology (3rd Edition), Amsterdam, **2004**, pp. 436- 454.
- [8]. P.L. H Mcsweeney, *Int. J. of Dairy Technol.*, **2004**, 57, 127.
- [9]. G. Urbach, *Int. J. of Dairy Technol.*, **1997**, 50, 79.
- [10]. F.A.M. Hassan, M.A.M. Abd El-Gawad, A.K. Enab, *Res. Precis. Instrum.*, **2013**, 2, 15.
- [11]. M. Mihaiu, S.D. Dan, C. Jecan, A. Tăbăran, *Inspectia și controlul alimentelor*, Risoprint Press., Cluj-Napoca, **2014**, chapter 4.
- [12]. E.C. Pappa, I. Kandarakis, H. Mallatou, *J. Food Eng.*, **2007**, 79: 143-149.
- [13]. Y.H. Hui, E.O. Evranuz, *Goat Milk Cheeses in Animal – Based Fermented Food and Beverage Technology*, CRC Press, England, **2012**, chapter 17.
- [14]. E.C. Pappa, *Food Cont.*, **2006**, 17, 570.
- [15]. T.K. Ritvanen, Ripened cheeses; the effects of fat modifications on sensory characteristics and fatty acid composition, Thesis dissertation, Helsinki, **2013**.
- [16]. A.M. Fuente, J. Fontecha, M. Juarez, Z. Lebensm. Unters. Forsch., **1993**, 196: 155.
- [17]. G.R. Olmedo, L. Coll-Hellin, *An. Bromatol.*, **1976**, 38: 21 I-340.
- [18]. A.M. Gatusso, G. Fazio, *Rivista Ztaliana akle Sostanze Grasse*, **1980**, 57, 535.
- [19]. T. Fryer, B.T. Reiter, R.C. Lawrence, *J. Dairy Sci.*, **1967**, 50: 7388.
- [20]. J. Stadhouders, H.A. Veringa, *Milk Dairy J.*, **1973**, 27: 77.

ISOLATION AND SCREENING OF LACTIC ACID BACTERIA FROM NATURALLY FERMENTED SOURCES WITH HIGH BIOTECHNOLOGICAL POTENTIAL

ÉVA LASLO^{a*}, MARA GYÖNGYVÉR^a, BERNADETT FUNKENHAUZER^a,
EMŐKE DOBRI^a, ROZÁLIA VERONIKA SALAMON^b,
SZabolcs Lányi^a, BEÁTA ÁBRAHÁM^a

ABSTRACT. A total number of 246 lactic acid bacteria were isolated from naturally fermented traditional foods and feed. These isolates were phenotypically characterized, classified and identified using 16S ribosomal DNA sequencing. 13 different species were detected from cheeses and from fermented plant materials. The isolates belonged to four genera: *Lactobacillus* genera 87%, *Pediococcus* 2%, *Enterococcus* 7%, *Leuconostoc* 4%. The fermentation capacity of the selected bacterial strains were tested in the presence of three different carbon sources. According to the results the most promising strains were *Lactobacillus plantarum* subsp. *plantarum* A5, *Lactobacillus plantarum* subsp. *plantarum* C5, *Lactobacillus paracasei* subsp. *Tolerans* N16 and *Lb. acidipiscis* H9. These strains were able to produce high amount of L-lactic acid, contributing to the pH-decrease of the medium. This result indicates that the selected bacterial strains shows potential for biotechnological application as starter cultures for silage fermentation.

Keywords: *lactic acid bacteria, isolation, bacteria selection, lactic acid fermentation, silage*

INTRODUCTION

Lactic acid bacteria (LAB) play a significant role in lactic acid fermentation processes. These bacteria are industrially important microorganisms with functional properties. They are involved in different applications as probiotics, dairy starters, silage inoculants and microbial cell factories. They inhabit in

^a Sapientia Hungarian University of Transylvania, Faculty of Economics, Socio-Human Sciences and Engineering, Department of Bioengineering, Libertății Sq. Nr. 1, 530104 Miercurea Ciuc, Romania.

^b Sapientia Hungarian University of Transylvania Faculty of Economics, Socio-Human Sciences and Engineering, Department of Food Science, Libertății Sq. Nr. 1, 530104 Miercurea Ciuc, Romania.

* Corresponding author: lasloeva@yahoo.com

different ecological niches containing rich sugar and organic nitrogen sources [1–3]. Genera of LAB include, among others, *Lactococcus*, *Enterococcus*, *Oenococcus*, *Pediococcus*, *Streptococcus*, *Leuconostoc* and *Lactobacillus*. They are Gram-positive organisms, that produce lactic acid by fermentation. The genus *Lactobacillus* is the largest group with over 100 species and subspecies [4]. The most common criteria for the selection of bacteria include rapid growth, intensive lactic acid production, and robustness to tolerate variable stress conditions in manufacturing processes where are involved [5,6]. Also the assessment of LAB used for feed additives for behavior in the presence of antibiotics is a requirement [7].

The LAB are associated with food and feed production due to their preservative action as acidification, flavor enhancement, texture and nutritive value. In forage preservation both homo- and heterofermentative LAB have potential advantages with positive effects.

Due to the production of lactic acid by homofermentative LAB, the pH is reduced faster, that inhibits the growth of undesirable microorganisms and improve the quality of fermentation. The heterofermentative LAB contribute to the good aerobic stability of the silages. Lactic acid and volatile fatty acids as acetic acid, propionic acid produced as the result of fermentation contribute to the energy supply of ruminant's [8]. The above mentioned and other well-known characteristics (e.g. bacteriocin production) expand the spectrum of biotechnological applicability of these microorganisms [4,9].

Natural fermented foods are often rich sources of beneficial LAB, whereas these are still potentially beneficial strains. The search of new LAB strains is (based on the identification of LABs with favorable combination of functional properties) an important issue, since a number of important LAB strains with beneficial properties still need to be characterized [4]. The most common criteria is the intensive lactic acid production that can be described also by fermentation capacity in different conditions.

Our aim was to realise a preliminary study for identification and characterization of LAB strains from naturally fermented sources with beneficial properties for biotechnological applications.

RESULT AND DISCUSSION

A number of 99 bacterial isolates with different colony size and morphology were screened for the most representative characteristics of LAB's as Gram staining, catalase absence, growth in the presence of NaCl (4% and 6.5%) microscopic morphology. The results showed that the majority of the isolates have a rod-like morphology, are catalase negative (85 isolate), and are Gram-positive (72

isolate). A number of 93 isolate showed growth in the presence of 4% NaCl and a number of 63 isolate in the presence of 6.5% NaCl. Bacterial isolates those characteristics suggested similarity with LAB strains were further studied.

A total number of 54 LAB isolates originated from different sources were identified by partial 16SrDNA, sequencing. Our results show that the LAB isolates belonged to 4 genera; 7 species from *Lactobacillus* genera (87%), 1 species from *Pediococcus* (2%), 4 species from *Enterococcus* (7%), 1 species from *Leuconostoc* (4%). 13 different species were detected from the cheeses and the fermented plant materials: *Lactobacillus pentosus*, *Lb. plantarum* subsp. *plantarum*, *Lb. gasseri*, *Lb. paracasei* subsp. *tolerans*, *Lb. buchneri*, *Lb. acidipiscis*, *Lb. brevis*, *Enterococcus faecalis*, *E. faecium*, *E. durans*, *E. italicus*, *Leuconostoclactis* and *Pediococcusparvulus*. Among lactobacilli, *Lb. pentosus* and *Lb. plantarum* subsp. *plantarum* were the most commonly isolated from different traditional cheeses originated from different regions.

Results of antibiotic susceptibility of the bacterial strains tested according to the guidelines reported by European Food Safety Authority [7] are shown in table 1.

Table 1. Minimal Inhibitory Concentration (MIC) of selected LAB strains

	Amp.	Tetr.	Chlo.	Kan.	Str.	Pen.	Gent.
<i>Lb. plantarum</i> subsp. <i>plantarum</i> A5	4	32	16	> 128	> 128	16	128
<i>Lb. paracasei</i> subsp. <i>tolerans</i> N16	1	2	16	> 128	128	1	64
<i>Lb. plantarum</i> subsp. <i>plantarum</i> C5	1	16	16	> 128	128	1	64
<i>Lb. pentosus</i> C10	4	64	4	> 128	> 128	1	128
<i>Lb. pentosus</i> C2	4	64	4	> 128	4	1	> 128
<i>Leuconostoclactis</i> N19	8	4	4	128	> 128	1	16
<i>Lb. buchneri</i> H1	4	> 128	64	> 128	32	1	64
<i>Lb. acidipiscis</i> H9	4	16	16	> 128	128	1	32
<i>Lb. brevis</i> H15	4	16	16	> 128	> 128	8	32

(**Amp.**: ampicillin, **Tetr.**: tetracycline, **Chlo.**: chloramphenicol, **Kan.**: kanamycin, **Str.**: streptomycin, **Pen.**: penicillin, **Gent.**: gentamicin)

The MIC test results against seven antibiotics (ampicillin, tetracycline, chloramphenicol, kanamycin, streptomycin, penicillin, gentamicin) are shown in table 1. For ampicillin with the exception of one strain (*Leuconostoclactis* N19, MIC=8 µg.ml⁻¹) all the others had a MIC ≤4 µg.ml⁻¹. In case of tetracycline with the exception of *Lb. buchneri* H1 (MIC>128 µg.ml⁻¹), the MIC values varied between 2-64 µg.ml⁻¹. For chloramphenicol the MIC values were between 4-16

$\mu\text{g.ml}^{-1}$, with exception of *Lb. buchneri H1* ($\text{MIC}=64 \mu\text{g.ml}^{-1}$). For kanamycin the MIC value with the assayed concentration was not detected exactly, but was higher than $128 \mu\text{g.ml}^{-1}$. For streptomycin, the MIC value were $128 \mu\text{g.ml}^{-1}$ for three of the studied LBA strains (*Lb. acidipiscis H9*, *Lb. plantarum* subsp. *plantarum C5* and *Lb. Paracasei* subsp. *Tolerans N16*). In case of four strains the MIC value was higher than $128 \mu\text{g.ml}^{-1}$. For *Lb. pentosus C2* strain the MIC value was $4 \mu\text{g.ml}^{-1}$ and *Lb. buchneri H1* strain was $32 \mu\text{g.ml}^{-1}$.

The lowest MICs where observed for penicillin, where only two strains has $\text{MIC}>1 \mu\text{g.ml}^{-1}$ (*Lb. plantarum* subsp. *plantarum*, $\text{MIC}=16 \mu\text{g.ml}^{-1}$ and *Lb. brevis H15* $\text{MIC}=8 \mu\text{g.ml}^{-1}$). For gentamicin the MIC values varied between $16-128 \mu\text{g.ml}^{-1}$ with the exception of *Lb. pentosus C2* ($\text{MIC}>128 \mu\text{g.ml}^{-1}$).

Phenotypic characterization of the selected LAB strains was realized with Biolog system using GEN III Microplates. The fermentation patterns of the selected strains are shown in table 2. The nine selected LAB showed differences in metabolic patterns.

All strains of LAB were able to ferment α -D-glucose. With the exception of *Lb. paracasei* subsp. *Tolerans N16* the strain were able to ferment D-maltose and with the exception of *Lb. buchneri H1* they were able to utilize N-acetyl-D-glucosamine. Five strain were able to utilize D-cellobiose (*Lb. plantarum* subsp. *plantarum C5*, *Lb. pentosus C10*, *Lb. pentosus C2*, *Leuconostoc* *lactis N19*, *Lb. acidipiscis H9*, *Lb. brevis H15*) D-fructose (*Lb. paracasei* subsp. *Tolerans N16* *Lb. plantarum* subsp. *Plantarum C5*, *Leuconostoc* *lactis N19*, *Lb. acidipiscis H9*, *Lb. brevis H15*), D-mannitol (*Lb. plantarum* subsp. *Plantarum A5*, *Lb. paracasei* subsp. *Tolerans N16*, *Lb. plantarum* subsp. *Plantarum C5*, *Lb. pentosus C10*, *Lb. pentosus C2*), and gentibiose (*Lb. plantarum* subsp. *Plantarum C5*, *Lb. pentosus C10*, *Lb. pentosus C2*, *Leuconostoc* *lactis N19*, *Lb. acidipiscis H9*).

Only three of the strains degraded sucrose (*Lb. plantarum* subsp. *plantarum C5*, *Lb. pentosus C2*, *Leuconostoc* *lactis N19*) and β -methyl-D-glucoside (*Lb. plantarum* subsp. *plantarum C5*, *Lb. pentosus C2*, *Lb. acidipiscis H9*). A single strain fermented D-raffinose (*Lb. buchneri H1*) and glycerol (*Lb. acidipiscis H9*). Two of the tested bacterial strains were able to decompose inosine (*Lb. buchneri H1* and *Lb. acidipiscis H9*), D- sorbitol (*Lb. plantarum* subsp. *plantarum C5*, *Lb. pentosus C2*), D-melibiose (*Lb. buchneri H1*, *Lb. brevis H15*), and D-salicin (*Lb. plantarum* subsp. *plantarum C5*, *Lb. pentosus C2*). Four LAB strains were able to utilize D-galactose (*Lb. paracasei* subsp. *Tolerans N16*, *Lb. plantarum* subsp. *plantarum C5*, *Lb. buchneri H1*, *Lb. acidipiscis H9*) and D-turanose (*Lb. plantarum* subsp. *plantarum C5*, *Lb. pentosus C10*, *Lb. pentosus C2*, *Leuconostoc* *lactis N19*). With the exception of two LAB strains (*Lb. buchneri H1* and *Lb. brevis H15*) the strains were able to ferment D-mannose. Carbohydrate fermentation results of the assayed strains showed a variability in the enzymatic activities. Chemical sensitivity showed that *Lb. brevis H15* is able to grow in the presence of rifamycin SV whereas *Lb. buchneri H1* showed

Table 2. Fermentation patterns and chemical sensitivity of the LBA strains

	A5	N16	C5	C10	C2	N19	H1	H9	H15
D-maltose	+	-	+	+	+	+	+	+	+
D-trehalose	-	+	+	-	-	-	-	+	-
D-cellobiose	-	-	+	+	+	+	-	+	-
Gentibiose	-	-	+	+	+	+	-	+	-
Sucrose	-	-	+	-	+	+	-	-	-
D-turanose	-	-	+	+	+	+	-	-	-
pH 6	-	-	-	-	-	-	+	-	+
pH 5	-	+	-	-	-	-	+	-	-
D-raffinose	-	-	-	-	-	-	+	-	-
α-D-lactose	+	+	+	+	+	+	-	-	-
D-melibiose	-	-	-	-	-	-	+	-	+
β-methyl-D-glucoside	-	-	+	-	+	-	-	+	-
D-salicin	-	-	+	-	+	-	-	-	-
N-acetyl-glucosamine	+	+	+	+	+	+	-	+	+
NaCl, 1%	-	+	-	-	-	-	+	-	-
α-D-glucose	+	+	+	+	+	+	+	+	+
D-mannose	+	+	+	+	+	+	-	+	-
D-fructose	-	+	+	-	-	+	-	+	+
D-galactose	-	+	+	-	-	-	+	+	-
Inosine	-	-	-	-	-	-	+	+	-
Sodium lactate, 1%	-	+	+	-	-	-	+	-	+
D-serine	-	+	-	-	-	-	+	-	-
D-sorbitol	-	-	+	-	+	-	-	-	-
D-mannitol	+	+	+	+	+	-	-	-	-
Glycerol	-	-	-	-	-	-	-	+	-
Rifamycin SV	-	-	-	-	-	-	-	-	+
Minocycline	-	-	-	-	-	-	+	-	-
D-galacturonic acid	-	-	-	-	-	-	-	-	+
D-gluconic acid	-	-	+	-	-	-	-	-	+
D-glucuronic acid	-	-	-	-	-	-	-	-	+
Vancomycin	-	+	-	-	-	-	+	-	+
L-alanine	-	-	-	-	-	-	-	-	+
L-lactic acid	-	-	-	-	-	-	+	-	-
Nalidixic acid	-	+	-	-	-	-	+	-	+
Potassium tellurite	-	-	-	-	-	-	+	-	+
Aztreonam	-	+	-	-	-	-	+	-	+

A5 *Lb. plantarum* subsp. *plantarum* A5, N16 *Lb. paracasei* subsp. *tolerans* N16 *Lb. plantarum* subsp. *plantarum* C5 *Lb. pentosus* C10 *Lb. pentosus* C2 *Leuconostoc* N19 *Lb. buchneri* H1 *Lb. acidipiscis* H9 *Lb. brevis* H15

activity in the presence of minocyclin. Three bacterial strains showed activity in the presence of vancomycin (*Lb. paracasei* subsp. *Tolerans N16*, *Lb. brevis H15*, *Lb. buchneri H1*), nalidixic acid (*Lb. paracasei* subsp. *Tolerans N16*, *Lb. brevis H15*, *Lb. buchneri H1*) and aztreonam (*Lb. paracasei* subsp. *Tolerans N16*, *Lb. Brevis H15*, *Lb. Buchneri H1*). Two strains showed growth in the presence of potassium tellurite (*Lb. brevis H15*, *Lb. buchneri H1*). The nine LAB strains also showed differences in the chemical sensitivity of the strains.

Fermentation capacity of the nine selected LAB strains was determined in the presence of three different carbon sources (glucose, mixture of glucose and xylose and distiller's dried grains with solubles (DDGS)). The cumulative L-lactic acid amounts after 72 h and the Y_{PX} are shown in table 3.

Table 3. The produced L-lactic acid (LA), acetic acid (AA) and the product yield coefficient after 72 h fermentation in the three different media.

A5	M ₁	M ₂	M ₃	A5	M ₁	M ₂	M ₃
LA g/l	39.09	28.10	5.80	AA g/l	7.84	3.12	2.10
$Y_{PX} \text{mgP/CFU X}$	1.27	0.23	0.37	$Y_{PX} \text{mgP/CFU X}$	0.02	0.001	0.18
N16				N16			
LA g/l	31.51	33.40	10.29	AA g/l	1.92	2.24	3.25
$Y_{PX} \text{mgP/CFU X}$	0.44	1.46	0.34	$Y_{PX} \text{mgP/CFU X}$	0.04	0.17	0.18
C5				C5			
LA g/l	29.80	29.39	6.53	AA g/l	2.33	3.75	3.50
$Y_{PX} \text{mgP/CFU X}$	0.28	0.88	0.22	$Y_{PX} \text{mgP/CFU X}$	0.03	0.08	0.14
C2				C2			
LA g/l	29.88	23.34	5.67	AA g/l	2.58	3.90	3.46
$Y_{PX} \text{mgP/CFU X}$	0.001	0.02	0.012	$Y_{PX} \text{mgP/CFU X}$	0.0006	0.004	0.02
N19				N19			
LA g/l	13.50	13.39	7.64	AA g/l	1.15	1.71	3.08
$Y_{PX} \text{mgP/CFU X}$	0.04	0.39	0.21	$Y_{PX} \text{mgP/CFU X}$	0.007	0.06	0.11
H1				H1			
LA g/l	20.30	19.78	5.91	AA g/l	2.25	4.11	2.45
$Y_{PX} \text{mgP/CFU X}$	0.08	0.07	0.16	$Y_{PX} \text{mgP/CFU X}$	0.01	0.01	0.08
H9				H9			
LA g/l	33.07	30.39	6.20	AA g/l	3.46	2.11	2.95
$Y_{PX} \text{mgP/CFU X}$	0.35	0.54	0.03	$Y_{PX} \text{mgP/CFU X}$	0.05	0.07	0.02
H15				H15			
LA g/l	20.10	21.46	4.23	AA g/l	2.56	4.26	2.12
$Y_{PX} \text{mgP/CFU X}$	0.029	0.02	0.006	$Y_{PX} \text{mgP/CFU X}$	0.005	0.007	0.005
C10				C10			
LA g/l	36.37	25.63	6.32	AA g/l	3.08	3.91	3.06
$Y_{PX} \text{mgP/CFU X}$	0.03	0.19	0.26	$Y_{PX} \text{mgP/CFU X}$	0.005	0.05	0.07

In case of *Lb. plantarum* subsp. *plantarum* A5 was detected the highest LA concentration and yield in the M₁ medium (39.092 g.l⁻¹, Y_{PX}=1.26 mg P/CFU X). In the case of growing in M₃ medium the cumulative LA was slightly smaller but the Y_{PX} was higher.

Bacterial isolate *Lb. paracasei* subsp. *Tolerans* N16 produced larger amount of LA in M₂ medium, where the Y_{PX} was also the highest (Y_{PX}=1.46 mg P/CFU X).

In the case of the two *Lb. pentosus* C10 and C2 the amount of accumulated lactic acid was high, but the Y_{PX} reached very small values (Y_{PX} values were 0.001 and 0.02 P/CFU X). In the case of the M₃ medium the cumulative amount of the LA was small but the Y_{PX} was higher compared to M₁ and M₂ media. The Y_{PX} in the case of *Lactobacillus plantarum* subsp. *plantarum* C5 fermentation process in M₂ medium reached the 0.883 value, even though the accumulated LA was same in M₁ and M₂ medium.

Leuconostoclactis N19 produced small amount of LA compared with other strains, the maximum value of Y_{PX} was 0.39 mg P/CFU X in the case of the M₂ medium.

The L-LA concentration exceeded 30 g/l in the case of the isolated bacterium *Lb. acidipiscis* H9 in both glucose containing media, whereas the Y_{PX} was higher than 0.5 (Y_{PX}=0.54 mg P/ CFU X) in medium containing xylose beside glucose.

Bacterial strains *Lb. buchneri* H1 and *Lb. brevis* H15 produced similar amount of L-lactic acid in both glucose containing media. In these media the accumulated L-lactic acid were 20.295 g.l⁻¹ and 20.102 g.l⁻¹ with small yield coefficient (Y_{PX}=0.08 mg P/ CFU X and 0.0288 mg P/ CFU X).

Meanwhile the amount of the acetic acid was small, didn't not exceeded the 8g/l. But in the most cases the concentration varied between 2-4 g.l⁻¹. The amount of accumulated LA was always higher than AA.

The selection of LAB as suitable starters for biotechnological processes as silage production is a complex process involving the evaluation of some fermentation performances and desired metabolic traits as well as the identification.

There are reports about microbial inoculants that are used to preserve the nutritive value of the crops [15,16]. However, few data are available for the fermentation characteristics in function of available carbohydrate source for natural lactic acid bacteria to enhance the silage fermentation.

Several authors characterised LAB from the natural traditionally produced dairy products, silages, and fermented vegetables [17–19].

In our study the majority of the isolated bacterial strains belong to *Lactobacillus* genera. The predominant strains were the *Lb. plantarum* subsp. *plantarum* and *Lb. pentosus*. The first one possess diverse metabolic activities,

due to the different environmental provenience. Bringel, F. et al., compared the genome of the two LAB species and observed a high similarity that makes difficult the differentiation between the two species [20].

The selected LAB showed differences in the phenotypic patterns, antimicrobial susceptibility and fermentation capacity. The differences might be explained by the adaptation to microhabitats and by the fact, that the LAB isolates has origins from different ecological niches [21].

One important selection and characterization criteria is the safety of the LAB strains, characterized by the antibiotic resistance profile. The antibiotic resistance was determined according to the guidelines reported by European Food Safety Authority EFSA[7]. The selected strains showed almost similar MIC values, except for chloramphenicol and tetracycline.

For determination of the fermentation capacity an important issue is to describe the production in quantitative terms correlated with growth rate. The product formation rate is closely related to biomass formation rate and is influenced by different environmental factors. The productivity is a significant factor, that describe the fermentation [22]. The quantity of lactic and acetic acid resulted from experimental data was used for calculation of product formation yield. The results point out that *Lactobacillus plantarum* subsp. *plantarum* A5 and *Lactobacillus paracasei* subsp. *Tolerans* N16 are the most promising strains from fermentation point of view. In both cases, the Y_{PX} was higher than 1 mg P/ CFU X. In case of *Lactobacillus plantarum* subsp. *plantarum* A5 the highest quantity of LA was observed in M₁ and M₂ media. Some researchers [23] studied also the lactic acid production in media containing the same components as in the case of M₂ media. The maximal LA formation rate (by inoculation with single LAB strain) was slower [23] than observed in case of our experiment. The results showed that the bacterial origin influenced the LA production. It was reported that some of the heterofermentative LAB such as *Lb. brevis* and *Lb. pentosus* are able to convert xylose (released from wheat straw) to lactic acid [24]. There are no data available for the conversion of DDGS to lactic acid. Our results revealed that the assayed nine LAB strains were able to produce lactic acid from this substrate. Our data suggests that the isolated LAB strains converted different substrate as DDGS in LA.

During the fermentation the pH variation caused by metabolites influenced the bacterial growth in all cases. With the increase of the LA concentration a slight decline of CFU was observed. The fluctuation of the lactic acid concentration is probably caused by the fact that some LAB strains can use it as substrate.

In order to establish a ranking criteria for the nine selected LAB strain, we determined the beneficial value index (BVI) for each bacterial strain. This was calculated taking into consideration the fermentation capacity and the fermentation pattern of the strains. Taking into account of the LA production

capacity in the presence of three different substrates, the strains were scored. In case when the value of the product yield coefficient was higher than 1 the strain was scored with 3, with 2 when the product yield was between 0.5-1 and 1 if was between 0.2-0.5. No score was given for a product yield lower than 0.2. In the case of carbon source utilization, the LAB with the maximal utilization was scored with 3, and the next two strains were scored with 2 and 1 respectively. The BVI was defined as the sum of the individual scores.

On basis of BVI, the most beneficial four LABs from substrate utilization point of view, in descending order was: *Lb. plantarum* subsp. *plantarum* C5 (BVI=7), *Lactobacillus paracasei* subsp. *Tolerans* N16 (BVI=6), *Lactobacillus plantarum* subsp. *plantarum* A5 (BVI=5), and *Lb. acidipiscis* H9 (BVI=4). In the case of the other five LABs the index was low (BVI ≤2).

CONCLUSION

This work represents a preliminary study for the selection of beneficial LAB for biotechnological processes. Our results revealed that the four strains (*Lb. plantarum* subsp. *plantarum* A5, *Lb. plantarum* subsp. *Plantarum* C5 and *Lactobacillus paracasei* subsp. *Tolerans* N16) shows potential to be used as starter cultures for silage fermentation, due by their safety assessment and fermentation capacity. Based on this assays they can be further studied as single inoculums or as consortia, to optimise their beneficial effects on different silage fermentation, improving this way the quality of the resulted feedstock.

EXPERIMENTAL SECTION

Isolation and screening of bacterial isolates

A total number of 246 lactic acid bacteria were isolated on de Man, Rogosa, and Sharpe (MRS) and Rogosa agar plates in aerobic and anaerobic conditions from different naturally fermented traditional foods and feed on as follows: eight different traditional cheese, cheese whey, artisanal sauerkraut, corn and vetch silage, [10].

Based on colony morphology and provenience 99 bacterial isolates were further analysed for the most representative characteristics of LAB as: Gram staining, absence of catalase, growth in the presence of (4% and 6.5%) NaCl, gas production and microscopic morphology [11].

Identification of the selected bacterial strains

For the identification at the species level of 54 LAB isolates were selected based on physiological characteristics. The identification was realized using 16SrDNA gene sequence analysis. Genomic DNA was isolated using AccuPrep® Genomic DNA Extraction Kit from Bioneer Isolation Kit, according to the manufacturer's protocol. A part of the bacterial 16SrDNAGene was amplified with the universal oligonucleotides 27f 5' AGAGTTTGATCMTGGCTCAG 3' and 1492r5'TACGGYTACCTTGTACGACTT3' primers flanking the bacterial 16SrDNA region. The amplification included an initial denaturation at 94 °C for 5 min, which was followed by 30 cycles of denaturation at 94 °C for 30 s, annealing at 55 °C for 30 s, extension at 72 °C for 1 min, and a final extension at 72 °C for 7 min. Sequencing were realized by LGC Genomics (Germany). The sequences were edited and aligned with Chromas (Technelysium Pty. Ltd., South Brisbane, Australia); phylogenetic analyses were conducted using Molecular Evolutionary Genetics Analysis 4 system [12] (www.megasoftware.net). The isolates were identified trough comparison of the sequences using the EzTaxon server on the basis of 16SrDNA sequence data [13] (www.ezbiocloud.net/eztaxon;).

Biochemical and phenotypic characterization of lactic acid bacteria

Metabolic patterning of the selected LAB strains was realized by BiologMicrolog Gen III (Biolog, Inc., Hayward, USA), including utilization of 71 carbon source and 23 chemical sensitivity assay.

Antibiotic susceptibility

Determination of antimicrobial susceptibilities of LAB's was realized according to the guidelines reported in EFSA (2008) [7]. For the assessment of the susceptibility to ampicillin, tetracyclin, chloramphenicol, kanamycin, streptomycin, penicillin, gentamicin, serial two-fold dilutions were realized ranging from 0 up to 128 µg.ml⁻¹, in MRS broth.

Fermentation capacity of bacterial strains

The fermentation capacity of the nine beneficial bacterial strains were determined in three different fermentation medium containing diverse fermentation substrates: glucose 20 g/l (M₁), a mixture of glucose and xylose 15 and 5 g/L (M₂), and dried distiller's grain with soluble (DDGS) 20 g/l (M₃). All the fermentation media were supplemented with 5 g/L yeast extract, 2 g/L K₂HPO₄, 0.05 g/L MnSO₄.H₂O, and 0.1 g/L MgSO₄.7H₂O. 2 mL of LAB inoculum was added into 45 mL vials containing 38 mL of fermentation medium [23].The fermentation tests were conducted at 37 °C. For the determination of lactic acid and acetic

acid samples were taken at 0, 24, 36, 48, 60 and 72 h. The amount of these acids were detected using high performance liquid chromatography (HPLC Varian Pro Star 210), equipped with TransgenomicCoregel87H3 column (Transgenomic, Inc., Omaha, USA) and UV detector at 50 °C, mobile phase 0.8 mM H₂SO₄, at a flow rate of 0.6 mL·min⁻¹.

Product formation was assayed by the measured concentration data, on which a polynomial function was fitted and calculated the yield coefficient related to the product. The fermentation capacity was determined by product yield coefficient (eq. 1), defined as the ratio of product formation rate (v_{RP}) (eq. 2) and the growth rate (v_{RX}) (eq. 3) of the tested lactic acid bacteria [14].

$$YPX = \frac{v_{RP}}{v_{RX}} \quad (1)$$

where the rate of product formation (v_{RP}) is (eq. 2)

$$v_{RP} = \frac{d CP}{dt} \quad (2)$$

and the growth rate (v_{RX}) (eq. 3)

$$v_{RX} = \frac{d CX}{dt} \quad (3)$$

ACKNOWLEDGMENTS

This work was supported by grant POSCCE-A2-O2.1.1-2010-2 (No.565/09.09.2013, Code: 45816, Acronym: SILOPREP). The authors are grateful to András Csaba Dezső and Molnos Éva for their help.

REFERENCES

- [1]. H. Zhang, Y. Cai, "Lactic Acid Bacteria - Fundamentals and Practice", Springer Science+Business Media, Dordrecht, **2014**, chapter 1.
- [2]. W.H. Holzapfel, B.J.B. Wood, "Lactic Acid Bacteria: Biodiversity and Taxonomy", John Wiley & Sons Ltd, **2014**, chapter 2.
- [3]. R.V. Rai, J.A. Bai, "Beneficial Microbes in Fermented and Functional Foods", CRC Press, Suite, **2015**, chapter 28.
- [4]. G. Giraffa, N. Chanishvili and Y. Widjastyutti, *Res Microbiol*, **2010**, 161, 480.
- [5]. E. Saarilalo, E. Skyttä, A. Haikara, T. Jalava and S. Jaakkola, *J. Appl. Microbiol*, **2007**, 102, 1 327.
- [6]. R. Rubio, A. Jofré, B Martín, T. Aymerich and M. Garriga, *Food Microbiol*, **2014**, 38, 303.

- [7]. EFSA (European Food Safety Authority), "Update of antibiotic resistance criteria" <<http://www.efsa.europa.eu/en/efsajournal/pub/732.htm>>, **2008**.
- [8]. J.K. Drackley, S.S. Donkin and C.K. Reynolds, *J Dairy Sci.*, **2006**, *89*, 1324.
- [9]. W.H. Holzapfel, B.J.B. Wood, " Lactic Acid Bacteria: Biodiversity and Taxonomy", John Wiley & Sons Ltd, **2014**, chapter 4.
- [10]. R. Atlas, "The Handbook of Microbiological Media for the Examination of Food", Suite, CRC Press, **2006**.
- [11]. Dunca, E. Nimitan, O. Ailiesei and M. Stefan, "Microbiologie aplicata", Iasi, Tehnpress, **2004**.
- [12]. K. Tamura, J. Dudley, M. Nei and S. Kumar, *MolBiolEvol*, **2007**, *24*, 1596–1599.
- [13]. O.S. Kim, Y.J. Cho, K. Lee, SH. Yoon, M. Kim and H. Na, *Int J Syst Evol Microbiol*, **2012**, *62*, 716.
- [14]. O. Muntean, V. Bales, A. Meszaros, "Biochemical Technology. Bucharest, Printech, **2003**.
- [15]. M.M. Chen, Q.H. Liu, G.R. Xin and J.G. Zhang, *Lett Appl Microbiol*, **2013**, *56*, 71.
- [16]. B.F. Carvalho, C.L.S. Ávila, M.G.C.P. Miguel, J.C. Pinto, M.C. Santos and R.F. Schwan, *Grass Forage Sci.*, **2014**, *70*, 308.
- [17]. J. Yang, Y. Cao, Y. Cai and F. Terada, *J Dairy Sci.*, **2010**, *93*, 3136–3145.
- [18]. M. Tohno, H. Kobayashi, M. Nomura, M. Kitahara, M. Ohkuma, R. Uegaki, Y. Cai, *Anim Sci J.*, **2012**, 111.
- [19]. J. Beganović, B. Kos, A. LebošPavunc, K. Uročić, M. Jokić and J. Šušković, *Microbiol Res.*, **2014**, *169*, 623.
- [20]. F. Bringel, A. Castioni, D.K. Olukoya, G.E. Felis, S. Torriani and F. Dellaglio, *Int J Syst Evol Microbiol*, **2005**, *55*, 1629.
- [21]. S. Chaillou, I. Lucquin, A. Najjari, M. Zagorec and M.C. Champomier-Vergès, *PLoS ONE*, **2013**, *8*, e73253.
- [22]. E.M.T. El-Mansi, C.F.A. Bryce, A.L. Demain, A.R. Allman, "Fermentation Microbiology and Biotechnology", Boca Raton: CRC Press, **2011**, chapter 2.
- [23]. F. Cui, Y. Li and C. Wan, *Bioresour Technol*, **2011**, *102*, 1831.
- [24]. Y. Zhang and P.V. Vadlani, *J. Biosci Bioeng*, **2015**, *119*, 694.

A SIMPLE TLC METHOD FOR EVALUATION OF NICOTINE IN CIGARETTES

ANAMARIA HOSU^a, CLAUDIA CIMPOIU^{a,*}

ABSTRACT. In this study, a rapid and sensitive thin-layer chromatographic method for evaluation of nicotine content in twelve popular cigarettes from Romanian market has been used. The TLC separation was performed on silica gel F254 plates using a mixture of ethyl acetate - methanol - conc. ammonia - water 80:25:0.2:15.8, v/v/v/v as mobile phase. Detection was made in UV light at 254nm and in visible light after derivatization with Dragendorff's reagent and the areas of the characteristic bands of nicotine were determined using ImageJ software. The results showed a significant variation of nicotine content in investigated cigarettes, but in good agreement with the concentrations of nicotine specified on the label.

Keywords: nicotine evaluation, thin-layer chromatography, cigarettes

INTRODUCTION

The highly toxic compound from tobacco alkaloids is nicotine, 3-(1-methyl-2-pyrrolidinyl) pyridine, a colorless, less to pale yellow, hygroscopic oily liquid present in the leaves of *Nicotiana tabacum*. Christopher Columbus have been found tobacco in the Americas in 1492, but historical sites show that tobacco has been smoked in Central America for at least three thousand years. Nicotine is a highly stimulant of central and peripheral nervous system generating short-term adverse health effects, like elevated blood pressure, heart rate, and blood glucose [1]. Long-term tobacco use is associated with increased cancer rates, incidence of atherosclerotic arterial disease, chronic obstructive pulmonary disease, hypertension and low birth weight of infants born to mothers who smoke [2]. Recent studies suggested that nicotine could have therapeutic applications in some neurodegenerative diseases like Alzheimer's [3].

^a Babeș-Bolyai University, Faculty of Chemistry and Chemical Engineering, 11 Arany Janos str., RO-400028, Cluj-Napoca, Romania.

* Corresponding author: ccimpoiu@chem.ubbcluj.ro

The determination of total nicotine alkaloids is very important to toxicology and medicine and also for the tobacco industry because the quality of the product can be determined by its nicotine content. The nicotine was analyzed in different types of samples such as tobacco leaves, cigarettes, smokes, urine, hair, human serum, plasma etc. Many analytical methods have been developed and employed for nicotine determination in tobacco leaves and cigarettes, such as GC [4, 5], GC-MS [6, 7], TLC [8 - 10], HPLC [11, 12], HPLC-MS/MS [13], AAS [14], SFC-IMD [15], capillary electrophoresis [16, 17], radio immunoassay [18], spectrophotometric methods [19 - 23], circular dichroism spectropolarimetry [24], FTIR [25], voltammetry [26] and recently flow injection with electrochemiluminescence detection [27]. All of these methods present a series of advantages and disadvantages.

The aim of this study is to evaluate and compare the nicotine content of twelve types of cigarette from popular brands available in the Romanian market. The analysis of nicotine in cigarettes is necessary due to the one global problem regarding counterfeit products trade. Some cigarettes contain more nicotine or the used tobacco can be of poor quality. In our original method different analytical parameters were optimized. This method is a good alternative to some of the reported expensive instrumental methods.

RESULTS AND DISCUSSION

Cigarettes contain various quantity of nicotine, depending on the brand, but only approximately 1 mg is actually absorbed in the human body [28]. The higher content of nicotine or tar content may cause serious health problems. Moreover, the nicotine addiction is related with higher risk for many kinds of diseases such as Alzheimer's, Parkinson's and even suicide [29, 30]. For these reasons the control of nicotine amount in tobacco products is obviously necessary.

On this line twelve cigarettes widely used and distributed in Romania were chosen for evaluation of nicotine content. For this aim a TLC method was developed and used.

After chromatographic runs using several mobile phases (**Table 1**) it can be concluded that the best separation was obtained using the mobile phase consisting in ethyl acetate - methanol - conc. ammonia - water 80:25:0.2:15.8, v/v/v/v (**Figure 1**).

The image of TLC separation obtained at 254nm (Figure 1a) clearly indicates the presence of different compounds in all of the analyzed extracts. The intensity of the bands separated on the chromatographic plate seem to be different in different sample, indicating that the concentration of these compounds depend on the type of cigarette. The chromatographic fingerprints of samples 3

and 5 present the most intense separated zones, therefore it can be admitted that they contain the highest amount of interest compound, including nicotine, that may correspond to one of these bands. Nevertheless, this image does not bring useful information about nicotine extracted from cigarettes, being a non-specific mode for identification of this compound.

Table 1. The tested mobile phases

No.	Solvent system	Composition (v/v/v/v)
1	Chloroform : methanol : acetic acid	11:8:1
2	Methanol : ammonia	200:3
3	Ethyl acetate : methanol : ammonia 0,1 M	80:25:16
4	Chloroform :methanol : ammonia	6:5:1
5	Dichloromethane : methanol : ammonia	83:15:2
6	Ethyl acetate : methanol : ammonia : water	80:25:0.2:15.8
7	Dichloromethane : methanol : ammonia : water	82:16:0.8:1.2
8	Acetonitrile : water	22:3

Thus, for certain identification of nicotine, the plate was sprayed with a specific color Dragendorff's reagent. This reagent usually forms an orange-red colored complex in the reaction with alkaloids. Consequently, the characteristic zone of nicotine appear as orange bands on a yellow background of derivatized chromatographic plate (**Figure 1b**). The image of the TLC separation indicates that all analyzed samples contain nicotine.

The different intensity of nicotine characteristic bands show that its concentration is different in the analyzed extracts. Thus, samples 3 and 5 seem to contain the highest amount of nicotine, being followed by samples 6 and 11. The smallest amounts of nicotine seem to be contained in samples 4 and 1. In order to confirm that some samples contain different concentration of nicotine and to prove that some types of cigarettes contain the same concentration of this compound, the areas of the characteristic bands of nicotine were determined using ImageJ software. The areas were calculated from the image taken in UV light at 254nm because the sensibility of determination is higher than that in visible light.

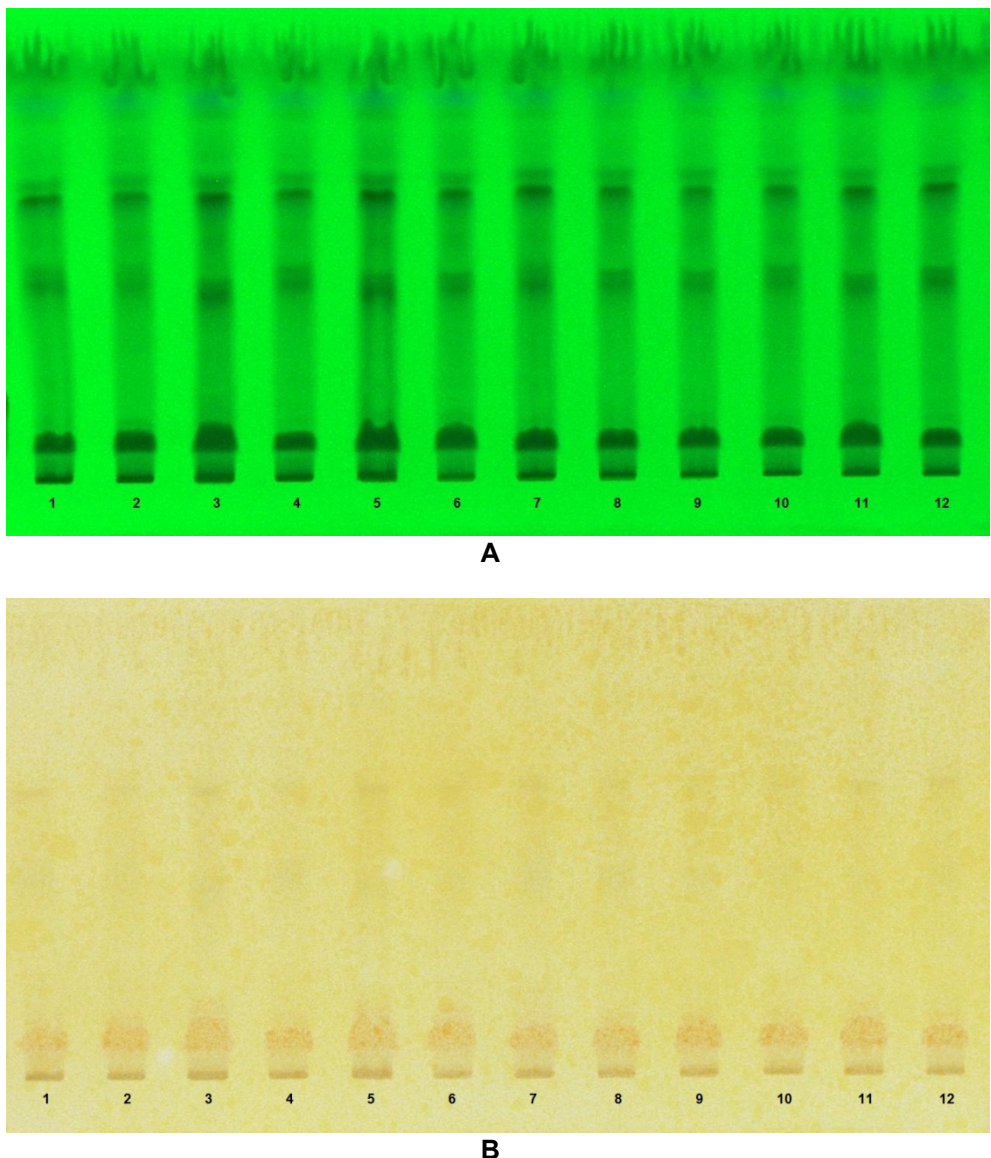


Figure 1. The TLC separation of nicotine from analyzed cigarettes:
A - UV light detection at 254nm; B - detection in visible light
after derivatization with Dragendorff's reagent.

The results (**Table 2**) show that samples 3 and 5 contain the same highest amounts of nicotine (label - 0.9mg nicotine/cigarette), followed by samples 6 and 11 (label - 0.8mg nicotine/cigarette), samples 2, 7 and 9 (label - 0.7mg nicotine/cigarette), samples 8 and 12 (label - 0.6mg nicotine/cigarette), sample 10 (label - 0.5 mg nicotine/cigarette), sample 4 (0.3mg nicotine/ cigarette), and the smallest determined area of nicotine band is that of sample 1 (label - 0.1mg nicotine/cigarette).

Table 2. The characteristics of analyzed cigarettes
and the obtained area of nicotine bands

Sample	Cigarette Type	Producer	Nicotine (mg)	Area (AU)
1	Kent 1 (White)	British American Tobacco Group	0.1	3280
2	Kent 8 (Blue)	British American Tobacco Group	0.7	4145
3	Dunhill classic blend	British American Tobacco Group	0.9	5453
4	Kent 4 (Silver)	British American Tobacco Group	0.3	3519
5	Winchester	JT International Manufacturing	0.9	5481
6	Kent classic	British American Tobacco Group	0.8	4623
7	L&M red label	Philip Morris	0.7	4299
8	Kent convertibles (iSwitch)	British American Tobacco Group	0.6	3987
9	Viceroy red international blend	British American Tobacco Group	0.7	4199
10	Kent 6 (Spectra)	British American Tobacco Group	0.5	3779
11	Marlboro classic flavor	Philip Morris	0.8	4746
12	Pall Mall charcoal filter	British American Tobacco Group	0.6	3990

These semi-quantitative results are in concordance with the concentrations of nicotine expressed in mg of nicotine/cigarette, which are specified by the producers on the label of each type of cigarettes used in this study (**Table 2**). Moreover, a significant variation of nicotine content was noticed among the twelve investigated types of cigarettes (Figure 2), the highest amounts of nicotine (Kent 8 - sample 5) being almost duplicated compared to lowest nicotine content (Kent 1 - sample 1).

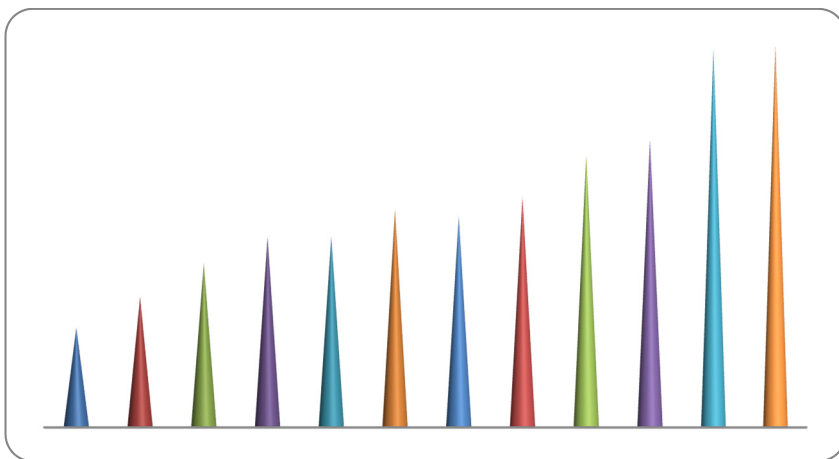


Figure 2. The areas variation depending on the type of cigarettes.

CONCLUSIONS

The developed method proved to be a powerful, low cost and simple tool for evaluation of nicotine in different sample. It allowed the simultaneous identification and semi-quantitative determination of nicotine from different types of cigarettes by TLC. Also, the determined areas of the characteristic bands of nicotine that are in keeping with the content of nicotine declared by producers enable to distinguish between cigarettes based on their content in nicotine. The method could be used for rapid detection of counterfeit cigarettes.

EXPERIMENTAL SECTION

Materials and reagents

All reagents and solvents used in the present research were of analytical grade and were purchased from Chimopar (Bucharest, Romania). The chromatographic plates were acquired from Merck (Darmstadt, Germany).

Twelve types of cigarettes from different producers were bought from tobacconist (**Table 2**).

Samples preparation

5mL of extraction solvent (ethanol-water 4:1, v/v) were added to 0.5g of tobacco from each type of cigarette. Extraction was performed by maceration at room temperature. After 10 days, the extracts were filtered and directly analyzed without any other treatments.

Chromatographic analysis

The chromatographic analysis was performed on silica gel F₂₅₄ TLC aluminum sheets (20x10cm). Several mobile phase (**Table 1**) were tested, the chosen one being ethyl acetate - methanol - conc. ammonia - water 80:25:0.2:15.8, v/v/v/v. 10µL of each ethanolic extract were applied on the plate as 6 mm bands at 1.5cm from the low edge of the plate, with a rate of 80nL/s, using a semi-automatic applicator device (Linomat 5 - Camag, Muttenz, Switzerland) controlled by winCats software. The plates were developed at room temperature into pre-saturated (30 minutes) normal chromatographic twin trough chamber (Camag) to a distance of 80mm. Detection was performed under UV light at 254nm and under visible light after spraying with Dragendorff's reagent solution. Documentation of the plate was performed using a TLC vizualizer device (Digistore 2 - Camag) and the images were stored as jpeg. files.

REFERENCES

- [1]. D. Yildiz, *Toxicon*, **2004**, 43, 619.
- [2]. K.B. Scheidweiler, D.M. Shakleya, M.A. Huestis, *Clinica Chimica Acta*, **2012**, 413, 978.
- [3]. M.R. Picciotto, M. Zoli, *Frontiers in Bioscience*, **2008**, 13, 492.
- [4]. O.H. Drummer, S.K. Horomidis, M.L. Sophie-Syrjanen, P. Tippett, *Journal of Analytical Toxicology*, **1994**, 18, 134.
- [5]. A. Millet, F. Stintzing, I. Merfort, *Journal of Pharmaceutical and Biomedical Analysis*, **2009**, 49, 1166.
- [6]. M.K.O. Koyano, Y. Oike, S. Goto, W. Osamu, K. Furuya, H. Matsushita, *Japanese Journal of Toxicology and Environmental Health*, **1996**, 42, 263.
- [7]. A.M. Hossain, S.M. Salehuddin, *Arabian Journal of Chemistry*, **2013**, 6, 275.
- [8]. G. Romano, G. Caruso, G. Masumarra, D. Povone, G. Guciani, *J. Planar Chromatography-Modern TLC*, **1994**, 7, 233.

- [9]. G. Bazylak, H. Brózik, W. Sabanty *Journal of Pharmaceutical and Biomedical Analysis*, **2000**, 24, 113.
- [10]. J.M. Badr, F.H. Bamane, N.S. El-Shaer, *Journal of Liquid Chromatography & Related Technologies*, **2012**, 35, 1213.
- [11]. S. Pichini, L. Altieri, A.R. Passa, M. Rosa, P. Zuccaro, R. Pacifici, *Journal of Chromatography A*, **1995**, 697, 383.
- [12]. F. Alali, A. Massadeh, *Acta Chimica Slovenica*, **2003**, 50, 251.
- [13]. P. Kubica, A. Kot-Wasik, A. Wasik, J. Namiesnik, *Journal of Chromatography A*, **2013**, 1289, 13.
- [14]. M.M. Ayad, S.E. Khayyal, N.M. Farag, *Spectrochimica Acta Part B: Atomic Spectroscopy*, **1985**, 40, 1127.
- [15]. C. Wu, W. F. Siems, H.H. Hill, Jr., R.M. Hannan, *Journal of Chromatography A*, **1998**, 811, 157.
- [16]. S.S. Yang, I. Smetena, *Chromatographia*, **1995**, 40, 375
- [17]. J.-Y. Sun, X.-Y. Xu, H. Yu, T.-Y. You, *Chemical Research in Chinese Universities*, **2012**, 28, 415.
- [18]. R. Pacifici, F. Aetieri, L. Gandini, A. Lenzi, R. Passa, S. Pichini, M. Rosa, P. Zuccaro, *Environmental Research*, **1995**, 69, 254.
- [19]. A. Asthana, R. Rastogi, G. Sunita, V.K. Gupta, *Journal of the Chinese Chemical Society*, **2004**, 51, 949.
- [20]. S. Suryani, T. Izzati, A.M. Noor, *Science International-(Lahore)*, **2012**, 24, 139.
- [21]. R. Manish, K.N. Ramachandran, V.K. Gupta, *Analyst*, **1994**, 119, 1883.
- [22]. H.A. Omara, S.M.M. Attaf, *World Journal of Pharmacy and Pharmaceutical Sciences*, **2014**, 3, 1327.
- [23]. S.A. Al-Tamrah, *Analytica Chimica Acta*, **1999**, 379, 75.
- [24]. M.V. Atkinson, M.H. Soon, N. Purdie, *Anal. Chem.* **1984**, 56, 1947.
- [25]. A. Gómez-Siurana, A. Marcilla, M. Beltrán, D. Berenguer, I. Martínez-Castellanos, S. Menargues, *Thermochimica Acta*, **2013**, 573, 146.
- [26]. H. Kassa, A. Geto, S. Admassie, *Bulletin of the Chemical Society of Ethiopia*, **2013**, 27, 321.
- [27]. Y. Zhang, Q. Cong, Y.F. Xie, B. Zhao, *Chemical Research in Chinese Universities*, **2009**, 30, 697.
- [28]. A. Levent, Y. Yardim, Z. Senturk, *Electrochimica Acta*, **2009**, 55, 190.
- [29]. S.J. Wang, H.W. Liaw, Y.C. Tsai, *Electrochemistry Communications*, **2009**, 11, 733.
- [30]. F. Moriya, Y. Hashimoto, J. Furumiya, *Forensic Science International*, **2007**, 168, 102.

RECENT DEVELOPMENT OF BIOAUGMENTATION METHODS FOR TOBACCO WASTEWATER TREATMENT

MILANA M. ZARIĆ^a, NENAD M. ZARIĆ^b, JELENA IVKOVIC^c,
DANIJELA SLAVNIC^d, BRANKO BUGARSKI^d

ABSTRACT. In production of cigarettes a lot of tobacco waste, with nicotine, goes into the environment. Hence, there is a need for an economic and efficient method to diminish the discharge of hazardous materials from tobacco wastewaters. Bioaugmentation using specialized bacteria strains could improve the efficiency of tobacco wastewater treatment. In this review paper we present bioaugmentation methods for tobacco wastewater treatment that were published in last few years. Bioaugmentation systems have proven to be very effective in removal of nicotine and TOC; it was shown that *Pseudomonas* sp. HF-1 and TW bacteria strains can be successfully used in reactors. Recent studies showed that controlling pH in the reactors can improve reactor performance in removing nicotine and TOC from tobacco wastewater.

Keywords: tobacco wastewater, nicotine, hazardous materials, bioaugmentation

INTRODUCTION

In production of cigarettes a lot of tobacco waste, that includes nicotine, aminobiphenyl, naphthylamine and benzo(a)pyrene goes into the environment [1, 2]. A non-recyclable, powdery, nicotine-containing waste is formed during tobacco production, which has an average nicotine content of 18 mg/kg dry weight [3]. These wastes are classified as “toxic and hazardous wastes” under European Union Regulations when the nicotine content exceeds 500 mg/kg dry weight [4].

^a Institute of Chemistry, Technology and Metallurgy, University of Belgrade, Njegoševa 12, 11000 Belgrade, Serbia.

^b Innovation center of Faculty of Technology and Metallurgy, University of Belgrade, Kariđelova 4, 11000 Belgrade, Serbia.

^c Faculty of Agriculture, University of Belgrade, Nemanjina 6, 11080 Belgrade, Serbia.

^d Faculty of Technology and Metallurgy, University of Belgrade, Kariđelova 4, 11000 Belgrade, Serbia.

* Corresponding author: mzaric@tmf.bg.ac.rs

For 1 t of cigarettes, more than 60 t tobacco wastewater is discharged [5]. Nicotine can dissolve in water and other organic solvents. It can cross blood-brain barrier and many other complicated biological membranes [6]. Because of this, nicotine is considered malignant pollutant among other things.

Analyses on the effluent of many sewage treatment plants (STPs) shows the presence of nicotine. Based on this it can be concluded that nicotine survives conventional treatment processes [7] and different methods for removal of nicotine from tobacco wastewaters are being developed. Nicotine adsorption by coconut fibers and saw dust is a good method for removal of nicotine from wastewaters [8], but it does not degrade nicotine. Teijon et al. [7] report that nicotine removal after conventional treatment processes based on flocculation-coagulation, lamellar clarification, filtration, and disinfection is about 79%, while after an additional treatment of chlorination the removal was about 97%. However, aqueous chlorination can react with natural organic matter and other organic compounds to form disinfection by-products (DBPs). These products have been shown to be more resistant to degradation and more toxic than the original compounds that they came from [9-11]. As can be seen denicotinization of tobacco wastes can be done with physio-chemical treatment, but compared to these methods, biological methods of nicotine degradation are more efficient and less costly [12].

Because of pollution problems and toxicity of nicotine, research on nicotine degradation by microorganisms (biodegradation) is very active field of research. Large numbers of microorganisms, able to degrade nicotine were identified [13]. Biochemical pathways for degradation as well as genes responsible for nicotine degradation were described in reviews [13, 14]. Moreover, new microorganisms that degrade nicotine were found and described in the last few years [15-17].

NICOTINE DEGRADING BACTERIA

Many types of nicotine degrading bacteria have been isolated and identified [18-21]. Some of them have been used to degrade nicotine in liquid medium.

Wang et al. [21] demonstrated that *Sphingomonas* sp. TY had a greater ability to degrade nicotine than strain HF-1, with complete degradation of 1.0 g/l of nicotine within 18h. Strain TY could grow and degrade nicotine in a range of pH from 3-8, and temperature range 15-45°C. However, best results were obtained when initial pH was 6.0-7.0 and temperature 25-30°C [21].

There are a few strains of *Pseudomonas* sp. used in nicotine degrading studies. As shown by Wang et al. *Pseudomonas* sp. S16 was able to degrade 3.0 g/l nicotine within 10h. The optimal temperature for nicotine degradation

was 30°C, while optimal pH was 7.0 [22]. Another *Pseudomonas* sp. strain designated as CS3 was used for nicotine degradation in liquid medium [23]. Optimal conditions for nicotine degradation by strain CS3 were 30°C and pH 7.0. However, this strain showed high nicotine-degrading capabilities within pH range from 6.0 to 10.0. Strain CS3 can decompose 1.0 g/l nicotine within 24h, and could endure up to 4.0 g/l nicotine in liquid media [23]. Strain *Pseudomonas plecoglossicida* TND35 can degrade 0.5-5 g/l nicotine within 8 to 44h, with optimal conditions of 30°C and pH 7.0 [17].

Newly isolated *Ochrobactrum* sp. Strain SJY1 was tested in degrading nicotine [24]. The study showed that strain SJY1 could grow in a range of pH from 5.0 to 9.0, where optimal pH was 7.0. The optimal temperature was 30°C. Under optimal conditions strain SJY1 could almost completely degrade 4.0 g/l nicotine within 10h [24].

BIOAUGMENTATION

For the treatment of tobacco wastewaters bioaugmentation using specialized bacteria strains has proven to be one of the most effective, considering costs and sustainability as well [25-27].

The bacteria used in bioaugmentation have to be active, persistent and compatible, hence one has to find microorganisms that are suitable for bioaugmentation [28, 29]. To avoid unpredictable bioaugmentation results it is important to choose the right strain [30]. Two strains, that showed high nicotine degrading ability, were used for bioaugmentation of tobacco wastewaters; *Pseudomonas* sp. HF-1 [3, 31-33] and *Acinetobacter* sp. TW [21].

The principle behind bioaugmentation is colonization. This means that the nicotine degrading bacteria has to have the ability to coexist with native bacteria and keep its activity in the activated sludge system [34]. A sharp increase in autoinducers, small molecules that bacteria use to communicate, can indicate a change in behavior of bacterial community [35, 36]. Communication using autoinducers enable bacteria to acclimatize themselves to the environment. This way of bacterial communication is called the theory of quorum sensing [37-39].

When microorganism come in contact with toxic substances oxidative stress occurs [40]. Nicotine is one of the substances that can induce oxidative stress in microorganisms [41]. Bacteria capable of reducing the toxicity of nicotine, and thus reducing oxidative stress, can be beneficial to other bacteria in the active sludge.

Several studies on bioaugmentation of sludge were performed. In this review paper we present methods of bioaugmentation for tobacco wastewater treatment that were published in last few years.

Bioaugmentation with *Pseudomonas* sp. HF-1

Sequencing batch reactor (SBR) can be used for tobacco wastewater treatment [42]. However, using this method with conventional activated sludge culture in tobacco industry is not very efficient because of toxicity of nicotine and other substances in tobacco wastewater [43]. For example, in tobacco production corporation Liqun (Hangzhou, China) using sequencing batch reactor resulted in w20% nicotine degradation and w50% chemical oxygen demand (COD) removal [44]. These data show that conventional activated sludge is not optimal for treatment of tobacco wastewater. Hence, it was proposed to use bioaugmentation to increase efficiency of sequencing batch reactor [44], as bacterial strains specialized in nicotine degradation can reduce toxicity to the microbial community [45].

Comparison of Bioaugmented and Non-Bioaugmented reactors

In the study by Wang et al. *Pseudomonas* sp. HF-1, that possess high ability for nicotine degradation, was used for bioaugmentation in SBR [44]. The influence of nicotine degradation by bioaugmentation strain *Pseudomonas* sp. HF-1, on the structure and activity of microbial community, was monitored. In the study two reactors with activated sludge from the Sibao Sewage Treatment Plant (Hangzhou, China), as the indigenous population, were used. One of the reactors was bioaugmented by *Pseudomonas* sp. HF-1, while the other one, without *Pseudomonas* sp. HF-1 was a control. Wastewater that was used in this study was prepared by mixing tobacco waste (collected from Liqun Cigarette Co. Ltd., Hangzhou, China) and tap water in a ratio of 7:100 (g/mL). Nicotine and COD concentrations were observed in the study as target pollutant indexes.

Both systems were able of complete removal of nicotine when concentration of nicotine was 40 and 80 mg/L; however, removal of nicotine in bioaugmented system was faster. When concentrations of nicotine were from 130 to 250 mg/L non-bioaugmented system was able only partially to remove nicotine in 48h, while bioaugmented system removed nicotine completely in 12h.

An increase of nicotine concentration resulted in decrease of COD removal in non-bioaugmented system; increase from 40 to 250 mg/L corresponded to COD removal of 89.9% and 64.6%. An increase of nicotine concentration almost did not influence COD removal in bioaugmented system; COD removal was between 84.8% and 90.6%. These results indicated that bioaugmentation by *Pseudomonas* sp. HF-1 improves removal of nicotine, but also removal of COD. Namely, nicotine as toxic substance inhibited growth and activity of indigenous sludge microorganism population. In bioaugmented system, *Pseudomonas* sp. HF-1 removed nicotine and enabled growth and activity of indigenous sludge microorganism contributing to increased COD removal.

Based on these results it was proposed that bioaugmentation with the nicotine-degrading *Pseudomonas* sp. strain HF-1 is a good and environmentally friendly alternative for tobacco wastewater treatment. Hence, this method has great potential for application on tobacco wastewater [44].

Biofilm Formation

The colonization of bioaugmented systems by the inoculated bacteria can be affected by many factors, such as competition from native bacteria [46]. The ability of bacteria to colonize a new environment can be improved by biofilms, multi-cellular communities formed by bacteria [47-49]. The process of biofilm formation has been reported to occur via quorum sensing, cell-cell communication among bacteria using auto-inducers [50, 51]. In order to develop better bacterial bioaugmentation system for tobacco wastewater treatment Wang et al. studied the roles and condition for release of acylated homoserine lactones (AHLs), the main auto-inducers that effect biofilm formation of *Pseudomonas* sp. HF-1.

Biofilm formation includes swarming by flagella and secretion of extracellular polymeric substances (EPS); these processes are induced by acylated homoserine lactones (AHLs). AHLs are released into and out of bacterial cells as the population of bacteria increases. Conditions influence the increases in bacteria population and affect the release and existence of auto-inducers [52].

The results on influence of temperature and pH on biofilm formation showed that during the start-up stage of the bioaugmentation, low temperature (20–25 °C) and acidic environment (pH value 6) were good for introduction of the strain culture. During biofilm formation, it was shown that temperature does not have significant influence, while alkaline environment (pH value 8) was beneficial for stable performance of the bioaugmentation

Biofilm formation can be also influenced by substances in the solution like nicotine and NaCl. Taking also concentrations of nicotine and NaCl, Wang et al. proposed conditions for biofilm formation [1]. Temperature of 25 °C, pH 5–6, concentrations of 3% inoculum, 1.5 g/L nicotine and 1% NaCl, was beneficial to the startup stage during bioaugmentation, since the amount of AHLs released was sufficient for quorum sensing of swarming and EPS formation for strain HF-1. Under conditions of pH 8 in the presence of 1.2–1.8 g/L of nicotine and 1% NaCl, the threshold for quorum sensing of biofilm formation was reached and the bioaugmentation system showed an efficient performance.

Influence of pH, inoculum amount and nicotine load on Reactor Performance

It is hypothesized that biofilm formation by *Pseudomonas* sp. HF-1 in a bioaugmented system was also regulated by quorum sensing [53]. Since it was found that pH had a significant effect on the release of auto-inducers by *Pseudomonas* sp. HF-1, it was investigated if regulation of pH could be used

to facilitate HF-1 colonization of activated sludge in bioaugmentation systems [1]. Reactor performance in removing nicotine and TOC is the most important evaluation in the experiment. Nicotine removal in pH controlled reactors remained at about 100% during whole experiment. In non-pH controlled reactors nicotine removal decreased after some time. Low pH (pH 5.5) in the beginning of the process induced the release of auto-inducers and increase in the swarming ability and EPS secretion for strain HF-1 biofilm formation. However, low pH hampered the growth of other bacteria in the activated sludge and caused low TOC removal in the beginning. Nevertheless, in the pH controlled reactor, in the later phases of process, when pH was 8.0, presents of strain HF-1 removed toxic nicotine, and enabled the growth of other bacteria and increased TOC removal. In non-pH controlled reactor, strain HF-1 did not make biofilm and disappeared in late phases of the process, which caused toxic nicotine to inhibit growth of other bacteria, resulting in decreased TOC removal.

Appropriate inoculum amount is crucial for successful setup of bioaugmentation system. Small inoculum may not be enough to degrade the amount of nicotine present in the reactor, while too large inoculum could destroy the ecological balance in the reactor [54]. The amount of inoculum that is most suitable for the colonization of strain HF-1 was 1.10 mg/g (dry weight of strain HF-1/dry weight of activated sludge) [55].

The set-up of strain HF-1 bioaugmented system was not inhibited by nicotine load. The successful setup of bioaugmented reactor was done with nicotine concentrations from 250 to 1200 mg/L. However, it needs to be mentioned that TOC removal efficiency decreased when nicotine was above 1000 mg/L [55].

Bioaugmentation with *Acinetobacter* sp. TW

Evaluation of whether the strain *Acinetobacter* sp. TW can colonize activated sludge, was done in a synthetic tobacco wastewater system [56]. Synthetic wastewater system was used to study the effects of native sludge bacteria on the colonization of TW strain, since actual tobacco wastewater contains many unknown toxic materials that can affect the experiment [57]. The activated sludge used in this study was obtained from the Qige wastewater treatment plant (Hangzhou, China).

Polymerase chain reaction-denaturing gradient gel electrophoresis (PCRDGGE), quorum sensing autoinducer detection, and toxicological indicators monitoring were used to give a view on ecological relationships involved in bioaugmentation.

Three reactors divided into two groups were used in this study. The first group was non-bioaugmented system (non-BA system) and the other group included two parallel bioaugmented systems (BA system-1 and BA system-2). All three reactors were started with 3200 ± 50 mg/L of initial COD and 1.0 ± 0.1 g/L of nicotine. The only difference between them was that the first group did not contain TW strain. BA system-1 and BA system-2 were inoculated with TW strain 6 times,

every 2 days. The inoculation ended on the 12th day. The performance was followed for 28 days.

To see whether the colonization of strain TW on the active sludge was successful a sample was taken and analyzed in the end of the experiment. For the detection of TW in the activated sludge a reverse transcriptase PCR (RT-PCR) was used because it can monitor gene expression in viable cells, as dead cells are not detected [58]. Young has reported that gene *hsp* is one of the most important genes involved in nicotine degradation in strain TW, as well as in *Pseudomonas* sp. strain HF-1 [44, 59]. The sequences for *hsp* was found in BA system -1 and BA system - 2, which indicates that strain TW was present. No such sequences were seen in the original activated sludge and non-BA system, indicating absence of strain TW. This proves that strain TW has successfully colonized the activated sludge in the two BA-systems

The experiment was divided into 2 stages [56]. First stage was the bioaugmentation stage that lasted until day 12 when the inoculation ended. The second stage started from day 13, when a stable synthetic wastewater influx was maintained.

In the first stage non-BA system had nicotine removal of only 10%, while in BA systems it was up to 95%. The second stage lasts the remaining 16 days. Although no more inoculations were carried out, the BA systems maintained nicotine removal at above 95%, while non-BA system had merely 0-10%. Considering that there were no other differences between the non-BA system and BA systems, except strain TW, the 98% removal of nicotine in BA systems can be almost totally contributed to nicotine degradation by strain TW, which also contributes to the conclusion that strain TW has colonized the active sludge.

The efficiency of the reactors was also evaluated by monitoring COD removal. On non-BA system the removal of COD was maintained above 60%, while in two BA systems it was from 80% to 90% during the whole process. This indicates that colonization of strain TW improves the efficiency of COD removal.

BA systems have proven to be very effective in removal of nicotine and COD, which goes to 95% and 80%-90% respectively. Nicotine toxicity has made it easier for TW strain to colonize the activated sludge, because it had caused oxidative stress in the native bacteria. Further degradation of nicotine protected the native bacteria from its toxic effects and increased the biodiversity of the active sludge. With the increase in biodiversity the overall efficiency of BA systems was also increased, including efficient COD removal. Microbial community in bioreactors is popularly tested by PCR-DGGE technique [60, 61]. After colonization of the active sludge by strain TW there was a change in the structure of the bacterial colony and the BA systems reached a new ecological balance. On the last day of the experiment the activated sludge in BA reactor-1 and BA reactor-2 contained more types of bacteria when compared to the original sludge. More complex reactors ecosystem means that it is more stable and resilient [62].

As was described above many bacterial strains can be used to degrade nicotine in liquid media. Except strains *Pseudomonas* sp. HF-1 and *Acinetobacter* sp. TW, others have not been used in bioaugmentation of tobacco wastewater. The future research should concentrate on studying the use of these bacterial strains in bioaugmented treatment of tobacco wastewater.

CONCLUSION

BA systems have proven to be very effective in removal of nicotine and COD; it was shown that *Pseudomonas* sp. HF-1 and *Acinetobacter* sp. TW bacteria strains can be successfully used in reactors. Recent studies showed that controlling pH in the reactors can improve reactor performance in removing nicotine and TOC from tobacco wastewater.

ACKNOWLEDGMENTS

This work was supported by Ministry of Education, Science and Technology Development, Republic of Serbia Projects no. III 46010 and 176006.

REFERENCES

1. M.Z. Wang, X. Zheng, H.Z. He, D.S. Shen, H.J. Feng, *Bioresoure Technology*, **2012a**, 125, 119.
2. X. Wang, L. Tang, Y.L. Yao, H.X. Wang, H. Min, Z.M. Lv, *Applied Microbiology and Biotechnology*, **2012b**, 97, 6077.
3. S.N. Wang, Z. Liu, H.Z. Tang, J. Meng, P. Xu, *Microbiology*, **2007a**, 153, 1556.
4. T.E. Novotnya, F. Zhaob, *Tobacco Control*, **1999**, 8, 75.
5. W.H. Zhong, C.J. Zhu, M. Shu, K.D. Sun, L. Zhao, C. Wang, Z.J. Ye, J.M. Chen, *Bioresour. Technol.*, **2010**, 101, 6935.
6. Y. Tega, S.-I. Akanuma, Y. Kubo, T. Terasaki, K.-I. Hosoya, *Neurochemistry International*, **2013**, 62, 173.
7. G. Teijon, L. Candela, K. Tamoh, A. Molina-Diaz, R.F. Fernandez-Alba, *Science of the Total Environment*, **2010**, 408, 3584.
8. Z. Basher, A.K. Gupta, A. Chattre, *IOSR Journal of Applied Chemistry*, **2014**, 8, 39.
9. J.M. Buth, M. Grandbois, P.J. Vikesland, K. McNeill, W.A. Arnold, *Environmental Toxicology and Chemistry*, **2009**, 28, 2555.
10. M. DellaGreca, M.R. Iesce, P. Pistillo, L. Previtera, F. Temussi, *Chemosphere*, **2009**, 74, 730.
11. M.R. Boleda, M.T. Galceran, F. Ventura, *Environmental Pollution*, **2011**, 159, 1584.
12. Y.J. Yuan, Z. X. Lu, N.L. Wu, J. Huang, F.X. Lu, X.M. Bie, *International Biodeterioration & Biodegradation*, **2005**, 56, 45.

13. R. Gurusamy, S. Natarajan, *The Scientific World Journal*, **2013**, Article ID 125385.
14. R. Brandsch, *Applied Microbiology and Biotechnology*, **2006**, 69, 493.
15. Y. Liu, L. Wang, K. Huang, W. Wang, X. Nie, Y. Jiang, S. Liu, P. Xu, H. Tang, *PLOS ONE*, **2014**, 9, 84399.
16. J. Petricevic, V. Gujanicic, D. Radic, J. Jovicic Petrovic, J. Jovic, V. Raicevic, *EGU General Assembly 2013*, 7-12 April, **2013**, Vienna, Austria
17. G. Raman, K.N. Mohan, V. Manohar, N. Sakthivel, *Biodegradation*, **2014**, 25, 95–107.
18. C.M. Chen, X.M. Li, J.K. Yang, X.W. Gong, B. Li, K.Q. Zhang, *International Biodeterioration and Biodegradation*, **2008**, 62, 226.
19. K.D. Sun, C.J. Zhu, W.H. Zhong, J.M. Chen, Z.J. Ye, P.J. Liu, Q. Zhou, *Acta Scientiae Circumstantiae*, **2008**, 28, 1294.
20. X.W. Gong, J.K. Yang, Y.Q. Duan, J.Y. Dong, W. Zhe, L. Wang, Q.H. Li, K.Q. Zhang, *Research in Microbiology*, **2009**, 160, 200.
21. M.Z. Wang, G.Q. Yang, X. Wang, Y.L. Yao, H. Min, Z.M. Lv, *World Journal of Microbiology and Biotechnology*, **2011**, 27, 1633.
22. S.N. Wang, P. Xu, H.Z. Tang, J. Meng, X.L. Liu, J. Huang, H. Chen, Y. Du, H.D. Blankespoor, *Biotechnology Letters*, **2004**, 26, 1493.
23. H.H. Wang, B. Yin, X.X. Peng, J.Y. Wang, Z.H. Xie, J. Gao, X.K. Tang, *Journal of Applied Microbiology*, **2012**, 112, 258.
24. H. Yu, H. Tang, X. Zhu, Y. Li, P. Xu, *Applied and Environmental Microbiology*, **2015**, 81, 272.
25. N. Weyens, D. van der Lelie, T. Artois, K. Smeets, S. Taghavi, L. Newman, R. Carleer, J. Vangronsveld, *Environmental Science Technology*, **2009**, 43, 9413.
26. R.B. Payne, H.D. May, K.R. Sowers, *Environmental Science Technology*, **2011**, 45, 8772.
27. N. Kuburovic, M. Todorovic, V. Raicevic, A. Orlovic, Lj. Jovanovic, J. Nikolic, V. Kuburovic, S. Drmanic, T. Solevic , *Desalination*, **2007**, 213, 123.
28. Z.T. Yu, W.W. Mohn, *Water Res.* **2001**, 35, 883.
29. Z.T. Yu, W.W. Mohn, *Water Res.*, **2002**, 36, 2793.
30. I.P. Thompson, C.J. van der Gast, L. Ceric, A.C. Singer, *Environmental Microbiology*, **2005**, 7, 909.
31. A. Ruan, H. Min, X. Peng, Z. Huang, Z., *Research in Microbiology*, **2005**, 156, 700.
32. Y.P. Wang, J.Y. Shi, H. Wang, Q. Lin, X.C. Chen, Y.X. Chen, *Ecotoxicology and Environmental Safety*, **2007b**, 67, 75.
33. H.Z. Tang, S.N. Wang, L.Y. Ma, X.Z. Meng, Z.X. Deng, D. Zhang, C.Q. Ma, P. Xu, *Applied and Environmental Microbiology*, **2008**, 74, 1567.
34. Y. Teng, Y.M. Luo, M.M. Sun, Z.J. Liu, Z.G. Li, P. Christie, *Bioresource Technology*, **2010**, 101, 3437.
35. E. Goo, C.D. Majerczyk, J.H. An, J.R. Chandler, Y. Seo, H. Ham, J.Y. Lim, H. Kim, B. Lee, M.S. Jang, E.P. Greenberg, I. Hwang, *Proceedings of the National Academy of Sciences of the United States of America*, **2012**, 109, 19775.
36. G.D. Geske, J.C. O'Neill, H.E. Blackwell. *Chemical Society Reviews*, **2008**, 37, 1432.
37. S.E. Darch, S.A. West, K. Winzer, S.P. Diggle, *Proceedings of the National Academy of Sciences of the United States of America*, **2012**, 109, 8259.

38. J.D. Shrout, R. Nerenberg, *Environmental Science and Technology*, **2012**, *46*, 1995.
39. M.B. Miller, B.L. Bassler, *Annual Review of Microbiology*, **2001**, *55*, 165.
40. K. Poole, *Trends in Microbiology*, **2012**, *20*, 227.
41. T.J. Shao, G.Q. Yang, M.Z. Wang, Z.M. Lu, H. Min, L. Zhao, *Ecotoxicology*, **2010**, *19*, 1117.
42. E. Celis, P. Elefsiniotis, N. Singhal, *Water Research*, **2008**, *42*, 3218.
43. Y.Y. Qu, J.T. Zhou, J. Wang, Z.Y. Song, L.L. Xing, X. Fu, *Biodegradation*, **2006**, *17*, 83.
44. M. Wang, G. Yang, H. Min, Z. Lu, X. Jia, *Water Research*, **2009**, *43*, 4187.
45. N. Boon, J. Goris, P. de Vos, W. Verstraete, E.M. Top, *Applied and Environmental Microbiology*, **2000**, *66*, 2906.
46. Y.L. Yao, Z.M. Lv, F.X. Zhu, H. Min, C.M. Bian, *Journal of Hazardous Materials*, **2013**, *261*, 550.
47. G.D. Geske, R.J. Wezeman, A.P. Siegel, H.E. Blackwell, *Journal of the American Chemical Society*, **2005**, *127*, 12762.
48. V. Lazar, *Anaerobic*, **2011**, *17*, 280.
49. B. Vu, M. Chen, R.J. Crawford, E.P. Ivanova, *Molecules*, **2009**, *14*, 2535.
50. G.M. Patriquin, E. Banin, C. Gilmour, R. Tuchman, E.P. Greenberg, K. Poole, *Journal of Bacteriology*, **2008**, *190*, 662.
51. B. Jiang, Y. Liu, *Chemosphere*, **2012**, *88*, 1058.
52. J.T. Byers, C. Lucas, G.P.C. Salmond, M. Welch, *Journal of Bacteriology*, **2002**, *184*, 1163.
53. M.Z. Wang, X. Zheng, K. Zhang, Y.C. Ding, H.Z. He, D.S. Shen, H.J. Feng, *Bioresource Technology*, **2014**, *169*, 229.
54. S.K. Garg, M. Tripathi, S.K. Singh, J.K. Tiwari, *International Biodeterioration and Biodegradation*, **2012**, *74*, 24.
55. K. Zhang, H.-Z. He, D.-S. Shen, X. Zheng, Z. Zhou, X.-J. Tao, M.-Z. Wang, *Journal of Chemistry*, vol. 2014, Art. ID 212596.
56. J.-H Wang, H.-Z. He, M.-Z. Wang, S. Wang, J. Zhang, W. Wei, H.-X. Xu, Z.-M. Lv, D.-S. Shen, *Bioresource Technology*, **2013**, *142*, 445-453
57. X. Quan, H. Tang, W. Xiong, Z. Yang, *Journal of Hazardous Materials*, **2010**, *179*, 1136.
58. J. Song, C. Lays, F. Vandenesch, Y. Benito, M. Bes, Y. Chu, G. Lina, P. Romby, T. Geissmann, S. Boisset, *PLoS One*, 2012, *7*, art. no. e37294.
59. G.Q. Yang, Isolation, identification and nicotine metabolism pathways analysis of two nicotine-degrading bacteria. Zhejiang University, Hangzhou, **2011**
60. S. Yao, J.R. Ni, Q. Chen, A.G.L. Borthwick, *Bioresource Technology*, **2013**, *127*, 151.
61. S. Zhang, A. Li, D. Cui, J.X. Yang, F. Ma, *Bioresource Technology*, **2011**, *102*, 4360.
62. M.M. Zein, M.T. Suidan, A.D. Venosa, *Environmental Science and Technology*, **2004**, *38*, 3449.

DIRECT SENSITIVITY ANALYSIS OF A WHITE WINE ALCOHOLIC FERMENTATION PROCESS

ANCA ȘIPOS^{a,*} and PAUL ȘERBAN AGACHI^b

ABSTRACT. Process engineering became, recently in historical terms, an extension of food engineering principles to other fields of manufacturing as the food biotechnology and beverage industry is. This article proposes a non-linear mathematical model that makes possible the simulation of the batch alcoholic fermentation of white wine. The model was developed on the basis of zone modelling principle, considering the physiological states of the yeast cells. The nonlinear mathematical model led to a good qualitative and quantitative description of the alcoholic fermentation process. The model was implemented as a Matlab S-function and the results were compared with experimental data. Further on, the mathematical model was used for the investigation of the dynamic behaviour of a batch fermentation process through direct sensitivity analysis method (DSA). The DSA of dynamic model allowed the calculus of the matrix of the sensitivity functions in order to determine the influence of the small deviations of initial state and parameters from their nominal values on the state trajectory and system output over the time.

Keywords: *alcoholic fermentation process, nonlinear mathematical model, process simulation, direct sensitivity analysis*

INTRODUCTION

Wine making is a complex ecological and biochemical process involving many interactions such as must variety, microbiota and several operations. It is often controlled empirically and traditionally. There are some factors that strongly affect the alcoholic fermentation. The most important ones are: fermentation temperature, grape juice composition, anaerobic conditions - due to CO₂

^a "Lucian Blaga" University of Sibiu, Faculty of Agricultural Sciences, Food Industry and Environmental Protection, 7-9 dr. Ion Ratiu Street, Sibiu 550012, Romania.

^b "Babes-Bolyai" University of Cluj-Napoca, Faculty of Chemical and Chemical Engineering, 11 Arany Janos Street, Cluj-Napoca 400028, Romania.

* Corresponding author: anca.sipos@ulbsibiu.ro

production, low media pH, sulphur dioxide concentration level, selected yeasts inoculation and interaction with other microorganisms [1]. The models developed for these cases consequently have various domains of applications but none of them include the whole oenological aspects of the process. The majority of the models are of “knowledge-based” models type and they take into consideration a great number of phenomena that have an important effect on the kinetics of the process fermentation [2].

The review [3] presented different approaches that have been taken for “knowledge-based” models, non-physiological mathematical descriptions, behaviour prediction models and empirical models and others authors [4, 5, 6, 7] used a kinetic model that assumes a limited oxidation capacity of yeast, leading to the formation of ethanol under conditions of oxygen limitation and/or high glucose concentration. Therefore they require the estimation of many variables which are often measured with difficulty.

On the other hand, the knowledge-based models inaccurately describe the end kinetics of the fermentation process [8]. In addition, there are other models resulting from the macroscopic analysis of the process fermentation [9, 10]. These models require less estimated variables but their physiological significance is difficult to analyse. These models describe very well the evolution of the main variables specific to the alcoholic fermentation process such as the substrate and alcoholic concentrations [11].

Recently, many studies are focused on models which use artificial intelligence techniques [12, 13] thus having a high capacity of generalization and a good stability. In [14] artificial neural networks are used. In [15] a control system using two feed-forward ANN models is proposed: the first network is incorporated in the hybrid model of the process, providing values for the plant output; the second network performs the task of feedback controller in the form of a plant with inverse plant dynamics. In [16] the neural network is adapted online using only the dissolved oxygen measurement to record varying operating conditions while other states of the system, namely the substrate, ethanol and biomass concentrations are not measured but predicted by the adapted network.

Although real results begin to appear, there is still necessary to validate these models on a wide range of fermentation processes. In other words, a complex data-base containing information about the kinetics of the alcoholic fermentation processes has to be created and used [17] so that the approach of the modelling of these processes through artificial intelligence model-based to be consistent. For these reasons, the modelling, simulation and control of these processes is not a fully solved problem yet and still remains a challenge for the specialists in control and in wine producing technology (question: is it possible to have an overall valid model at all sort of wines?). This paper proposes a general mathematical model of the alcoholic fermentation process. A study regarding

the analysis of this model on the basis of the sensitivities in relation with the initial state and the main parameters is carried out, having the goal of designing and implementing a control strategy of the alcoholic fermentation process [18].

The paper structure is as follows: after a brief introduction, in the second part the present article proposes a non-linear model for white wine alcoholic fermentation process which, besides the detailed kinetic model, involves equations corresponding to the physiological phases of yeast cells, the inhibitory effect of ethanol, heat transfer equations and the dependence of kinetic parameters on temperature. In the third part of the paper the dynamic behaviour of a batch fermentation process using the direct sensitivity analysis (DSA) is investigated. Finally, the last section is dedicated for conclusions.

RESULTS AND DISCUSSION

Result and discussion regarding the mathematical model simulation

The nonlinear mathematical model of the batch fermentation process (Table 1) used in this work contains the following equations:

- an equation for the latent phase of fermentation that describes the dependence of the phase time of the process temperature;
- the model proposed by Aiba [17] for the growing phase with the three equations of biomass, alcohol production and substrate consumption;
- the model presented by Bovée-Strehaino [9] for the decay phase with two equations: one for the substrate consumption and the other for alcohol formation;
- an equation that describes the biomass behaviour along the phase no. 3 (the model proposed by Sipos in [19, 20]);
- an energy-balance model in which the rate of change of the medium's temperature (dT^0/dt) is a result of the balance between the rate of the heat generation due to fermentation and the rate of the heat transfer to the cooling medium inside the bioreactor jacket.

The model proposed by Aiba includes the inhibitory effects of the fermentation product (alcohol). In the growing phase the value of the maximum specific growth rate of the biomass corresponds to the real one. The non-physiological model proposed by Bovée and Strehaino was chosen because it accurately describes the substrate consumption and the evolution of the alcohol concentration in the growing and decay phases. This model proposes the use of a semi empirical model in which the velocity of sugar consumption is described by a chemical law that depends on substrate and product contents. The parameters of the model are adjusted by means of non-linear programming methods, which

compare model predictions with experimental data and minimise errors [19, 20]. The Bovée and Strehaino model is capable of predicting the fermented sugar (and thus thermal planning) within an error of 3.3% [4]. Thus, the model offers a good qualitative and quantitative description of the behaviour of the alcoholic fermentation process.

Figures 1, 2 and 3 show the simulation results of the model presented in Table 1 considering the following initial values: the initial substrate concentration was $210 \text{ g} \cdot \text{L}^{-1}$ and the fermentation temperature was 301K.

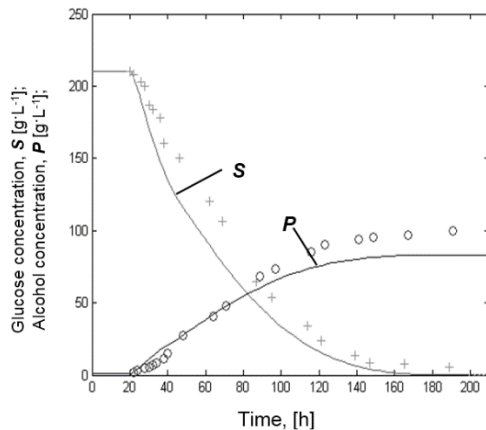


Figure 1. Evolution of glucose and alcohol concentrations; a comparison between experimental values (o - glucose and + - alcohol) and simulation results (continuous lines)

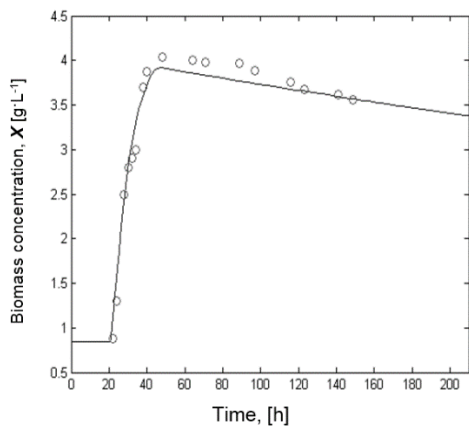


Figure 2. Comparison between the biomass simulation results (continuous line) and experimental data (o)

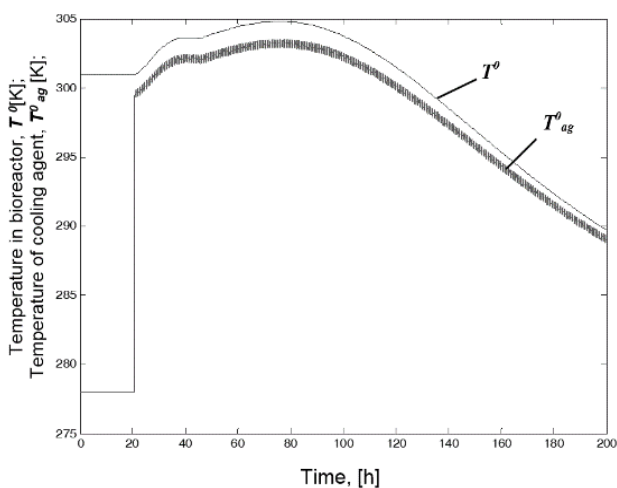


Figure 3. Temperatures of the fermentation medium and cooling agent (simulation results)

The equation of the latent phase is valid for a time interval [0, 100 h] and the model has been tested for a grape juice variety with an initial concentration of the substrate varying between 180 and 210 g·L⁻¹, a fermentation temperature between 299 and 303 K and without aeration.

DSA results and discussion

DSA with respect to the initial state

Figures 4 – 6 present the graphs of the sensitivity functions. Based on these graphs the following remarks can be drawn:

- The substrate consumption, the biomass production and the fermentation temperature present the same sensitivity with respect to the initial concentration variation of the biomass (Figure 4). The influence of this variation is significant throughout the exponential growing phase and then it decreases when the process reaches the decay phase. This influence proves that the substrate consumption depends on both viable biomass concentration and biomass growth rate.

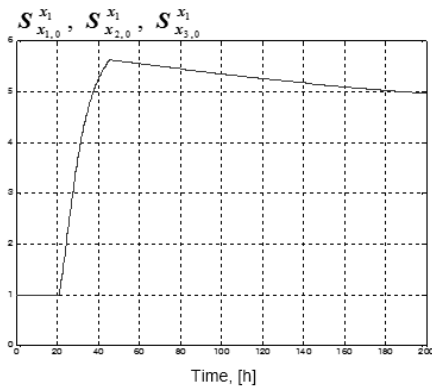


Figure 4. Graphs of the biomass sensitivity functions in relation with the variation of: biomass initial concentration, $S_{x_1,0}^{x_1}$ [(g·L⁻¹ biomass)/(g·L⁻¹ biomass)₀]], substrate initial concentration, $S_{x_2,0}^{x_1}$ [(g·L⁻¹ biomass)/(g·L⁻¹ substrate)₀]] and process initial temperature, $S_{x_3,0}^{x_1}$ [(g·L⁻¹ biomass)/(K)₀]]

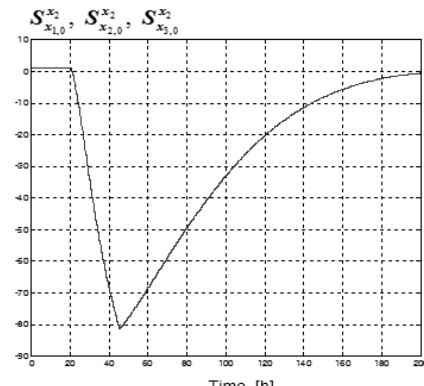


Figure 5. Graphs of the substrate sensitivity functions in relation with the variation of: biomass initial concentration, $S_{x_1,0}^{x_2}$ [(g·L⁻¹ substrate)/(g·L⁻¹ biomass)₀]], substrate initial concentration, $S_{x_2,0}^{x_2}$ [(g·L⁻¹ substrate)/(g·L⁻¹ substrate)₀]] and process initial temperature, $S_{x_3,0}^{x_2}$ [(g·L⁻¹ substrate)/(K)₀]]

- The change of the initial concentration of the substrate in relation with the three variables (substrate, biomass and fermentation temperature) reaches a maximum (negative) at the end of exponential growing phase (Figure 5). The influence exists only in this phase which is the most important one in fermentation.

The initial concentration of the substrate has a strong influence in the exponential growing phase which may lead to a modification of the fermentation duration with all the consequences that may occur. A short duration leads to a tumultuous fermentation, because the initial concentration of substrate is too lower or not all substrate is metabolized wholly through fermentation or the alcohol production rate is too high and has an inhibitory effect on the biomass development. A long duration leads to a slow fermentation, with lower alcohol concentration at the end.

- The change of the initial temperature of the fermentation over the substrate, biomass and temperature inside the bioreactor presents a positive maximum at the beginning of the exponential growing phase and after that decreases in time. The possibility that the fermentation duration may be changed is once again confirmed and so the consequences that can appear.

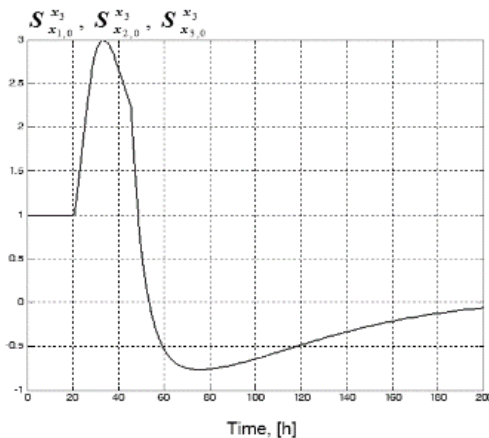


Figure 6. Graphs of the process initial temperature sensitivity functions in relation with the variation of: biomass initial concentration, $S_{x_1,0}^{x_3}$ $[(K)/(g \cdot L^{-1} \text{ biomass})_0]$, substrate initial concentration, $S_{x_2,0}^{x_3}$ $[(K)/(g \cdot L^{-1} \text{ substrate})_0]$ and process initial temperature, $S_{x_3,0}^{x_3}$ $[(K)/(K)_0]$

DSA with respect to the parameters of the mathematical model

The parameters' sensitivity (Figures 7–9) highlights that the process kinetics (substrate consumption, biomass production and fermentation temperature) is strongly influenced by the modification of the two kinetics parameters (A and E_a), whose values are frequently determined with uncertain precision. The alcoholic batch fermentation of white wine being a process controlled by temperature, the heat transfer area modification lead to changes in the fermentation conditions and, as a consequence, these can affect the process duration and the wine quality and characteristics.

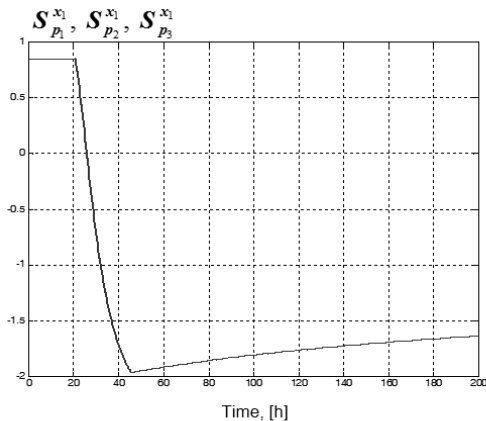


Figure 7. Graphs of the biomass sensitivity functions in relation with the variation of parameters:
 $S_{p_1}^{x_1}$ [(g·L⁻¹ biomass)/(h⁻¹)], $S_{p_2}^{x_1}$ [(g·L⁻¹ biomass)/(K)]
 and $S_{p_3}^{x_1}$ [(g·L⁻¹ biomass)/(m²)]

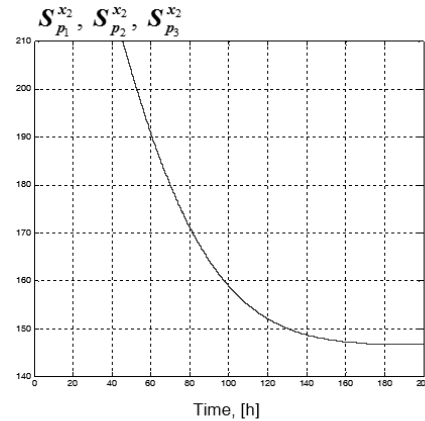


Figure 8. Graphs of the substrate sensitivity functions in relation with the variation of parameters:
 $S_{p_1}^{x_2}$ [(g·L⁻¹ substrate)/(h⁻¹)], $S_{p_2}^{x_2}$ [(g·L⁻¹ substrate)/(K)]
 and $S_{p_3}^{x_2}$ [(g·L⁻¹ substrate)/(m²)]

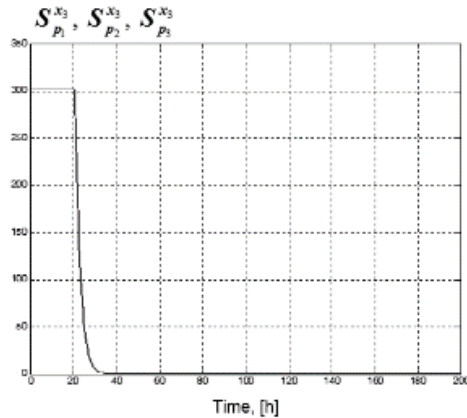


Figure 9. Graphs of the process initial temperature sensitivity functions in relation with the variation of parameters: $S_{p_1}^{x_3}$ [(K)/(h⁻¹)], $S_{p_2}^{x_3}$ [(K)/(K)] and $S_{p_3}^{x_3}$ [(K)/(m²)]

CONCLUSIONS

The dynamic model presented in this paper enables the prediction of the evolutions and final concentrations of biomass, alcohol and substrate during a batch alcoholic fermentation. The model involves equations corresponding to the physiological phases of yeast cells, the inhibitory effect of ethanol, heat transfer equations and the dependence of kinetic parameters on temperature.

The model was validated through four experiments considering two different temperatures and two different initial concentrations of substrate for the same must. So, by this general model, the possibility to simulate real, oenological aspects that can appear during the alcoholic fermentation process it was obtained. Also, based on this model, the direct sensitivity analysis was realized. The sensitivity functions matrix calculated with DSA allowed mono and multivariable estimation of the influences of input variables and parameters. Considering the DSA it were proved that the initial concentrations of the biomass, the changes of the initial concentration of the substrate and initial values of temperature have a strong influence in the exponential growing phase, which is the most important one in fermentation because the maximum growth rate of the selected strain depends on operating conditions which must be known exactly.

The parameters' sensitivity analysis pinpointed the process' kinetics aspects as are the strongly influences of the fermentation process by the modification of the two kinetics parameters (the pre-exponential factors in Arrhenius' equation and the activation energies), whose values are frequently determined with uncertain precision.

The results obtained in this study will allow the possibility to develop state observers (substrate, biomass and product concentrations) using temperature measurements and to design an appropriate control system.

EXPERIMENTAL

The article proposes a complex nonlinear wine fermentation model based on previous researches of the authors [19, 20] followed by a sensitivity analysis designed to develop state observers (substrate, biomass and product concentrations) using only temperature measurements and to configure the control scheme of the process.

Experimental conditions

To evaluate the total fermentation yield losses under different operating conditions, four experiments were carried out and based on the data obtained within these experiments, a mathematical model was proposed. The strain and the culture medium, the equipment and the experimental conditions together with the measurements of the fermentation parameters were presented by Sipos and co-workers [19, 20]. For the experiments the *Saccharomyces cerevisiae* YEPD wine yeast was used, being seeded on a culture medium with the following composition: $5 \text{ g}\cdot\text{L}^{-1}$ KH_2PO_4 , $2 \text{ g}\cdot\text{L}^{-1}$ $(\text{NH}_4)_2\text{SO}_4$, $0.4 \text{ g}\cdot\text{L}^{-1}$ $(\text{MgSO}_4)\cdot 7\text{H}_2\text{O}$, $1 \text{ g}\cdot\text{L}^{-1}$ yeast extract, $50 \text{ g}\cdot\text{L}^{-1}$ glucose and Mauzac must (sterilized through flash pasteurization). The sugar content of the grape must was supplemented with sucrose up to $180 \text{ g}\cdot\text{L}^{-1}$ and $40 \text{ mL}\cdot\text{h}^{-1}\cdot\text{L}^{-1}$ tiaminol were added. The SO_2 content

reached $50 \text{ mg}\cdot\text{L}^{-1}$ and the pH was adjusted at $3.8 \text{ mg}\cdot\text{L}^{-1} \text{ H}_3\text{PO}_4$. Both the fermentation medium and the bioreactor were autoclaved for 20 minutes at 393 K. A New-Brunswick continuously stirred bioreactor equipped with pH and temperature sensors was used.

The following operating conditions were:

- Working volume – 8 L;
- Temperature – 291 K and 301 K;
- Stirring speed – 150 rpm;
- pH – 3.8;
- Influent glucose concentrations – $180 \text{ g}\cdot\text{L}^{-1}$ and $210 \text{ g}\cdot\text{L}^{-1}$;
- Without aeration, the necessary oxygen was dissolved in must.

The mathematical model

The mathematical model of the alcoholic fermentation process was determined on the basis of the approach of the zone modelling principle, taking into consideration the evolution of the viable biomass ($X_v(t)$). Based on the analysis of the phenomenological aspects of the alcoholic fermentation process, the evolution of $X_v(t)$ was divided in three parts (Figure 10) as follows:

- latent phase (1);
- growing phase (2);
- decay phase (3).

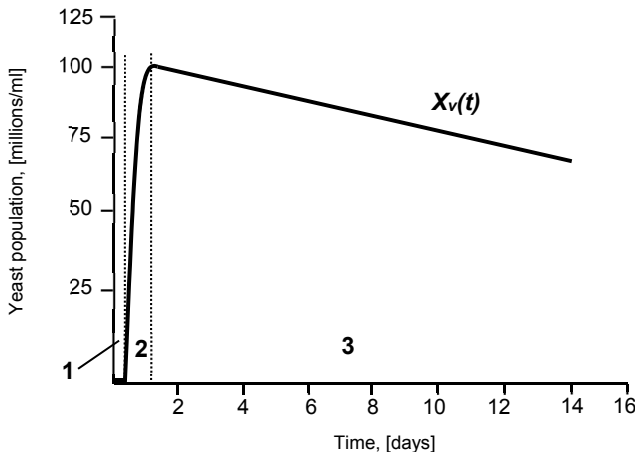


Figure 10. Evolution of the viable biomass concentration $X_v(t)$

Table 1 presents the equations of the model. The parameters are adjusted through the non-linear programming method, which compares the model predictions with experimental data and minimises the errors.

Table 1. The model of the alcoholic fermentation process

Current phase	Model equations
Kinetic model	
Latent phase [19, 20] $t_{lat} = \frac{a}{T^0} + b$	- biomass: $\frac{dX}{dt} = \mu_{max} \cdot \left(\frac{S}{K_s + S} \right) \cdot e^{-K_p \cdot P} \cdot X ;$
Exponential growing phase [17]	$\mu_{max} = A_1 \cdot e^{\frac{E_a_1}{R \cdot T^0}} - A_2 \cdot e^{\frac{E_a_2}{R \cdot T^0}}$ - alcohol: $\frac{dP}{dt} = q_{pmax} \cdot \left(\frac{S}{K_{sp} + S} \right) \cdot e^{-K_{pp} \cdot P} \cdot X$ - substrate: $\frac{dS}{dt} = -\left(\frac{1}{Y_{xs}} \cdot \frac{dX}{dt} \right) - \left(\frac{1}{Y_{ps}} \cdot \frac{dP}{dt} \right)$
Decay phase [9, 19, 20]	- biomass: $\frac{dX}{dt} = f \cdot X \cdot k ; k = A \cdot e^{\frac{E_a}{R \cdot T^0}}$ - alcohol: $P = P_0 + \eta \cdot (S_0 - S)$ - substrate: $\frac{dS}{dt} = -k \cdot S^\alpha \cdot P^\beta$
Energetic model	
All phases [18, 19]	- for the bioreactor: $\frac{\Delta H_r \cdot \frac{dS}{dt}}{\rho \cdot c_p} - \frac{K_r \cdot A_r}{V \cdot \rho \cdot c_p} (T^0 - T_{ag}^0) = \frac{dT^0}{dt}$ - for the bioreactor's jacket: $\frac{F_{ag}}{V_{ag}} (T_{agi}^0 - T_{ag}^0) + \frac{K_r A_r}{V_{ag} \cdot \rho_{ag} \cdot c_{pag}} (T^0 - T_{ag}^0) = \frac{dT_{ag}^0}{dt}$

Tables 2 and 3 present the list of the variables and parameters of the mathematical model.

Table 2. Variables and parameters of the kinetic model

X	Biomass concentration	$\text{g} \cdot \text{L}^{-1}$
S	Substrate concentration	$\text{g} \cdot \text{L}^{-1}$
P	Alcohol concentration	$\text{g} \cdot \text{L}^{-1}$
k	Kinetic constant	h^{-1}
A	Pre-exponential factor in Arrhenius' equation	148 (calculated using experimental data)
		h^{-1}

DIRECT SENSITIVITY ANALYSIS OF A WHITE WINE ALCOHOLIC FERMENTATION PROCESS

E_a	Activation energy	21424 (calculated using experimental data)	J·mol ⁻¹
A_1	Pre-exponential factor in Arrhenius' equation	9.5 *10 ⁸ ^a	h ⁻¹
E_{a1}	Activation energy	55000 ^a	J·mol ⁻¹
A_2	Pre-exponential factor in Arrhenius' equation	2.55*10 ³³	h ⁻¹
E_{a2}	Activation energy	220000 ^a	J·mol ⁻¹
R	Universal gas constant	8.31	J·mol ⁻¹ K ⁻¹
T^0	Temperature in bioreactor	291 and 301	K
K_s	Substrate limitation constant	0.2 ^a	g·L ⁻¹
d	Pseudo-constant of the biomass	1.67 (calculated using experimental data)	
f	Pseudo-constant of the biomass	0.34	
α	Pseudo-order of the substrate	0.69 ^b	
β	Pseudo-order of the alcohol	0.32 ^b	
η	Efficiency in alcohol of fermentation reaction	48 ^b	%
S_0	Steady-state operation point of substrate	180	g·L ⁻¹
P_0	Steady-state operation point of alcohol	0	g·L ⁻¹
t	Time		h
μ_{max}	Maximum specific growth rate		h ⁻¹
K_P	Alcohol limitation constant	0.14 ^c	g·L ⁻¹
q_{pmax}	Maximum specific alcohol production rate	1.02 ^c	g·g ⁻¹ ·cells ⁻¹ ·h ⁻¹
K_{SP}	Constant in the substrate term for ethanol production	1.68 ^c	g·L ⁻¹
K_{PP}	Constant of fermentation inhibition by ethanol	0.07 ^d	g·L ⁻¹
Y_{XS}	Ratio of cell produced per glucose consumed for growth	0.607 ^d	g·g ⁻¹
Y_{PS}	Ratio of ethanol produced per glucose consumed for fermentation	0.435 ^c	g·g ⁻¹

^a [21, 22, 23], ^b[9], ^c [10], ^d [24]

Table 3. Parameters of the kinetic model

K_T	Heat transfer coefficient	3.6.10 ⁵ ^a	J·m ⁻² K ⁻¹ h ⁻¹
A_T	Heat transfer area	0.8 ^b	m ²
F_{ag}	Flow of cooling agent	0.01 ^b	m ³ ·h ⁻¹
V_{ag}	Volume of the jacket	0.2 ^b	m ³
V	Volume of the mass of reaction	1 ^b	m ³
T_{agi}^0	Temperature of cooling agent entering to the jacket	278 ^b	K
ΔH_r	Reaction heat of fermentation	-98465 ^c	J·mol ⁻¹
ρ	Density of the mass of reaction	1100 ^b	kg·m ⁻³
ρ_{ag}	Density of cooling agent	999.8 ^a	kg·m ⁻³
C_p	Heat capacity of mass of reaction	3391 ^b	J·kg ⁻¹ K ⁻¹
C_{pag}	Heat capacity of cooling agent	4217 ^a	J·kg ⁻¹ K ⁻¹
T_{ag}^0	Temperature of cooling agent in the jacket		K

^a [25], ^b experimental data, ^c [26]

The state vector is given by eq. (1)

$$\mathbf{x} = \begin{pmatrix} \mathbf{X} \\ \mathbf{S} \\ \mathbf{T}^0 \end{pmatrix} = \begin{pmatrix} \mathbf{x}_1 \\ \mathbf{x}_2 \\ \mathbf{x}_3 \end{pmatrix} \quad (1)$$

where \mathbf{S} represents the substrate concentration, \mathbf{X} - the biomass concentration and \mathbf{T}^0 - the temperature inside the bioreactor. The state vector of the process is extended with other two state variables: the concentration of the metabolism product (\mathbf{P}), noted with \mathbf{x}_4 and the temperature of the cooling agent inside the jacket, \mathbf{T}_{ag}^0 , noted with \mathbf{x}_5 . It has to be mentioned that for the last two state variables the DSA method was not applied.

The flow of the cooling agent (F_{ag}) is considered the control variable: $u_1 = F_{ag}$. The parameters of the mathematical model are the following: the pre-exponential factors in Arrhenius' equation (\mathbf{A} and \mathbf{A}_1), the ratios between the activation energy and the universal gas constant ($\frac{E_a}{R}$ and $\frac{E_{a1}}{R}$) as kinetics characteristics and the heat transfer area (A_T) as a design characteristic. The parameters' vector is as follows:

- for the exponential growing phase

$$\mathbf{p} = \begin{pmatrix} \mathbf{A}_1 \\ \frac{E_{a1}}{R} \\ \mathbf{A}_T \end{pmatrix} = \begin{pmatrix} \mathbf{p}_1 \\ \mathbf{p}_2 \\ \mathbf{p}_3 \end{pmatrix} \quad (2)$$

- for the decay phase

$$\mathbf{p} = \begin{pmatrix} \mathbf{A} \\ \frac{E_a}{R} \\ \mathbf{A}_T \end{pmatrix} = \begin{pmatrix} \mathbf{p}_1 \\ \mathbf{p}_2 \\ \mathbf{p}_3 \end{pmatrix} \quad (3)$$

Considering the notations from eqs. (1), (2) and (3) the mathematical model presented in Table 1 has been transformed, as shown in Table 4.

Table 4. The state space mathematical model of the alcoholic fermentation process

Current phase	Equations
Kinetic model	
Latent phase	$t = \frac{a}{x_3} + b$
Exponential growing phase	- biomass: $\mu_{max} = p_1 \cdot e^{-\frac{p_2}{T^0}} - A_2 \cdot e^{-\frac{E_{a2}}{R T^0}}$

Current phase	Equations
	$\frac{dx_1}{dt} = \mu_{\max} \cdot \left(\frac{x_2}{K_s + x_2} \right) \cdot e^{-K_p \cdot x_4} \cdot x_1$ <p>- alcohol: $\frac{dx_4}{dt} = q_{p\max} \cdot \left(\frac{x_2}{K_{sp} + x_2} \right) \cdot e^{-K_{pp} \cdot x_4} \cdot x_1$</p> <p>- substrate: $\frac{dx_2}{dt} = - \left(\frac{1}{Y_{xs}} \cdot \frac{dx_1}{dt} \right) - \left(\frac{1}{Y_{ps}} \cdot \frac{dx_4}{dt} \right)$</p>
Decay phase	<p>- biomass: $\frac{dx_1}{dt} = f \cdot x_1 \cdot p_1 \cdot e^{\frac{p_2}{x_3}}$</p> <p>- alcohol: $\frac{dx_4}{dt} = -\eta \cdot \frac{dx_2}{dt}$</p> <p>- substrate: $\frac{dx_2}{dt} = -p_1 \cdot e^{\frac{-p_2}{x_3}} \cdot x_2^\alpha \cdot x_4^\beta$</p>
Energetic model	
All phases	<p>- for bioreactor: $\frac{dx_3}{dt} = 5.54 \cdot \frac{\Delta H_r \cdot \frac{dx_2}{dt}}{\rho \cdot c_p} - \frac{K_r \cdot p_3}{V \cdot \rho \cdot c_p} \cdot (x_3 - x_5)$</p> <p>- for the bioreactor's jacket:</p> $\frac{dx_5}{dt} = \frac{u}{V_{ag}} \cdot (T_{agi}^0 - x_5) + \frac{K_r \cdot p_3}{V_{ag} \cdot \rho_{ag} \cdot c_{pag}} \cdot (x_3 - x_5)$

The following initial conditions have been taken into consideration for the simulation of the mathematical model:

$$x_0 = \begin{pmatrix} x_{1,0} \\ x_{2,0} \\ x_{3,0} \end{pmatrix} = \begin{pmatrix} X_0 \\ S_0 \\ T_i^0 \end{pmatrix} \quad (4)$$

Direct sensitivity analysis (DSA)

The analysis of the dynamic system, based on the aforementioned mathematical model, was carried out using DSA. As it has been specified before, the main purpose of the DSA is the study of how the variation in the inputs of a model (biomass, substrate concentrations and temperature) can be apportioned, qualitatively or quantitatively, to different sources of variation.

Direct sensitivity analysis in relation with the initial state

The sensitivities' matrix in relation with the initial state, $S_{x_0}^x(t, t_0)$, is defined by the relation (5) as mentioned in [18]:

$$S_{x_0}^x(t, t_0) = \left\{ \lim_{\Delta x_{j,0} \rightarrow 0} \frac{\Delta_{j,0} \mathbf{x}_i(t)}{\Delta x_{j,0}} \right\}_{\substack{i=1, \dots, n \\ j=1, \dots, n}} = \left\{ \frac{\partial \mathbf{x}_i}{\partial x_{j,0}} \right\}_{\substack{i=1, \dots, n \\ j=1, \dots, n}} \quad (5)$$

The eq. (5) is equivalent with eq. (6)

$$\Delta_{x_0} \mathbf{x}(t) = S_{x_0}^x(t, t_0) \Delta x_0 \quad (6)$$

The state vector's variation, $\Delta_{x_0} \mathbf{x}(t)$ corresponding to a Δx_0 variation of the initial state vector, satisfies the differential equation:

$$\dot{\Delta}_{x_0} \mathbf{x}(t) = f_x(\mathbf{x}(t), p) \Delta_{x_0} \mathbf{x}(t) \quad (7)$$

where $f_x(\mathbf{x}(t), p)$ is the Jacobean matrix and p – the parameters' vector (in this case they are constant). In eq. (6) it can be noticed that $S_{x_0}^x(t, t_0)$ is the transition matrix of the states. This matrix represents the solution of the sensitivity differential equation:

$$\dot{S}_{x_0}^x(t, t_0) = f_x(\mathbf{x}(t), p) S_{x_0}^x(t, t_0) \quad (8)$$

Table 5 presents the elements of the Jacobian matrix, f_x , for the sensitivity analysis in relation with the initial state.

Table 5. Jacobian matrix for the sensitivity analysis
in relation with the initial state

Current phase	Equations
Kinetic model	
Exponential phase	$f_{x_{1,1}} = \mu_{\max} \cdot \left(\frac{\mathbf{x}_2}{K_s + \mathbf{x}_2} \right) \cdot e^{-K_p \cdot x_4}; f_{x_{1,2}} = \mu_{\max} \cdot \left[\frac{K_s}{(K_s + \mathbf{x}_2)^2} \right] \cdot e^{-K_p \cdot x_4} \cdot \mathbf{x}_1$ $f_{x_{1,3}} = \left(p_1 \cdot p_2 \cdot e^{-\frac{p_2}{x_3}} - A_2 \cdot \frac{E_{a1}}{R} \cdot e^{-\frac{E_{a1}}{R \cdot x_3}} \right) \cdot \mathbf{x}_1 \cdot \frac{1}{\mathbf{x}_3^2} \cdot \frac{\mathbf{x}_2}{K_s + \mathbf{x}_2} \cdot e^{-K_p \cdot x_4}$ $f_{x_{2,1}} = -\frac{1}{Y_{xs}} \cdot \mu_{\max} \cdot \left(\frac{\mathbf{x}_2}{K_s + \mathbf{x}_2} \right) \cdot e^{-K_p \cdot x_4} - \frac{1}{Y_{ps}} \cdot q_{p \max} \cdot \left(\frac{\mathbf{x}_2}{K_{ps} + \mathbf{x}_2} \right) \cdot e^{-K_{pp} \cdot x_4}$

Current phase	Equations
	$\mathbf{f}_{x_2,2} = -\frac{1}{Y_{xs}} \cdot \mu_{max} \cdot \left[\frac{\mathbf{K}_s}{(\mathbf{K}_s + \mathbf{x}_2)^2} \right] \cdot e^{-K_p \cdot x_4} \cdot \mathbf{x}_1 - \frac{1}{Y_{ps}} \cdot q_{pmax} \cdot \left[\frac{\mathbf{K}_{ps}}{(\mathbf{K}_{ps} + \mathbf{x}_2)^2} \right] \cdot e^{-K_{pp} \cdot x_4} \cdot \mathbf{x}_1$ $\mathbf{f}_{x_2,3} = 0; \mathbf{f}_{x_3,1} = 5.54 \cdot \frac{\Delta H_r}{\rho \cdot c_p} \cdot \mathbf{f}_{x_2,1}; \mathbf{f}_{x_3,2} = 5.54 \cdot \frac{\Delta H_r}{\rho \cdot c_p} \cdot \mathbf{f}_{x_2,2};$ $\mathbf{f}_{x_3,3} = -\frac{\mathbf{K}_T \cdot p_3}{V \cdot \rho \cdot c_p}$
	$\mathbf{f}_{x_1,1} = \mathbf{f} \cdot \mathbf{p}_1 \cdot e^{-\frac{p_2}{x_3}}; \mathbf{f}_{x_1,2} = 0; \mathbf{f}_{x_1,3} = \mathbf{f} \cdot \mathbf{x}_1 \cdot \mathbf{p}_1 \cdot \frac{p_2}{x_3^2} \cdot e^{-\frac{p_2}{x_3}}$ $\mathbf{f}_{x_2,1} = 0; \mathbf{f}_{x_2,2} = -k \cdot \alpha \cdot x_2^{\alpha-1} \cdot x_4^\beta;$
Decay phase	$\mathbf{f}_{x_2,3} = -\mathbf{p}_1 \cdot \frac{p_2}{x_3^2} \cdot e^{-\frac{p_2}{x_3}} \cdot x_2^\alpha \cdot x_4^\beta; \mathbf{f}_{x_3,1} = 0; \mathbf{f}_{x_3,2} = 5.54 \cdot \frac{\Delta H_r}{\rho \cdot c_p} \cdot \mathbf{f}_{x_2,2};$ $\mathbf{f}_{x_3,3} = 5.54 \cdot \frac{\Delta H_r}{\rho \cdot c_p} \cdot \mathbf{f}_{x_2,3} - \frac{\mathbf{K}_T \cdot p_3}{V \cdot \rho \cdot c_p}$

Direct sensitivity analysis in relation with the parameters

The sensitivities' matrix in relation with the parameters, $S_p^x(t, t_0)$, is defined by the eq. (9) as mentioned in [18]:

$$S_p^x(t, t_0) = \left\{ \lim_{\Delta p_j \rightarrow 0} \frac{\Delta_{p_j} x_i(t)}{\Delta p_j} \right\}_{\substack{i=1, n \\ j=1, n}} = \left\{ \frac{\partial x_i}{\partial p_j} \right\}_{\substack{i=1, n \\ j=1, n}} \quad (9)$$

It is equivalent with eq. (10)

$$\Delta_p x(t) = S_p^x(t, t_0) \Delta p \quad (10)$$

The sensitivity's differential equation is the following:

$$\dot{S}_p^x(t, t_0) = f_p(x(t), p) S_p^x(t, t_0) \quad (11)$$

Table 6 presents the elements of the Jacobian matrix, \mathbf{f}_x , for the sensitivity analysis in relation with the model parameters.

Table 6. The equations of the Jacobean matrix, \mathbf{f}_x , for the sensitivity analysis of the process state in relation with the time-invariant parameters

Current phase	Equations
Kinetic model	
Exponential phase	$\mathbf{f}_{x_1,1} = e^{\frac{-p_2}{x_3}} \cdot \frac{\mathbf{x}_2}{K_s + \mathbf{x}_2} \cdot e^{-K_p \cdot x_4} \cdot \mathbf{x}_1 \quad \mathbf{f}_{x_1,2} = -p_1 \cdot \frac{\mathbf{x}_1}{x_3} \cdot e^{\frac{-p_2}{x_3}} \cdot \frac{\mathbf{x}_2}{K_s + \mathbf{x}_2} \cdot e^{-K_p \cdot x_4};$ $\mathbf{f}_{x_1,3} = 0; \mathbf{f}_{x_2,1} = 0; \mathbf{f}_{x_2,2} = 0; \mathbf{f}_{x_2,3} = 0; \mathbf{f}_{x_3,1} = 0; \mathbf{f}_{x_3,2} = 0;$ $\mathbf{f}_{x_3,3} = -\frac{K_r}{V \cdot \rho \cdot c_p} \cdot (\mathbf{x}_3 - \mathbf{x}_5)$
Decay phase	$\mathbf{f}_{x_1,1} = \mathbf{f} \cdot \mathbf{x}_1 \cdot e^{\frac{-p_2}{x_3}}; \mathbf{f}_{x_1,2} = -\mathbf{f} \cdot \mathbf{x}_1 \cdot \frac{p_1}{x_3} \cdot e^{\frac{-p_2}{x_3}}; \mathbf{f}_{x_1,3} = 0$ $\mathbf{f}_{x_2,1} = -e^{\frac{-p_2}{x_3}} \cdot \mathbf{x}_2^\alpha \cdot \mathbf{x}_4^\beta; \mathbf{f}_{x_2,2} = -\frac{p_1}{x_3} \cdot e^{\frac{-p_2}{x_3}} \cdot \mathbf{x}_2^\alpha \cdot \mathbf{x}_4^\beta; \mathbf{f}_{x_2,3} = 0;$ $\mathbf{f}_{x_3,1} = 5.54 \cdot \frac{\Delta H_r}{\rho \cdot c_p} \cdot \mathbf{f}_{x_2,1}; \mathbf{f}_{x_3,2} = 5.54 \cdot \frac{\Delta H_r}{\rho \cdot c_p} \cdot \mathbf{f}_{x_2,2};$ $\mathbf{f}_{x_3,3} = -\frac{K_r}{V \cdot \rho \cdot c_p} \cdot (\mathbf{x}_3 - \mathbf{x}_5)$

REFERENCES

- [1] P. Ribereau-Gayon, D. Dubourdieu, B. Doneche, A. Lonvaud, "Handbook of Enology. The Microbiology of Wine and Vinifications", vol. I, Wiley. West Sussex, England, **2000**.
- [2] C. Svendsen, T. Skov, F.W. J. van den Berg, *Journal of Chemical Technology and Biotechnology*, **2015**, 90, 244.
- [3] Y.C. Chung, I.L. Chien, D.M. Chang, *Journal of Process Control*, **2006**, 16, 9. <http://dx.doi.org/10.1016/j.jprocont.2005.05.003>.
- [4] M. Remedios, *American Journal of Enology and Viticulture*, **1999**, 50(2), 166.
- [5] F. Renard, A. Vande Wouwer, *Computers & Chemical Engineering*, **2007**, 2(6), 1238. <http://dx.doi.org/10.1016/j.compchemeng.2007.05.008>.
- [6] G. Szederkenyi, N.R. Kristensen, K.M. Hangos, S. Bay Jorgensen, *Journal of Computers & Chemical Engineering*, **2002**, 26, 659.
- [7] Y. Zhang, M.A. Henson, Y.G. Kevrekidis, *Chemical Engineering Science*, **2003**, 58, 429.
- [8] C. Flanzy, "Œnologie-fondements scientifiques et techniques", Technique & Documentation, Paris, **1998**, 465.

- [9] J.P. Bovée, P. Strehaiano, G. Goma, Y. Sevely, *Biotechnoly and Bioengineering*, **1984**, 26, 328.
- [10] L. Dengfeng, X. Ling, X. Weili, Z. Hong-Tao, L. Chi-Chung, J. Lihua, X. Baoguo, *Hindawi Publishing Corporation, Mathematical Problems in Engineering*, **2014**, Article ID 289492, <http://dx.doi.org/10.1155/2014/289492>.
- [11] S.C. de Oliveira, H.F. de Castro, A.E.S. Visconti, R. Giudici, *Bioprocess and Biosystems Engineering Journal*, **2015**, 38, 469, DOI 10.1007/s00449-014-1286-2.
- [12] C. Karakuzu, M. Turker, S. Ozturk, *Control Engineering Practice*, **2006**, 14(8), 959.
- [13] J.R. Banga, E. Balsa-Canto, C.G. Moles, A. Alonso, *Food Science and Technology International*, **2003**, 14, 131.
- [14] S. Vlassides, J.G. Ferrier, D.E. Block, *Biotechnoly and Bioengineering*, **2001**, 73/1, 55.
- [15] A. Andrásik, A. Mészáros, S.F. De Azevedo, *Computers & Chemical Engineering*, **2004**, 28, 1499.
- [16] K.G. Gadkar, S. Mehra, J. Gomes, *Computers & Chemical Engineering*, **2005**, 29, 1047.
- [17] S. Caraman, E. Ceangă, L. Frângu, G. Mencinicopschi, "Modelarea și conducederea proceselor biotecnologice (The modelling and control of biotechnological processes)", Editura Didactică și Pedagogică, Bucharest, **2002**.
- [18] S. Ungureanu, "Sensibilitatea sistemelor dinamice (cu aplicații în industria și Ingineria chimică). (The dynamic systems sensitivity (with applications in industry and chemical engineering))", Editura Tehnică, Bucharest, **1988**.
- [19] A. Sipos, X.M. Meyer, P. Strehaiano, *Acta Alimentaria Hungarica*, **2007**, 36, 429.
- [20] A. Șipoș, A. Imre-Lucaci, *Studia Universitatis Babeș-Bolyai Chemia*, **2014**, 3, 17.
- [21] M. Krothapally, S. Palanki, *ISA Transactions*, **1999**, 38, 383.
- [22] S. Valentinnotti, B. Srinivasan, U. Holmberg, D. Bonvin, C. Cannizzaro, M. Rhiel, U. von Stockar, *Control Engineering Practice*, **2003**, 11, 665.
- [23] F. Lei, M. Rotboll, S.B. Jorgensen, *Journal of Biotechnology*, **2001**, 88, 205.
- [24] L.S. Ferreira, M.B. De Souza Jr., R.O.M. Folly, *Sensors and Actuators B*, **2001**, 75, 166.
- [25] M.A.J. Torija, N. Rozès, M. Poblet, J.M. Guillamón, A. Mas, *International Journal of Food Microbiology*, **2003**, 80, 47.
- [26] A.C. Costa, D.I.P. Atala, F. Maugeri, R. Maciel, *Process Biochemistry*, **2001**, 37, 125.

SENSITIVITY ANALYSIS USING ADM1 MODEL FOR BIOGAS PRODUCTION

ABHILASH NAIR^a, ALEXANDRINA ZUZA^{a*}, PAUL-ȘERBAN AGACHI^a,
ARPITA DAS^a, MARIUS BREHAR^b, GYŐZŐ FERENCZ BARABÁS^c

ABSTRACT. This study is aimed for a sensitivity analysis to understand the effects of various stoichiometric and kinetic parameters, input composition, carbon and nitrogen composition in the Anaerobic Digestion Model No. 1 (ADM1). The ADM1 has been modified based on the design parameters and process conditions from Cluj-Napoca WWTP. It has to be further calibrated to simulate the steady-state anaerobic digestion of activated sludge at municipal wastewater. For this purpose, it is extremely important to understand the effect of various model parameters on the output variables. The modified model is able to predict the output with 2% error in biogas flow rate and 10% error in the digester pressure. The sensitivity analysis performed identifies the parameters that have a major impact over the output. This report also presents a list of parameters that have to be modified to calibrate the ADM1 model.

Keywords: *ADM1, WWTP, activated sludge, sensitivity analysis, simulation, calibration*

INTRODUCTION

Anaerobic processes have been widely used for the treatment of municipal and industrial wastewater through the fermentation of activated sludge, particularly in Europe [1]. The ADM1 structured model initially includes multiple steps describing complex biochemical and physico-chemical processes. The biochemical steps include breakdown from homogeneous particulates to carbohydrates (CHO), proteins (PRO) and lipids (LIP); extracellular hydrolysis of these particulate substrates to sugars, amino acids (AA), and long chain fatty acids (LCFA),

^a Faculty of Chemistry and Chemical Engineering, Babes-Bolyai University of Cluj-Napoca

^b Waste Water Treatment Plant Cluj-Napoca

^c Waste Water Treatment Plant Budapest

* Corresponding author: alexandrinazuza@chem.ubbcluj.ro

respectively; acidogenesis from monosaccharides (MS) and amino acids (AA) to volatile fatty acids (VFAs): propionic (HPr), butyric (HBu) and valeric acid (HVa) along with H₂; acetogenesis of LCFA and VFAs to acetate (C₂H₃O₂⁻); and separate methanogenesis steps from C₂H₃O₂⁻ to H₂ and CO₂ into CH₄ (Figure 1). These complex bio-chemical and physico-chemical reactions are implemented mathematically to analyze the amount of methane that can be generated from anaerobic digestion. There is also a need to analyze how much of the energy content in the produced methane could be used to generate heat and electricity.

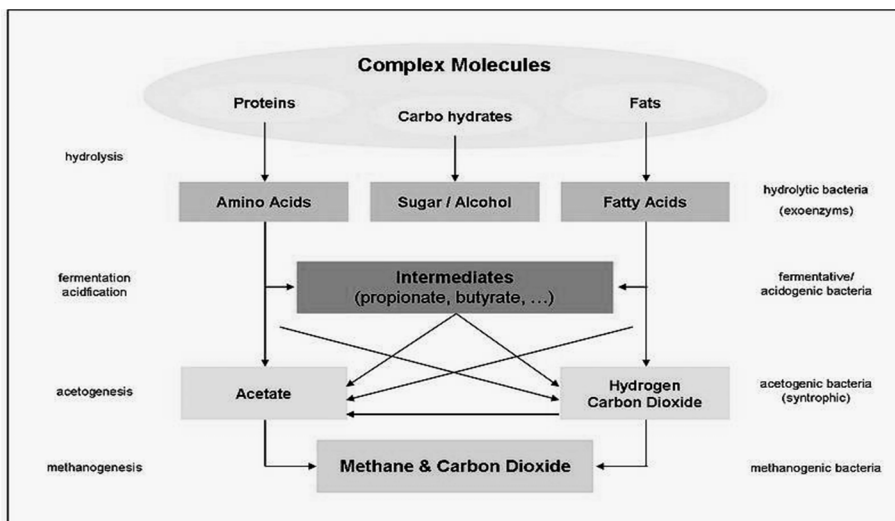


Figure 1. Anaerobic digestion conversion processes [2]

The ADM1 [3] has been used for the mathematical simulation of the fermentation of different substrates [4]. Since its development in 2002 and up to now the ADM1 has been tested and used on different substrates where a great number of research works are reported in the literature. Amongst others, investigations were done on mathematical simulation of special substrates of international interest, like starch [5], blackwater [6] or olive pulp [7]. Boubaker and Cheikh Ridha [8] investigated on the mesophilic anaerobic co-digestion of olive mill wastewater with olive mill solid waste. Page, Di. et al. [9], has modified the kinetic parameters of ADM1 in order to simulate dairy manure anaerobic digesters and thermophilic anaerobic co-digestion of olive mill wastewater and olive mill solid waste. Zaher, U. et al. [10], has developed a general integrated solid waste co-digestion model, for optimization and assessment of co-digestion of any combination of solid waste streams. This very important tool estimates

particulate waste fractions of carbohydrates, proteins, lipids and inerts and thus generates inputs for ADM1, which subsequently predicts biogas generation. In fact, anaerobic digestion of the organic fraction of the municipal solid wastes alone or combined with organic sludge can contribute efficiently to solid waste reduction and biogas production as described by many researchers: Zuza et al. [11], Bolzonella et al. [12], Mace et al. [13] and Bolzonella et al. [14], for solid waste treatment under mesophilic or thermophilic conditions.

Since the introduction of activated sludge models (ASMs) by Henze et al., [15] the activated sludge processes have been studied using dynamic simulations in order to design, upgrade and optimize a range of configurations of the activated sludge unit in wastewater treatment plants (WWTPs). Later, the introduction of the anaerobic digestion model [3] extended the modeling further to the sludge line.

EXPERIMENTAL SECTION

ADM1 in the treatment of activated sludge at municipal wwtp context

In this current study, primary sludge from the primary settling tank and secondary sludge from the secondary clarifier are treated dried and mixed with polyelectrolyte and ferric chloride (Q), which are pumped subsequently into the digesters for the anaerobic digestion and biogas production. To maintain an inner constant process temperature of the digester, the sludge is recycled through heat exchangers. After the production of sufficient biogas, 20-25% of biogas is being recirculated into the digester for mixing purposes (Figure 2).

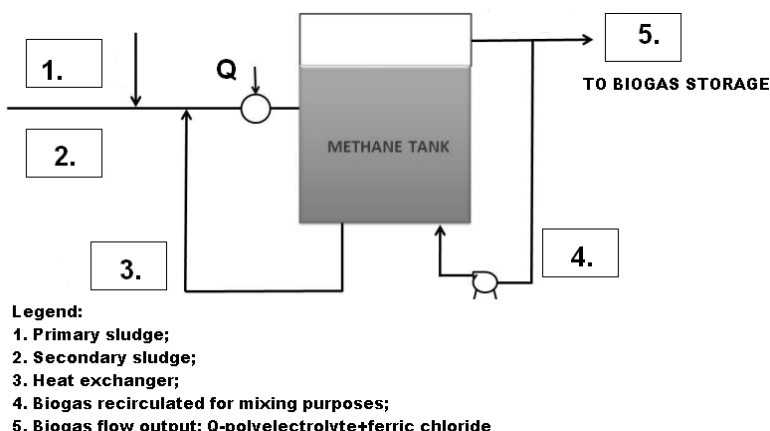


Figure 2. Sludge and biogas process lines

Materials and methods

The main process parameters of the anaerobic digestion: flows, temperature, pressure and concentrations are presented in Table 1.

Table 1. General plant design and process parameters

PROCESS PARAMETERS	SLUDGE LINE	ANAEROBIC
		FERMENTERS
<i>Primary sludge</i>		
Fermentation temperature: 37-39 °C	Flow: 260 m ³ /day	Unit: 4
Working Pressure: 20-25 mbar	Content of MS ⁷ : 27%	Volume: 3500 m ³
HRT ¹ : 21-25 days	Content of VS ⁸ : 73%	Type: Monostadium
Influent/Effluent Flow: 2500-13000 m ³ /h	Fixed residue: ~1800 mg/L	with recirculation
Heat exchangers thermal agent input/output temperature: 80/60 °C	<i>Secondary sludge</i>	Height: 12 m
Procentage of OMT ² : 30-50%	Flow: 280 m ³ /day	Diameter: 19 m
OL ³ : <<2 kg VSS/m ³	Content of MS: 29%	Biogas production: average of 3000
pH: 7-8	Content of VS: 71%	m ³ /day
Turbidity: <35 mg/L	Fixed residue: ~35000 mg/L	
Ortho-P ⁴ influent/effluent: 8 -1 mg/L	<i>Fermented sludge</i>	
D.O. ⁵ : 2-3.5 mg/L	Flow: 540 m ³ /day	
Nitrates: <40 mg/L	Content of MS: 40%	
Ammonia influent/effluent: 70/1 mg/L	Content of VS: 60%	
TSS ⁵ : 7500-9000 mg/L	Fixed residue: ~19000 mg/L	
TOC ⁶ : <125 COD/L		

Nomenclature:

¹ Hydrolic Retention Time	⁵ Dissolved Oxygen
² Organic Matter Transformation	⁶ Total Suspended Solids
³ Organic Load	⁷ Total Organic Carbon
⁴ Ortho-Phosphates	⁸ Mineral substances
	⁹ Volatile Substance

Simulink model

The ADM No.1 Simulink model [16], has been modified based on the process conditions presented in the previous table. The balance equations presented [3] has been modified slightly to include the sludge recycle and the gas recycles into the digester. The original ADM1 model is built under the assumption that the reactor is a thermodynamically isolated system. But under industrial conditions, a heating system has to be provided to maintain the digester temperature within the desired range. This is done by continuously recycling

the digester fluids through a heat exchanger. This recycle of internal fluids could have a certain influence on the compositions and hence this recycle has to be included in the model. The ADM 1 model equations consider the system to be a CSTR. In an actual plant operation, these CSTR conditions are achieved either by a mechanical action of a stirrer or by pumping gas through the digester. In this model under consideration, a bio-gas recycle is used to achieve this condition. This recycle has serious effects on the digester pressure, methane concentration in the biogas and quantity of biogas produced. Hence, the effects of the gas- recycle has to be included to make the mathematical model close to the industrial condition.

The first equation, Eq. (1) and Eq. (2), presents the change in the process conditions that are incorporated in the ADM1 model. Since the tank has been modelled as a perfectly mixed vessel, the influence of these recycles on physical conditions of mixing and other hydrodynamic effects can be ignored. Figure 3 presents the model that has been build up to study the digester section of WWTP. The 4 digester model has been converted to a single digester system, to produce an equivalent model; this can be done by simple addition of all the process conditions because in real situation all the 4 digesters work parallel, under uniform flow conditions.

For Liquid stream:

$$\frac{dS_i}{dt} = \frac{q_{in}S_{in,i}}{V_{liq}} + \frac{q_{rec,s}S_i}{V_{liq}} - \frac{q_{out}S_i}{V_{liq}} - \sum_{j=1-19} \rho_j v_{i,j} \quad (1)$$

S_i (i=1:24) – State variables

ρ_j	– Kinetic rates
$v_{i,j}$	– Stoichiometric coefficients
$q_{rec,s}$	– Sludge recycle flow
q_{in}	– Sludge input
q_{out}	– Sludge output
V_{liq}	– Volume of the liquid fraction

For Gas section:

$$\frac{dS_i}{dt} = \frac{q_{rec,g}S_i}{V_{gas}} - \frac{q_{out}S_i}{V_{gas}} + k_L a_{gas} (S_{gas,liq} - K_{H,gas} P_{gas}) \quad (2)$$

gas	– biogas composition ($S_{CO_2}+S_{CH_4}+S_{H_2}$)
$k_L a_{gas}$	– Gas Liquid mass transfer coefficient
$K_{H,gas}$	– Henrys Constant for the corresponding gas
$q_{rec,s}$	– Gas recirculation flow rate
P_{gas}	– Partial pressure of the biogas
V_{gas}	– Volume of the gas fraction

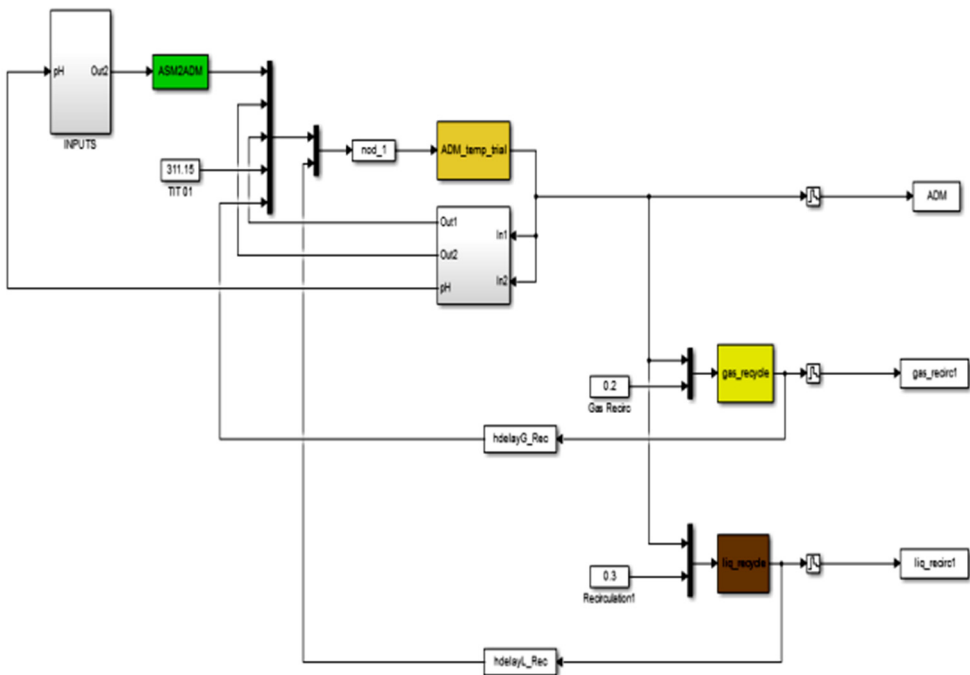


Figure 3. Simulink model with sludge and gas recycle

ASM-ADM1 Simulink® interface

The ADM No.1 model is often connected to an ASM-ADM converter [17] which provides a detailed algorithm to convert the ASM1 model parameters to ADM1. Attaching a converter to the ADM No 1 has two major advantages. Firstly this provides the need for having less complex ASM 1 input variables compared to the ADM 1 input which has about 25 input state variables. Secondly it also would be convenient to link it to the Waste Water treatment model to create a Benchmark for a complete Waste Water Treatment Plant (BSM No.2).

Even after the implementation of ASM-ADM interface in the digester model, the input variables used are completely different from the values that are regularly monitored in the industry. There are no available methods for direct measurement of these input variables. The values of these inflow composition provided in the literature [18] cannot be directly used in a digester model, due to the huge variations in waste-water sludge composition. Apart from the immeasurable input parameters, there is also a possibility of various parameters that could be different from those used in the ADM No. 1 [3].

The default values of influent sludge composition, conversion parameters of the ASM-ADM converter, stoichiometric and kinetic parameters presented in the ADM1 fails to give the required tank pressure and methane production rates. Hence there is a need for calibrating these values to match the values obtained from the WWTP.

Sensitivity analysis

Before we tune the model parameters to obtain the desired output, it is necessary to understand the effect of various parameters (Table 2) on the output variables.

Table 2. Inflow Composition [18]

PARAMETER	PARAMETER ABBREVIATION	Value
Soluble inert organic matter	S_I	30
Readily biodegradable substrate	S_S	68.22
Particulate inert organic matter	X_I	7148.21
Slowly biodegradable substrate	X_S	27987.36
Active heterotrophic biomass	$X_{B,H}$	4043.27
Active autotrophic biomass	$X_{B,A}$	8.49
Particulate products arising from biomass decay	X_P	26.02
Soluble biodegradable organic nitrogen	S_{ND}	0.1
Particulate biodegradable organic nitrogen	X_{ND}	0.19

These parameters used to describe the model, have been obtained by experimentations and have been successfully implemented in various WWTPs, but as mentioned before, some of them still have a possibility of change. With such a huge list of variables that could be varied to fit in the data, a suitable choice has to be made to select the ones that can provide significant influence in the output variable. It has to be taken into account the parameters chosen that are most likely to be affected by the change in feed composition. Table 3 shows the list of variables that are most likely to represent the parameters that is depended on the type of sludge. The parameters such as Henry's law coefficients, acid-base equilibrium constant, acid-base rate constant are considered dependent completely on temperature and hence remain constant. The same is the case with the specific Monod maximum uptake rate, first order decay rate for biomass death, Monod half saturation constant, which are maintained same as the default values due to its extremely complex dependency function on the output variables.

Table 3. Stoichiometric and kinetic parameters

Parameter	Description	UNIT
C_i	carbon content of component	kmoleC/kgCOD
k_{LA}	gas–liquid transfer coefficient	days
N_i	nitrogen content of component i	kmoleN/kg COD
$Y_{\text{substrate}}$	yield of biomass on substrate	kgCOD_X/kgCOD_S
$f_{\text{product,substrate}}$	yield of product on substrate	kgCOD/kgCOD ⁻¹

where,

i - Components/state variables used in the ADM1
(Batstone *et al.* 2002)

RESULTS AND DISCUSSION

The simulation outputs: in Figures 4-6 it is presented the simulation output for biogas production rate, methane concentrations and tank pressure from the initial conditions to the time it reaches steady state. These graphs present a preliminary idea of the time taken for the process to reach steady state conditions. The comparison of the simulated variables and the industrial data is provided in Table 4. The table clearly shows that the methane concentration clearly matches the values of the design parameters, but the flowrate and the digester pressure varies from the design values. Hence a tuning of parameters has to be done to match the values.

Table 4. Output parameters

OUTPUT	units	SIMULATED VALUE	INDUSTRY VALUE
Steady state pressure	mbarg	49.42	25
Methane concentration	dimensionless	69.37	70%
Biogas flowrate	m ³ /day	3312	3000

The values given in Table 5 are the base operating condition. Which implies that the model has been run based on the stoichiometric values from the literature. Now these values from the literature are increased by 10 times and are used to run simulations until it reaches the steady state conditions. The final values of biogas flowrate (q) and tank pressure (P) have been recorded at the end of each run. The values of % P and % q can be mathematically explained by the flowing equation.

SENSITIVITY ANALYSIS USING ADM1 MODEL FOR BIOGAS PRODUCTION

$$\%P = \frac{P_{new} - P_{base}}{P_{base}} \quad (3)$$

where,

P_{new} – the value of tank pressure after the change in the selected parameter

P_{base} – the value of tank pressure obtained with literature data parameter simulation

$$\%q = \frac{q_{new} - q_{base}}{q_{base}} \quad (4)$$

where,

q_{new} – the value of biogas flowrate after the change in the selected parameter

q_{base} – the value of biogas flowrate obtained with literature data parameter simulation

The value of methane concentrations has shown extremely low sensitivity to the variation in inflow sludge composition, stoichiometric and kinetic parameters. Hence the prime focus has been put to study the influence on biogas flowrate q and methane tank pressure p .

While calibrating the model, it is now known which parameters have to be varied. In case of a major deviation of model data from the industrial data, the results showing higher values of $\%P$ and $\%q$ could be varied and later the values with lower $\%P$ and $\%q$ could be further varied to fit the model.

Table 5. Parameters that have negative effects on pressure and biogas production

Default value	Parameter	Description	mbarg	m ³ /day	%P	%q
0.41	f_ac_su	Yield (acetates from sugars)	24.17	1631.8	-2.36	-50.87
0.08	Y_aa	Yield of biomass on amino acids	24.44	1649.4	-2.33	-50.34
0.007	N_aa	Nitrogen contend of amino acids	24.67	1665.5	-2.31	-49.86
0.13	f_bu_su	Yield (butyrate from sugars)	33.18	2239.4	-1.51	-32.58
0.27	f_pro_su	Yield (propionate from sugars)	34.50	2328.8	-1.38	-29.88
0.05	f_pro_aa	Yield (Propionate from amino acids)	36.71	2477.6	-1.18	-25.40
0.0217	C_fa	Carbon content in fatty acids	42.26	2852.7	-0.65	-14.11
0.03	C_si	Carbon content in soluble inert	42.29	2854.9	-0.65	-14.04
0.1	Y_su	Yield of biomass on sugar	43.10	2909.3	-0.57	-12.41
0.02786	C_xc	Carbon content in Composite	44.24	2986.5	-0.47	-10.08
0.06	Y_fa	Yield of biomass in fatty acids	44.25	2986.9	-0.47	-10.07
0.04	Y_pro	Yield of biomass on propionates	44.83	3026.3	-0.41	-8.88

Table 6. Effect of changes in input composition

Default value	Parameter	Description	mbarg	m ³ /day	%P	%q
0.03	C_pr	Carbon content in proteins	865.4	58412.2	76.8	1658.7
0.022	C_li	Carbon content in lipids	222.9	15045.1	16.3	353.0
0.0313	C_ch	Carbon content in carbohydrates	196.4	13258.6	13.9	299.2
0.95	f_fa_li	Yield (fatty acids from lipids)	120.1	8109.1	6.7	144.2
0.0313	C_ac	Carbon content in acetic acid	77.7	5248.1	2.7	58.0
0.4	f_ac_aa	Yield (acetic acid from amino acid)	71.3	4813.9	2.1	44.9
0.26	f_bu_aa	Yield (butyric acid from amino acids)	61.6	4158.4	1.2	25.2

Table 7. Effect of 6 most important variables

Default value	Parameter	Description	mbarg	m ³ /day	%P	%q
14024	X _S	Slowly biodegradable substrate	140.1	7102.2	184.7	113.8
30315.3	X _{BH}	Active Heterotrophic biomass	210	8904.7	326.7	168.1
744.6	X _{ND}	Particulate biodegradable organic nitrogen	63	3489.4	28.0	5.0
1643.7	X _{BA}	Active Autotrophic biomass	52	3364.8	5.6	1.3
33.3	S _S	Readily biodegradable substrate	50.1	3321.9	1.8	0.2
3.6	S _{ND}	Soluble biodegradable organic nitrogen	49.99	3315.5	1.5	0.1

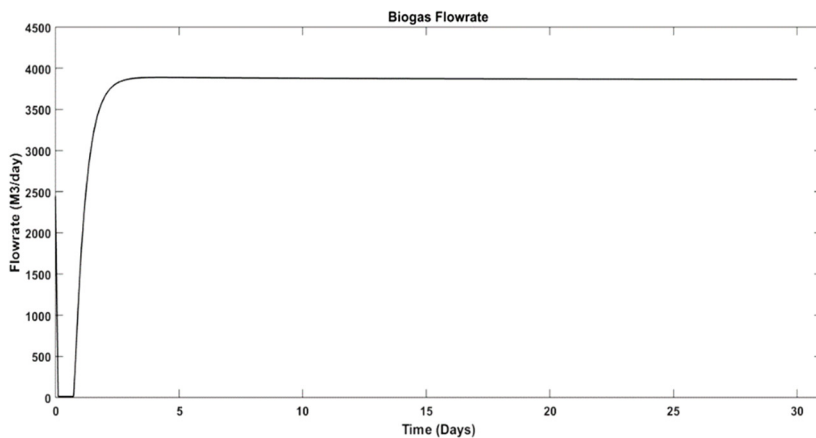


Figure 4. Biogas Flowrate in time

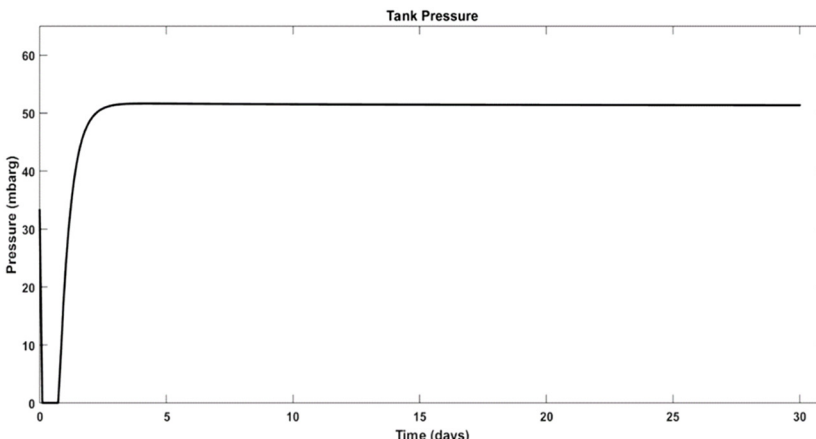


Figure 5. Pressure in time

SENSITIVITY ANALYSIS USING ADM1 MODEL FOR BIOGAS PRODUCTION

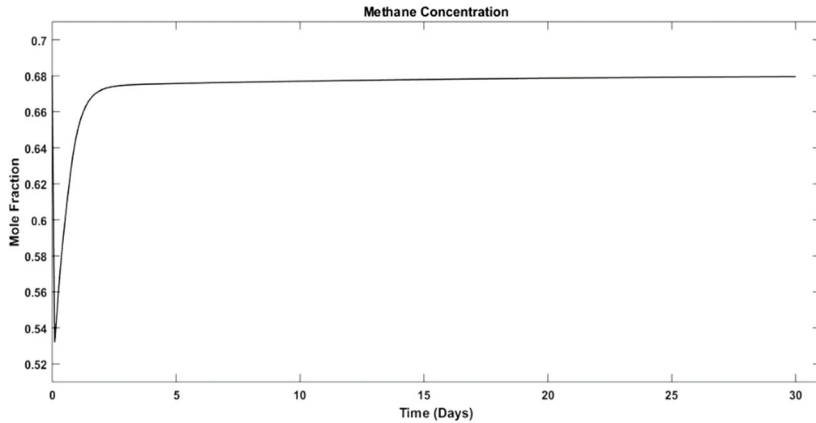


Figure 6. Methane concentrations in time

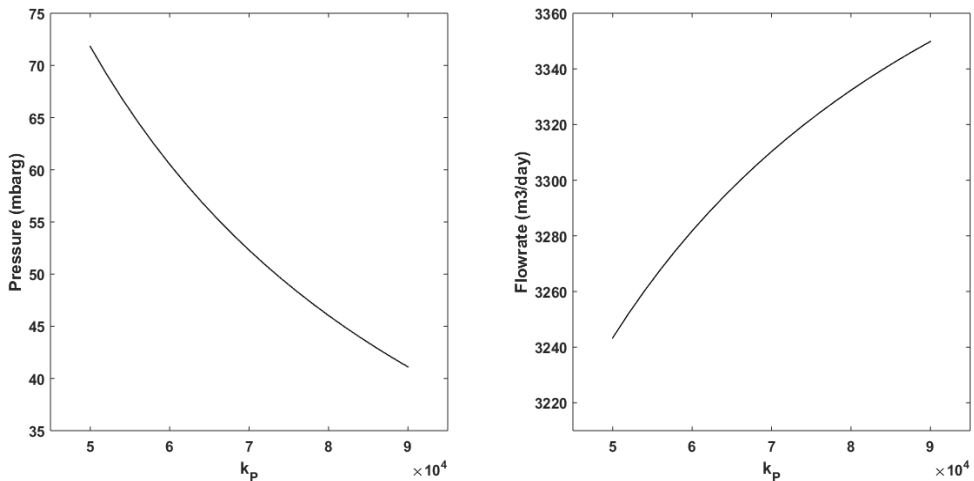


Figure 7. Effect of k_p on tank pressure and flowrate

The results of the sensitivity analysis that was performed has been presented in Table 5.

The first table presents the variables that have a positive influence on the pressure and biogas flowrate. The ones presented in Table 6 have a negative influence on the total output parameters. These parameters are presented in the descending order of their sensitivities to have an idea about the order in which they have to be varied to get fit the ADM1 model to an industrial digester.

Table 6 presents the effect of changes that has been presented in the input composition. It has been observed the inserts have no effect on the output variables, but the rest of the compositions show its effect. The effect of 6 most important variables has been presented in Table 7.

$$q = k_p * (P_{digester} - P_{atms}) \quad (5)$$

The parameter k_p which is the correlation factor between the digesters pressure and the gas flowrate, as mentioned by equation (5), has a unique influence in the model. In the ADM 1, a change in k_p increases the biogas flowrate, this can be directly observed from the equation. But in this case study, analysing the simulation results, it has been observed to also reduce the tank pressure. This effect may be due to the presence of a gas recycle equations which has been included in the ADM model. These results are presented in Figure 7. Due to this unique property, this parameter could be of vital use in tuning the ADM1 model.

CONCLUSIONS

ADM1 has been modified based on the design parameters and process conditions from Cluj-Napoca WWTP and has to be further calibrated to simulate the steady-state anaerobic digestion of activated sludge at municipal wastewater, in the production of biogas.

The sensitivity analysis performed identifies the parameters that have a major impact over the output.

The simulation outputs: biogas production rate, digester pressure and the methane concentration fit the industrial data. The methane concentration (69.37) clearly matches the values of the design parameters (70%), but the flowrate (3312 m³/day) and the digester pressure (49.42 mbarg) varies slightly from the design values (3000 m³/day and 25 mbarg respectively).

Parameter k_p which is the correlation factor between the digesters pressure and the gas flowrate has a unique influence in the model, because a rise in the digester pressure simultaneously decreases the flow rate. The model has to be calibrated to bring the simulation results within acceptable error margins of industrial data. The knowledge of calibration parameters and its effect on the output variables would act as a basis to either manually vary or develop an optimisation algorithm to perform the calibration exercise.

ACKNOWLEDGMENTS

This paper is a result of a doctoral research made possible by the financial support of the Sectoral Operational Program for Human Resources Development 2007-2013, co-financed by the European Social Fund, under the project POSDRU/159/1.5/S/132400- "Young successful researchers – professional development in an international and interdisciplinary environment".

REFERENCES

- [1]. Mata-Alvares J., Mace S. and Libres P., *Bioresource Technology*, **2000**, 74, page 3-16.
- [2]. Web link: <http://www.rec-energy.com/>, accessed 08.09.2015.
- [3]. Batstone, D.J., Keller J., Angelidaki, I., Kalyuzhnyi, S.V., Pavlovstathis, S.G., Rozzi, A., Sanders, W.T.M., Siegrist, H., Vavilin, V.A., **2002**, Anaerobic Digestion Model No. 1. IWA Task Group on Mathematical Modelling of Anaerobic Digestion Processes. IWA Scientific and Technical Report No. 13, ISBN–1900222787.
- [4]. Batstone, D.J., Keller, J., Steyer, J.P., *Wat. Sci. Tech.*, **2006**, 54, 1–10.
- [5]. Sanders W.T., Geerink M., Zeeman G., Lettinga G., *Water Science and Technology*, **2000**, 41, page 17-24.
- [6]. Feng, Y., Behrendt, J., Wendland, C., Otterpohl, R., *Wat. Sci. Tech.*, **2006**, 54, 139–148.
- [7]. Kalfas, H., Skiadas, I., Gavala, H., Stamatelatou, K., Lyberatos, G., *Wat. Sci. Tech.*, **2006**, 54, 149–156.
- [8]. Boubaker, F., Cheikh Ridha, B., *Biores. Tech.*, **2008**, 99, 9004–9008.
- [9]. Page, D.I., Hickey, K.L., Narula, R., Main, A.L., Grimberg, S.J., *Water Sci. Technol.*, **2008**, 58, 689–695.
- [10]. Zaher, U., Li, R.; Jeppsson, U., Steyer, J., Chen, *Water Res.*, **2009**, 43, 2717–2727.
- [11]. Zuza A., Agachi P.S, Cristea V.M, Nair A, Tue N.N., Deac C., *Environmental Engineering Management Journal*, **2015**, 14, 357-360.
- [12]. Bolzonella, D., Innocenti, L., Pavan, P., Traverso, P. and Cecchi, F., *Bioresource Technology*, **2003**, 86, 123-129.
- [13]. Mace S., Bolzonella D., Cecchi F. and Mata Alvarez J., *Water Science and Technology*, **2003**, 48, 21-28.
- [14]. Bolzonella, D., Fatone, F., Pavan, P. and Cecchi, F., *Ind. Eng. Chem. Res.*, **2005**, 44, 3412-3418.

- [15]. Henze M. et al., Activated sludge Model No. 1, IAWPRC Scientific Technical Report, **1987**, London <http://dx.doi.org/10.4172/2155-6199.S4-003>.
- [16]. Rosen C. And Jeppsson U., Aspects on ADM1 implementation within the BSM2 framework, **2006**, Lund University.
- [17]. Nopens I., et al., *Water research*, **2009**, *43*, 1913–1923.
- [18]. Gernaey, K.V., Rosen, C., Jeppsson, U., *Water Sci. Technol.*, **2006**, *53*, 225–234.

PURIFICATION OF CRUDE GLYCEROL BY SHORT PATH EVAPORATION. THEORETICAL AND PRACTICAL ANALYSIS OF PROCESS PARAMETERS

ANCUȚA ROXANA TRIFOI^{a,b,*}, AUGUSTIN CRUCEAN^b,
LUCICA STĂNULET^b, OLIMPIU BLĂJAN^b, PAUL ȘERBAN AGACHI^a

ABSTRACT. Crude glycerol, the by-product from biodiesel production process, increased drastically as rapid growth of biodiesel industry. This by-product contains many impurities such as water, soaps, free fatty acids, esters etc. This paper presents a process development based on molecular distillation or short path evaporation, for glycerol purification up to 99%. Several experiments and theoretical analysis have been carried out to identify the effect of important parameters (mean free path, Knudsen number, evaporation rate, feed flow rate and evaporation temperature) which determine the performance of the molecular distillation process. The purified glycerol is collected in the distillate while the residue is enriched in higher molar mass components. High performance liquid chromatography (HPLC) was employed to determine the purity of glycerol.

Keywords: glycerol, molecular distillation, mean free path

INTRODUCTION

The glycerol market is currently undergoing radical changes, driven by very large supplies of glycerol arising from biodiesel production, because the production of 10 kg of biodiesel by the transesterification process yields about 1 kg of crude glycerol as co-product [1-3]. The crude glycerol contains many impurities such as water, organic and inorganic salts, soaps, alcohol, traces of mono- and diglycerides and vegetable colours. High purity glycerol is still required as it is an important industrial feedstock for applications in food, cosmetic, pharmaceutical industries or other uses [4]. In this study the molecular distillation process has been studied as a technique for glycerol purification.

^a Babeș-Bolyai University, Faculty of Chemistry and Chemical Engineering, 11 Arany Janos Str., RO-400028, Cluj-Napoca, Romania.

^b The Research Institute for the Auxiliary Organic Products, 8 Carpati str., RO-551022, Mediaș, Romania.

* Corresponding author: atrifoi@chem.ubbcluj.ro

Characteristics of the molecular distillation process are: the small distance between the evaporator and condenser, low temperatures, short residence times and low pressure in the distillation gap. In contrast to the conventional distillation, molecular distillation does not occur at any well-defined temperature, as long as there is a thermal gradient between the condenser and the evaporator. Consequently, the distilling vapour molecules pass directly from the vaporizing surface to the condensing surface and no equilibrium exists between the vapor and the liquid phases. Ideal distillation conditions are attained when the rate of evaporation is equal to the rate of condensation and no vapour molecules returning to the liquid phase [5-8]. The condition for the molecular distillation is that the mean free path (λ) for the light molecules to be greater than the distance between the evaporator and the condenser [9-10]. In contrast, the heavy molecules can not reach the condenser and return to the evaporator [11]. Schematic representation of molecular distillation is shown in Figure 1.

The objective of this paper is the estimation of the molecular distillation parameters for glycerol evaporation.

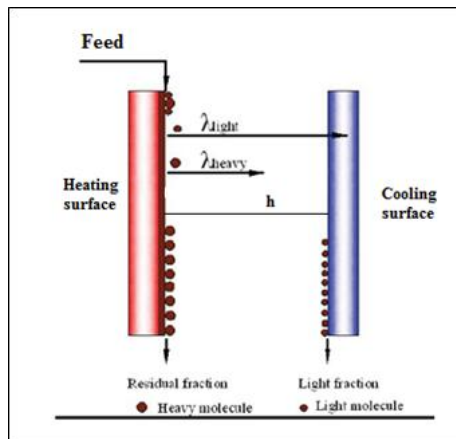


Figure 1. Schematic representation of molecular distillation process [12]

RESULTS AND DISCUSSION

(1) The mean free path [7]

$$\lambda = 2.3 \cdot 10^{-20} \frac{T}{p\sigma^2}, [\text{cm}]$$

where: T-temperature (K); p- gas pressure (torr); σ - molecule diameter (cm).

The mean free path was calculated at pressures below 1mmHg at different temperatures in order to select the operating parameters of the process because the mean free path must be higher than 0.8 cm, which is the distance between the evaporator and condenser, for the equipment used and presented in Figure 7. The mean free path of the glycerol molecules at different temperatures is shown in Figure 2.

The glycerol molecules can reach the cooling surface at pressure below 0.3 mmHg. The mean free path of the impurities (such as methyl ester, free fatty acid, mono-, di- and triglycerides) is smaller and the distance between the evaporator and condenser and can be separated effectively due to the difference between mean free paths and molar masses.

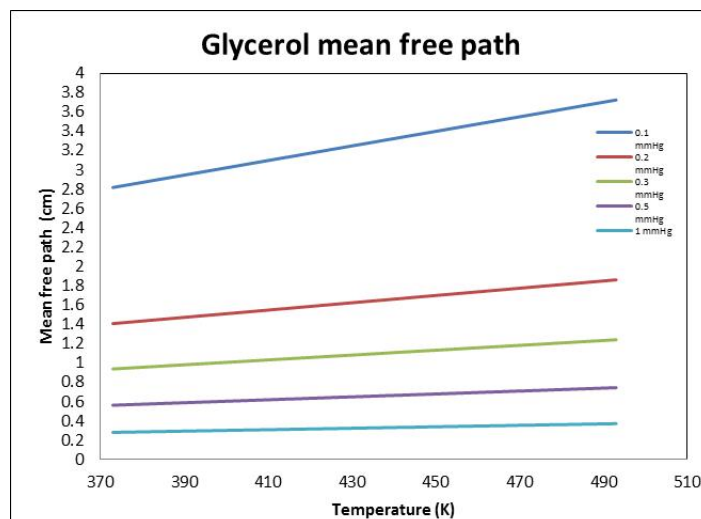


Figure 2. Effect of temperature on glycerol mean free path

(2) The Knudsen number [13]:

$$Kn = \frac{\lambda}{h}$$

where: λ - the mean free path (cm); h - distance between the evaporator and condenser (cm).

The distillation at 0.3 mmHg is in the intermediate range ($0.05 < Kn < 10$) and it is a proper distillation rate, see Figure 3. The thermal decomposition of glycerol in these conditions is reduced.

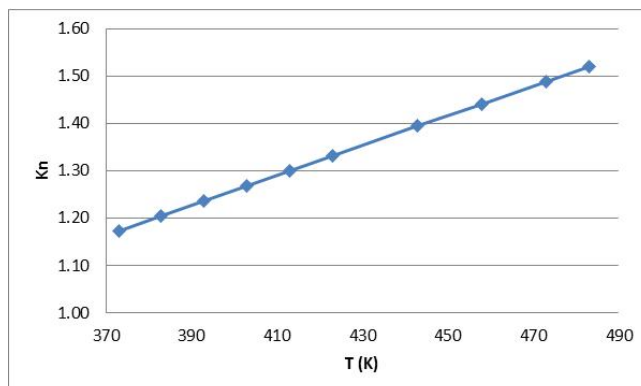


Figure 3. Effect of temperature on Knudsen number

(3) The relative evaporation rate [7]

$$M_0 = 5.83 \cdot 10^{-2} \cdot p \left(\frac{M^0}{T} \right)^{1/2}, \quad [g \cdot cm^{-2} \cdot s^{-1}]$$

where: p- vapour pressure (torr); T-temperature (K); M⁰- molecular mass (g.mol).

(4) The effective evaporation rate [7]

$$M_r = 5.83 \cdot 10^{-2} \cdot f \cdot p \left(\frac{M^0}{T} \right)^{1/2}, \quad [g \cdot cm^{-2} \cdot s^{-1}]$$

where f is the efficiency factor, determined with the formula

$$f = F + (1 - F)(2 \cdot e^{-N} - e^{-2N}) \quad [9]$$

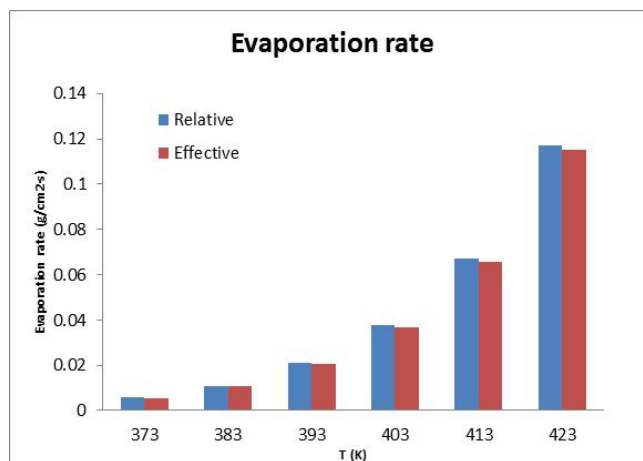
F is the surface ratio

$$F = \frac{A_{evap}}{A_{evap} + A_{cond}} \quad [9]$$

$$N = \frac{h}{k \cdot \lambda} \quad [9]$$

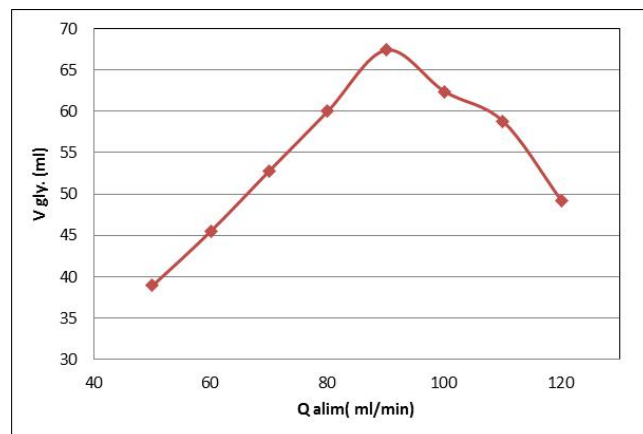
$$\log k = 0,2 \cdot F + 1,38(F + 0,1)^4 \quad [9]$$

The effect of temperature on evaporation rate is shown in Figure 4. An increased heat supply to the evaporated liquid causes its temperature to rise and thus induces the rise of saturated vapor pressure and distillation rate increase. The efficiency factor f is 0.98, the difference between the relative and effective evaporation rate is very small.

**Figure 4.** Effect of temperature on evaporation rate

The purity obtained for glycerol was about 99% (98.6-99.24%) in the temperature range of 373K-423K.

At 423 K, the maximum quantity of separated glycerol, was at feed flow rate of 90 ml/min and then decreased, as shown in Figure 5. This can be explained by the thickness of the evaporating falling film. At higher feed flow rates, the thickness of the film is larger, the velocity of the film is bigger and the contact with the heated surface is not enough for evaporation. At 90 ml/min, the glycerol yield is 80%, at a purity of about 99%. This is very important, because the yield we obtained by classical distillation was no higher than 58.85 %.

**Figure 5.** Effect of feed flow rate on distillate volume of glycerol

CONCLUSIONS

Molecular distillation is an effective tool to purify glycerol up to 99%, after the water and the volatiles were removed. The purification is possible due to the differences between mean free path, molar mass and volatilities of glycerol and impurities. The low residence time and using a higher vacuum in molecular distillation process, increased the glycerol yield and productivity.

EXPERIMENTAL SECTION

Materials

The material used to make the study is crude glycerol obtained from the biodiesel plant of SC EXPUR Slobozia, with the following composition:

Table 1. Crude glycerol (EXPUR) characteristics

Crt.	Properties	Specifications
1	Glycerol content (%)	84.6
2	Water (%)	9.1
3	MONG	1.5
4	Alcalinity (meq/100g)	1.8
5	Methanol (%)	0.04
6	Ash (%)	4.8

This glycerol has already been pre-treated, the methanol was recovered and the soap and free fatty acids were removed, because the MONG content is reduced. After the water was removed by conventional batch distillation ($T=373\text{ K}$ and 40 mmHg), the glycerol was distillated by molecular distillation. The glycerol content after water removal was 92.28%.

Equipment

The distillation was performed using a laboratory falling film type molecular distillation column, shown in Figure 2, made of four concentric cylindrical Pyrom glass tubes, that allows the visual inspection of the distillation process. The thermal agent (silicon oil) is introduced into the central tube, through the connection hose-b and it comes back from the column to the thermostat, by connection hose-c. The raw glycerol solution is degased and is introduced from the tank-1 connected to the column by the inlet hose-j and it is uniformly distributed on the external surface of the second tube, which acts as evaporator, through the inlet holes. The solution passes through the surface of the second tube in a falling film and the volatiles components evaporate. The

vapors condensate on the internal surface of the third tube and the condensate is collected in the round flask- 3. The heavier components are collected in the round flask-4. The fourth tube is for the cooling agent, and it has two connection hoses – inlet/outlet. The whole installation is connected to a vacuum pump through the connection hose -f.

The distance between the evaporation and cooling surface is 0.8 cm. The surface area of the evaporator is 0.097968 m^2 and the area of the condenser is 0.158256 m^2 . The operational temperature was up to 150°C and the pressure of the system was kept constant to 0.3 mmHg.

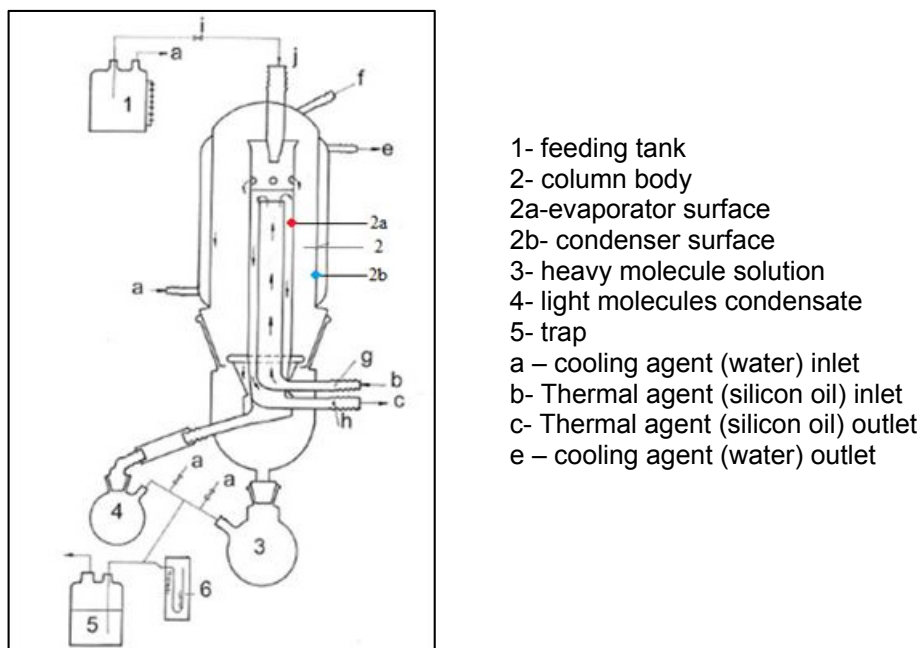


Figure 7. Laboratory falling film distillation column

Analytical procedures

For the glycerol concentration determination, HPLC analyses were carried out on a Jasco Chromatograph (Japan) equipped with an intelligent HPLC pump (Model PU-980), a ternary gradient unit (Model LG-980-02), an intelligent column thermostat (Model CO-2060 Plus), an intelligent reflex index detector (Model RI-2031 Plus) and an injection valve equipped with a $20 \mu\text{L}$ sample loop (Rheodyne). Samples were manually injected with a Hamilton Rheodyne Syringe (50 mL). This system was controlled and data were processed with the ChromPass software.

The separation was achieved on a Carbosep Coregel 87H3 column (300 x 7.8 mm) at temperature of 70 °C. The mobile phase was a sulphuric acid 0.01 M solution. The flow rate was 1 mL min⁻¹ and the injection volume was 20 µL. All samples and standards were filtered through PVDF 0.45 µm syringe filters (Teknokroma) and manually injected into the HPLC system. Each run was completed within 14 min.

ACKNOWLEDGMENTS

This work was supported by the II National Program-Inovation, Eureka, under the project number 320E/04.09.2012 and by Sectorial Operational Program for Human Resources Development 2007-2013, co-financed by the European Social Fund, under the project number POSDRU/159/1.5/S/132400 with the title “Young successful researchers – professional development in an international and interdisciplinary environment”.

REFERENCES

- [1]. L.E. Rincon, J.J. Jaramillo, C.A. Cardona CA., *Renewable Energy*, **2014**, 69, 479.
- [2]. J. Calero, D. Luna, E.D. Sancho, C. Luna, F.M. Bautista, A.A. Romero et al., *Renewable and Sustainable Energy Reviews*, **2015**, 42, 1437.
- [3]. A.G.C. Quispe, C.J.R. Coronado, J.A. Carvalho, *Renewable and Sustainable Energy Reviews*, **2013**, 27, 475.
- [4]. N. Saifuddin, H. Refal, P. Kumaran, *Research Journal of Applied Sciences, Engineering and Technology*, **2014**, 7, 593.
- [5]. V.I. Roibu, “*Distilare –Fractionare*”, Editura Tehnica Bucuresti, **1963**, chapter 14.
- [6]. L. Oniciu, I. Zsako. “*Chimie Fizica 2. Starile de agregare si termodinamica chimica*”, Editura Tehnica Bucuresti, **1968**, chapter 3.
- [7]. C. Drugarin, “*Distilarea moleculara*”, Editura Facultatea Timisoara, 1985, chapter 2 and 3.
- [8]. S.S. Handa, S.P.S. Khanuja, G. Longo, D.D. Rakesh, “*Extraction Technologies for Medicinal and Aromatic Plants*”, International Centre for Science and High Technology, Trieste, **2008**, chapter 8.
- [9]. J. Shi, L.R. Posada, Y. Kakuda, S.J. Xue, *Separation Science and Technology*, **2007**, 42, 3029.
- [10]. E.A. Bratu, “*Operatii unitare in ingineria chimica*”, Editura Tehnica Bucuresti, **1984**, chapter 27.
- [11]. J. Lutisan, J. Cvengros, *The Chemical Engineering Journal*, **1995**, 56, 39.
- [12]. W. Shurong, “*High-Efficiency Separation of Bio-Oil. Biomass Now - Sustainable Growth and Use*”, **2013**, Chapter 16.
- [13]. Z. Kawala, P. Dakiniewicz, *Separation Science and Technology*, **2002**, 37, 1877.

ELECTROCHEMICAL BEHAVIOR OF $\text{CaBaCo}_2\text{O}_{5\pm\delta}$ IN NEUTRAL AQUEOUS SOLUTION

MIRCEA LAURENTIU DAN^a, NICOLAE VASZILCSIN^a,
NARCIS MIHAI DUȚEANU^{a,*}

ABSTRACT. This paper presents the effect of Y^{3+} substitution with Ca^{2+} ions on the electrochemical behavior of Y-112 perovskite in neutral aqueous solution during oxygen insertion/release. Perovskite electrochemical behavior was studied by cyclic voltammetry and chrono-electrochemical methods. In correlation with these techniques the compound morphology was determined by scanning electron microscopy (SEM). Based on obtained results the electrochemical reactions occurring at interface compound – electrolyte have been identified.

Keywords: cobalt mixed oxides, $\text{CaBaCo}_2\text{O}_{5\pm\delta}$, Ca^{2+} ions insertion, cyclic voltammetry, chrono- electrochemical methods.

INTRODUCTION

Cobalt layered perovskites with 112 type structure attract a great attention in recent years due to a wide magnetic and electrical properties. Compounds from series $\text{LnBaCo}_2\text{O}_{5+\delta}$ ($\text{Ln} = \text{Nd-Ho}$ and Y) are promising materials for applications as solid-oxide fuel cell (SOFC) cathodes or as ceramic membranes for oxygen separation [1]. These new technologies provide the enormous economic and environmental advantages.

Electrical charge transfer of those perovskites is achieved by a complex mechanism involving electronic and ionic conductivity, due to the presence of simultaneous deficit of electrons and oxygen holes into the crystalline structure. The oxygen intake/release process in 112 cobaltate perovskites modifies the concentration of electric charges carriers with direct effect on the internal resistance and consequently on the electrical conductivity of these compounds [2,3].

The compounds from 112 series present a tetragonal structure with space group $P4/mmm$ or orthorhombic (pseudotetragonal) structure with space group $Pmmm$ or $Pmma$ [4]. The substitution of Y^{3+} ions with Ca^{2+} is achieved deformation of the perovskite Y-112 initial structure.

^a University Politehnica Timișoara, Faculty of Industrial Chemistry and Environmental Engineering, 300223, Parvan 6, Timisoara, Romania.

* Corresponding author: narcis.duteanu@upt.ro

Compound $\text{CaBaCo}_2\text{O}_{5-\delta}$ was obtained by substitution of Y^{3+} with Ca^{2+} ions. The diminished interest for this perovskite is due to the fact that the valence of Co ions in perovskite structure is +3, which has a negative effect on cobalt 112 perovskites electrical and magnetic properties [5,6].

Oxygen content of Ca 112 mixed oxide is depending on the metallic cation nature included in to the oxide structure, which is determining for the nominal valence of Co ions. Oxygen nonstoichiometry in the perovskite structure is influenced by oxygen content variations which affecting the oxygen permeability and diffusion, and also has a highly importance in order to reveal the perovskite structure. From electrochemical point of view, studied Ca 112 mixed oxide can be attractive due to his oxygen insertion/release capacity.

RESULTS AND DISCUSSION

The purity of obtained Ca-112 compound was checked by X-Ray powder diffraction (Philips X-pert Pro). The result is presented in figure1.

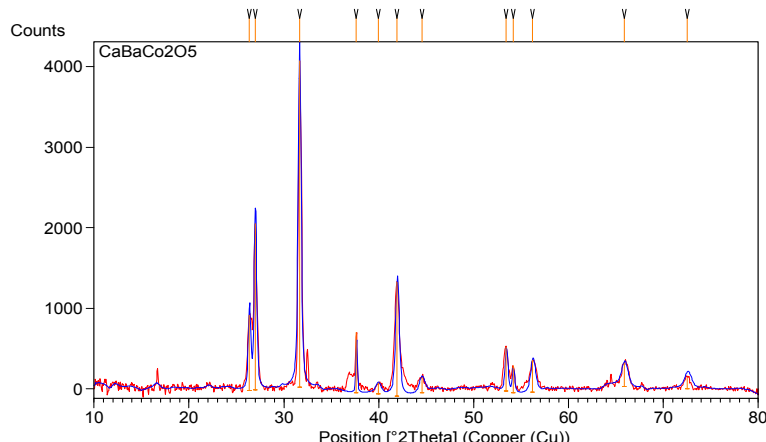


Figure 1. X-ray diffraction pattern for $\text{CaBaCo}_2\text{O}_5$ obtained by the solid state reaction at 1100°C.

XRD diffraction spectra were recorded for 2θ range between 0 and 80°, after that all peaks from recorded spectra were identified using ICC data base. From that can conclude that the obtained product is the desired $\text{CaBaCo}_2\text{O}_5$ mixed oxide.

Also, the 112 perovskite composition was confirmed by EDAX analysis performed after sintering stage and the results are presented in figure 2. Although, these analyzes provide approximate information about the compound

composition, especially as analyzes are dependent on the compound uniformity and homogeneity, the atomic and mass percentages of the elements from the inserted table confirm the Ca-112 composition.

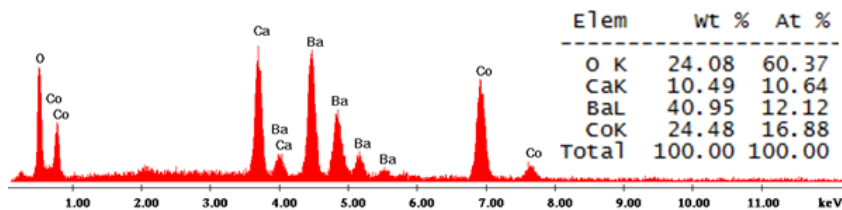


Figure 2. EDAX spectrum for compound $\text{CaBaCo}_2\text{O}_5$.
Inserted the atomic and mass percentages of the components.

Thermal behavior of Ca-112 compound was studied in similar conditions as used in thermal studies of Y-112 compound: nitrogen flow, and temperature range between 30 and 1000 °C. The thermogram obtained is depicted in figure 3.

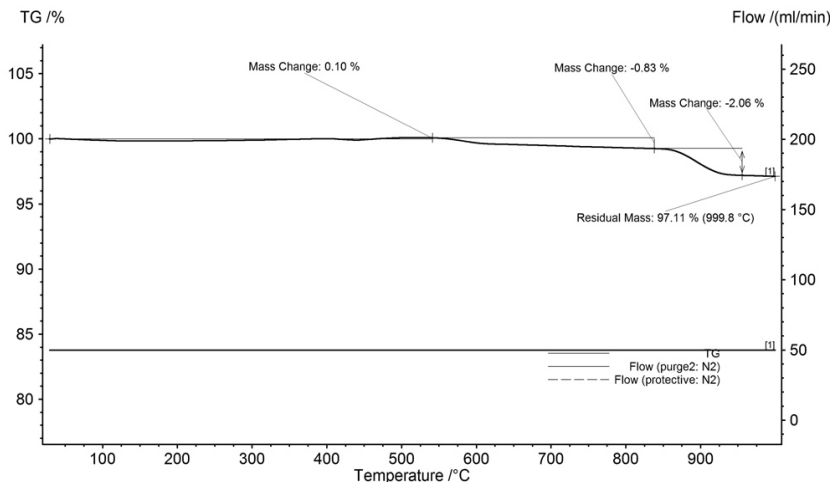


Figure 3. Weight change of $\text{CaBaCo}_2\text{O}_{5\pm\delta}$ with temperature in nitrogen flow.

During thermal study, the compound Ca-112 can intake or release oxygen, which is equivalent with the modification of the average oxidation number of cobalt ions presented in perovskite structure, which may vary between +2 and +4, as indicated the studies performed on Ca-112 compound.

In table 1 the weight variations obtained for studied compound and also the oxygen excess/deficiency (δ) versus temperature under a nitrogen flow are presented.

Table 1. Δm values and δ in temperature range 30-1000°C (gas flow: nitrogen)

Gas flow	Temperature range [°C]	Δm [%]	δ in $\text{CaBaCo}_2\text{O}_{5+\delta}$
Nitrogen	30-550	0.10	+ 0.02
	550-830	-0.83	- 0.17
	830-950	-2.06	- 0.65

Ca-112 thermal behavior under nitrogen flow is specific for cobalt perovskite, especially up to 800°C. The amount of accepted oxygen in studied compound up to 350°C is very low (+ 0.02 ions O²⁻/mol), probably due to + 3 oxidation number of Co ions in the Ca-112 structure. When the temperature is increasing, Y-112 characteristic perovskite structure is distorted, becoming more compact, and the oxidation of cobalt ions at + 4 is more difficult. In temperature range of 305 -750°C, the amount of oxygen release is much higher than the accepted one which confirms the tendency to released oxygen from this perovskite crystal structure in an inert atmosphere.

In terms of crystalline structure, intake/release of a small amount of oxygen not produce major changes in the original structure, and most probably a rearrangement of bonds in the Ca-112 structure occurs. At temperatures over 750°C, sudden release of 0.65 ions/mol of oxygen may have a destruction effect on 112 layered structures and consequently, other oxides of constituents are formed [10].

An important factor influencing kinetics of oxidation process is the surface morphology; studied by scanning electron microscopy immediately after the sintering stage and also after the electrochemical studies. SEM images obtained for Ca-112 electrodes involved in this work are presented in figure 3.

It can be observed that perovskite has a compact structure, with few channels existing in excrescences (figure 4a), which facilitate access of the reactants and favor oxygen adsorption/desorption process. Also, in the SEM image recorded after electrochemical oxidation (figure 4b) an advanced compaction of electrode surface is observed. This can be associated with the deployment of electrochemical processes especially at interface electrode/ electrolyte. The oxidation/reduction process in the bulk electrode will be more difficult.

The equilibrium of Ca-112 electrode in 0.5 mol L⁻¹ Na₂SO₄ solution is quasi-stationary, equilibrium potential value (OCP) is modified after each determination and it is in a correlation with compound oxygen content variation (δ). Versus initial equilibrium potential, it can have negative values in case of oxygen deficiency (5- δ) or positive when an excess of oxygen (5 + δ) was observed. OCP determined by chronopotentiometry at zero current in 0.5 mol L⁻¹ Na₂SO₄, for 12 hours, was $E_{\text{ech}} = + 0.255$ V, displaced by approximately 200 mV towards more positive values in comparison with the values obtained for Y-112 electrode. At this value of potential we can consider that the studied perovskite has preserved his stoichiometry and the oxygen excess (δ) in compound remains 0, which is equivalent with an oxidation number of +3 for cobalt ions.

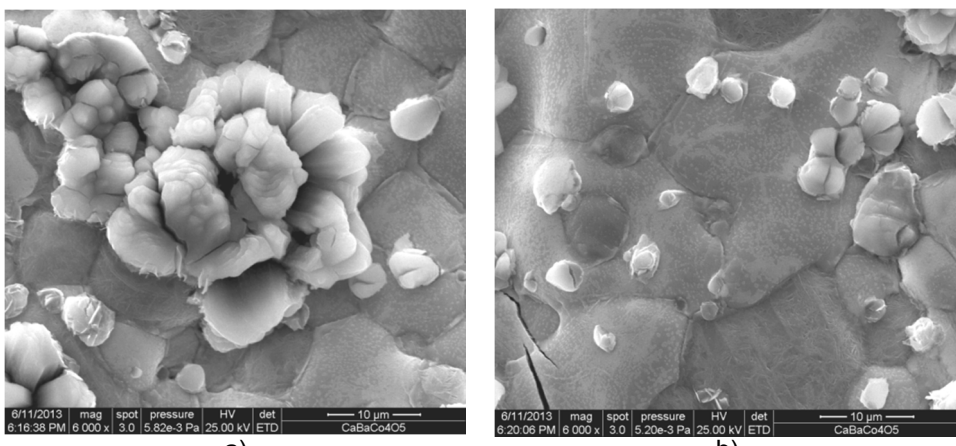


Figure 4. SEM images of the Y-112 electrodes surface before (a) and after electrochemical oxidation/reduction (b) at 6000x magnification

Preliminary voltammetric studies show that in neutral medium in a wide range of potential (+ 2.5 and - 2 V), Ca-112 electrode behaves as a support material, being observed only oxygen and hydrogen evolution reaction on the electrode. This behavior can be explained either by surface morphology presented previously or through the fact that, at anodic polarization, Co³⁺ ions from perovskite are oxidized very slowly and only in some conditions at Co⁴⁺, while at cathodic polarization the quantity of electricity which passes the interface is not large enough to initiate the reduction process of Co³⁺ to Co²⁺.

Therefore, preliminary studies demonstrated the need of an initial superficial activation stage by pre-polarizing the electrode at -1.00 V versus Ag/AgCl in order to reduce a part of Co³⁺ ions. After a superficial activation, the peak separation corresponding to the processes occurring at interface CaBaCo₂O₅ – electrolyte solution can be observed or recorded voltammograms (scan rate less than 50 mV s⁻¹).

In cyclic voltammograms depicted in fig. 5.a (5 cycles recorded starting from OCP towards positive potentials, scan rate 50 mV s⁻¹) can be observed at the occurrence of an anodic peak (1) associated with the oxidation process (Co²⁺ → Co³⁺ + e⁻), followed by a current limit plateau (2). When, the electrode potential is more positive, oxygen evolution reaction can be observed (3). On the CV backward scan it can be observed a limiting current plateau (4) associated with the oxidation of superficial remanent oxygen. When the electrode potential is shifted to more negative values a cathodic peak (5) associated with Co³⁺ reduction process appear around -0.8 V. At more negative potentials, the current increase can be associated with hydrogen evolution reaction (2H⁺ + 2e⁻ ↔ H₂).

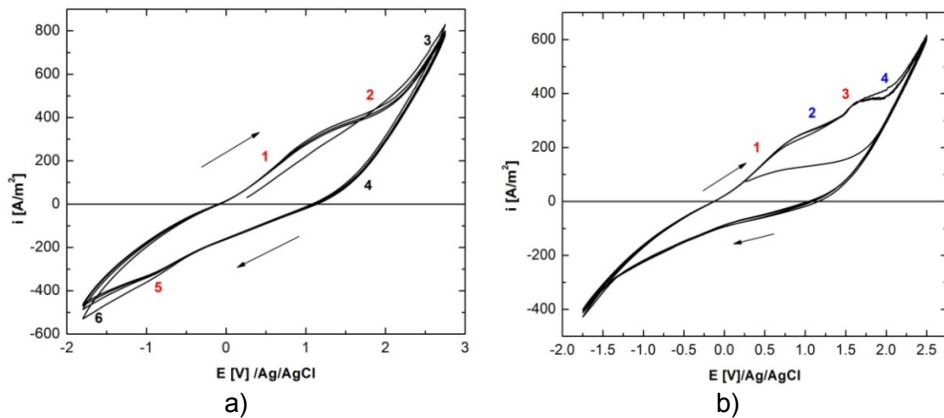


Figure 5. Cyclic voltammograms (5 cycles) on Ca-112 working electrode in 0.5 mol L^{-1} Na_2SO_4 solution, pH 6.8 at 50 mV s^{-1} (a) and 10 mV s^{-1} (b) scan rate.

When the CV's were recorded at 10 mV s^{-1} (fig. 5.b) it can be observed the occurrence of a new peak (3) and also of a new plateau (4), which can be associated with interfacial Co^{3+} ions oxidation ($\text{Co}^{3+} \rightarrow \text{Co}^{4+} + \text{e}^-$) or with bulk oxidation of Co^{2+} ($\text{Co}^{2+} \rightarrow \text{Co}^{3+} + \text{e}^-$) ions, because the electrode surface is completely oxidized.

When the CV are recorded using lower scan rate (5 mV s^{-1}) anodic peak 1 was associated with Co^{2+} oxidation, followed by a limiting current plateau 2, alongside hydrogen and oxygen evolution reactions (fig. 6).

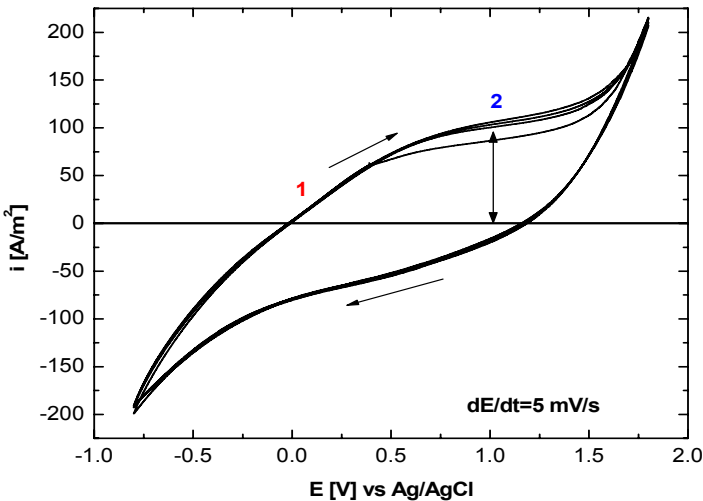


Figure 6. Cyclic voltammograms (5 cycles) on Ca-112 working electrode in 0.5 mol L^{-1} Na_2SO_4 solution at 5 mV s^{-1} scan rate.

Global reaction which occurs at interface electrode/electrolyte is:



Similar with chronoamperometric and chronocoulometric studies performed in case of Y-112 compound, in order to calculate the amount of oxygen introduced in Ca-112 crystalline structure by electrochemical methods, were chosen two potential values significant for the electrochemical oxidation of studied perovskite in neutral aqueous solution: one corresponding for oxidation peak (+ 0.50V/Ag/AgCl) and the second for the current limit plateau (+1.00V/Ag/AgCl). These tests were performed in order to study the oxygen intake capacity for different times intervals. Based on chronocoulometry data was estimated the amount of oxygen (δ) introduced into the crystalline structure for different oxidation times (table 2). Should be noted that before each chrono-coulometric study, electrodes suffer a cathodic polarization in order to sufficiently reduce the Co³⁺ ions quantity, such that during oxidation stage the amount of oxygen introduced in perovskite structure not exceed compound initial stoichiometry.

Table 2. δ variation in the electrochemical oxidation of Ca-112

Electrolyte	Time [min]	δ in YBaCo ₂ O _{5+δ}	
		$E = 0,50$ V/Ag/AgCl	$E = 1,00$ V/Ag/AgCl
Na ₂ SO ₄ 0,5 mol L ⁻¹	15	$0,48 \times 10^{-3}$	$1,02 \times 10^{-3}$
	30	$0,79 \times 10^{-3}$	$1,36 \times 10^{-3}$
	60	$1,11 \times 10^{-3}$	$1,88 \times 10^{-3}$
	120	$1,34 \times 10^{-3}$	$2,25 \times 10^{-3}$

From data presented in table 2 can be observed that the studied compound present all the characteristic specific to layered cobalt perovskite – the oxygen intake / release capacity. Also, due to smaller amount of oxygen accepted in Ca-112 perovskite structure, in same time interval, oxygen intake / release process occurs with smaller speed, in comparison with the speed observed in case of Y-112 perovskites.

CONCLUSIONS

The results obtained in this first electrochemical study performed in neutral sollection studies showed that the Ca-112 mixed oxide is sensitive at anodic or cathodic polarization, oxidation process consists in oxygen insertion in crystal structure. Consequently, during oxidation the Ca-112 crystalline network becomes denser, so that the oxygen diffusion rate is lowered. The compaction of Ca-112 during oxidation imposes a partial irreversible character of the oxidation process. Although, the δ obtained for Ca-112 oxidation are lower than ones obtained for Y-112.

EXPERIMENTAL SECTION

Ca-112 mixed oxide was obtained using a solid state reaction, by mixing the precursors: CaCO_3 (Aldrich 99.99%), BaCO_3 (Aldrich 99.99%) and $\text{CoO}_{4/3}$ (Normapur 99.9%), according to the stoichiometric cation ratio. Preparation method of selected perovskite was similar with that used for the preparation of Y-112 cobalt perovskite [7-9]. After decarbonization at 900°C for 6 hours, the powder was pressed into pellets with geometrical active surface of 1 cm^2 , later fired in air for 48 h at 1100°C and then removed quickly from oven and set to ambient temperature [7-9]. Compound purity was checked by X-Ray powder diffraction (Philips X-pert Pro). Surface morphology of Ca-112 electrodes has been characterized by scanning electron microscopy (SEM) using a FEI INSPECT S microscope.

Electrochemical studies were carried out using a BioLogics SP150 potentiostat/galvanostat. The electrochemical cell was equipped with two graphite counter electrodes positioned symmetrically against the working electrode (Ca-112 electrode) and an Ag/AgCl reference electrode. All potentials used in this work are given versus the Ag/AgCl reference electrode. All electrochemical measurements were performed in $0.5 \text{ mol L}^{-1} \text{ Na}_2\text{SO}_4$ electrolyte solution.

REFERENCES

- [1]. K. Zhang, L. Ge, R. Ran, Z. Shao, S. Liu, *Acta Materialia*, **2008**, *56*, 4876.
- [2]. X.T. Zhang, H.S. Hao, X. Hu, *Physica B - Physics of Condensed Matter*, **2008**, *403*, 3406.
- [3]. J. Xue, Y. Shen, T. He, *Journal of Power Sources*, **2011**, *196*, 3729.
- [4]. B. Raveau, Md. M. Seikh, "Cobalt Oxides: From Crystal Chemistry to Physics", First Edition, Wiley-VCH Verlag GmbH & Co, **2012**, chapter 5.
- [5]. H. Wang, E. Enriquez, G. Collins , C. Ma, M. Liu, Y. Zhang, C. Dong, C. Chen, *Journal of Materomics*, **2015**, in press.
- [6]. W. J. Ge, Advanced Materials Research, **2013**, *830*, 130.
- [7]. Y. Liu, *Journal of Alloys and Compounds*, **2009**, *477*, 860.
- [8]. A.S. Urusova, V.A. Cherepanov, T.V. Aksanova, L.Ya. Gavrilova, E.A. Kiselev, *Journal of Solid State Chemistry*, **2013**, *202*, 207.
- [9]. J.H. Kim, Y. N. Kim, Z. Bi, A. Manthiram, M. P. Paranthaman, A. Huq, *Solid State Ionics*, **2013**, *253*, 81.
- [10]. M. Dan, A. Kellenberger, N. Vaszilcsin, N. Duteanu, *Environmental Engineering and Management Journal*, in press.

CORROSION RESISTANCE OF LASER CLADDED NiCrBSi COMPOSITE COATINGS

IOSIF HULKA^{a*}, V.A. SERBAN^a, D. UTU^a, NARCIS DUTEANU^{a*},
A. PASCU^b, I.C. ROATA^b

ABSTRACT. NiCrBSi powders were deposited on medium alloy steel substrate using laser cladding process and electrochemically tested at room temperature by immersing the specimens in 3.5% NaCl solution in order to study their corrosion behavior. The coatings were obtained using different cladding parameters like scanning speed and overlap percentage. Investigations techniques such as scanning electron microscopy (SEM), energy dispersive X-ray spectroscopy (EDS), potentiodynamic polarization and electrochemical impedance spectroscopy (EIS) measurements were employed to study the microstructure and chemical properties of the coatings. It was found that the microstructural characteristic and corrosion behavior are linked to coatings thickness, dilution and diffusion of Fe within the coating.

Keywords: *laser cladding, powders, coatings, corrosion, NiCrBSi;*

INTRODUCTION

Laser cladding, is one of the surface modification technologies widely employed for deposition of protective coating on cheaper substrate or materials with poor wear and corrosion resistance like carbon steel [1]. The process uses lasers as a concentrated heat source to manufacture coatings with a very good metallurgical bond with the substrate. The coatings are meant to increase the lifetime of different components by preventing them from severe wear and corrosion [2]. The process is superior to other deposition methods like hard-facing in terms of feedstock material consumption, high productivity and low distortion. During cladding, a melt pool is formed on the substrate by the laser beam while it scans the surface and the filler material, which usually is a

^a Politehnica University of Timisoara, Piața Victoriei Nr. 2, 300006 Timișoara, Romania

^b Transilvania University of Brasov, Materials Engineering and Welding Department, 29 Eroilor Blvd., 500036, Brasov, Romania

* Corresponding authors: hulka_iosif@yahoo.com, narcis.duteanu@upt.ro

powder or wire, is addend and fused to the substrate. During the process, high heating and rapid cooling rates occurs resulting fine microstructures and metastable phases during solidification [3]. If the cooling rate is too fast, the melt-pool solidifies rapidly, and crack formation might occur which is a major drawback for laser cladding. Cracking is detrimental to the corrosion behavior of the coatings because they act as sites for crevice and pitting corrosion [4].

Ni-based self-fluxing alloys are mainly used in petro-chemical industry, glass industry and others for applications as mud purging elements, hot working punches, fan blades, earth working machine elements, etc. [5]. Their advantages are related to easy coating of large sized components.

NiCrBSi is one of the alloys used in laser cladding to enhance wear and corrosion resistance at moderate and elevate temperatures. Si and B, present in the filler material, increase the self-fluxing capabilities of the alloy, improving the ability to obtain depositions by melting process. The role of Cr is to improve the mechanical properties as a consequence of its combination with other elements to produce hard precipitates [6].

The aim of the present research was to investigate the influence of different deposition parameters such as scanning speed and overlapping percentage of laser tracks on the microstructure, hardness and also their influence on corrosion behavior, in a 3.5% NaCl solution at room temperature, on the obtained NiCrBSi laser cladded coatings.

RESULTS AND DISCUSSION

Powder Characterization

Figure 1a shows spherical powder particles with surface dimples caused by the collision of particles during atomization. In cross-section (Fig. 1b) the powder consists of fine cellular and dendritic microstructures. Some pores might be noticed as well. The powder composition (Fig. 1c) determined by EDS analysis confirm the chemical elements presented in Table 2.

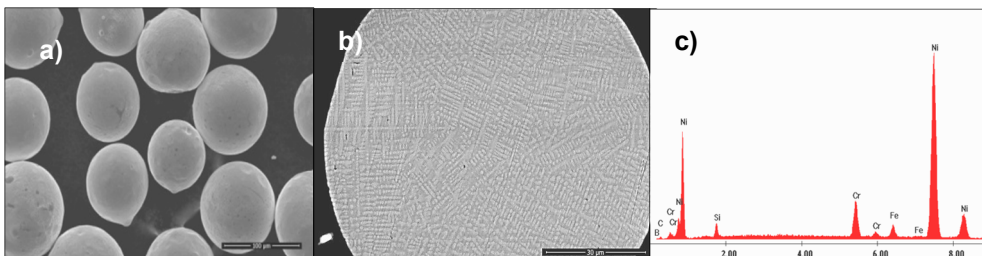


Figure 1. SEM image of (a) NiCrBSi gas atomized powder particles, (b) cross-section of powder particle and (c) EDS analysis of powder

Coating Microstructure and Chemical Composition

The optical micrographs (OM) of the coatings (Fig. 2) revealed a good adhesion between the cladded material and substrate, indicating that the powder was melted complete and sufficiently. All of the coatings exhibit dense structure with reduced porosity. Depending on the deposition parameters, presented in Table 1, different coating thicknesses were obtained, thus influencing the dilution process. At lower overlapping areas and higher deposition speed growth the coatings were thinner.

The dilution, present in the laser cladded coatings, quantifies the relative amount of substrate material melted during the deposition process and mixed with molten material from the new cladded coating. In order to obtain high quality cladded coatings some dilution is required between the substrate and cladded coating to ensure a good metallurgical bond. Even if the dilution it is required, it must stay low otherwise it may degrade the coating properties [7].

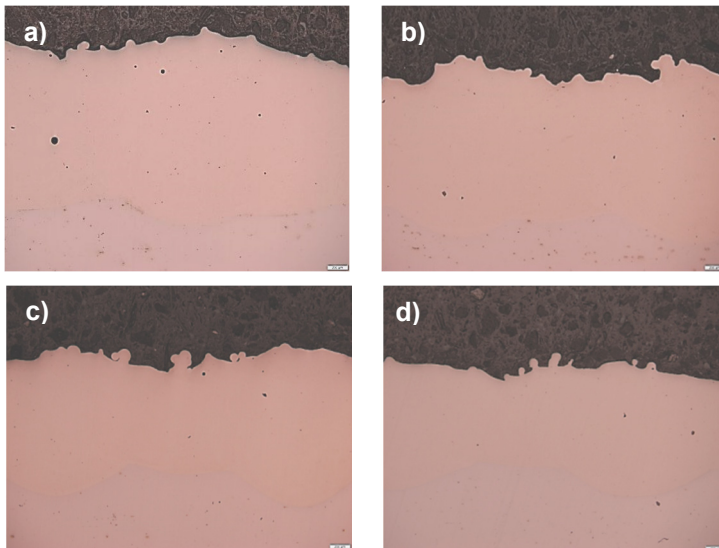


Figure 2. OM of laser cladded coatings (a) Sample 1; (b) Sample 2; (c) Sample 3; (d) Sample 4.

Figure 3a illustrates the etched microstructure, the chemical composition being revealed by the EDS spectrum (Fig. 3b). For all sample the morphology of the NiCrBSi coatings was similar. The matrix phase consists from a solid solution of Ni with Cr and Fe providing a dendritic structure. Between the dendritic structures an intermetallic laminar eutectic phase is present. The microstructure and chemical composition of the laser cladded coatings is similar to results presented by authors for similar alloys [8].

Dilution in a thicker laser cladded coating formed by overlapping can be expected to be smaller because part of the beam energy is consumed in order to melt the overlapped track [7], this being a reason why in present study the thicker the coating the smaller the dilution is.

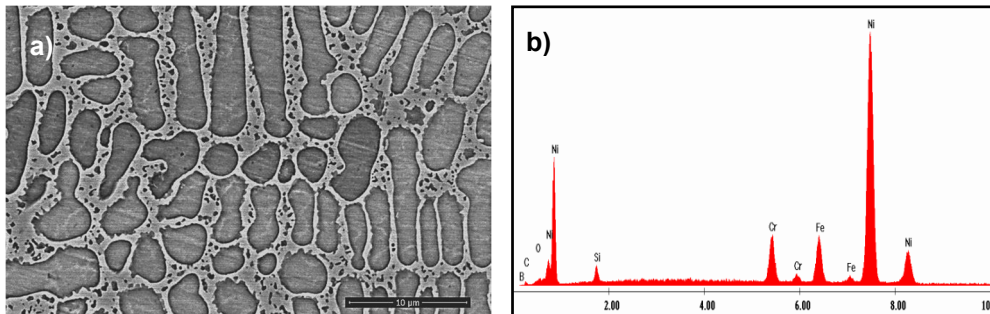


Figure 3. Close-up SEM of NiCrNSi laser cladded coating of the dendritic structure (a) and EDS analysis (b).

Results of micro-hardness measurements, thickness and porosity of coatings are presented in Table 1. Hardness measurements were performed along a straight line in all the laser cladded coatings. The average hardness value of the coatings decreased as the coating became thinner because of the Fe diffusion from the substrate that was melted. The thicknesses of the coatings differ, depending of their different deposition parameters like scanning speed and overlap percentage, thus Sample 1 is the thickest. The reduced amount of porosity, less than 1%, indicated dense and compact coatings. Small differences between the values might be attributed due to different deposition angles.

Table 1. Micro-hardness and coating thicknesses

Sample	Hv _{0.3}	Thickness [mm]	Porosity %
1	431.8 ± 11.2	1.81 ± 0.19	0.67 ± 0.92
2	408.8 ± 20.3	1.43 ± 0.23	0.06 ± 0.05
3	407.4 ± 21.2	1.21 ± 0.21	0.55 ± 0.66
4	376.1 ± 37.5	0.98 ± 0.18	0.03 ± 0.03

The chemical compositions of different areas, in cross-section of the coatings, were studied as it is indicated in Figure 4 in the upper (a), middle (b) and lower (c) part of the coating and as well in the coating-substrate interface (d). The results are summarized in Table 4. Boron could not be detected clearly in the EDS quantification due to its relatively low atomic mass and it was not included in the analysis as well as oxygen and carbon.

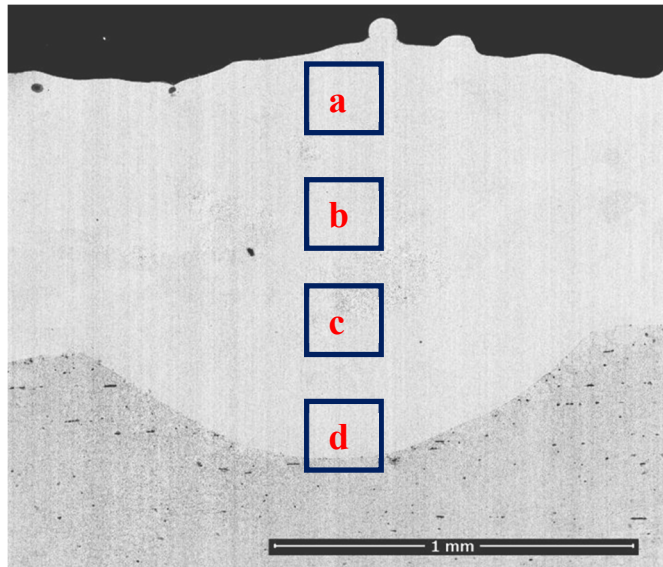


Figure 4. SEM of laser cladded NiCrBSi coating indicating EDS areas of interest

It might be noticed that the Ni, Cr and Si content is more concentrated in the upper part of the coating while this values changed, reaching lower values at the coating-substrate interface while Fe content proved the opposite. This is might be due to diffusion process from the substrate. The high temperature reached during the cladding process may have also been contributed to the Fe diffusion.

Table 2. EDX quantification results

	Sample 1				Sample 2			
El. wt%	a	b	c	d	a	b	c	d
Ni	68.58	67.2	66.83	35.5	67.56	67.01	65.15	34.67
Cr	9.71	7.98	8.17	2.44	8.44	7.39	7.29	2.25
Si	13.54	14.54	13.08	7.93	14.55	13.54	14.09	5.20
Fe	8.17	10.29	11.91	54.0	9.45	12.05	12.66	57.89
	Sample 3				Sample 4			
El. wt%	a	b	c	d	a	b	c	d
Ni	63.9	63.04	60.83	33.03	65.63	64.16	58.2	35.33
Cr	7.85	7.7	6.76	2.38	8.88	7.87	6.41	2.87
Si	17.68	18.27	14.61	16.11	20.09	14.84	15.57	8.42
Fe	10.57	10.99	17.8	55.91	5.40	13.13	19.82	53.38

Corrosion Tests

Potentiodynamic polarization studies

Potentiodynamic polarization curves of NiCrBSi laser cladded coatings are shown in Figure 5. Prior to start the corrosion tests all coatings were ground and polished to the same roughness in order to allow similar testing conditions to avoid differences which might affect the test results.

According to obtained linear polarization curves at room temperature, the parameters values like corrosion rate, corrosion current density (i_{corr}), corrosion potential (E_{corr}) in conformity with Tafel slopes associated with anodic (b_a) and cathodic (b_c) processes, were determined by extrapolating the linear part of recorded curves using GPES software.

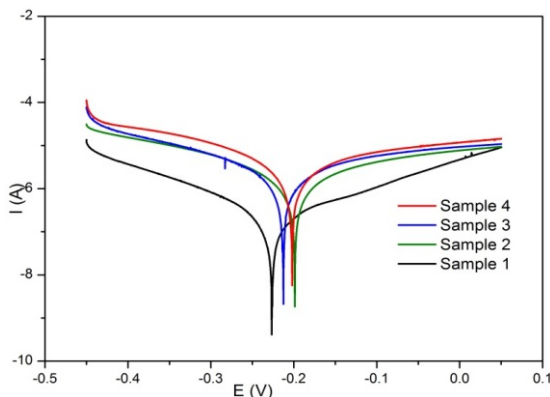


Fig. 5. Potentiodynamic polarization curves for laser cladded NiCrBSi coatings in 3.5% NaCl solution at 22°C

Linear polarization curves recorded for laser cladded coatings are presented in Figure 5. It is possible to calculate the polarization resistance from the linear polarization curves by using Stern and Geary equation [9] and the corrosion rate can be then calculated based on Faraday's Law [10] and the obtained data is presented in Table 3. Analyzing the data it might be noticed that the current density and corrosion rate corresponding for the corrosion process is lower for Sample 1 and higher for Sample 4.

Table 3. Corrosion parameters calculated from the polarization curves with 28.82 [g] equivalent weight and 8.14 [g/cc] density values

Sample	i_{corr} [A]	E_{corr} [V]	Corr. Rate [mm/year]
1	2.021E-7	-225	1.853E-3
2	1.542E-6	-372	1.413E-2
3	1.357E-6	-416	1.245E-2
4	2.708E-6	-353	2.484E-2

This can be explained by the higher coating thickness and reduced Fe dissolution compared to the other coatings, which makes the material nobler.

Electrochemical Impedance Spectroscopy EIS

The Nyquist plot depicted in Figure 6 shows the presence of a semi-circle – depressed capacitive loop at high to intermediary frequencies range [11], followed by an almost linear dependence which is associated with a mixed kinetic and diffusion control of the process [5]. Presence of the capacitive loop can be associated with the charge transfer resistance and appear from time constant of electrical double layer [11, 12].

Analyzing the EIS spectra presented in Figure 6 can observe that the semi-circle diameter is increasing in order sample 1, sample 2, sample 3 and sample 4. Deviation from the perfect circular shape observed in recorder EIS spectra was generally attributed to electrode superficial inhomogeneity and also to the mass transport resistance [13, 14]. Also, this inhomogeneity can be associated with different interfacial phenomena or with surface toughness [13]. Electrochemical theory express that the first intersection with x axis represents the solution resistance and the second one is associated with the charge transfer resistance (semicircle diameter). It is expected that the corrosion resistance is increase when the charge transfer resistance increase.

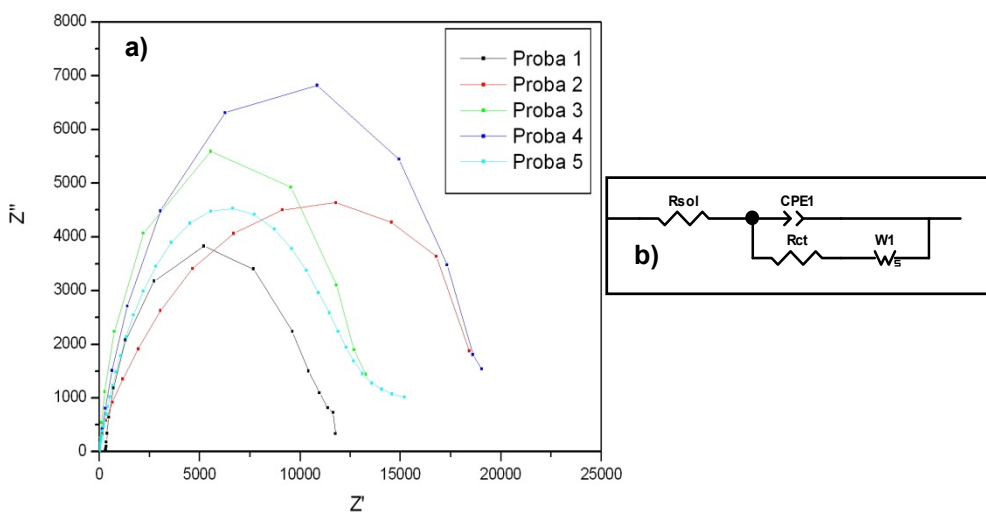


Figure 6. Nyquist plot (a) and equivalent circuit for spectra modelation (b)

Parameters associated with corrosion process were obtained by modeling the recorded impedance spectra using the electrical equivalent circuit presented in Figure 6b which describe the metal / electrolyte interface.

Equivalent circuit used is represented by a serial connection of solution resistance with a constant phase element (CPE) which is in parallel with a charge transfer resistance connected in series with a Warburg impedance. Usage of this Warburg element can be associated with mass transport process and suggests that the studied corrosion process is limited by mass transport [15]. In same time, CPE represent a modified capacitance describe by equation:

$$Z_{CPE} = \frac{1}{Y_0} (j\omega)^n \quad (1)$$

where Y_0 represent one parameter which can be related with the double layer capacitance, and n represent an exponent between 0 and 1 describing the constant phase angle of CPE [12].

Considering the case of a finite length thickness of the diffusion layer δ , can describe the impedance of Warburg element using the equation 2 [16]:

$$Z_w = (R_w(jw\tau_D)^{-\theta}) \tanh(jw\tau_D)^{-\theta} \quad (2)$$

R_w – diffusion resistance; τ_D – diffusion time constant given by $\tau_D = \delta^2/D$, where δ – diffusion thickness and D – diffusion coefficient; φ – an exponent whit values between 0 and 1.

Based on R_s , R_{ct} and CPE values can calculate the double layer capacity using equation 3 [11]:

$$C_{dl} = \left[\frac{T}{\left(\frac{1}{R_s} - \frac{1}{R_{ct}} \right)^{1-n}} \right]^{1/n} \quad (3)$$

In Table 4 are listed the values of electrochemical impedance parameters obtained by CNLS fitting of experimental data.

Analyzing data presented in Table 4 can observe that the charge transfer resistance is increasing in order: sample 1, sample 2, sample 3, sample 4, which can be associated with increase of corrosion resistance in same order. Also, it can be observed that all of the samples have reduced porosity, suggesting that the corrosion mechanism is similar in all 4 cases. Decrease of C_{dl} value, in same order, suggests that the number of active sites presented on the surface of the samples is increasing.

Table 4. Electrochemical impedance parameters obtained by CNLS fitting of experimental data

Sample	Resistances [$\Omega \text{ cm}^{-2}$]		CPE1		W			C_{dl} [$\mu\text{F cm}^{-2}$]
	R_{sol}	R_{ct}	Y_0 [$\text{F cm}^{-2} \text{ S}^n$]	n (0 – 1)	R_w [$\Omega \text{ cm}^{-2}$]	T_D [s]	Φ	
1	15.2	12204	1.5919E-5	0.90985	0.254	6.7223E-4	0.23924	6.98
2	12.95	12989	2.6328E-5	0.92386	0.00145	2.3366E-7	0.38522	6.01
3	15.5	18101	4.1223E-5	0.62274	0.164	0.2338	0.06002	6.00
4	15.15	19853	2.5589E-5	0.83775	5.472E-4	1.1394E-7	0.38637	5.59

CONCLUSIONS

The influence of scanning speed and overlap percentage on the properties and corrosion behavior of NiCrBSi laser cladded coatings, from commercial feedstock powder, was studied.

From the experimental results, the following conclusions can be drawn:

Using laser cladding process and NiCrBSi powder, dense and almost pore-free coatings might be manufactured with different microstructural characteristics due to different deposition parameters.

According to EDS quantification and due to diffusion process, the Fe content decreases from top of the coatings to interface, reaching higher values at the coating-substrate interface, while for the other elements exactly the opposite occurs.

The hardness of the coating decreases slightly as the coatings becomes thinner, due to dilution process.

The corrosion test indicated that the thicker coating (Sample 1) due to higher overlapping percentage of laser tracks (60%) is nobler and presents better corrosion behavior.

EXPERIMENTAL SECTION

Coating deposition

Laser cladding has been carried out using a Coherent 1000F diode laser and a Precitec YC50 water cooled cladding module manipulated by a CLOOS welding robot. The laser beam is in infrared field with a wavelength of 975 nm and a maximum divergence of 56 mm*mrad. The powder was provided to the cladding head with AT-1200HPHV Termach feeding system and Argon gas was used for shielding and carrier of the powder. The influence of scanning speed and overlap percentage on coatings properties was investigated. The cladding parameters used in the present study are presented in Table 5.

Powder characterization

The used cladding material is a Metco 12 C gas-atomized nickel based self fluxing powder with nominal size in the range of -125+53 µm, the relevant characteristics are presented in Table 6.

The powders morphology and microstructure was studied by scanning electron microscopy (SEM) equipped with energy dispersive X-ray (EDX) micro-analyzer.

Table 5. Cladding parameters

	Laser power [W]	Power density [kW/cm ²]	Speed [cm/min]	Powder feed rate [g/min]	OverlapPercent [%]
Sample 1	780	24.8	16	5	60
Sample 2	780	24.8	20	5	50
Sample 3	780	24.8	24	5	45
Sample 4	780	24.8	30	5	40

Table 6. Chemical composition in wt% of NiCrBSi feedstock powder

Powder	Supplier	Trade name	Chemical properties	Ni %	Cr %	B %	Si %	Fe %	C %
				Balance	10	2,5	2,5	2,5	0,15
NiCrBSi	Sulzer Metco	Metco 12 C							

Coatings characterization

The samples were metallographically prepared by using abrasive papers and polishing clothes with diamond suspension. Coatings microstructures were evaluated by means of optical microscopy, scanning electron microscopy (SEM), and energy dispersive X-ray analysis (EDX). Cross-section images of the samples were taken by an Olympus optical microscope and the SEM images with a Quanta FEG 250 (FEI, The Netherlands) equipped with EDAX analyzer. An Olympus Vickers micro-hardness tester was employed to ascertain the micro-hardness of the laser cladded coatings under a 300 gf load.

Corrosion tests

Electrochemical tests were performed at room temperature with an Autolab 302 N potentiostat/galvanostat using a 100 ml cell equipped with three electrodes: working electrode consisting of NiCrBSi laser cladded samples, Ag/AgCl reference electrode and a platinum mesh used as counter electrode. For the experiments the exposed surface of specimens were 1 cm², submerged and kept in a 3.5 wt.% NaCl solution (synthetic sea water) for 30 min to achieve the equilibrium. After the equilibrium was reached the polarization curves were

recorded using GPES software in order to evaluate the corrosion rate. All linear polarization curves were recorded in the potential range ± 250 mV versus open circuit potential at a scan rate of 0.5 mV s $^{-1}$. Electrochemical Impedance Spectroscopy (EIS) data were recorded using the FRA (Frequency Response Analyzer) module. All EIS experiments were performed at E_{corr} after 30 min equilibrium time, when the stationary stage were reached in frequency range 100 KHz to 100 mHz. Recorded EIS data were modelled with ZView software using a complex non-linear procedure (CNLS). Measurements were carried out in aerated solution at room temperature.

ACKNOWLEDGEMENTS

This work was supported by the strategic grant POSDRU/159/1.5/S/137070 (2014) of the Ministry of Labour, Family and Social Protection, Romania, co-financed by the European Social Fund – Investing in People, within the Sectoral Operational Programme Human Resources Development 2007-2013.

REFERENCES

- [1]. X. Lou, L. Li, G.J.Li, *Journal of Alloys and Compounds*, **2015**, 626, 102.
- [2]. P. Nie, O.A. Ojo, Z. Li, *Surface and Coatings Technology*, **2014**, 258, 1048.
- [3]. A. Ray, K. S. Arora, S. Lester, M. Shone, *Journal of Materials Processing Technology*, **2014**, 214, 1566.
- [4]. S. Zhou, Y. Huang, X. Zeng, Q. Hu, *Material Science and Engineering A*, **2008**, 480, 564.
- [5]. N. Serres, F. Hlawka, S. Costil, C. Langlade, F. Machi, *Journal of Materials Processing Technology*, **2011**, 211, 133.
- [6]. T.G-del Rio, M.A. Garrido, J. E. Fernandez, M. Cadenas, J. Rodrigues, *Journal of Materials Processing Technology*, **2008**, 204, 304.
- [7]. U. de Oliveira, V. Ocelik, J.Th.M. De Hosson, *Surface and Coatings Technology*, **2005**, 197, 127.
- [8]. T.E. Abioye, D.G. McCartney, A.T. Clare, *Journal of Material Processing Technology*, **2015**, 217, 232.
- [9]. Princeton Applied Research, Application note CORR1
<http://www.princetonapplied>.
- [10]. Stansbury, E.E.; Buchanan, R.A., Fundamentals of electrochemical corrosion, published by ASM Int., Mater. Park, Ohio, **2000**, ISBN 0871706768.
- [11]. H. Ashassi-Sorkhabi, N. Ghalebsaz-Jeddi, F. Hashemzadeh, H. Jahani, *Electrochimica Acta*, **2006**, 51, 3848.

- [12]. Application note – Gamry instruments, <http://www.gamry.com/application-notes/basics-of-electrochemical-impedance-spectroscopy/>
- [13]. A. Lecante, F. Robert, P.A. Blandinieres, C. Roos, *Current Applied Physics*, **2011**, 11, 714.
- [14]. K.F. Khaled, *Material Chemistry and Physics*, **2008**, 112, 290.
- [15]. E.M. Sheriff, Su-Moon Park, *Electrochimica Acta*, **2006**, 51, 1313.
- [16]. M. Dan, N. Vaszilcsin, A. Kellenberger, N. Duteanu, *Studia UBB Chemia*, **2011**, 1, 119.

QSAR STUDY ON SEROTONIN DERIVATIVES

SARA ERSALI^a AND MIRCEA V. DIUDEA^{a*}

ABSTRACT. A set of 40 serotonin derivatives, downloaded from the PubChem database, was submitted to a QSAR study, following Diudea's algorithm, in the frame of a hypermolecule, which mimics the „alignment” of drug molecules to the biological receptors. The best models describing $\log P$ of this set of serotonin were validated by the leave-one-out procedure, in the external test set and in a new version of prediction by using clusters of similar molecules. The structures have been optimized at PM3 level of theory. Topological indices have been computed by TOPOCLUJ software program.

Keywords: Serotonin, QSAR, Hypermolecule, $\log P$.

INTRODUCTION

Serotonin or 5-hydroxytryptamine (5-HT) is a monoamine neuro-transmitter. Biochemically derived from tryptophan, serotonin is primarily found in the gastrointestinal tract, blood platelets, and the central nervous system (CNS) of animals, including humans. It is popularly thought to be a contributor to feelings of well-being and happiness [1].

Approximately 90% of the human body's total serotonin is located in the enterochromaffin intestine cells, where it is used to regulate intestinal movements [2,3]. It is also synthesized in serotonergic neurons of the CNS, where it has various functions, including the regulation of mood, appetite, and sleep. Serotonin also has some cognitive functions, including memory and learning. Modulation of serotonin at synapses is thought to be realized by several classes of antidepressants. Serotonin secreted from the enterochromaffin cells eventually arrives in the blood, acting on blood platelets, which store it. When the platelets bind to a clot, they release serotonin, where it serves as a vasoconstrictor and helps to regulate hemostasis and blood clotting. Serotonin also is a growth factor for some types of cells, possibly involved in wound healing. There are various serotonin receptors.

^a Babeș-Bolyai University, Faculty of Chemistry and Chemical Engineering, 11 Arany Janos Str., RO-400028, Cluj-Napoca, Romania.

* Corresponding author: diudea@chem.ubbcluj.ro

Serotonin is metabolized mainly to 5-HIAA, in the liver; metabolism starts with oxidation of serotonin by monoamine oxidase to the corresponding aldehyde. This is followed by oxidation by aldehyde dehydrogenase to 5-HIAA, an indole acetic acid derivative and finally excreted by the kidneys. Because of serotonin's growth-promoting effect on cardiac myocytes [4], it could be involved in heart cancer.

In addition to animals, serotonin is found in fungi and plants [5]. Serotonin's presence in insect venoms and plant spines cause pain, which is a side-effect of serotonin injection. Serotonin is produced by pathogenic amoebae, and its effect on the intestine causes diarrhea. Its presence in seeds and fruits may stimulate the digestive tract into expelling the seeds.

STRUCTURAL MOLECULAR DATA

A set of 40 serotonin derivatives, taken from PubChem Database [6], were divided into a training set (the first 25 molecules) and a test set (the last 15 molecules), taken randomly; the modelled property was log P (Table 1).

On the set of 40 serotonins, a hypermolecule [7] was built up, as a reunion of their substructures (Figure 1).

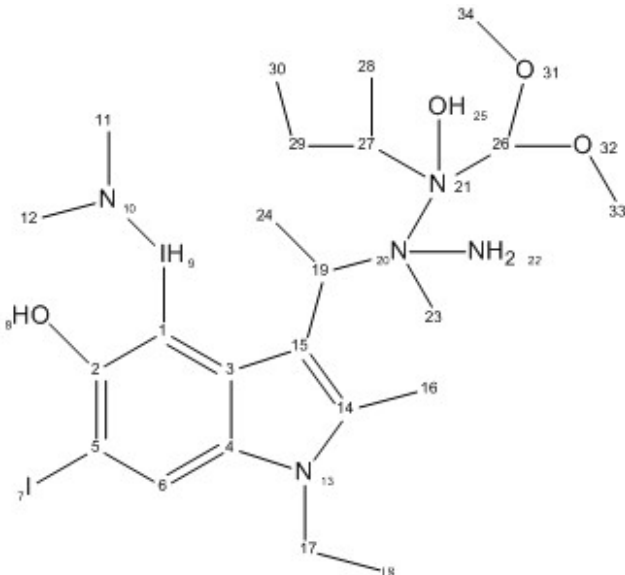


Figure 1. The hypermolecule built on 40 serotonin derivatives of the dataset

Table 1. Molecular structures (in SMILES code) of Serotonin derivatives with their log P and CID (taken from PubChem)

Mol.	Canonical SMILES	log P	CID
1	C1=CC2=C(C=C1O)C(=CN2)CCN	0.2	5202
4	C1=CC2=C(C=C1O)C(=CN2)CCCN	0.6	19438874
5	CC(C)CC1=CNC2=C1C=C(C=C2)O	2.5	69951223
6	CCC(C)C1=CNC2=C1C=C(C=C2)O	2.6	69950621
7	CC(CNC)C1=CNC2=C1C=C(C=C2)O	1.1	57825670
8	C1=CC(=C(C2=C1NC=C2CCN)I)O	2	57620180
10	CC(CC1=CNC2=C1C=C(C=C2)O)NC	1.2	23531057
14	CC(C)(CC1=CNC2=C1C=C(C=C2)O)N	0.8	15137728
16	CC(CN)C1=CNC2=C1C=C(C=C2)O	0.5	115292
18	CN(C)CCC1=CNC2=C1C=C(C=C2)O	1.2	10257
19	CC(CC1=CNC2=C1C=C(C=C2)O)N	0.6	2107
20	CC(C)N(CCC1=CNC2=C1C=C(C=C2)O)C(C)C	2.8	71360804
21	CC(C)(C)NCC1=CNC2=C1C=C(C=C2)O	1.2	71040304
22	CCCN(CCC)CCC1=CNC2=C1C=C(C=C2)O	3	169764
23	C1=C2C(=CC(=C1O)I)NC=C2CCN	2	57620181
24	C1=CC2=C(C=C1O)C(=CN2)CCNO	0.2	53831394
25	CC1=C(C=CC2=C1C(=CN2)CCN)O	1.4	23373052
27	CCN1C=C(C2=C1C=CC(=C2)O)CCN	1.3	70378769
28	CNCCCC1=CN(C2=C1C=C(C=C2)O)C	1.5	11447050
29	CN1C=C(C2=C1C=CC(=C2)O)CCN	1	440945
30	CC(=O)NCCC1=CNC2=C1C=C(C=C2)O	0.5	903
31	CC(CC1=CN(C2=C1C=C(C=C2)O)C)N	1.4	72523641
32	C1=CC2=C(C=C1O)C(=CN2)CCNC(=O)O	0.5	67228616
33	CC1=C(C2=C(N1)C=CC(=C2)O)CCNC	1.9	57825649
40	CC1=C(C2=C(N1)C=CC(=C2)O)CC(C)N	1.8	72523635
2	C1=CC2=C(C=C1O)C(C=N2)CCN	0.1	46228506
3	C1=CC2=C(C=C1O)C(=CN2)C=CN	0.6	50937459
9	C1=CC2=C(C=C1O)C(=CN2)CCN(F)F	1.3	54301972
11	CC(C)C1=CNC2=C1C=C(C=C2)O	2	22669491
12	CCCC1=CNC2=C1C=C(C=C2)O	2.2	15366338
13	CCC1=CNC2=C1C=C(C=C2)O	1.7	15366337
15	CC1=CNC2=C1C=C(C=C2)O	1.3	192734
17	CCN(CC)CCC1=CNC2=C1C=C(C=C2)O	1.9	26395
26	C1=C2C(=CC(=C1O)F)NC=C2CCN	0.3	194142
34	CC(C1=CNC2=C1C=C(C=C2)O)O	0.4	18615721
35	CNC(=O)NCCC1=CNC2=C1C=C(C=C2)O	0.3	18360650
36	CN(C)CC1=C(C=CC2=C1C(=CN2)CCN)O	0.8	10922434
37	CC(=NCCC1=CNC2=C1C=C(C=C2)O)C(=O)O	0.7	10043102
38	CCC(=O)NCCC1=CNC2=C1C=C(C=C2)O	0.9	594440
39	C1=C2C(=C(C(=C1F)O)F)C(=CN2)CCN	1.2	194143

COMPUTATIONAL DETAILS

The structures have been optimized at Molecular Mechanics level of theory (Table 2).

Table 2. Log P, correlating descriptor SD, and topological indices (total adjacency AD, 3D distance sum D3D and detour DE) for the set of 40 serotonin in Table 1

Mol.	log P	SD	AD	D3D	DE
1	0.2	-19.518	14	198	568
2	0.1	-19.518	14	198	678
3	0.6	-19.592	14	198	667
4	0.6	-18.122	15	254	658
5	2.5	-17.664	15	238	772
6	2.6	-17.859	15	232	795
7	1.1	-18.807	16	291	780
8	2	-17.442	16	291	768
9	1.3	-18.539	16	305	658
10	1.2	-18.611	16	297	790
11	2	-17.785	14	184	667
12	2.2	-18.122	14	198	1318
13	1.7	-18.048	13	152	904
14	0.8	-19.039	16	279	1350
15	1.3	-19.153	12	117	794
16	0.5	-19.256	15	232	678
17	1.9	-17.939	18	441	673
18	1.2	-18.734	16	305	792
19	0.6	-19.060	15	238	795
20	2.8	-17.039	20	564	673

21	1.2	-18.544	17	355	928
22	3	-16.839	20	606	783
23	2	-18.122	16	305	928
24	0.2	-19.430	15	254	797
25	1.4	-18.839	15	230	785
26	0.3	-19.518	16	286	568
27	1.3	-18.812	16	299	568
28	1.5	-18.313	15	237	790
29	1	-18.674	17	384	558
30	0.5	-19.206	16	281	568
31	1.4	-18.377	17	384	471
32	0.5	-19.206	16	295	386
33	1.9	-17.994	15	238	1048
34	0.4	-18.889	14	184	672
35	0.3	-19.539	18	467	558
36	0.8	-18.838	18	374	1070
37	0.7	-19.054	19	543	1062
38	0.9	-19.206	18	467	1214
39	1.2	-18.838	16	277	1070
40	1.8	-17.985	16	277	786

Topological indices have been computed by TOPOCLUJ software [8]; some of them (Connectivity = C, Total adjacency = Ad, Detour = De, Distance = Di, D3D, SD), and log P are listed in Table 2.

RESULTS AND DISCUSSION

In this paper, mass fragments are used for weighting the binary vector of ligand superposition over the statistically significant positions of the hypermolecule, according to Diudea's algorithm [9].

Data reduction

The local correlation-weighted descriptors are summed to give SD global descriptor, over the following significant positions in the hypermolecule: H1, H14, H16, H17, H20, H21, H22, H23, H24, H26, H27, H28, H29, H30, H32, H34. SD correlation with $\log P = 19.839 + 0.999 \times \text{XSD}$, $R^2 = 0.839$, $n = 40$, $s = 0.310$, $F = 199.179$, and the best results are listed below and in Table 3.

QSAR models

The models were performed on the training set (the first 25 structures in Table 1) and the best results are listed below and in Table 3. The number of descriptors was limited to three, to fulfil the considerations of Topliss and Costello [10].

Table 3. Best models in describing $\log P$ in the training set of serotonin in Table 1

	Descriptors	R^2	Adjust. R^2	St. Error	F
1	SD	0.847	0.841	0.321	128.053
2	AD	0.277	0.246	0.699	8.830
3	D3D	0.236	0.203	0.719	7.128
4	SD, D3D	0.8483	0.8346	0.3277	61.552
5	SD, Di	0.8482	0.8344	0.3278	61.466
6	SD, CjDe	0.8483	0.8345	0.3277	61.515
7	SD, CfDe	0.8482	0.8344	0.3279	61.331
8	SD, D3D, AD	0.8588	0.8387	0.3235	42.603
9	SD, CjDi, CjDe	0.8575	0.8371	0.3251	42.139
10	SD, CjDe, CfDi	0.8558	0.8352	0.3270	41.552
11	SD, Di, D3D	0.8520	0.8308	0.3313	40.298
12	SD, De, CjDi	0.8509	0.8296	0.3325	39.972

(i) Monovariate regression

$$\log P = 20.392 + 1.031 \times SD$$

(ii) Bivariate regression

$$\log P = 20.818 + 1.050 \times SD - 0.0003 \times D3D$$

(iii) Trivariate regression

$$\log P = 15.76 + 1.02 \times SD + 0.4 \times D3D - 0.005 \times AD$$

Model Validation

(a) Leave-one-out

The performances in leave-one-out analysis related to the models listed as the best in Table 3 are presented in Table 4 [11, 12].

Table 4. Leave-one-out analysis for best log P models (Table 3).

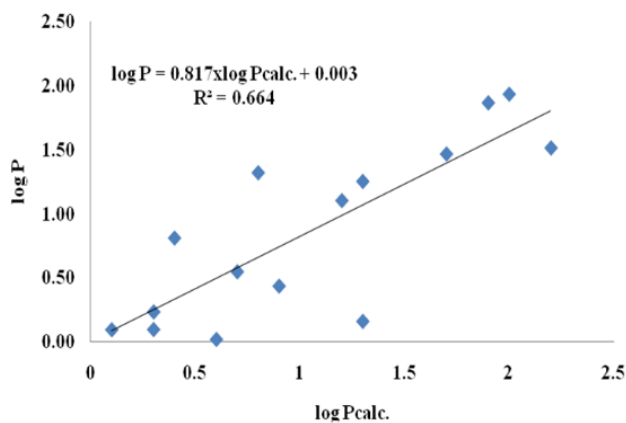
	Descriptors	Q²	R²-Q²	St. Error_{loo}	F_{loo}
1	SD	0.8272	0.205	0.3421	110.134
4	SD, D3D	0.8105	0.037	0.3583	98.371
8	SD, D3D, AD	0.7848	0.074	0.3817	83.911

(b) External Validation

The values log P for the test set of serotonin (Table 1, last 15 molecules) were calculated by using the best equation (with three variables) in Table 3, entry 8. Data are listed in Table 5 and the monovariate correlation: $\log P = 0.35 \times \log P_{\text{calc.}} + 0.813$; n=15; R²=0.664; s=0.41; F=25.785 is plotted in Figure 2.

Table 5. Calculated values of log P for the molecules in the test set (Table 1)

Mol.	log P	log P _{calc.}
2	0.1	0.10
3	0.6	0.02
9	1.3	1.25
11	2	1.93
12	2.2	1.52
13	1.7	1.47
15	1.3	0.16
17	1.9	1.87
26	0.3	0.24
34	0.4	0.81
35	0.3	0.10
36	0.8	1.32
37	0.7	0.55
38	0.9	0.44
39	1.2	1.10

**Figure 2.** The plot log P vs. log P_{calc.} for the test set (external validation)

Clearly, the model (Table 3, entry 8) is not a predictive one; we only used this model to select the best independent descriptors for log P in the set of studied serotonin.

(c) Similarity Cluster Validation

Validation can be performed by calculating log P for the molecules in the test set with equations learned on clusters of similarity: each of the 15 molecules is the leader in its own cluster, selected by (2D) similarity among the 25 structures of the initial learning set [13]. The values log P_{calc.} for each of the

15 molecules in the test set were computed by 15 new equations (the leader being left out) with the same descriptors as in eq. 8, Table 3. Data are listed in Table 6 and the monovariate correlation: $\log P = 0.184 \times \log P_{\text{calc.}} + 1.014$; n=15; R²=0.913; s=0.21; F=136.053 is plotted in Figure 3.

Table 6. Calculated values of log P by similarity clusters, for the molecules in the test set (Table 1)

Mol.	log P	log P _{calc.}
2	0.1	0.05
3	0.6	0.12
9	1.3	1.14
11	2	1.92
12	2.2	1.66
13	1.7	1.20
15	1.3	1.10
17	1.9	1.88
26	0.3	0.25
34	0.4	0.52
35	0.3	0.16
36	0.8	0.70
37	0.7	0.40
38	0.9	0.52
39	1.2	1.15

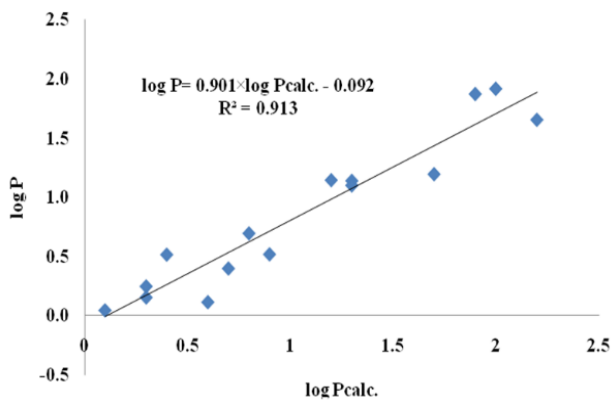


Figure 3. The plot log P vs. log P calc. for the test set (similarity clusters)

From Figure 3 one can see the better fitting of data predicted by clustering the test set according to (2D) similarity of each of the 15 molecular structures, taken as leaders.

CONCLUSIONS

A set of 40 serotonin derivatives, downloaded from the PubChem database, was submitted to a QSAR study. The best models have been validated in the external test set and in a new version of validation/prediction by using clusters of similarity, that provides „quasi-congeneric” structures, important for a prediction that surpasses the model. This punctual prediction is much more important in comparison with a more general model but with a lower predictability.

REFERENCES

- [1]. S.N. Young, *Rev. Psychiatr. Neurosci.* **2007**, 32, 394.
- [2]. M.W. King, Med. Biocbem. Page. Indiana Univ. School Med. Retrieved 1 Dec. **2009**.
- [3]. M. Berger, J.A. Gray, B.L. Roth, *Annu. Rev. Med.* **2009**, 60, 355.
- [4]. P. Bianchi, D.R. Pimentel, M.P. Murphy, W.S. Colucci, A. Parini, *Federation of American Societies for Experimental Biology Journal*, **2005**, 19, 641.
- [5]. K. Kang, S. Park, Y.S. Kim, S. Lee, K. Back, *Appl. Microbiol. Biotechnol.* **2009**, 83, 27.
- [6]. PubChem database, accessed 20.08. **2014**.
- [7]. A.T. Balaban, A. Chiriac, I. Motoc, Z. Simon, Steric Fit in QSAR (Lectures Notes in Chemistry, Vol. 15), Springer Berlin, **1980**.
- [8]. O. Ursu, M.V. Diudea, TOPOCLUJ software program, Babes-Bolyai University, Cluj, **2005**.
- [9]. C.D. Moldovan, A. Costescu, G. Katona, M.V. Diudea., *J. Math. Chem.*, **2008**, 45, 442.
- [10]. J.G. Topliss, R.J. Costello, *J. Med. Chem.*, **1972**, 15, 1066.
- [11]. D.M. Hawkins, S.C. Basak, D. Mills, *J. Chem. Inf. Comput. Sci.*, **2003**, 43, 579.
- [12]. L. Jäntschi, AcademicDirect Library of software, **2005**. Available at:
<http://l.academicdirect.org/Chemistry/SARs/SARs/loo/>
- [13]. A.M. Harsa, T.E. Harsa, S.D. Bolboacă, M.V. Diudea, *Curr. Comput.-Aided Drug Des.* **2014**, 10, 115.

QSAR STUDY ON DIOXINS

RALUCA MĂTIEŞ^a, BEATA SZEFLER^b and MIRCEA V. DIUDEA^{a*}

ABSTRACT. This paper presents a QSAR study realized on a set of 40 dioxins, known as pollutants, substances that are toxic for the environment. The study is based on the hypermolecule approach and on the prediction by similarity clustering. The results show a good modeling of logP parameter with the correlation weighted descriptor and some topological indices derived from Cluj matrices and also with the calculated HOMO energy level for the set of studied molecules.

Keywords: *dioxin, hypermolecule, QSAR, Cluj descriptors*

INTRODUCTION

Dioxins are unwanted pollutants in the environment, occurring in industrial processes (incineration pulp and paper bleaching with chlorine), also in the manufacture of pesticides, fungicides or herbicides [1].

The term dioxin refers to dibenzo-p-dioxins (PCDD), polychlorinated dibenzofurans (PCDF) and coplanar polychlorinated biphenyls (PCBs) which show similar biological and toxicological properties. These compounds are contaminants of lipophilic fat and concentrate in biological systems.

PCDDs/ PCDFs and PCBs have toxic effects on the nervous system, immune, endocrine and reproductive systems. International Agency for Research on Cancer has classified 2,3,7,8-TCDD as the most toxic congener of polychlorinated dibenzo-p-dioxins and classified in Group 1 carcinogen to humans [2-3].

Dioxins are odorless and colorless organic compounds, insoluble in water but soluble in fat. These compounds have in their structure carbon, hydrogen, oxygen and chlorine. Dioxins are biodegradable, but are persistent and bio-accumulates in foods [4].

^a Department of Chemistry, Faculty of Chemistry and Chemical Engineering, Babeş-Bolyai University, 400028 Cluj, Romania.

^b Department of Physical Chemistry, Collegium Medicum, Nicolaus Copernicus University, Kurpińskiego 5, 85-096, Bydgoszcz, Poland.

* Corresponding author: diudea@chem.ubbcluj.ro

In general, exposure to dioxins in humans cause serious health problems such as cancer, chloracne, reproductive and developmental disorders. Human exposure to dioxins is achieved through diet (about 95%) and only a small amount of dioxins taken by breathing or absorbed through the skin. Dioxins focus on the food chain, accumulate in animal fat, which explains why animals and animal products show a higher content of dioxins than plants or water. [5]

TCDD is a carcinogen, an endocrine disrupter, an agent that induces oxidative stress both in humans and in vertebrates. TCDD exposure causes cardiovascular dysfunction, neuronal degeneration and even craniofacial malformations. [6-8]

Chemical Graph Theory is a branch of mathematics applied to Chemistry. A *graph* $G(V,E)$ is a pair of two sets, V (vertices) and E (edges), the last one being a binary relation defined on V [9]. A molecular graphs, in which vertices are atoms and edges are covalent bonds, can be represented by a number, a sequence number, a matrix or polynomial. A single number representing a graph is also called a topological index and is useful in QSAR/QSPR (Quantitative Structure–Activity/ Property Relationships) studies.

DATA SET

From the PubChem [10] database, we selected 40 molecular structures of dioxins with their log P associated values. LogP is a measure of hydrophobic interactions of ligands with a biological receptor. LogP values can be determined experimentally or computationally. Table 1 lists the dioxin names (IUPAC, cf. Figure 1, left, numbering) and their logP values. On the set of all dioxin structures, a hypermolecule (Figure 1, right) was built up, as a collection of common skeletal and uncommon substructures [11].

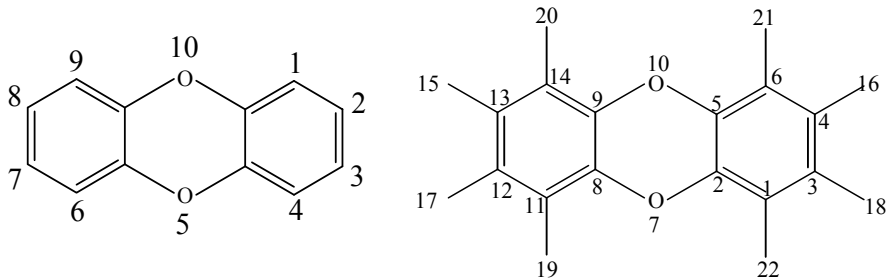


Figure 1. Dioxin IUPAC (left) and the hypermolecule (right) with atom numbering

Table 1. Dioxins –IUPAC name (cf. Figure 1, left) and their log P

	Name	log P
1	2,3,7,8-tetrachlorodibenzo-p-dioxin	6.4
2	Octachlorodibenzo-4-dioxin	8.1
3	2,7-dichlorodibenzo-4-dioxin	4.3
4	1,2,3,6,7,8-hexachlorodibenzodioxin	7.4
5	1,2,3,4,7,8-hexachlorodibenzodioxin	8.4
6	1,2,3,4,6,7,8-heptachlorodibenzodioxin	7.5
7	2-chlorodibenzo-4-dioxin	5
8	2,8-dichlorodibenzo-4-dioxin	4.3
9	1-Chlorodibenzo-p-dioxin	5
10	2,3-dichlorodibenzo-4-dioxin	5.2
11	1,2,3,7,8-pentachlorodibenzo-p-dioxin	6.6
12	1,2,4-trichlorodibenzo-1,4-dioxin	4.9
13	1,2,3,4-tetrachlorodibenzodioxin	7.2
14	1,2,7,8-tetrachlorodibenzo-p-dioxin	6
15	1,3,7,8-tetrachlorodibenzo-4-dioxin	6.3
16	1,6-Dichlorodibenzo-para-dioxin	5.7
17	1,3,6,8-tetrachlorodibenzo-p-dioxin	6.3
18	1,3,7-Trichlorodibenzo-p-dioxin	5.7
19	1,2,3,6,7,9-hexachlorodibenzo-p-dioxin	6.9
20	1,2,3,4,6,7,9-Heptachlorodibenzodioxin	7.5
21	1,2,3,8-tetrachlorodibenzo-p-dioxin	6
22	1,3-Dichlorodibenzo-para-dioxin	5
23	1,2,4,6,7,9-hexachlorodibenzo-p-dioxin	6.8
24	1,2,3,4,7-pentachlorodibenzo-p-dioxin	7.8
25	2,3,7-trichlorodibenzo-p-dioxin	5.8
26	1,2,6,8-tetrachloro dibenzo-p-dioxin	6.4
27	1,4,7,8-tetrachloro dibenzo-p-dioxin	6.4
28	1,4,6,9-tetrachloro dibenzo-p-dioxin	5.6
29	1,2,6,9-tetrachloro dibenzo-p-dioxin	5.6
30	1,2,3,7-tetrachloro dibenzo-p-dioxin	6
31	1,2,4,7,8-pentachlorodibenzo-p-dioxin	6.2
32	1,2,4,8-tetrachloro dibenzo-p-dioxin	6.4
33	1,2,4,7-tetrachloro dibenzo-p-dioxin	6.4
34	1,2,4,6-tetrachloro dibenzo-p-dioxin	5.6
35	1,2,3,9-tetrachloro dibenzo-p-dioxin	6.4
36	1,2,3,6-tetrachloro dibenzo-p-dioxin	6.4
37	1,3,6,9-tetrachloro dibenzo-p-dioxin	6.3
38	1,2,4,9-tetrachloro dibenzo-p-dioxin	5.6
39	1,2,4,6,8,9-hexachloro dibenzo-p-dioxin	6.8
40	1,2,3,4,6,8-hexachloro dibenzo-p-dioxin	7.2

COMPUTATIONAL DETAILS

The structures of dioxins have been optimized, in gas phase, at the Hartree-Fock HF (6-31g(d,p)) level of theory by Gaussian 09 [12]. Topological indices (see Table 2) have been computed by TOPOCLUJ software [13]; HOMO energy (in au) was computed by Gaussian 09.

Table 2. Topological descriptors and HOMO energy (au)

Mol.	Adjacency	Detour	Distance	IE [CfMax]	IE [CfMin]	IP [CfMax]	IP [CfMin]	HOMO
1	20	1700	570	62	620	420	2800	-0.318
2	24	2700	920	130	950	760	4600	-0.337
3	18	1300	410	36	460	300	2000	-0.308
4	22	2200	730	92	780	590	3600	-0.328
5	22	2200	730	93	770	580	3600	-0.328
6	23	2400	820	110	860	670	4100	-0.332
7	17	1200	340	26	390	250	1600	-0.301
8	18	1300	410	36	460	300	2000	-0.307
9	17	1200	330	26	380	250	1600	-0.302
10	18	1300	410	37	460	300	1900	-0.307
11	21	1900	650	77	690	500	3200	-0.323
12	19	1500	460	49	510	380	2200	-0.314
13	20	1700	540	64	580	440	2600	-0.317
14	20	1700	560	62	610	430	2800	-0.318
15	20	1700	560	62	610	430	2800	-0.320
16	18	1400	400	36	450	320	1900	-0.310
17	20	1700	550	61	600	430	2700	-0.322
18	19	1500	480	48	530	360	2300	-0.315
19	22	2200	720	92	770	590	3600	-0.330
20	23	2400	810	110	850	680	4000	-0.334
21	20	1700	560	62	600	430	2700	-0.318
22	18	1400	400	37	450	310	1900	-0.308
23	22	2200	710	91	760	600	3500	-0.332
24	21	2000	630	77	680	510	3100	-0.323
25	19	1500	490	49	540	360	2400	-0.313
26	20	1700	550	61	600	440	2700	-0.320
27	20	1700	550	62	600	430	2700	-0.321
28	20	1800	540	61	580	450	2600	-0.325
29	20	1700	540	61	590	450	2700	-0.322
30	20	1700	560	62	610	430	2700	-0.318
31	21	2000	640	76	690	500	3200	-0.325
32	20	1700	550	62	600	440	2700	-0.320
33	20	1700	550	62	600	440	2700	-0.320
34	20	1800	540	62	590	450	2600	-0.322
35	20	1700	550	62	590	440	2700	-0.319
36	20	1700	550	62	590	440	2700	-0.320
37	20	1700	540	61	590	440	2700	-0.324
38	20	1800	540	62	590	450	2600	-0.322
39	22	2200	710	91	760	590	3500	-0.332
40	22	2200	720	92	760	590	3500	-0.330

The hypermolecule works like a biological receptor, over which the ligands (i.e. dioxins) are superposed/aligned. According to this superposition, *binary vectors* were constructed, with 1 when for a given position of the hypermolecule exists an atom in the current molecule, and zero, otherwise. In the so built binary vectors, the values 1 are next replaced by the partial charges (given as Supplementary data, at request) of ligand atoms, as computed at the HF level of theory.

RESULTS AND DISCUSSION

Data Reduction

In this step, the descriptors with variance <10% and intercorrelation > 0.80 (two descriptors highly correlated bring quite the same information on the molecule, one of them being sufficient) were discarded.

Evaluation of hypermolecule statistically significant positions was made by removing columns of data that contributes little to the correlation coefficient. From 22 initial positions we selected 16 positions (1, 2, 3, 4, 5, 8, 9, 10, 12, 13, 14, 16, 18, 19, 20 and 21). Correlation weighting [14] was performed on all the statistically significant positions in the hypermolecule: the local descriptors (actually the partial charges, computed at HF level of theory), have been multiplied by the corresponding correlation coefficients thus resulting new weighted vectors CD_{ij} . Next, these new descriptors are summed to give a global descriptor, which is a linear combination of the local correlating descriptors for the significant positions in the hypermolecule [15-17].

Modeling log P

The 40 structures were divided into two sets: the learning set (25 molecules) and the test set (15 molecules: 2; 3; 5; 6; 12; 13; 14; 17; 18; 21; 24; 26; 27; 28 and 37).

The models were performed on the learning set, the best results being listed below and in Table 3. The number of descriptors was limited to three, to fulfill the considerations of Topliss and Costello [18].

- (i) Monovariate regression
 $\log P = 21.806 + 0.918 \times DS$
- (ii) Bivariate regression
 $\log P = 19.822 + 0.823 \times DS + 0.001 \times Distance$
- (iii) Three-variate regression
 $\log P = 17.628 + 0.842 \times DS + 0.220 \times Adj. - 0.001 \times Detour$

Table 3. QSAR models and their statistics

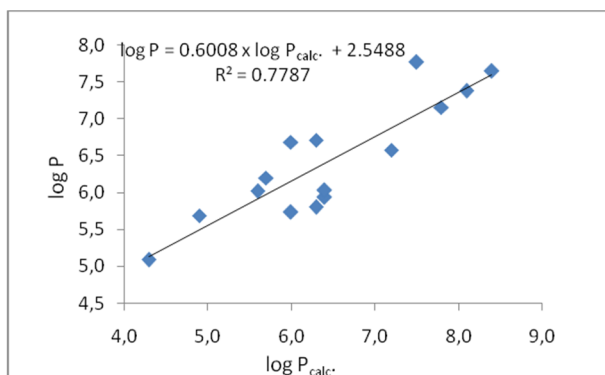
	Descriptors	R ²	Adjust. R ²	St. Error	F
1	DS	0.908	0.904	0.253	226.639
2	Distance	0.832	0.825	0.341	114.197
3	IP min	0.828	0.820	0.345	110.431
4	IE min	0.826	0.818	0.347	108.872
5	IE max	0.824	0.816	0.349	107.438
6	Adjacency	0.817	0.809	0.356	102.717
7	DS, Adjacency	0.909	0.901	0.257	109.741
8	DS, Distance	0.909	0.901	0.257	109.879
9	DS, IE max	0.909	0.900	0.257	109.279
10	DS, IE min	0.909	0.901	0.257	109.639
11	DS, HOMO	0.908	0.900	0.257	109.069
12	Distance, IE min	0.845	0.831	0.335	60.045
13	DS, Adjacency, Detour	0.912	0.899	0.259	72.272
14	DS, Detour, IE max	0.911	0.898	0.260	71.706
15	Distance, IE max, IE min	0.847	0.825	0.340	38.809
16	Adjacency, Detour, Distance	0.839	0.816	0.350	36.399
17	Detour, Distance, IE max	0.838	0.815	0.350	36.225
18	Detour, IE max, IP max	0.8352	0.8117	0.3534	35.4878

External Validation

For the 25 molecules in the learning set, the best model was recorded for the trivariate model (DS, Adjacency and Detour), as shown in Table 3, (eq. 13). This model was used to predict log P of the molecules in the test set (15 molecules). Data for this external validation are listed in Table 4 while the plot of calculated logP vs. database-values is shown in Figure 2.

Table 4. LogP calc. cf (13) Table 3 on the molecules of the test set

Molecule	log P	log P _{calc.}
2	8.1	7.4
3	4.3	5.1
5	8.4	7.7
6	7.5	7.8
12	4.9	5.7
13	7.2	6.6
14	6	5.7
17	6.3	6.7
18	5.7	6.2
21	6	6.7
24	7.8	7.2
26	6.4	5.9
27	6.4	6.0
28	5.6	6.0
37	6.3	5.8

**Figure 2.** The plot log P vs. log P_{calc.} for the test set (external validation)

Prediction by Clusters of Similarity

For the molecules in the test set, prediction can be done by means of similarity clusters: each of the 15 molecules in the test set is the leader of its own cluster, selected by 2D similarity among the 25 structures of the learning set (each cluster comprising about 15-20 molecules). The values $\log P$ were predicted by 15 new equations (the leader being left out) with the same descriptors as in eq. 13, Table 3. Data are listed in Table 5 and the monovariate correlation:

$$\log P = 0.763 \times \log P_{\text{calc.}} + 1.392; n = 15; R^2 = 0.924; s = 0.331; F = 157.899$$

is plotted in Figure 3.

Table 5. Log $P_{\text{calc.}}$ on molecules leading to clusters of similarity

Molecule	$\log P$	$\log P_{\text{calc.}}$
2	8.1	7.8
3	4.3	4.6
5	8.4	7.6
6	7.5	7.7
12	4.9	5.2
13	7.2	6.7
14	6	5.8
17	6.3	6.3
18	5.7	5.9
21	6	6.3
24	7.8	7.1
26	6.4	5.9
27	6.4	6.2
28	5.6	5.7
37	6.3	6

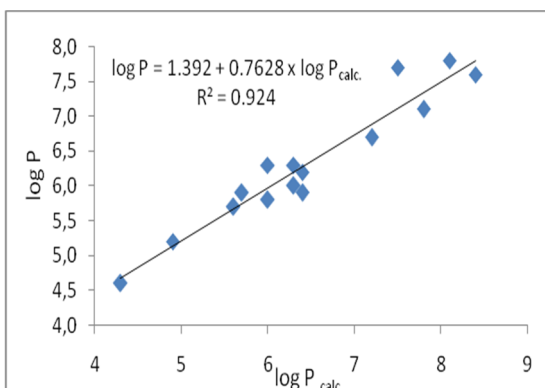


Figure 3. The plot $\log P$ vs. $\log P_{\text{calc.}}$ by similarity clusters

CONCLUSION

A regression analysis was performed for 40 molecules of dioxins class. The study was focused on the correlation weighting of predictor variables describing the hypermolecule built up on the data set and prediction by clusters of similarity. The results showed a good modeling of $\log P$ by Cluj topological indices, HOMO energy level and the descriptor summing the contributions of the statistically significant positions in the hypermolecule. Validation of the model was done by an external set as well as by means of similarity clusters. Similarity calculation (in 2D) was done using the program TOPOCLUJ.

ACKNOWLEDGEMENS

R.M. acknowledges to Project POSDRU/159/1.5/S/132400, “Tineri cercetători de succes – dezvoltare profesională în context interdisciplinare și internațional”.

REFERENCES

- [1] Schecter, L. Birnbaum, J.J. Ryan, J.D. Constable, *Environmental Research*, **2006**, 419, 428.
- [2] B. Olanca, G.C. Cakirogullari, Y. Ucar, D. Kirisik, D. Kilic, *Chemosphere*, **2014**, 94, 13.
- [3] J.M. Llobet, J.L. Domingo, A. Bocio, C. Casas, A. Teixidó, L. Müller, *Chemosphere*, **2003**, 50, 1193.
- [4] P.L. Galbenu, *Lucrări Științifice Medicină Veterinară*, Timișoara, **2009**, XLII (2).
- [5] M. De Vries, R.P. Kwakkel and A. Kijlstra, *NJAS*, **2006**, 54-2, 207.
- [6] Q. Liu, M.L. Rise, J.M. Spitsbergen, T.S. Hori, M. Mierity, S. Geis, J.E. McGraw, G. Goety, J. Larson, R.J. Huty, M.J. Carvan III, *Aquatic Toxicology*, **2013**, 140-141, 356.
- [7] G. Xu, Q. Zhou, C. Wan, Y. Wang, J. Liu, Y. Li, X. Nie, C. Cheng, G. Chen, *NeuroToxicology*, **2013**, 37, 63.
- [8] Y. Li, G. Chen, J. Zhao, X. Nie, C. Wan, J. Liu, Z. Duan, G. Xu, *Toxicology*, **2013**, 312, 132.
- [9] M.V. Diudea, I. Gutman, L. Jäntschi, *Molecular Topology*, NOVA, New York, 2002.
- [10] PubChemdatabase; accessed 23.03. 2015.
- [11] A.T. Balaban, A. Chiriac, I. Motoc, and Z. Simon, Steric Fit in QSAR (*Lectures Notes in Chemistry*, Vol. 15), Springer, Berlin, **1980**.
- [12] **Gaussian 09**, Gaussian Inc Wallingford CT, Revision A.1, M.J. Frisch, G.W. Trucks, H.B. Schlegel, G.E. Scuseria, M.A. Robb, J.R. Cheeseman, G. Scalmani, V. Barone, B. Mennucci, G.A. Petersson, H. Nakatsuji, M. Caricato, X. Li, H.P. Hratchian, A.F. Izmaylov, J. Bloino, G. Zheng, J.L. Sonnenberg, M. Hada, M. Ehara, K. Toyota, R. Fukuda, J. Hasegawa, M. Ishida, T. Nakajima, Y. Honda, O. Kitao, H. Nakai, T. Vreven, J.A. Montgomery, J.E. Peralta, F. Ogliaro, M Bearpark, J.J. Heyd, E. Brothers, K.N. Kudin, V.N. Staroverov, R. Kobayashi, J. Normand, K. Raghavachari, A. Rendell, J.C. Burant, S.S. Iyengar, J. Tomasi, M. Cossi, N. Rega, N.J. Millam, M. Klene, J.E. Knox, J.B. Cross, V. Bakken, C. Adamo, J. Jaramillo, R. Gomperts, R.E. Stratmann, O. Yazyev, A.J. Austin, R. Cammi, C. Pomelli, J.W. Ochterski, R.L. Martin, K. Morokuma, V.G. Zakrzewski, G.A. Voth, P. Salvador, J.J. Dannenberg, S. Dapprich, A.D. Daniels, Ö. Farkas, J.B. Foresman, J.V. Ortiz, J. Cioslowski, D.J. Fox. **2009**.
- [13] O. Ursu, M.V. Diudea, “TOPOCLUJ software program”, Babes-Bolyai University, Cluj, **2005**.
- [14] A.A. Toropov, A.P. Toropova, *J. Mol. Struct. (Theochem)*, **2001**, 538, 287.
- [15] C.D. Moldovan, A. Costescu, G. Katona, M.V. Diudea, *MATCH Commun. Math. Comput. Chem.*, **2008**, 60, 977.
- [16] T.E. Harsa, A.M. Harsa, B. Szefler, *Cent. Eur. J. Chem.*, **2014**, 12, 365.
- [17] A.M. Harsa, T.E. Harsa, S. Bolboaca, M.V. Diudea, *Curr. Comput.-Aided Drug Design*, **2014**, 10, 115.
- [18] J.G. Topliss, R.J. Costello, *J. Med. Chem.*, **1972**, 15, 1066.

QSAR AND DOCKING STUDY ON INDOLIZINES BY SIMILARITY CLUSTERING

BEATA SZEFLER^{a*}, TEODORA E. HARSA^b, ALEXANDRA M. HARSA^b

ABSTRACT. A Quantitative Structure-Activity Relationship study, based on molecular descriptors calculated with correlation weights within the hypermolecule, that mimics the investigated correlational space, was performed on a set of 25indolizines (PubChem database). The best models describing IC50 of this set of indolizines were validated by the leave-one-out procedure, in the external test set and in a new version of prediction by using clusters of similar molecules. The best prediction was provided by the similarity cluster procedure.

Keywords: *Indolizines, QSAR (Quantitative Structure-Activity Relationships), IC50, similarity, Hypermolecule, Docking, Binding energy.*

INTRODUCTION

Indolizines represent a class of heteroaromatic compounds (of pharmacological importance) containing two condensed (5- and 6-memebered) rings bridged by a nitrogen atom. Other names for indolizines in literature include pyrindole, pyrrodine, pyrrolo [1,2-a]pyridine and pyrrocoline. The aromatic indolizine does not occur in nature, but the reduced derivatives are natural products. The biological activities include antimicrobial, antioxidant, anti-inflammatory, anti-tuberculosis, anticonvulsant activity, enzymes inhibition activity and cardiovascular activity (as calcium entry blocker) [1].

Many indolizine derivatives have been isolated from plants, insects, animals, marine lives, and microbes [2]. The importance of indolizines has promoted a variety of synthetic routes in medicinal chemistry (e.g. Tschitschibabin reaction, 1,3-dipolar cycloadditions, or various cyclisation reactions [3]), targeting

^a Department of Physical Chemistry, Collegium Medicum, Nicolaus Copernicus University, Kurpińskiego 5, 85-950, Bydgoszcz, Poland.

^b Babes-Bolyai University, Faculty of Chemistry and Chemical Engineering, Arany Janos street 11, Cluj-Napoca, RO-400028, Romania.

* Corresponding author: beatas@cm.umk.pl

indolizines with well-defined substitution patterns. Synthetic indolizines are important as histamine H3 receptor antagonists, 5-HT3 receptor antagonists, microtubule inhibitors showing strong antitumor activities [4].

In the present study, a molecular docking analysis has been performed on indolizine derivatives on the proteins 1GA0, 4O0Z, 4O10, then we made a QSAR study to predicting IC₅₀ of indolizine derivatives.

STRUCTURAL MOLECULAR DATA

A set of 25 indolizine were taken from PubChem Database [5] (Table 1) and were divided into a training set (15 molecules) and a test set (10 molecules), taken randomly. The property chosen for modeling was IC₅₀ (μM) 15-LO from soybeans (see Table 1) [6].

Table 1. IC₅₀ (μM) 15-LO from soybeans, Smiles code and CID (PubChem) for 25 indolizines

	Canonical SMILES	CID	IC ₅₀
1	C1=C(C=C[N]2C1=CC(=C2C3=CC=CC=C3)C4=CC=CC=C4)C#N	482634	30±2
2	C1=C(C=C[N]2C1=C(C(=C2C3=CC=CC=C3)C4=CC=CC=C4)OC)C#N	10853428	33±2
3	C1=CC=C(C=C1)COC2=C3C=C(C=CN3C(=C2C4=CC=CC=C4)C5=CC=CC=C5)C#N	57399922	31±2
4	[N]12C(=C(C(=C1C=C(C=C2)C#N)C3=CC=CC=C3)C4=CC=CC=C4)C5=CC=CC=C5	491919	27±2
5	[N]12C(=C(C(=C1C=C(C=C2)C#N)C3=CC=CC=C3)C4=CC=CC=C4)C5=CC=CC=C5	482635	28±1
6	COCl=CC=CC=C1C2=C3C=C(C=CN3C(=C2C4=CC=CC=C4)C5=CC=CC=C5)C#N	10644682	20±1
7	COCl=CC=CC(=C1)C2=C3C=C(C=CN3C(=C2C4=CC=CC=C4)C5=CC=CC=C5)C#N	10668699	20±1
8	C1=CC=C(C=C1)C2=C(N3C=CC(=CC3=C2C=O)C#N)C4=CC=CC=C4	491918	29±1
9	CC(=O)C1=C2C=C(C=CN2C(=C1C3=CC=CC=C3)C4=CC=CC=C4)C#N	491856	23±1
10	C1=CC(=CC=C1C2=C(N3C=CC(=CC3=C2)C#N)C4=CC=C(C=C4)F)F	57394641	30±6
11	O(C1=C4[N](C(=C1C2=CC=CC=C2)C3=CC=CC=C3)C=C(C=C4)C#N)C(=O)C	10066595	31±2
12	CC(C1=C2C=C(C=CN2C(=C1C3=CC=CC=C3)C4=CC=CC=C4)C#N)O	491916	26±2
13	CC1=C2C=C(C=CN2C(=C1C3=CC=CC=C3)C4=CC=CC=C4)C#N	491857	27±2
14	C1=CC=C(C=C1)C2=C(N3C=CC(=CC3=C2C(=O)C4=CC=CC=C4)C#N)C5=CC=CC=C5	491920	23±1
15	C1=CC=C(C=C1)C2=C(N3C=CC(=CC3=C2CO)C#N)C4=CC=CC=C4	491917	26±1
16	C1=CC=C(C=C1)C2=C(N3C=CC(=CC3=C2OS(=O)(=O)C4=CC=CC=C4)C#N)C5=CC=CC=C5	57394621	24±3
17	CN(C)S(=O)(=O)OC1=C2C=C(C=CN2C(=C1C3=CC=CC=C3)C4=CC=CC=C4)C#N	57396377	25±2
18	C1=CC(=CC=C1C2=C(N3C=CC(=CC3=C2)C#N)C4=CC=C(C=C4)Cl)Cl	57392897	33±7
19	C1=C(C=C[N]2C1=C(C(=C2C3=CC=CC=C3)C4=CC=CC=C4)OCC5=CC=C(C=C5)C#N	57401703	37±4

	Canonical SMILES	CID	IC ₅₀
20	C1=C(C=C[N]2C1=CC(=C2C3=CC=CC=C3)C4=CC=CC=C4)C#N	482634	30±2
21	CC1=CC=C(C=C1)C2=C(N3C=CC(=CC3=C2)C#N)C4=CC=C(C=C4)C	57392898	27±3
22	CO(C1=CC=CC=C1)C2=C3C=C(C=CN3C(=C2C4=CC=CC=C4)C5=CC=CC=C5)C#N	491877	21±3
23	CS(=O)(=O)OC1=C2C=C(C=CN2C(=C1C3=CC=CC=C3)C4=CC=CC=C4)C#N	53855501	22±2
24	CCS(=O)(=O)OC1=C2C=C(C=CN2C(=C1C3=CC=CC=C3)C4=CC=CC=C4)C#N	57403346	28±6
25	C1=CC=C(C=C1)COCOC2=C3C=C(C=CN3C(=C2C4=CC=CC=C4)C5=CC=CC=C5)C#N	57403432	46±4

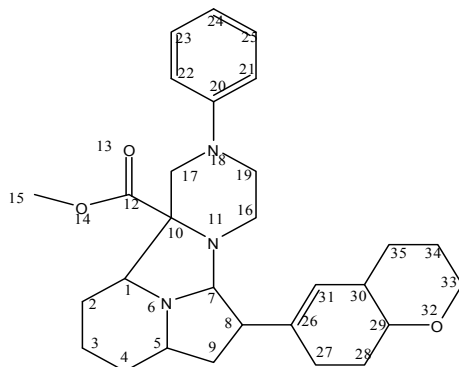


Figure 1. The hypermolecule comprising the common features of the dataset

Three proteins: beta lactamase (Figure 2, left), nicotinamide phosphoribosyltransferases (Figure 2, middle, right), were downloaded from RCSB protein data bank with the PDB code-1GA0, 4O0Z, 4O10 [7].

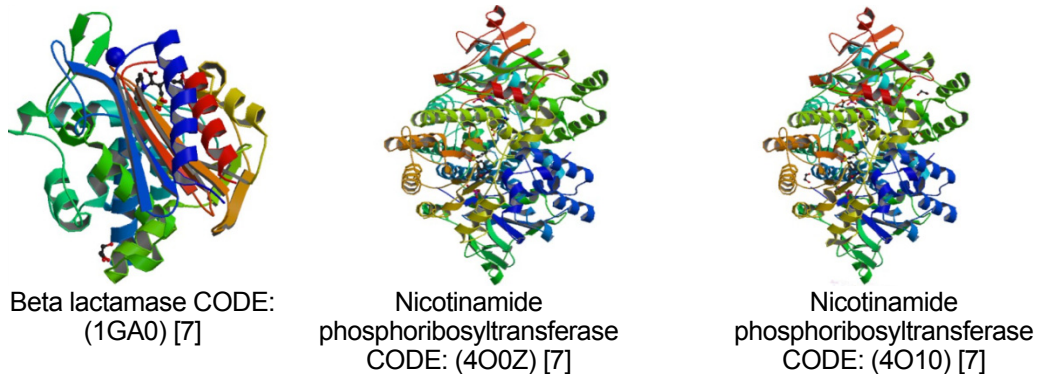


Figure 2. The proteins (beta lactamase, nicotinamide phosphoribosyltransferases) (RCSB PDB CODE: 1GA0, 4O0Z, 4O10).

Using the latest version of AutoDock4.2, the protein molecule is loaded and stored as protein.pdb after assigning hydrogen bonds [8]. The investigative ligand was loaded and their torsions along their rotatable bonds (see Table 2) are assigned and the file was saved as ligand.pdbqt. The grid menu is toggled [9]; after loading protein.pdbqt the map files were selected directly with setting up the grid points appropriate for the searching of ligand within the active site of the protein molecule. In case of protein 4O10 docking was made for two active sides of the enzyme. This way the grid parameter files are created with setting up the map files directly. The docking parameter files were completed by using the Lamarckian genetic algorithm [10].

Table 2. Starting parameters of docking for the investigated ligands

CID of Ligand	Molecular Weight	Molecular Formula	H-Bond Donor	H-Bond Acceptor	Torsions (rotatable bonds)
1	482634	<u>C₂₁H₁₄N₂</u>	0	1	4
2	10853428	<u>C₂₂H₁₆N₂O</u>	0	2	4
3	57399922	<u>C₂₈H₂₀N₂O</u>	0	2	5
4	491919	<u>C₂₈H₂₀N₂</u>	0	1	8
5	482635	<u>C₂₇H₁₈N₂</u>	0	1	8
6	10644682	<u>C₂₈H₂₀N₂O</u>	0	2	4
7	10668699	<u>C₂₈H₂₀N₂O</u>	0	2	3
8	491918	<u>C₂₂H₁₄N₂O</u>	0	2	4
9	491856	<u>C₂₃H₁₆N₂O</u>	0	2	7
10	57394641	<u>C₂₁H₁₂F₂N₂</u>	0	3	10
11	10066595	<u>C₂₃H₁₆N₂O₂</u>	0	3	7
12	491916	<u>C₂₃H₁₈N₂O</u>	1	2	8
13	491857	<u>C₂₂H₁₆N₂</u>	0	1	6
14	491920	<u>C₂₈H₁₈N₂O</u>	0	2	7
15	491917	<u>C₂₈H₁₈N₂O</u>	0	2	10
16	57394621	<u>C₂₇H₁₈N₂O₃S</u>	0	4	3
17	57396377	<u>C₂₃H₁₉N₃O₃S</u>	0	5	1
18	57392897	<u>C₂₁H₁₂Cl₂N₂</u>	0	1	3
19	57401703	<u>C₂₉H₂₂N₂O</u>	0	2	4
20	482634	<u>C₂₁H₁₄N₂</u>	0	1	8
21	57392898	<u>C₂₃H₁₈N₂</u>	0	1	5
22	491877	<u>C₂₉H₂₂N₂O</u>	0	2	2
23	53855501	<u>C₂₂H₁₆N₂O₃S</u>	0	4	4
24	57403346	<u>C₂₃H₁₈N₂O₃S</u>	0	4	3
25	57403432	<u>C₂₉H₂₂N₂O₂</u>	0	3	9

DOCKING RESULTS

Table 3. The final lamarckian genetic algorithm docked state – Binding energy of ligands with the active site of **Beta lactamase (1GA0)** during nine conformations

CID of Ligand	1	2	3	4	5	6	7	8	9	Docked Energy (kcal/mol)
1	482634	-7.5	-7.3	-6.8	-6.8	-6.5	-6.5	-6.3	-6.2	-6.2
2	10853428	-6.5	-6.2	-6.1	-6.1	-6.1	-6.0	-5.9	-5.8	-5.7
3	57399922	-7.3	-7.3	-7.0	-7.0	-6.9	-6.9	-6.9	-6.8	-6.8
4	491919	-8.1	-7.8	-7.6	-7.2	-7.0	-7.0	-6.9	-6.9	-6.8
5	482635	-7.5	-7.4	-7.0	-6.9	-6.9	-6.8	-6.7	-6.6	-6.6
6	10644682	-6.7	-6.7	-6.6	-6.4	-6.4	-6.2	-6.1	-6.0	-5.9
7	10668699	-7.8	-7.7	-7.5	-7.4	-7.3	-7.0	-7.0	-7.0	-6.9
8	491918	-7.0	-6.8	-6.5	-6.5	-6.4	-6.1	-6.0	-5.9	-5.8
9	491856	-7.5	-7.2	-7.0	-6.9	-6.9	-6.8	-6.7	-6.7	-6.5
10	57394641	-7.0	-6.9	-6.9	-6.9	-6.9	-6.8	-6.8	-6.8	-6.8
11	10066595	-6.1	-6.0	-5.8	-5.6	-5.6	-5.6	-5.6	-5.5	-5.5
12	491916	-7.0	-6.5	-6.4	-6.0	-6.0	-5.9	-5.9	-5.9	-7.0
13	491857	-7.8	-7.6	-7.5	-7.3	-7.2	-7.2	-6.8	-6.7	-6.7
14	491920	-7.1	-6.9	-6.7	-6.6	-6.4	-6.3	-6.3	-6.3	-6.0
15	491917	-7.0	-6.9	-6.8	-6.6	-6.4	-6.2	-6.2	-6.2	-7.0
16	57394621	-9.8	-8.9	-8.8	-8.3	-8.2	-8.1	-7.9	-7.6	-7.6
17	57396377	-7.6	-7.3	-6.8	-6.6	-6.3	-6.2	-6.1	-6.1	-6.0
18	57392897	-7.4	-6.6	-6.5	-6.4	-6.3	-6.1	-6.0	-6.0	-7.4
19	57401703	-8.0	-7.8	-7.3	-6.9	-6.3	-6.1	-6.0	-6.0	-8.0
20	482634	-7.2	-7.2	-7.1	-7.0	-7.0	-6.7	-6.7	-6.5	-6.4
21	57392898	-6.5	-6.4	-6.2	-6.1	-6.1	-5.9	-5.9	-5.8	-5.7
22	491877	-7.7	-7.1	-6.7	-6.7	-6.7	-6.7	-6.6	-6.6	-6.5
23	53855501	-7.2	-7.2	-7.0	-6.7	-6.6	-6.2	-6.2	-5.9	-5.8
24	57403346	-7.4	-7.3	-7.0	-7.0	-6.9	-6.9	-6.9	-6.9	-7.4
25	57403432	-7.3	-7.1	-6.9	-6.8	-6.8	-6.8	-6.8	-6.7	-7.3

*Num_modesarg (=9) maximum number of binding modes to generate.

The free energy of binding elicited at the vicinity of the active site by the ligands can be found in Tables 3, 4, 5.

Table 3 shows the affinity of Beta lactamase 1GA0 for further ligands, Table 4 the affinity of Nicotinamide phosphoribosyltransferase 4O0Z and Tables 5 of Nicotinamide phosphoribosyltransferase 4O10.

In Table 3, among the ligands, two possess the lowest binding energies: -9.8 and -8.1 kcal/mol while the highest is -6.1 kcal/mol. It seems that the high affinity ligand – enzyme depends of the number of rotatable bonds.

Table 4. The final lamarckian genetic algorithm docked state: binding energy of ligands with the active site of **Nicotinamide phosphoribosyltransferase (4O0Z)** during nine conformations

CID of Ligand	1	2	3	4	5	6	7	8	9	Docked Energy (kcal/mol)
1	482634	-8.4	-7.9	-7.9	-7.8	-7.6	-7.0	-6.9	-6.9	-8.4
2	10853428	-7.3	-7.2	-7.2	-7.0	-6.6	-6.6	-6.6	-6.3	-7.3
3	57399922	-8.3	-7.8	-7.7	-7.6	-7.6	-7.6	-7.5	-7.4	-8.3
4	491919	-9.4	-9.2	-8.9	-8.8	-8.8	-8.6	-8.6	-8.1	-9.4
5	482635	-7.7	-7.7	-7.6	-7.5	-7.5	-7.4	-7.3	-7.3	-7.7
6	10644682	-8.8	-7.7	-7.3	-7.3	-7.2	-7.1	-7.0	-6.9	-8.8
7	10668699	-7.8	-7.8	-7.7	-7.6	-7.5	-7.3	-7.0	-6.9	-7.8
8	491918	-5.2	-5.2	-4.6	-4.5	-3.6	-1.7			-5.2
9	491856	-8.8	-8.2	-8.2	-8.1	-7.9	-7.7	-7.7	-7.4	-8.8
10	57394641	-8.1	-8.0	-8.0	-7.9	-7.9	-7.7	-7.7	-7.6	-8.1
11	10066595	-7.6	-7.2	-7.2	-7.1	-6.7	-6.6	-6.5	-6.5	-7.6
12	491916	-8.3	-8.0	-7.9	-7.4	-7.0	-6.9	-6.7	-6.6	-8.3
13	491857	-8.8	-8.6	-8.5	-8.2	-8.1	-8.1	-7.9	-7.9	-8.8
14	491920	-8.1	-8.0	-7.8	-7.7	-7.6	-7.4	-7.4	-7.1	-8.1
15	491917	-8.4	-8.3	-8.3	-7.7	-7.6	-7.6	-7.6	-7.4	-8.4
16	57394621	-9.7	-9.5	-8.9	-8.6	-8.6	-8.6	-8.6	-8.6	-9.7
17	57396377	-7.9	-7.8	-7.8	-7.6	-7.5	-7.5	-7.5	-7.2	-7.9
18	57392897	-7.7	-7.7	-7.4	-7.3	-7.2	-6.9	-6.8	-6.3	-7.7
19	57401703	-8.0	-7.8	-7.8	-7.8	-7.8	-7.8	-7.7	-7.6	-8.0
20	482634	-9.7	-9.7	-9.4	-9.1	-8.4	-8.4	-8.3	-8.2	-9.7
21	57392898	-7.5	-7.0	-6.7	-6.7	-6.7	-6.6	-6.5	-6.4	-7.5
22	491877	-8.1	-7.7	-7.5	-7.5	-7.3	-7.2	-6.4	-6.4	8.1
23	53855501	-8.2	-8.1	-8.1	-7.9	-7.8	-7.2	-7.2	-6.9	-8.2
24	57403346	-9.0	-8.9	-8.6	-8.4	-8.2	-8.0	-7.	-7.8	-9.0
25	57403432	-8.9	-8.7	-8.7	-8.3	-8.3	-8.0	-8.0	-7.9	-8.9

Among the ligands in Table 4, the lowest binding energies were: -9.7 and -9.4 kcal/mol while the highest, -5.2 kcal/mol. In case of ligand with CID 491918, only 6 conformations were found.

Table 5. The final lamarckian genetic algorithm docked state – Binding energy of ligands with the active site of **Nicotinamide phosphoribosyltransferase (4O10)** during nine conformations

CID of Ligand	1	2	3	4	5	6	7	8	9	Docked Energy (kcal/mol)
1	482634	-5.8	-5.7	-5.5	-5.4	-5.4	-5.4	-5.3	-5.3	-5.3
2	10853428	-5.8	-5.4	-5.3	-5.3	-5.2	-5.1	-5.1	-4.9	-4.9
3	57399922	-6.3	-6.2	-6.1	-6.0	-5.9	-5.8	-5.7	-5.7	-5.7
4	491919	-6.3	-6.1	-6.1	-5.7	-5.6	-5.4	-5.3	-5.1	-5.0
5	482635	-6.5	-6.4	-6.4	-6.3	-6.0	-5.9	-5.9	-5.8	-5.8
6	10644682	-6.0	-5.7	-5.6	-5.3	-5.3	-5.3	-5.2	-5.2	-5.2
7	10668699	-6.8	-6.3	-6.2	-6.0	-6.0	-5.8	-5.7	-5.7	-5.6
8	491918	-4.1	-3.9	-3.8	-3.7	-3.7	-3.4	-2.7	-1.4	-1.2
9	491856	-6.4	-6.2	-5.9	-5.8	-5.8	-5.8	-5.6	-5.5	-5.5
10	57394641	-6.5	-6.2	-6.2	-6.0	-5.9	-5.9	-5.9	-5.8	-5.6
11	10066595	-5.5	-5.4	-5.4	-5.4	-5.3	-5.1	-5.0	-4.9	-4.8
12	491916	-5.5	-5.5	-5.3	-5.3	-5.2	-5.1	-5.1	-5.1	-5.5
13	491857	-6.6	-6.4	-6.3	-6.3	-6.0	-5.9	-5.8	-5.8	-6.6
14	491920	-5.9	-5.7	-5.7	-5.7	-5.7	-5.5	-5.4	-5.4	-5.9
15	491917	-5.8	-5.5	-5.5	-5.4	-5.3	-5.3	-5.2	-5.2	-5.8
16	57394621	-7.7	-7.3	-7.2	-7.2	-7.1	-7.1	-7.0	-6.9	-6.7
17	57396377	-6.4	-6.4	-6.0	-5.9	-5.6	-5.6	-5.6	-5.5	-6.4
18	57392897	-5.2	-5.2	-5.1	-5.1	-5.0	-4.9	-4.7	-4.7	-4.6
19	57401703	-6.0	-5.9	-5.3	-5.3	-5.2	-5.2	-5.1	-4.9	-4.9
20	482634	-6.4	-6.1	-6.1	-5.9	-5.8	-5.8	-5.7	-5.7	-6.4
21	57392898	-6.3	-6.0	-5.8	-5.7	-5.4	5.4	-5.3	-5.3	-6.3
22	491877	-6.6	-6.4	-6.3	-6.1	-5.8	-5.6	-5.6	-5.6	-6.6
23	53855501	-5.8	-5.5	-5.5	-5.4	-5.4	-5.4	-5.4	-5.3	-5.8
24	57403346	-6.4	-6.3	-6.1	-6.0	-5.9	-5.9	-5.8	-5.7	-6.4
25	57403432	-6.4	-5.9	-5.8	-5.7	-5.7	-5.6	-5.6	-5.6	-6.4

The first active site of 4O10 strongly interacts with the ligands, and the energies vary from -7.7 and -6.8 kcal/mol to -4.1 kcal/mol. The highest affinity was -7.7 kcal/mol (for the ligand CID 57394621) while the smallest energy was -4.1 kcal/mol (for the ligand CID 491918). For the other ligands, the interaction was quite similar to each other.

COMPUTATIONAL DETAILS

The structures have been optimized at Hartree-Fock HF (6-31g(d,p)) level of theory, by Gaussian 09 [11]. Topological indices have been computed by TOPOCLUJ software [12]; some of them (Connectivity= C, CS[Sh[Charges]]= Ch, SD), are listed in Table 6.

Table 6. Topological indices computed for the indolizine in case IC50 Table 1

Mol.	IC ₅₀ (μM)	SD	C.	Ch.
482634	30	-19.374	38	23
10853428	33	-17.745	40	25
57399922	31	-16.665	49	30
57403432	46	-4.228	52	33
491857	27	-22.428	39	24
491919	27	-25.495	49	30
482635	28	-21.307	48	29
491918	29	-22.428	41	25
491920	23	-27.119	51	31
491917	26	-22.428	40	25
57394641	30	-17.874	38	23
482634	30	-22.428	40	25
482634	27	-22.374	40	25
57403346	28	-24.043	46	29
57394621	24	-26.336	54	33
10066595	31	-18.45	43	27
10644682	20	-28.727	50	31
10668699	20	-29.375	50	31
491856	23	-22.428	42	26
491916	26	-22.423	41	26
57392897	33	-17.874	40	25
491877	21	-25.898	51	32
53855501	22	-24.043	45	28
57396377	25	-24.332	47	30
57401703	37	-11.519	51	32

QSAR models (for IC50)

The models were performed on the training set (the 15 structures in Table 1) and the best results are listed below and in Table 7 [13].

(i) Monovariate regression

$$IC50 = 48.475 + 0.923 \times SD$$

(ii) Bivariate regression

$$IC50 = 47.767 + 0.911 \times SD + 3.129 \times Ch$$

(iii) Three-variate regression

$$IC50 = 47.354 + 0.927 \times SD - 0.105 \times HOMO + 2.688 \times Ch$$

Table 7. Best models in describing IC50 in the training set of indolizines

	Descriptors	R²	Adjust. R²	St. Error	F
1	SD	0.923	0.915	1.530	155.683
2	Ch	0.047	0.027	5.381	0.635
3	IP_{max}	0.119	0.051	5.174	1.750
4	IE_{max}	0.079	0.008	5.288	1.121
5	SD, Ch	0.935	0.924	1.459	86.696
6	SD, IE_{max}	0.928	0.916	1.537	77.556
7	SD, Adj	0.926	0.914	1.560	75.170
8	SD, C	0.925	0.913	1.569	74.223
9	SD, D3D	0.925	0.912	1.572	73.859
10	SD, HOMO	0.924	0.911	1.580	73.119
11	SD, C, Ch	0.945	0.930	1.406	62.929
12	SD, Adj, C	0.939	0.922	1.483	56.176
13	SD, De, IE_{max}	0.934	0.915	1.544	51.558
14	SD, D3D, De	0.927	0.907	1.621	46.399
15	SD, HOMO, Adj	0.927	0.907	1.622	46.338
16	SD, C, D3D	0.925	0.905	1.639	45.361

Leave-one-out

The performances in leave-one-out analysis related to the models listed as best in Table 7 are presented in Table 8 [14].

Table 8. Leave-one-out analysis for best IC50 models

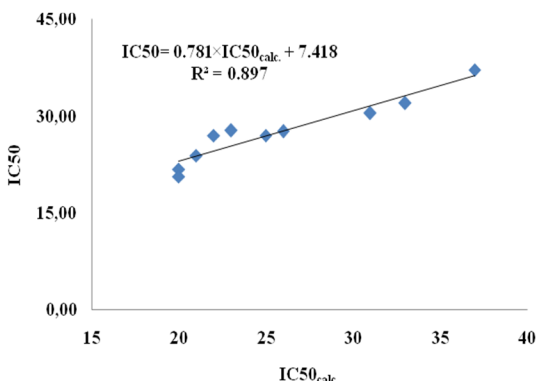
	Descriptors	Q²	R²-Q²	St. Error_{loo}	F_{loo}
1	SD	0.863	0.06	2.038	82.057
5	SD, Ch	0.880	0.055	1.908	95.519
11	SD, C, Ch	0.894	0.051	1.792	109.920

External Validation

The values IC50 for the test set of indolizines (10 molecules) molecules best scored in the docking step, were calculated by using the best equation in Table 7, entry 5. Data are listed in Table 9 and the monovariate correlation: $IC50 = 0.781 \times IC50_{calc} - 7.418$; n=10; R²=0.897; s=2.027; F=69.333 is plotted in Figure 3 [15].

Table 9. Calculated values of IC₅₀ for the molecules in the test set (Table 1)

Molecules	IC ₅₀	IC ₅₀ _{calc.}
10066595	31	30.49
10644682	20	21.78
10668699	20	20.67
491856	23	27.78
491916	26	27.69
57392897	33	32.05
491877	21	23.94
53855501	22	27.06
57396377	25	27.04
57401703	37	37.19

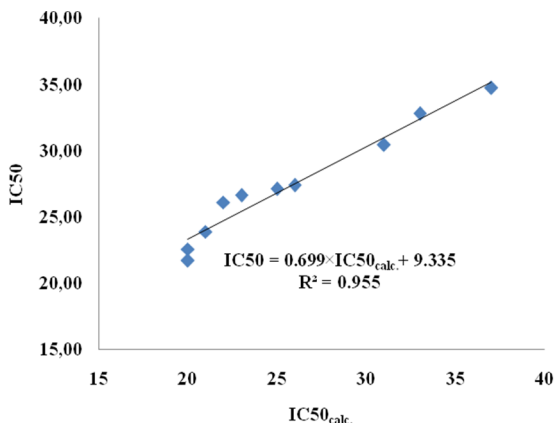
**Figure 3.** The plot IC₅₀ vs. IC₅₀_{calc.} for the test set (external validation)

Similarity Cluster Validation

Validation can be performed by calculating IC₅₀ for the molecules in the test set with equations learned on clusters of similarity: each of the 10 molecules is the leader in its own cluster best scored in the docking step, selected by (2D) similarity among the 15 structures of the initial learning set [16]. The values IC₅₀_{calc.} for each of the 10 molecules in the test set were computed by 10 new equations (the leader being left out) with the same descriptors as in eq. 11, Table 7. Data are listed in Table 10 and the monovariate correlation: n=10; R²=0.955; s=1.329; F=171.735 is plotted in Figure 4 [17].

Table 10. Calculated values of IC₅₀ by similarity clusters, for the molecules in the test set

Molecules	IC ₅₀	IC ₅₀ _{calc.}
10066595	31	30.47
10644682	20	22.59
10668699	20	21.75
491856	23	26.63
491916	26	27.43
57392897	33	32.81
491877	21	23.91
53855501	22	26.12
57396377	25	27.14
57401703	37	34.76

**Figure 4.** The plot IC₅₀ vs. IC₅₀_{calc.} by similarity clusters

CONCLUSIONS

A set of 25indolizine, downloaded from the PubChem database, was submitted to a QSAR study. The set was split into a learning set (15 molecules) and a test set (10 molecules), the test set being used for the validation of the models.

Beta lactamase and nicotinamide phosphoribosyltransferase, has been investigated for its potential binding affinity with selective indolizine derivatives. The docking result of the study of 25 molecules demonstrated that the binding energies when we use Beta lactamase were in the range of -9.8 kcal/mol to -6.1 kcal/mol, when use nicotinamide phosphoribosyltransferase were in the range of -9.7 kcal/mol to -5.2 kcal/mol.

ACKNOWLEDGMENTS

This paper is a result of a doctoral research made possible by the financial support of the Sectoral Operational Programme for Human Resources Development 2007-2013, co-financed by the European Social Fund, under the project POSDRU/159/1.5/S/137750 - "Doctoral and postdoctoral programs - support for increasing research competitiveness in the field of exact Sciences".

REFERENCES

- [1]. G.S. Singh, E.E. Mmatli, *Eur. J. Med. Chem.*, **2011**, 46, 5237-5257.
- [2]. T. Przewloka, S. Chen, Zh. Xia, H. Li, Sh. Zhang, D. Chimmanamada, E. Kostik, D. James, K. Koya, L. Sun, *Tetrahedron Letters*, **2007**, 48, 5739–5742.
- [3]. I.V. Seregin, A.W. Schammel, V. Gevorgyan, *Tetrahedron*, **2008**, 64, 6876–6883.
- [4]. S.S. Juang, M. Chang, L.F. Wang, J.L. Han, C.H. Ong, *Tetrahedron*, **2005**, 61, 1693-1697.
- [5]. PubChem database, accessed 10.05. **2014**.
- [6]. G.S. Singh, E.E. Mmatli, *European Journal of Medicinal Chemistry*, **2011**, 465237-5257.
- [7]. H.M. Berman, K. Henrick, H. Nakamura, Announcing the worldwide Protein Data Bank *Nature Structural Biology*, **2003**, 10, 12, 98.
- [8]. O. Trott, A.J. Olson, *Journal of Computational Chemistry*, **2010**, 31, 455-461.
- [9]. K. Dhananjayan, K. Kalathil, A. Sumathy, P. Sivanandy, *Der Pharma Chemica*, **2014**, 6, 2, 378-387.
- [10]. R. Abagyan, M. Totrov, *Curr Opin Chem Biol.*, **2001**, 5: 375-82.

- [11]. Gaussian 09, Gaussian Inc C.T. Wallingford, Revision A.1 M.J. Frisch, G.W. Trucks, H.B. Schlegel, G.E. Scuseria, M.A. Robb, J.R. Cheeseman, G. Scalmani, V. Barone, B. Mennucci, G.A. Petersson, H. Nakatsuji, M. Caricato, X. Li, H.P. Hratchian, A.F. Izmaylov, J. Bloino, G. Zheng, J.L. Sonnenberg, M. Hada, M. Ehara, K. Toyota, R. Fukuda, J. Hasegawa, M. Ishida, T. Nakajima, Y. Honda, O. Kitao, H. Nakai, T. Vreven, J.A. Montgomery, J.E. Peralta, F. Ogliaro, M. Bearpark, J.J. Heyd,E. Brothers, K.N. Kudin, V.N. Staroverov, Kobayashi R., Normand J., Raghavachari K., Rendell A., Burant J.C., Iyengar S.S., Tomasi J., Cossi M., Rega N., N.J. Millam,M. Klene, J.E. Knox, J.B. Cross, V. Bakken, C. Adamo, J. Jaramillo, R. Gomperts, R.E. Stratmann, O. Yazeyev, A.J. Austin, R. Cammi, C. Pomelli, J.W. Ochterski, R.L. Martin, K. Morokuma, V.G. Zakrzewski, G.A. Voth, P. Salvador, J.J. Dannenberg, S. Dapprich, A.D. Daniels, Ö. Farkas, J.B. Foresman, J.V. Ortiz, J. Cioslowski, D.J. Fox, **2009**.
- [12]. O. Ursu, M.V. Diudea, TopoCluj software program. Babes-Bolyai University Cluj, **2005**.
- [13]. J.G. Topliss, R. J. Costello, *J. Med. Chem.* **1972**, 15, 1066-1068.
- [14]. L. Jäntschi, LOO Analysis (LOO: leave one out), Academic Direct Library of software, 2005. Available at:
http://academicdirect.org/Chemistry/SARs/MDF_SARs/loo/
- [15]. T.E. Harsa, A.M. Harsa, B. Szeffler, *Cent. Eur. J. Chem.*, **2014**, 12, 365-376.
- [16]. S.D. Bolboacă, L. Jäntschi, and M.V. Diudea, *Current Computer-Aided Drug Design*, **2013**, 9, 2, 195-205.
- [17]. A.M. Harsa, T.E. Harsa, S.D. Bolboacă, M.V. Diudea, *Current Computer-Aided Drug Design*, **2014**, 2, 10, 115-128.

STRUCTURAL MODELING OF PHENYLALANINE AMMONIA-LYASES AND RELATED MIO-CONTAINING ENZYMES – AN INSIGHT INTO THERMOSTABILITY AND IONIC INTERACTIONS

GERGELY BÁNÓCZI^a, CSONGOR SZABÓ^a,
ZSÓFIA BATA^{a,b}, ALINA FILIP^c,
GÁBOR HORNYÁNSZKY^a, LÁSZLÓ POPPE^{a,d *}

ABSTRACT. Biocatalysis and bioinformatics are powerful tools to analyze and enhance the properties of biocatalysts for industrial technologies. In this work, the three-dimensional structures of various phenylalanine ammonia-lyases and other 5-methylene-3,5-dihydro-4H-imidazol-4-one (MIO) dependent enzymes were investigated, analyzed, and constructed. The three-dimensional structures of MIO-containing aromatic ammonia-lyases and 2,3-aminomutases from the PDB database were analyzed. In several instances the structural deficiencies and inactive conformations were modified to approach the active states. The checked / modified PDB structures of the MIO-enzymes served as templates for the large scale homology modeling for phenylalanine ammonia-lyase (PAL) sequences with unknown structure. Multiple settings were tested in the modeling workflow to result in structures with intact active center, good overall protein quality and reasonable number of salt bridges. The experimental temperature optima of the investigated PALs were correlated with two common factors of thermal stability: salt bridge and disulfide bridge numbers. Our study indicate *i*) a moderate correlation between salt bridge numbers and temperature optima, *ii*) and negligible effects of disulfide bridges. The two examples which do not correlate with the others indicate the presence of other important factors contributing to thermal stability of the MIO-enzymes. The modified PDB structures can serve further molecular modeling projects such as functional studies with a QM/MM approach.

Keywords: 3,5-dihydro-5-methylidene-4H-imidazol-4-one, MIO prosthetic group, homology modeling, phenylalanine ammonia-lyase, thermal stability, salt bridge

^a Budapest University of Technology and Economics, Department of Organic Chemistry and Technology, Műegyetem rkp. 3., H-1111 Budapest, Hungary.

^b Hungarian Academy of Sciences, Research Centre for Natural Sciences, Institute of Enzymology, Magyar tudósok körútja 2., H-1117 Budapest, Hungary.

^c Babes-Bolyai University, Biocatalysis and Biotransformation Research Group, Str. Arany János nr. 11, RO-400028 Cluj-Napoca, Romania.

^d SynBiocat LLC, Lázár deák u. 4/1., H-1173 Budapest, Hungary.

* Corresponding author: poppe@mail.bme.hu

INTRODUCTION

As nowadays industrial development needs more efficient, yet green processes, new methods must meet more criteria than ever before. Biotechnology, one of the disciplines that were proven to successfully fulfill this task, can provide enzymes that are efficient and green catalysts. Enzymes, as biocatalysts, can be applied under mild conditions and at ambient temperature, can be highly selective, and can avoid the production of hazardous materials during their whole lifecycle. Bioinformatics can contribute to the experimental work required to select and develop the suitable biocatalyst by reducing the amount of required experimental work and increasing the amount of information extracted from the experiments.

An important feature of enzymes is their temperature tolerance. At elevated temperatures the reaction rates are higher and the probability of the biocatalyst digestion by microbial infection is lower. Generally, thermophile enzymes can tolerate heat treatment, as well as higher denaturing agent and substrate concentrations [1]. On the other hand, the biotechnological value of cold-adapted enzymes (aka psychrophiles) stems from their high catalytic activity at low to moderate temperatures providing energy savings to processes. Also, the use of psychrophiles can lower the risk of undesirable chemical reactions and can enable the transformation of thermally labile substrates [2].

The structural features of thermotolerance of enzymes have been intensively researched in the previous decades yielding a vast amount of data. Szilágyi *et al.* [3] concluded that different protein families adapt to higher temperatures by different sets of structural devices. Regarding the structural parameters, the only generally observed rule was an increase in the number of salt bridges with increasing growth temperature of host organisms. Other parameters showed just a trend, whereas the number of hydrogen bonds and the polarity of buried surfaces exhibited no clear-cut tendency to change with growth temperature. They suggested that proteins from extreme thermophiles are stabilized in different ways compared to the moderately thermophilic ones. The preferences of these two groups are different with regards to the number of ion pairs, the number of cavities, the polarity of exposed surface and the secondary structural composition.

Similarly, according to Scandurra *et al.* [1], stability of a protein from a thermophile, compared to its mesophilic homologue, is a property acquired through many small structural differences such as the modulation of the canonical forces, electrostatic (hydrogen bonds and ion-pairs) and hydrophobic interactions. Thermophilic proteins – produced by thermo- and hyperthermophilic microorganisms growing between 45 and 110 °C – show structural restriction on flexibility, which allows them to be functionally competent at elevated

temperatures, but renders them unusually rigid and less active at mesophilic temperatures (10–45 °C) due to increased compactness. From a comparative analysis of several families of proteins including at least one thermophilic structure in each family, it appeared that thermal stabilization was accompanied by an increase in hydrogen bonds and salt bridges [1]. Thermostability appeared to correlate also with a better packing within buried regions.

Kurnikova *et al.* [4] have determined flexible regions for four homologous pairs from thermophilic and mesophilic organisms by two computational methods: FoldUnfold [5] which is based on amino acid sequences, and MD/First [6] which use three-dimensional structures and molecular dynamics (MD). Both methods allowed determining flexible regions in protein structures. Supporting the previous statement by Scandurra *et al.* [1], MD simulations showed that thermophilic proteins were more rigid in comparison to their mesophilic homologues. It has been also found that the local networks of salt bridges and hydrogen bonds in thermophiles render their structure more stable with respect to fluctuations of individual contacts. This ionic network connects α -helices and rigidifies the structure. Mesophiles can be characterized by standalone salt bridges and hydrogen bonds or small ionic clusters. Such difference in the network of salt bridges results in different flexibility of homologous proteins. Despite these generalizations, no universal rules were found as structural factors leading to enhanced thermostability within a certain family of enzymes.

In contrast to their thermophilic counterparts, the structures of thermolabile, cold-adapted enzymes generally permit high flexibility [7,8]. According to Saunders *et al.* [9] and Siddiqui *et al.* [7], psychrophilic enzymes tend to possess various combinations of the following features: decreased core hydrophobicity, increased surface hydrophobicity, lower arginine/lysine ratio, more and longer loops, decreased secondary structure content, more glycine residues, less proline residues in loops and more proline residues in α -helices, a reduced number of disulfide bridges, fewer electrostatic interactions, reduced oligomerization, and an increase in conformational entropy of the unfolded state.

Aromatic ammonia-lyases catalyze the non-oxidative ammonia elimination from aromatic (2S)-amino acids, producing α,β -unsaturated carboxylic acids. The members of this enzyme family are the histidine ammonia-lyase (HAL, EC 4.3.1.3) [10,11], tyrosine ammonia-lyase (TAL, EC 4.3.1.23) [12], and phenylalanine ammonia-lyase (PAL, EC 4.3.1.24) [13] catalyzing the deamination of the corresponding (2S)-amino acids to (*E*)-cinnamic acid, (*E*)-urocanic acid, and (*E*)-coumaric acid, respectively (Figure 1/a). In plants, PAL catalyzes the first step of the phenylalanine degradation pathway, and thus the biosynthesis of several classes of phenylpropanoids, such as lignins, flavonoids, and coumarins [14]. The synthetic application of PAL is based on the stereoconstructive reverse reaction yielding (2S)-phenylalanine derivatives

from achiral precursors or the kinetic resolution of racemic amino acids providing access to (2*R*)-phenylalanine derivatives as residual substrates [15]. From an environmental point of view it is important that PAL lies at the branch of primary and secondary metabolism in plants and therefore it is a target for herbicides [16].

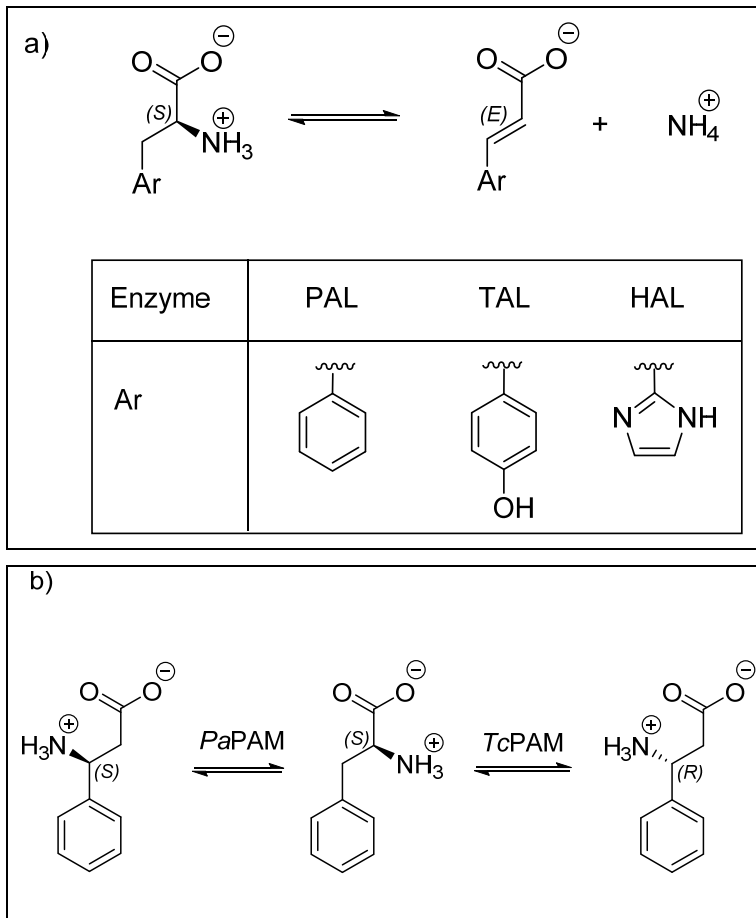


Figure 1. (a) reactions catalyzed by the aromatic ammonia-lyases and
(b) phenylalanine 2,3-aminomutases.

The X-ray structure of HAL [17] revealed first that the enzyme contains a post-translationally formed 5-methylene-3,5-dihydro-4*H*-imidazol-4-one (MIO) as the electrophilic prosthetic group (Figure 2) [18]. This prosthetic group is formed autocatalytically by the elimination of two water molecules from an inner tripeptide Ala-Ser-Gly (in some cases Thr-Ser-Gly).

This prosthetic group can also be found in tyrosine 2,3-aminomutases (TAM, EC 5.4.3.6) and phenylalanine 2,3-aminomutases (PAM; (3*R*)-phenylalanine forming: EC 5.4.3.10; (3*S*)-phenylalanine forming: EC 5.4.3.11), which catalyze the selective formation of the 3-amino acids (Figure 1/b).

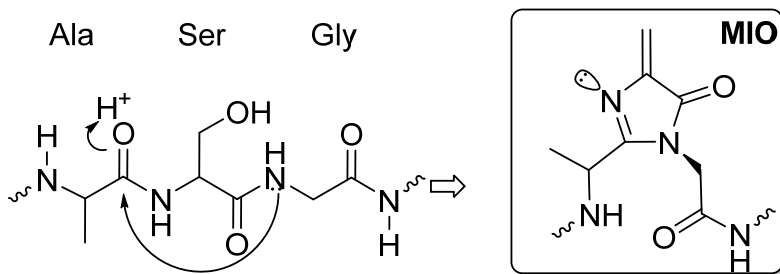


Figure 2. Formation of the 5-methylene-3,5-dihydro-4*H*-imidazol-4-one (MIO) prosthetic group from an Ala-Ser-Gly peptide fragment.

Only (3*S*)-tyrosine producing TAM structures have been determined so far, in contrary to PAMs, where both (3*R*)- and (3*S*)-phenylalanine producing structures are known (e. g. *Taxus canadensis* and *Pantoea agglomerans* PAM, respectively) [19].

In the Protein Data Bank (PDB) X-ray structures are available for enzymes from ten different organisms in which the MIO prosthetic group was identified: *Pseudomonas putida* HAL (PDB: 1GKM) [20], *Rhodosporidium toruloides* PAL (PDB: 1Y2M) [21], *Petroselinum crispum* PAL (PDB: 1W27) [22], *Anabaena variabilis* PAL (PDB: 3CZO) [23], *Nostoc punctiforme* PAL (PDB: 2NYF) [24], *Rhodobacter sphaeroides* TAL (PDB: 2O6Y) [25], *Streptomyces globisporus* TAM (PDB: 2QVE) [26], *Taxus canadensis* PAM (PDB: 3NZ4) [27], *Taxus chinensis* PAM (PDB: 2YII) [28], and *Pantoea agglomerans* PAM (PDB: 3UNV) [29].

In several cases, more than one structure is available, although only one representative is listed here for each MIO-enzyme.

An important structural difference between the previously listed enzymes is the presence of a ~170 amino acid long multihelix domain in the C-terminal region in enzymes with eukaryotic origin, against a ~7-19 amino acid long corresponding sequence segment in enzymes with prokaryotic origin (Figure 3/a). However, despite this considerable difference along with different substrates and function, the catalytic core domains of these proteins are remarkably similar in their tertiary and quaternary structures, deviating from a common fold considerably mainly in disordered, loop regions, and forming tetramers in every case (Figure 3/b).

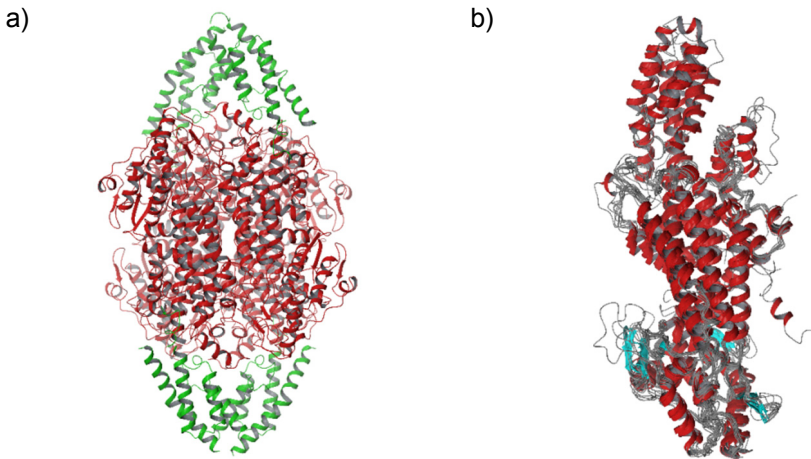


Figure 3. (a) Tetramer structure of *TchinPAM* (PDB: 2YII). Ribbons in red indicate the catalytic core domain, common in MIO enzymes of both eukaryotic and prokaryotic origin. Ribbons in green represent the C-terminal multihelix domain, characteristic for enzymes of eukaryotic origin. (b) Overlay of the single chains of all MIO-enzymes listed in Table 1 indicated high structural conservation in the colored ordered secondary structure regions and less conservation in loop regions.

Mutagenesis studies proved the similarity of PAL [30] and HAL [31], and the importance of the Tyr110(PAL)/78(HAL) residue which was essential for the catalytic activity. This Tyr is situated in a flexible loop which is often missing from the crystal structures (PDB: 1Y2M) [21] or is in a supposedly inactive conformation (PDB: 1W27) [22]. However, in the structures of *Anabaena variabilis* PAL (PDB: 3CZO) [23], and *Rhodospirillum toruloides* TAL (PDB: 1Y2M) [21] compact active centers were found with tight Tyr-loop conformations, showcasing the supposedly active conformation.

EXPERIMENTAL

Experimentally determined protein structures from the Protein Data Bank (PDB) [32] were selected as representatives for each MIO-enzyme type (encoded by genes of different organisms, Table 1). Selection criteria were active site compactness, resolution, *R*-value, and *R*-free values. After the overlay of the single chains of the various MIO-enzymes, they were systematically checked for missing side chains, residues, and loops, for inactive Tyr-loop conformations and for large backbone deviations. Errors were corrected as much as possible by using partial homology modeling of the missing/erroneous part(s). The templates for homology modelling were chosen

based on the maximum similarity of the corresponding amino acid segments. The resulting checked/corrected experimental structures served as templates for the large scale homology modeling for those MIO-enzymes which did not have experimental structures.

In the *PcPAL* structure the Tyr-loop and an adjacent loop were present in a catalytically inactive “loop-out” conformation [33], therefore these regions were reconstructed. Templates for the residues 98-131 and 324-350 were taken from *TchiPAM*.

The Tyr-loop and a further loop which were both partly missing and deformed from the structure of *RtPAL* crystal structure were modeled as well. The coordinates for the missing residues 103-124 and 343-358 of *RtPAL* were taken from *TchiPAM* as well.

In the *PpHAL* and *TcanPAM* structures the Tyr-loop is in a “loop-in” conformation [33], albeit in a partially open, non-active state. Residues 46-68 for *PpHAL* and 68-88 for *TcanPAM* were remodeled using the templates 2O6Y and 2YII, respectively.

Table 1. Experimental structures of aromatic ammonia-lyases and 2,3-aminomutases (occasionally with partial corrections) chosen as homology modeling templates

Organism	Function	Abbreviation	PDB code	Uniprot code	Errors	Correction template
<i>Anabaena variabilis</i>	PAL	AvPAL	3CZO	Q3M5Z3	-	-
<i>Petroselinum crispum</i>	PAL	PcPAL	1W27	P24481	Inactive loop conformations	2YII
<i>Rhodosporidium toruloides</i>	PAL/TAL	RtPAL	1Y2M	P11544	Missing Tyr-loop and residues	2YII
<i>Pseudomonas putida</i>	HAL	PpHAL	1GKM	P21310	Non-tight Tyr-loop	2O6Y
<i>Rhodobacter sphaeroides</i>	TAL	RsTAL	2O6Y	Q3IWBO	-	-
<i>Streptomyces globisporus</i>	TAM	SgTAM	2QVE	Q8GMG0	-	-
<i>Taxus canadensis</i>	PAM	TcanPAM	3NZ4	Q6GZO4	Non-tight Tyr-loop	2YII
<i>Pantoea agglomerans</i>	PAM	PaPAM	3UNV	Q84FL5	-	-
<i>Taxus chinensis</i>	PAM	TchiPAM	2YII	Q68G84	Missing residues	1W27

In the BRENDA enzyme database 13 different MIO-containing phenylalanine ammonia-lyases were found with known temperature optima but without experimentally determined structure [34] (Table 2). For each of the various PALs sixteen homology models of the catalytically active homotetrameric form were constructed each time, using MODELLER [35]. From the beginning

of the optimization process, the ASG amino acid triads in the conserved position of the MIO prosthetic group were replaced by the corresponding MIO-structures. Symmetry constraints were applied to the monomers forming the homotetramer.

Refinement of the raw models constructed by MODELLER was performed with Maestro [36] and Protein Preparation Wizard [37,38] (bond order assignment, addition of hydrogens). The refined models were minimized with TINKER [39] (forcefield: OPLS, minimization method: TNCG).

For the refinement of the initial models of *Rubrobacter xylanophylus* PAL [40], multiple settings were tested (max. 8 models for each) for MODELLER and for post-minimization with within TINKER. Varied settings were *i*) in MODELLER: the level of simulated annealing, all-atom/heavy atom-only modeling, monotemplate/multitemplate modeling, different sequence alignments, number of refinement stage iterations; *ii*) in TINKER post-minimization: solvent model (vacuum or implicit water) and convergence criterion (1.0, 0.1, and 0.05 kcal mol⁻¹ Å⁻¹ RMS gradient).

Table 2. Phenylalanine ammonia-lyases with known temperature optima but without experimentally determined structures

Organism	Isoform	Abbreviation	Uniprot code	Reference
<i>Arabidopsis thaliana</i>	1	AtPAL1	Q3M5Z3	41
<i>Arabidopsis thaliana</i>	2	AtPAL2	P24481	41
<i>Arabidopsis thaliana</i>	3	AtPAL3	Q7N4T3	41
<i>Arabidopsis thaliana</i>	4	AtPAL4	P11544	41
<i>Bambusa oldhamii</i>	1	BoPAL1	P21310	42
<i>Bambusa oldhamii</i>	2	BoPAL2	Q7N296	42
<i>Bambusa oldhamii</i>	4	BoPAL4	Q3IWBO	42
<i>Cistanche deserticola</i>	-	CdPAL	Q8GMG0	43
<i>Gossypium hirsutum</i>	-	GhPAL	Q6GZO4	44
<i>Helianthus annuus</i>	-	HaPAL	Q84FL5	45
<i>Jatropha curcas</i>	-	JcPAL	Q9KHJ9	46
<i>Oryza sativa</i>	-	OsPAL	A2X7F7	47
<i>Ustilago maydis</i>	-	UmPAL	Q96V77	48

The number of salt bridges were determined in the final models (which were evaluated by the active site geometry and overall protein health). For salt bridge statistics ANOVA, Mann-Whitney U-tests, and Wilcoxon matched-pair tests were applied, using Statistica [49]. The structures were validated with PROCHECK [50] using SAVES (Structure Analysis and Verification Server).

Salt bridge numbers were determined with VMD with default parameters [51]. Sulfur atoms of cysteine residues were considered as disulfide bridge candidates with an interatomic distance less than or equal to 4 Å, or less than or equal to 7 Å when at least one of the residues was located on a loop.

The final procedure consisted of multitemplate modeling followed by a thorough simulated annealing and minimization in vacuum to a RMS gradient threshold of 1.0 kcal mol⁻¹ Å⁻¹ followed by further geometry optimization with implicit water solvation to a RMS gradient of 1.0 kcal mol⁻¹ Å⁻¹.

RESULTS AND DISCUSSION

Our aim with this work was to investigate, analyze and construct the three-dimensional structures of various phenylalanine ammonia-lyases and further MIO-dependent enzymes. Partial and full homology models were created to check the possible correlations between common factors of thermostability and temperature optima (i.e. temperature of maximum reaction velocity).

Modeling in monomeric form followed by construction of the tetramer resulted in inappropriate, non-interacting adjacent loops and side chains, steric clashes. Furthermore, energy minimization of such tetrameric structures led to more distorted structures than that obtained by tetrameric homology modelling. This effect could be visualized in the case of partial homology modelling of the PAL1 from *Petroselinum crispum* (*PcPAL*, see Figure 4). Therefore, the structures of the MIO-containing enzymes in this study were always modeled in tetrameric form.



Figure 4. Comparison of the chains A and B of two different homology models of *PcPAL*. Model 1 (*chain A: brown, chain B: orange*) was modeled in monomeric form which was assembled to tetramer, Model 2 (*chain A: blue, chain B: green*) was modeled as a tetramer from the beginning of the modelling process.

The tetrameric structures for *PcPAL* were minimized to $0.1 \text{ kcal mol}^{-1} \text{ Å}^{-1}$ RMS gradient in both cases using our standard procedure. Significant differences were found between the depicted loops of the two models. In the case of the tetramer built from monomeric model (Model 1), energy minimization resulted in a distortion of a helical part of chain B caused by the loop region of chain A highlighting the importance of modeling the homotetrameric structures as a complex (Model 2). Because the active site of the MIO-containing enzymes is formed by three different chains of the tetramer, such effects could not be neglected.

Although there is little consensus about the structural factors of thermostability, experts mainly agree on the importance of disulfide bridges and electrostatic interactions such as salt bridges, hydrogen bonds. Therefore, by using the modeled tetrameric structures of several phenylalanine ammonia-lyases, several modeling procedures resulting in high quality structures were analyzed with regards to active center compactness, overall protein health and reasonable salt bridge numbers. All tested settings (see experimental section) resulted in compact active centers, and structures with good protein health.

Unfortunately, because of the large deviations in salt bridge numbers among models within each test settings, all factors proved statistically insignificant (at $p < 0.05$). Among the varied test settings, two factors showed remarkable effects on salt bridge numbers and protein health. The most significant changes were caused by the variations in the convergence criterion of post-minimization and by the use of implicit water model. Optimizations with the use of implicit water model resulted in better overall protein quality but significantly lower number of salt bridges. It is likely that the solvent model dampens the electrostatic attraction between ionized side chains preventing them from forming salt bridges. On the other hand, during extensive minimization with lower gradient thresholds, with or without solvent modeling, the protein quality deteriorated as the energy decreased, although the salt bridge numbers increased every time. This resulted in overestimation of salt bridge numbers.

Therefore, the most reasonable optimization protocol consisted of a pre-optimization of the models without solvent model to $1.0 \text{ kcal mol}^{-1} \text{ Å}^{-1}$ RMS gradient followed by further optimization with solvent model to $1.0 \text{ kcal mol}^{-1} \text{ Å}^{-1}$ RMS gradient again. Noteworthy that further optimization of the models to $0.05 \text{ kcal mol}^{-1} \text{ Å}^{-1}$ RMS gradient resulted in higher salt bridge numbers, but also significantly worse protein health statistics. Also worth mentioning, that for the further optimized structures the salt bridge number statistics showed worse correlation with the experimental temperature optima values than in case of the less optimized ($1.0 \text{ kcal mol}^{-1} \text{ Å}^{-1}$ RMS gradient) structures. This indicates a possible over-refinement in the protocol including extensive minimization.

The average salt bridge numbers in the tetrameric models obtained in this way were correlated with the temperature optima (Table 3 and Figure 5).

Table 3. Salt bridge and disulfide bridge statistics of theoretical (as the average of numbers in the 16 models of each enzyme) and experimental PAL structures

Enzyme	Salt bridge No. (Mean)	Salt bridge No. (RMSD)	Salt bridge fraction in the core region [%]	Salt bridge fraction in C-terminal domain [%]	Salt bridge fraction between the two regions [%]	Possible disulfide bridge number	Temp. optimum (°C)
Eukaryotic PALs							
AtPAL1	230	8.9	70.7	18.9	10.5	0	47
AtPAL2	110	6.5	71.5	22.1	6.4	2	48
AtPAL3	116	6.3	69.9	14.7	15.4	0	31
AtPAL4	259	15.7	68.5	19.9	11.6	0	47
BoPAL1	253	11.3	70.1	18.9	11.0	4	60
BoPAL2	246	13.8	69.3	19.8	10.9	4	60
BoPAL4	238	9.7	72.9	17.9	9.2	8	50
CdPAL	253	12.7	68.1	21.5	10.4	4	55
GhPAL	244	8.0	68.6	21.0	10.3	2	30
HaPAL	214	8.7	67.1	21.8	11.1	0	55
JcPAL	243	13.2	71.6	17.3	11.1	2	60
OsPAL	248	9.5	68.4	20.1	11.5	4	50
PcPAL ^a	208	-	67.0	22.7	11.3	0	58
UmPAL	177	14.5	80.5	14.6	4.9	0	30
Prokaryotic PAL							
AvPAL ^b	74	-	94.6	5.4 ^c	0	0	40

^a Partial homology model ^b Experimental structure (PDB: 3CZO) ^c Fraction of saltbridges in the sequence segment corresponding to the C-terminal multihelix domain in enzymes with eukaryotic origin [%]

The MIO-containing PALs of eukaryotic origin in Table 3 could be split into two groups. When the correlation analysis was performed with inclusion of all points, almost no correlation between the salt bridge numbers and temperature optima were found ($R^2=0.21$). In contrary, a much better correlation ($R^2=0.56$) was found when outliers (AtPAL2 and GhPAL) representing a group different

from the main group were omitted from the analysis (Figure 5). The results for the main group, based on the comparison of salt bridge numbers from sophisticated homology models and experimental temperature optima of the modeled MIO-enzymes, implied reasonable correlation between salt bridges and temperature optima despite the heavily multivariate nature of the temperature optima of maximum reaction velocities. The two non-correlating enzymes in the other group indicated the importance of other factors which could also significantly contribute to the thermal dependence of the enzyme activity which may be influenced by local factors. Such local factors may be alterations of flexibility of the catalytically essential Tyr-containing loop.

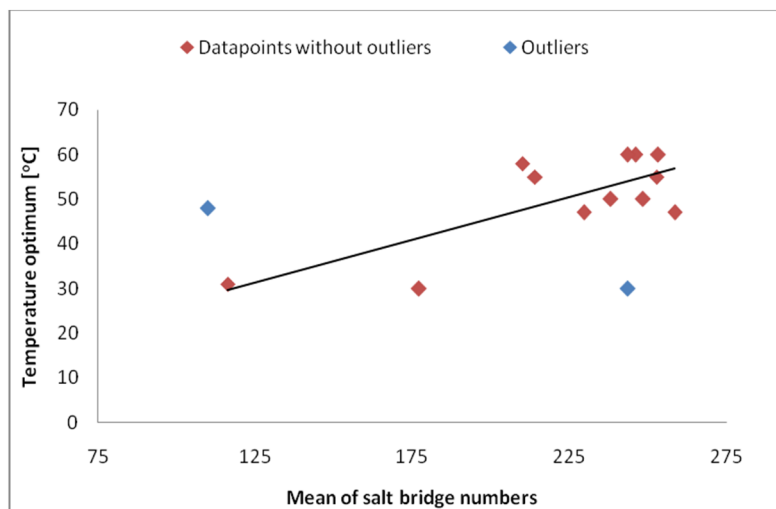


Figure 5. Graphical representation of the eukaryotic PAL salt bridge numbers (split into two groups) versus the temperature optima of maximum reaction velocities

Regarding enzymes of eukaryotic and prokaryotic origin, the salt bridge numbers were also decomposed, based the domain they belong to (Table 3). Surprisingly, there is no correlation between the calculated fractions and temperature optima, indicating that the C-terminal multihelix domain may not need additional ionic interactions, other than the overall increase in salt bridges, to stabilize.

The extremely low salt bridge number of AvPAL indicated that PALS of prokaryotic origin may need significantly less salt bridges to achieve a high temperature optima than those of eukaryotic origin. Although building a hypothesis upon only one data pair may be inadequate, this result would

further support the hypothesis on the Tyr-loop destabilizing / controlling role of the extended C-terminal helix domain in the eukaryotic PALs, which is not present in the prokaryotic ones [33]. To test the validity of this assumption, gathering more data in the future is required.

The number of possible disulfide bridges, however, showed no correlation with temperature optima independently of the method of modeling. One reason behind the absence of correlation between the disulfide bridges and temperature optima may be the lack of certain disulfide bridges despite the opportunity to be formed. This assumption lead to a warning: it could be possible that in several cases the actual recombinant host organisms were not the most appropriate ones to form all the possible disulfide bonds.

CONCLUSIONS

Our study indicated i) a moderate correlation between salt bridge number and temperature optimum, ii) and negligible effect of disulfide bridges with the temperature optima of phenylalanine ammonia-lyases. The two examples which do not correlate with the others indicate the presence of other important factors contributing to thermal dependence of activity for the MIO-enzymes, which may differ from the global thermostability. The modified PDB structures can support further molecular modeling projects such as functional studies by QM/MM approaches to identify and design better biocatalysts.

ACKNOWLEDGMENTS

We are thankful to Dr. Ödön Farkas for his remarks regarding this work. Financial support from OTKA (NN-103242) and from New Hungary Development Plan (*"Talent care and cultivation in the scientific workshops of BME" project, TÁMOP-4.2.2.B-10/1-2010-0009*) is acknowledged. AF thanks for the financial support of the Sectorial Operational Program for Human Resources Development 2007-2013, co-financed by the European Social Fund, under the project number POSDRU/159/1.5/S/132400.

REFERENCES

- [1]. R. Scandurra, V. Consalvi, R. Chiaraluce, L. Politi, P.C. Engel, *Biochimie*, **1998**, 80, 933.
- [2]. R. Cavicchioli, T. Charlton, H. Ertan, S.M. Omar, K.S. Siddiqui, T.J. Williams, *Microbial Biotechnology*, **2011**, 4(4), 449.
- [3]. A. Szilágyi, P. Závodszky, *Structure*, **2000**, 8, 493.
- [4]. T.B. Mamonova, A.V. Glyakina, O.V. Galzitskaya, M.G. Kurnikova, *Biochimica et Biophysica Acta*, **2013**, 1834, 854.
- [5]. O.V. Galzitskaya, S.O. Garbuzyntsiy, M.Y. Lobanov, *Bioinformatics*, **2006**, 22, 2948.
- [6]. T. Mamonova, B. Hespenheide, R. Straub, M.F. Thorpe, M. Kurnikova, *Physical Biology*, **2005**, 2, 137.
- [7]. K.S. Siddiqui, R. Cavicchioli, *Annual Review of Biochemistry*, **2006**, 75, 403.
- [8]. G. Feller, „Protein Adaptation in Extremophiles”, Nova Science Publishers, New York, **2008**, pp. 35–69.
- [9]. N.F. Saunders, T. Thomas, P.M. Curmi, J.S. Mattick, E. Kuczek, R. Slade, *Genome Research*, **2003**, 13, 1580.
- [10]. I.L. Givot, T.A. Smith, R.H. Abeles, *Journal of Biological Chemistry*, **1969**, 244, 6341.
- [11]. R.B. Wickner, *Journal of Biological Chemistry*, **1969**, 244, 6550.
- [12]. J.A. Kyndt, T.E. Meyer, M.A. Cusanovich, J.J. Van Beeumen, *FEBS Letters*, **2002**, 512, 240.
- [13]. D.S. Hodgins, *Journal of Biological Chemistry*, **1971**, 246, 2977.
- [14]. K.R. Hanson, E.A. Havar, *Recent Advances in Phytochemistry*, **1978**, 12, 91.
- [15]. L. Poppe, J. Rétey, *Current Organic Chemistry*, **2003**, 7, 1297.
- [16]. L. Poppe, J. Rétey, *Angewandte Chemie, International Edition*, **2005**, 44, 3668.
- [17]. T.F. Schwede, J. Rétey, G.E. Schulz, *Biochemistry*, **1999**, 38(17), 5355.
- [18]. L. Poppe, *Current Opinion in Chemical Biology*, **2001**, 5, 512.
- [19]. W. Szymanski, B. Wu, B. Weiner, S. Wildeman, B.L. Feringa, D.B. Janssen, *Journal of Organic Chemistry*, **2009**, 74, 9152.
- [20]. M. Baedeker, G.E. Schulz, *European Journal of Biochemistry*, **2002**, 269(6), 1790.
- [21]. L. Wang, A. Gamez, C.N. Sarkissian, M. Straub, M.G. Patch, G.W. Han, S. Striepeke, P. Fitzpatrick, C.R. Scriven, R.C. Stevens, *Molecular Genetics and Metabolism*, **2005**, 86, 134.
- [22]. H. Ritter, G.E. Schulz, *Plant Cell*, **2004**, 16, 3426.
- [23]. L. Wang, A. Gamez, H. Archer, E.E. Abola, C.N. Sarkissian, P. Fitzpatrick, D. Wendt, Y. Zhang, M. Vellard, J. Bliesath, S.M. Bell, J.F. Lemontt, C.R. Scriven, R.C. Stevens, *Journal of Molecular Biology*, **2008**, 380, 623.
- [24]. M.C. Moffitt, G.V. Louie, M.E. Bowman, J. Pence, J.P. Noel, B.S. Moore, *Biochemistry*, **2007**, 46(4), 1004.

- [25]. G.V. Louie, M.E. Bowman, M.C. Moffitt, T.J. Baiga, B.S. Moore, J.P. Noel, *Chemistry and Biology*, **2006**, 13, 1327.
- [26]. S.D. Christenson, W. Liu, M.D. Toney, B. Shen, *Journal of the American Chemical Society*, **2003**, 125(20), 6062.
- [27]. L. Feng, U. Wanninayake, S. Strom, J. Geiger, W.D. Walker, *Biochemistry*, **2011**, 50(14), 2919.
- [28]. B. Wu, W. Szymański, G.G. Wybenga, M.M. Heberling, S. Bartsch, S. de Wildeman, G.J. Poelarends, B.L. Feringa, B.W. Dijkstra, D.B. Janssen, *Angewandte Chemie International Edition*, **2012**, 51(2), 482.
- [29]. S. Strom, U. Wanninayake, N.D. Ratnayake, K.D. Walker, J.H. Geiger, *Angewandte Chemie International Edition*, **2012**, 51(12), 2898.
- [30]. D. Röther, L. Poppe, S. Viergutz, B. Langer, J. Rétey, *European Journal of Biochemistry*, **2001**, 268, 6011.
- [31]. D. Röther, L. Poppe, G. Morlock, S. Viergutz, J. Rétey, *European Journal of Biochemistry*, **2002**, 269, 3065.
- [32]. H.M. Berman, J. Westbrook, Z. Feng, G. Gilliland, T.N. Bhat, H. Weissig, I.N. Shindyalov, P.E. Bourne, *Nucleic Acids Research*, **2000**, 28, 235.
- [33]. S. Pilbák, A. Tomin, J. Rétey, L. Poppe, *The FEBS Journal*, **2006**, 273, 1004.
- [34]. M. Scheer, A. Grote, A. Chang, I. Schomburg, C. Munaretto, M. Rother, C. Söhngen, M. Stelzer, J. Thiele, D. Schomburg, *Nucleic Acids Research*, **2011**, 39, 670.
- [35]. A. Sali, T.L. Blundell, *Journal of Molecular Biology*, **1993**, 234, 779.
- [36]. Maestro, version 9.7, Schrödinger, LLC, New York, NY, **2014**.
- [37]. Protein Preparation Wizard 2014-1; Epik version 2.4, Schrödinger, LLC, New York, NY, 2014; Impact version 5.9, Schrödinger, LLC, New York, NY, 2014; Prime version 3.2, Schrödinger, LLC, New York, NY, 2014.
- [38]. G.M. Sastry, M. Adzhigirey, T. Day, R. Annabhimoju, W. Sherman, *Journal of Computer-Aided Molecular Design*, **2013**, 27, 221.
- [39]. TINKER Suite 7.1; <http://dasher.wustl.edu/tinker/>
- [40]. K. Kovács, G. Bánóczi, A. Varga, I. Szabó, A. Holczinger, G. Hornyánszky, I. Zagyva, C. Paizs, G.B. Vértesy, L. Poppe, *PLoS ONE* **2014**, 9(1), e85943.
- [41]. C.F. Cochrane, B.L. Davin, G.N. Lewis, *Phytochemistry*, **2004**, 65, 1557.
- [42]. L.S. Hsieh, G.J. Ma, C.C. Yang, P.D. Lee, *Phytochemistry*, **2010**, 71, 1999.
- [43]. S.G. Hu, M.J. Jia, J.Y. Hur, S.Y. Chung, H.J. Lee, J.D. Yuun, S.W. Chung, H.G. Yi, H.T. Kim, H.D. Kim, *Molecular Biology Reports*, **2011**, 38, 3741.
- [44]. A.J. Dubery, F. Smit, *Biochimica et Biophysica Acta*, **1994**, 1207, 24.
- [45]. J. Jorrín, R. López-Valbuena, M. Tena, *Biochimica et Biophysica Acta*, **1988**, 964, 73.
- [46]. J. Gao, S. Zhang, F. Cai, X. Zheng, N. Lin, X. Qin, Y. Ou, X. Gu, X. Zhu, Y. Xu, F. Chen, *Molecular Biology Reports*, **2012**, 39, 3443.
- [47]. D.A. Sarma, R. Sharma, *Phytochemistry*, **1999**, 50, 729.
- [48]. H.S. Kim, W.J. Kronstad, E.B. Ellis, *Phytochemistry*, **1996**, 43/2, 351.
- [49]. StatSoft, Inc. (2014). STATISTICA (data analysis software system), version 12. www.statsoft.com.

- [50]. R.A. Laskowski, M.W. MacArthur, D.S. Moss, J.M. Thornton, *Journal of Applied Crystallography*, **1993**, *26*, 283.
- [51]. W. Humphrey, A. Dalke, K. Schulter, *Journal of Molecular Graphics*, **1996**, *14*, 33.

SYNTHESIS AND CHARACTERIZATION OF FULLERENE-PYRIDYL ARENE RUTHENIUM COMPLEXES

DIVAMBAL APPAVOO^a, ROBERT DESCHENAUX^{a*},
BRUNO THERRIEN^{a*}

ABSTRACT. Association of [60]fullerene with arene ruthenium moieties has been achieved for the first time. Two fullerenopyrrolidine derivatives ($N_{\text{pyr}}\text{-C}_{60}$) were synthesized *via* a 1,3-dipolar cycloaddition, and coordinated to arene ruthenium complexes to form two half-sandwich complexes of the general formula (*p*-cymene)RuCl₂($N_{\text{pyr}}\text{-C}_{60}$). The coordination of the fullerenopyrrolidines to the arene ruthenium unit was evidenced by NMR spectroscopy and mass spectrometry, thus confirming the formation of these novel arene ruthenium complexes.

Keywords: fullerene; arene ligand; ruthenium; pyridyl ligand; half-sandwich complexes

INTRODUCTION

In the last 25 years, a lot of progress has been made to the chemistry of fullerenes [1]. However, the most stable and abundant member of the fullerene family, [60]fullerene (C₆₀), remains the most popular derivative [2]. In spite of this popularity, its direct application is often hampered by its poor solubility and processability. Functionalization of the C₆₀ by reactions such as Bingel and 1,3-dipolar cycloaddition has allowed an expansion of the fullerene chemistry [3]. A wide range of fullerene derivatives have since been synthesized by combining the electron acceptor fullerene with various donors such as tetrathiafulvalenes, conjugated oligomers, porphyrins and ferrocenes [4]. The study of these materials for their intramolecular photo-induced energy and electron transfer processes has shown useful properties for applications in

^a Université de Neuchâtel, Institut de Chimie, Avenue de Bellevaux 51, 2000 Neuchâtel, Switzerland.

* Corresponding authors: robert.deschenaux@unine.ch; bruno.therrien@unine.ch

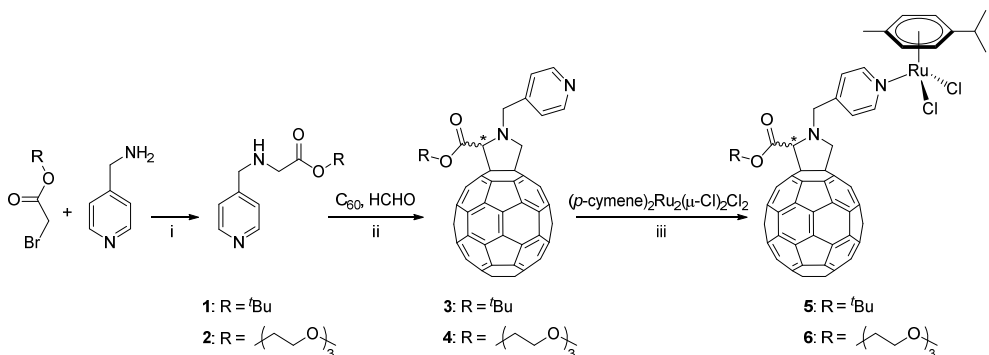
solar cell technologies [5]. This photochemical property of fullerene has been particularly interesting in systems containing coordinating metals. Complexes combining fullerene and d^6 or d^{10} metal ions have shown to exhibit long lived metal-to-ligand charge transfer excited state which stimulated photo-induced electron transfer to the fullerene sphere [6]. Such systems are good candidates for photovoltaic devices. For example, fullerene-based tris(2,2'-bipyridine)ruthenium(II) complexes have been found to possess good energy conversion efficiencies [7]. Other ruthenium-fullerene complexes have been synthesized, like $(\eta^5\text{-C}_{60}\text{Me}_5)\text{RuCl}(\text{CO})_2$, for potential applications in material science and catalysis, yet, the association of fullerene with ruthenium remains generally unexplored [8].

Half-sandwich arene ruthenium complexes, which are an important part of the ruthenium chemistry, have been increasingly used in the development of organometallic chemistry [9]. The arene ligand provides a better control for the coordination of ligands to the metal center and protects the ruthenium center from rapid oxidation [10]. These complexes adopt a pseudo-tetrahedral geometry, with the potential of coordinating three different ligands to the ruthenium center. Mono- and polydentate pyridyl-based ligands have been used extensively for coordination to arene ruthenium moieties, thus resulting in mono- and polynuclear supramolecular assemblies. Moreover, arene ruthenium complexes have found applications in different fields, including anticancer research [11], catalysis [12] and liquid-crystalline material [13].

Despite widespread studies in these two individual fields, to the best of our knowledge, the combination of fullerene with arene ruthenium unit has yet to be accomplished. We hereby report the synthesis and characterization of the first fullerene-based arene ruthenium complexes.

RESULTS AND DISCUSSION

The $N_{\text{pyr}}\text{-C}_{60}$ compounds **3** and **4** (Scheme 1) were synthesized under standard 1,3-dipolar cycloaddition conditions by the addition of the pyridine *N*-modified glycines **1** or **2** to [60]fullerene in the presence of formaldehyde. Compounds **1** and **2** were in turn prepared by reacting the commercially available 4-(aminomethyl)pyridine with the corresponding alkyl bromides, *tert*-butyl bromoacetate and 2-[2-(2-methoxyethoxy)ethoxy]ethyl bromoacetate, respectively. Treatment of **3** and **4** with 0.5 molar equivalent of $(p\text{-cymene})_2\text{Ru}_2(\mu\text{-Cl})_2\text{Cl}_2$ gave the neutral half-sandwich $(p\text{-cymene})\text{RuCl}_2(N_{\text{pyr}}\text{-C}_{60})$ complexes **5** and **6**, which were isolated in excellent yields as dark solids. The two complexes showed good solubility in organic solvents, but remained insoluble in water.



Scheme 1. Synthesis of complexes **5** and **6**, and the $N_{\text{pyr}}\text{-C}_60$ derivatives **3** and **4**

starting from alkyl bromides and primary amines. Reagents and conditions:

- i. NEt_3 , THF, 0°C to *rt*, 16*h*, 1: 60%, 2: 32%, ii. toluene, 110°C , 16*h*, 3: 51%, 4: 24%, iii. CH_2Cl_2 , reflux, 24*h*, in the dark, 5: 98%, 6: 92%.

The ^1H NMR spectra of the $N_{\text{pyr}}\text{-C}_60$ derivatives **3** and **4** revealed the expected signals for this family of fullerenopyrrolidines [15]. One characteristic feature of such compounds is that the methylene protons located in α positions with respect to the pyrrolidine nitrogen are diastereotopic due to the asymmetric carbon on the pyrrolidine unit (the asymmetric carbon being identified with an asterisk in Scheme 1). For instance, the protons of the CH_2 group linking the pyrrolidine to the pyridine, which appear as a doublet at $\delta = 3.30$ ppm in compound **1** (see experimental section), can be seen as two doublets in **3**, at $\delta = 4.93$ and 4.30 ppm, respectively. Similarly, the CH_2 protons of the pyrrolidine group ($\delta = 3.81$ ppm in **1**) are now observed as two doublets at $\delta = 4.69$ and 4.14 ppm in **3** (Figure 1). Moreover, complexation to the ruthenium center results in a major downfield shift of the signal corresponding to the protons of the pyridyl groups, mainly H_α ($\Delta\delta = +0.4$ ppm) and H_β ($\Delta\delta = +0.1$ ppm) (Figure 1). This is characteristic for the coordination of a pyridyl moiety to an arene ruthenium unit [16]. However, the other protons of the $N_{\text{pyr}}\text{-C}_60$ ligands **3** and **4** do not undergo any significant shift as a result of the complexation.

The formation of the complexes was also confirmed by electrospray mass spectrometry (ESI-MS). However, the two complexes behave differently under the ESI-MS conditions. Complex **5** showed a cationic species at $m/z = 1225.1$, which can be assigned to complex **5** after the loss of a chloride anion, $[\mathbf{5} - \text{Cl}]^+$, while in **6**, a sodium adduct was found at $m/z = 1363.2$, $[\mathbf{6} + \text{Na}]^+$. The loss of a chloride atom in dichloropyridyl arene ruthenium complexes is relatively common under ESI-MS conditions [17]. Similarly, the formation of sodium adducts has been observed previously [18]. In addition to the peak $[\mathbf{5} - \text{Cl}]^+$ for complex **5**, the mass peak observed at $m/z = 1475.3$ corresponds to a dinuclear species in which the ^tBu group is lost and insertion of a (*p*-cymene) RuCl unit occurs, thus giving rise to the adduct $[\mathbf{5} - \text{^tBu} + (\text{p-cymene})\text{RuCl} + \text{H}]^+$ (Figure 2).

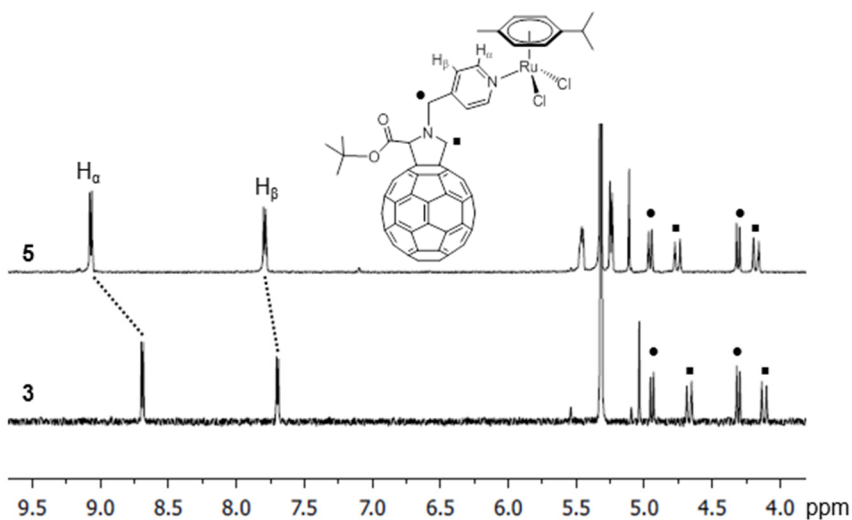


Figure 1. Comparative ¹H NMR spectra of compounds **3** and **5** (400 MHz, CD₂Cl₂). The pyrrolidine CH₂ protons and the exocyclic CH₂ are indicated with ■ and ●, respectively.

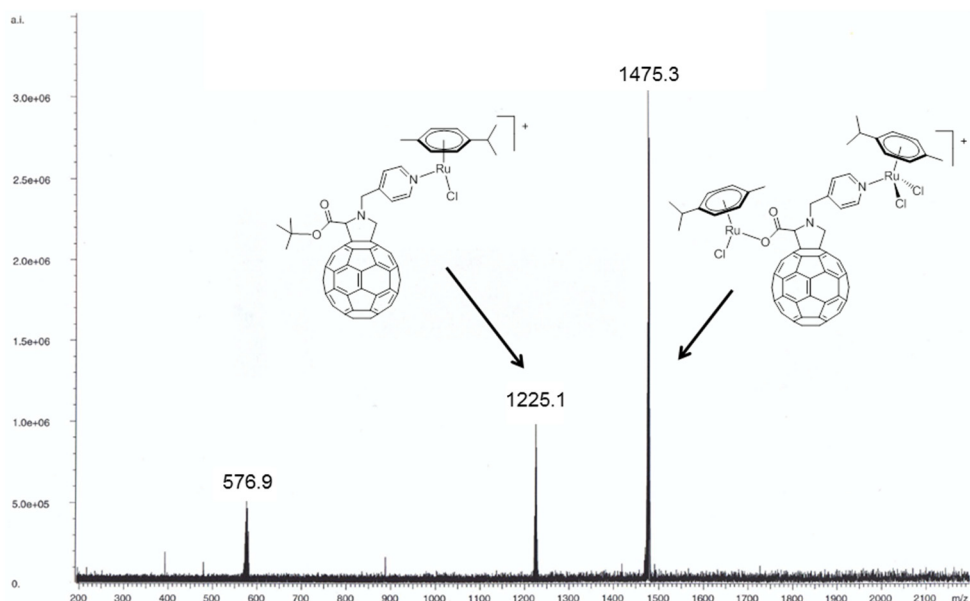


Figure 2. ESI mass spectrum of **5** (in CHCl₃/CH₃CN).

CONCLUSIONS

Two (*p*-cymene)RuCl₂(*N*_{pyr}-C₆₀) complexes have been synthesized and characterized by NMR spectroscopy and ESI mass spectrometry. These complexes can be exploited for further reactions to afford other derivatives (to be published). Such fullerene-based arene ruthenium complexes and their congeners can be of interest for applications in biomedical, catalysis and material science.

EXPERIMENTAL SECTION

Toluene (NaH, under N₂), THF (K and Na, under N₂) and CH₂Cl₂ (P₂O₅, under N₂) were distilled prior to use. [60]Fullerene (99.9%) was purchased from Materials and Electrochemical Research (MER) Corporation, Tucson (AZ), USA. 4-(Aminomethyl)pyridine and all other reagents were commercially available (Sigma-Aldrich), while (*p*-cymene)₂Ru₂(μ -Cl)₂Cl₂ was prepared according to literature [19].

Column chromatography was performed using silica gel (Chemie Brunschwig, Basel, Switzerland, 63-200, 60Å). Size exclusion chromatography was carried out using size exclusion gel Bio-Rad SX1 with the range of mass operation between 600 and 14000 Da. NMR spectra were measured in CDCl₃ or in CD₂Cl₂ on a Bruker AMX-400 (400 and 100 MHz) or a Bruker Advance-400 spectrometer and are reported in ppm on the δ scale. The mass spectrometry measurements were performed on a LCQ-IT Finnigan or on a Bruker FRMS 4.7T BioAPEX II for ESI.

Preparation of *tert*-butyl(pyridin-4-yl-methyl)glycinate, **1**

To a solution of 4-(aminomethyl)pyridine (0.81 g, 7.50 mmol) and triethylamine (1.52 g, 15.00 mmol) in dry THF (40 mL), a THF solution (25 mL) of *tert*-butyl bromoacetate (0.98 g, 5.00 mmol) was added dropwise at 0°C. After 16h of reaction at RT, the solvent was evaporated and the residue was dissolved in dichloromethane (50 mL). The organic phase was washed (H₂O), dried (MgSO₄) and evaporated. Purification of the residue by column chromatography (eluent CH₂Cl₂/MeOH 10/0.75) gave pure **1** as an orange/red liquid with a yield of 60% (0.66 g). ¹H NMR (400 MHz, CDCl₃, ppm): δ = 8.54 (d, ³J_{H-H} = 6.0 Hz, 2H, H_α pyridine), 7.27 (d, ³J_{H-H} = 5.6 Hz, 2H, H_β pyridine), 3.81 (s, 2H, CH₂CO₂^tBu), 3.30 (s, 2H, CH₂C_{pyridine}), 2.09 (s, 1H, NH), 1.46 (s, 9H, C(CH₃)₃). ¹³C NMR (100 MHz, CDCl₃, ppm): δ = 171.25, 149.54, 148.92, 123.18, 81.63, 51.89, 50.79, 28.12. MS (ESI(+)) = 223.3 [M + H]⁺.

Preparation of 2-(2-(2-methoxyethoxy)ethoxy)ethyl(pyridin-4-ylmethyl)glycinate, **2**

Compound **2** was prepared and purified as **1**, from 4-(aminomethyl)pyridine (0.16 g, 1.50 mmol), triethylamine (0.30 g, 3.00 mmol), 2-(2-(2-methoxyethoxy)ethoxy)ethyl bromoacetate (0.28 g, 1.00 mmol) and dry THF (80 mL). Product **2** was isolated as a pale yellow liquid with a yield of 32% (0.10 g). ¹H NMR (400 MHz, CDCl₃, ppm): δ = 8.56 (d, ³J_{H-H} = 6.1 Hz, 2H, H_α pyridine), 7.28 (d, ³J_{H-H} = 6.1 Hz, 2H, H_β pyridine), 4.30 (t, ³J_{H-H} = 4.7 Hz, 2H, H_{peg}), 3.87 (s, 2H, CH₂C_{pyridine}), 3.68-3.71 (m, 2H, H_{peg}), 3.63-3.66 (m, 6H, H_{peg}), 3.53-3.55 (m, 2H, H_{peg}), 3.45 (s, 2H, CH₂CO₂peg), 3.37 (s, 3H, OCH₃). ¹³C NMR (100 MHz, CDCl₃, ppm): δ = 171.86, 149.27, 123.31, 71.90, 70.58, 68.96, 64.04, 61.64, 59.00, 51.72, 49.82. MS (ESI(+)) = 313.3 [M + H]⁺.

Preparation of *tert*-butyl(*N*-ethylpyridine)fullerenopyrrolidine carboxylate, **3**

To a solution of [60]fullerene (0.36 g, 0.50 mmol) in dry toluene (300 mL), a suspension of **1** (0.11 g, 0.50 mmol) and *para*-formaldehyde (0.07 g, 2.50 mmol) in dry toluene (10 mL) was added. The mixture was stirred under reflux for 16h in the dark and evaporated to dryness. Purification of the solid by column chromatography (first with toluene to eliminate unreacted [60]fullerene, and then with toluene/MeOH 20:1) gave **3** as a shiny black solid with a yield of 51% (0.24 g). ¹H NMR (400 MHz, CD₂Cl₂, ppm): δ = 8.69 (d, ³J_{H-H} = 5.2 Hz, 2H, H_α pyridine), 7.70 (d, ³J_{H-H} = 5.3 Hz, 2H, H_β pyridine), 5.04 (s, 1H, CHCO₂tBu), 4.96 (d, ³J_{H-H} = 9.3 Hz, 1H, HCHC_{pyridine}), 4.69 (d, ³J_{H-H} = 14.0 Hz, 1H, HCH_{pyrrolidine}), 4.32 (d, ³J_{H-H} = 9.3 Hz, 1H, HCHC_{pyridine}), 4.14 (d, ³J_{H-H} = 14.0 Hz, 1H, HCH_{pyrrolidine}), 1.53 (s, 9H, C(CH₃)₃). ¹³C NMR (100 MHz, CD₂Cl₂, ppm): δ = 168.58, 154.49, 153.76, 152.44, 151.22, 150.14, 147.34, 146.95, 146.23, 146.01, 145.33, 145.21, 144.58, 144.44, 143.02, 142.56, 142.17, 142.11, 142.05, 142.04, 141.74, 140.18, 140.13, 138.69, 139.28, 136.33, 135.99, 132.27, 123.61, 83.16, 76.79, 72.76, 69.49, 67.73, 64.85, 54.73, 27.98. MS (ESI(+)) = 956.1 [M + H]⁺.

Preparation of 2-(2-(2-methoxyethoxy)ethoxy)ethyl(*N*-ethylpyridine)fullerenopyrrolidine carboxylate, **4**

Compound **4** was prepared as **3**, from [60]fullerene (0.13 g, 0.16 mmol), *para*-formaldehyde (0.02 g, 0.70 mmol), and **2** (0.04 g, 0.14 mmol) in dry toluene (250 mL). Purification of the solid by column chromatography (first with toluene and then with CH₂Cl₂/MeOH 20:1) and a size exclusion column of Bio-Rad SX1 (eluent toluene) afforded **4** as a brown solid with a yield of 24% (0.07 g).

¹H NMR (400 MHz, CD₂Cl₂, ppm): δ = 8.69 (d, ³J_{H-H} = 4.9 Hz, 2H, H_α pyridine), 7.70 (d, ³J_{H-H} = 5.6 Hz, 2H, H_β pyridine), 5.23 (s, 1H, CH_{peg}CO₂), 4.97 (d, ³J_{H-H} = 9.4 Hz, 1H, HCH_{pyrrolidine}), 4.68 (d, ³J_{H-H} = 14.1 Hz, 1H, HCH_{pyrrolidine}), 4.44-4.48 (m, 2H, H_{peg}), 4.35 (d, ³J_{H-H} = 9.5 Hz, 1H, HCHC_{pyridine}), 4.14 (d, ³J_{H-H} = 14.1 Hz, 1H, HCHC_{pyridine}), 3.62-3.73 (m, 2H, H_{peg}), 3.54-3.45 (m, 8H, H_{peg}), 3.30 (s, 3H, OCH₃). ¹³C NMR (100 MHz, CD₂Cl₂, ppm): δ = 170.12, 155.00, 150.79, 147.31, 146.87, 146.69, 145.65, 146.63, 146.37, 146.24, 146.21, 145.85, 145.83, 143.25, 143.22, 143.19, 142.83, 142.81, 142.67, 142.54, 142.39, 142.37, 142.36, 124.30, 77.12, 73.32, 72.45, 71.09, 70.99, 70.06, 69.44, 65.45, 65.19, 59.20, 55.40, 30.26. MS (ESI(+)) = 1045.4 [M + H]⁺.

Preparation of dichloro(*p*-cymene)(*tert*-butyl(*N*-ethylpyridine)fullerenopyrrolidine carboxylate)ruthenium(II), **5**

A solution of (*p*-cymene)₂Ru₂(μ-Cl)₂Cl₂ (0.05 g, 0.10 mmol) and **3** (0.19 g, 0.20 mmol) in dry CH₂Cl₂ (50 mL) was stirred under reflux for 24h. After evaporation to dryness, product **5** was obtained as a brown solid with a yield of 98% (0.24 g). ¹H NMR (400 MHz, CD₂Cl₂, ppm): δ = 9.08 (d, ³J_{H-H} = 6.6 Hz, 2H, H_α pyridine), 7.79 (d, ³J_{H-H} = 6.1 Hz, 2H, H_β pyridine), 5.45-5.47 (m, 2H, H_{cymene}), 5.25 (d, ³J_{H-H} = 6.0 Hz, 2H, H_{cymene}), 5.11 (s, 1H, CHCO₂tBu), 4.97 (d, ³J_{H-H} = 9.4 Hz, 1H, HCHC_{pyridine}), 4.77 (d, ³J_{H-H} = 15.1 Hz, 1H, HCH_{pyrrolidine}), 4.32 (d, ³J_{H-H} = 9.4 Hz, 1H, HCHC_{pyridine}), 4.20 (d, ³J_{H-H} = 15.1 Hz, 1H, HCH_{pyrrolidine}), 2.98 (sept, ³J_{H-H} = 6.9 Hz, 1H, CH(CH₃)₂), 2.09 (s, 3H, CH₃C_{arom}), 1.53 (s, 9H, C(CH₃)₃), 1.33 (d, ³J_{H-H} = 7.0 Hz, 6H, CH(CH₃)₂). ¹³C NMR (100 MHz, CD₂Cl₂, ppm): δ = 169.09, 155.45, 150.82, 147.06, 146.86, 146.63, 146.38, 146.26, 146.19, 145.98, 145.83, 145.22, 145.02, 143.60, 143.23, 142.77, 142.66, 142.37, 140.78, 136.89, 136.64, 124.62, 103.86, 97.57, 84.01, 83.50, 83.38, 82.75, 82.72, 77.42, 73.28, 70.11, 65.44, 54.67, 53.46, 31.23, 30.24, 28.61, 22.57, 22.55, 18.53. MS (ESI(+)) = 1225.12 [M - Cl]⁺.

Preparation of dichloro(*p*-cymene)(2-(2-(2-methoxyethoxy)ethoxy)ethyl(*N*-ethylpyridine)fullerenopyrrolidine carboxylate)ruthenium(II), **6**

Compound **6** was prepared and purified as **5**, from (*p*-cymene)₂Ru₂(μ-Cl)₂Cl₂ (0.01 g, 0.02 mmol), **4** (0.05 g, 0.04 mmol) in dry CH₂Cl₂ (5 mL). Product **6** was obtained as a black solid with a yield of 92% (0.05 g). ¹H NMR (400 MHz, CD₂Cl₂, ppm): δ = 9.08 (d, ³J_{H-H} = 6.7 Hz, 2H, H_α pyridine), 7.80 (d, ³J_{H-H} = 6.4 Hz, 2H, H_β pyridine), 5.44-5.47 (m, 2H, H_{cymene}), 5.31 (s, 1H, CH_{peg}CO₂), 5.25 (d, ³J_{H-H} = 5.9 Hz, 2H, H_{cymene}), 4.98 (d, ³J_{H-H} = 9.5 Hz, 1H, HCH_{pyrrolidine}), 4.77 (d, ³J_{H-H} = 15.1 Hz, 1H, HCH_{pyrrolidine}), 4.44-4.47 (m, 2H, H_{peg}), 4.35 (d, ³J_{H-H} = 9.4 Hz, 1H, HCHC_{pyridine}), 4.20 (d, ³J_{H-H} = 15.1 Hz, 1H,

HCHC_{pyridine}), 3.71-3.60 (m, 2H, H_{peg}), 3.45-3.55 (m, 8H, H_{peg}), 3.31 (s, 3H, OCH₃), 2.95-3.02 (m, 1H, CH(CH₃)₂), 2.09 (s, 3H, CH₃C_{arom}), 1.33 (d, ³J_{H-H} = 6.9 Hz, 6H, CH(CH₃)₂). ¹³C NMR (100 MHz, CD₂Cl₂, ppm): δ = 170.04, 155.47, 154.99, 154.74, 153.71, 151.40, 150.60, 148.00, 149.86, 147.05-145.85, 145.23, 145.11, 144.96, 143.63, 143.21, 142.81, 142.68-142.44, 142.38, 140.88, 140.81, 140.29, 140.15, 138.25, 136.93, 136.82, 136.10, 124.66, 103.90, 97.55, 83.45, 83.36, 82.76, 77.09, 73.20, 72.43, 71.05, 70.97, 70.95, 70.05, 69.36, 65.42, 65.28, 59.20, 31.24, 22.56, 18.54. MS (ESI(+)) = 1363.2 [M + Na]⁺.

ACKNOWLEDGEMENTS

The Authors thank the University of Neuchatel and the Swiss National Science Foundation (grant no. 200020-152716) for financial support.

REFERENCES

- [1]. J.L. Delgado, S. Filippone, F. Giacalone, M.Á. Herranz, B. Illescas, E.M. Pérez, N. Martín, *Topics in Current Chemistry*, **2014**, 350, 1.
- [2]. (a) H.W. Kroto, J.R. Heath, S.C. O'Brien, R.F. Curl, R.E. Smalley, *Nature*, **1985**, 318, 162. (b) R.C. Haddon, L.E. Brus, K. Raghavachari, *Chemical Physics Letters*, **1986**, 125, 459. (c) R.C. Haddon, *Journal of the American Chemical Society*, **1997**, 119, 1797. (d) A. Hirsch, “*Principles of Fullerene Reactivity*”, Vol. 199, Springer, Berlin, **1999**. (e) N. Martín, *Chemical Communications*, **2013**, 49, 1039.
- [3]. (a) C. Bingel, *Chemische Berichte*, **1993**, 126, 1957. (b) M. Maggini, G. Scorrano, M. Prato, *Journal of the American Chemical Society*, **1993**, 115, 9798. (c) M. Prato, M. Maggini, *Accounts of Chemical Research*, **1998**, 31, 519. (d) K. Kordatos, T. Da Ros, S. Bosi, E. Vázquez, M. Bergamin, C. Cusan, F. Pellarini, V. Tomberli, B. Baiti, D. Pantarotto, V. Georgakilas, G. Spalluto, M. Prato, *Journal of Organic Chemistry*, **2001**, 66, 4915.
- [4]. (a) D.M. Guldi, *Chemical Society Reviews*, **2002**, 31, 22. (b) M. Sawamura, Y. Kuninobu, M. Togano, Y. Matsuo, M. Yamanaka, E. Nakamura, *Journal of the American Chemical Society*, **2002**, 124, 9354. (c) M. Segura, L. Sánchez, J. de Mendoza, N. Martín, D.M. Guldi, *Journal of the American Chemical Society*, **2003**, 125, 15093. (d) D.M. Guldi, G.M. Aminur Rahman, V. Sgobba, C. Ehli, *Chemical Society Reviews*, **2006**, 35, 471.
- [5]. (a) B.C. Thompson, J.M.J. Fréchet, *Angewandte Chemie International Edition*, **2008**, 47, 58. (b) C.J. Brabec, S. Gowrisanker, J.J.M. Halls, D. Laird, S. Jia, S.P. Williams, *Advanced Materials*, **2010**, 22, 3839.

- [6]. (a) M. Maggini, A. Donò, G. Scorranoa, M. Prato, *Journal of the Chemical Society; Chemical Communications*, **1995**, 846. (b) N. Armaroli, C. Boudon, D. Felder, J.-P. Gisselbrecht, M. Gross, G. Marconi, J.-F. Nicoud, J.-F. Nierengarten, V. Vicinelli, *Angewandte Chemie International Edition*, **1999**, 38, 3730. (c) K. Barthelmes, J. Kübel, A. Winter, M. Wächtler, C. Fribe, B. Dietzek, U.S. Schubert, *Inorganic Chemistry*, **2015**, 54, 3159.
- [7]. F. Cardinali, J.-L. Gallani, S. Schergna, M. Maggini, J.-F. Nierengarten, *Tetrahedron Letters*, **2005**, 46, 2969.
- [8]. (a) Y. Matsuo, E. Nakamura, *Organometallics*, **2003**, 22, 2554. (b) C.-H. Chen, C.-S. Chen, H.-F. Dai, W.-Y. Yeh, *Dalton Transactions*, **2012**, 41, 3030. (c) F.L. Bowles, M.M. Olmstead, A.L. Balch, *Journal of the American Chemical Society*, **2014**, 136, 3338. (d) W.-Y. Yeh, *Journal of Organometallic Chemistry*, **2014**, 751, 351. (e) C.-H. Chen, A. Aghabali, C. Suarez, M.M. Olmstead, A.L. Balch, L. Echegoyen, *Chemical Communications*, **2015**, 51, 6489.
- [9]. (a) B. Therrien, *Coordination Chemistry Reviews*, **2009**, 253, 493. (b) A.K. Singh, D.S. Pandey, Q. Xu, P. Braunstein, *Coordination Chemistry Reviews*, **2014**, 270-271, 31.
- [10]. (a) K. Severin, *Chemical Communications*, **2006**, 3859. (b) B. Therrien, *European Journal of Inorganic Chemistry*, **2009**, 2445.
- [11]. (a) A.F.A. Peacock, P.J. Sadler, *Chemistry: An Asian Journal*, **2008**, 3, 1890. (b) G. Süss-Fink, *Dalton Transactions*, **2010**, 39, 1673. (c) G.S. Smith, B. Therrien, *Dalton Transactions*, **2011**, 40, 10793. (d) T.R. Cook, V. Vajpayee, M.H. Lee, P.J. Stang, K.-W. Chi, *Accounts of Chemical Research*, **2013**, 46, 2464. (e) A.A. Nazarov, C.G. Hartinger, P.J. Dyson, *Journal of Organometallic Chemistry*, **2014**, 751, 251.
- [12]. (a) L. Delaude, A. Demonceau, *Dalton Transactions*, **2012**, 41, 9257. (b) A.L. Noffke, A. Habtemariam, A.M. Pizarro, P.J. Sadler, *Chemical Communications*, **2012**, 48, 5219. (c) G. Süss-Fink, *Journal of Organometallic Chemistry*, **2014**, 751, 2. (d) P. Kumar, R.K. Gupta, D.S. Pandey, *Chemical Society Reviews*, **2014**, 43, 707.
- [13]. A. Pitt-Barry, N.P.E. Barry, V. Russo, B. Heinrich, B. Donnio, B. Therrien, R. Deschenaux, *Journal of the American Chemical Society*, **2014**, 136, 17616.
- [14]. G. Porzi, S. Sandri, *Tetrahedron: Asymmetry*, **1996**, 7, 189.
- [15]. (a) C.-H. Andersson, G. Berggren, S. Ott, H. Grennberg, *European Journal of Inorganic Chemistry*, **2011**, 1744. (b) C.-H. Andersson, L. Nyholm, H. Grennberg, *Dalton Transactions*, **2012**, 41, 2374. (c) B. Jin, J. Shen, R. Peng, C. Chen, S. Chu, *European Journal of Organic Chemistry*, **2014**, 6252. (d) A. Parveen, V. Suganya, S. Nagarajan, *RSC Advances*, **2015**, 5, 20351.
- [16]. (a) P. Govender, N.C. Antonels, J. Mattsson, A.K. Renfrew, P.J. Dyson, J.R. Moss, B. Therrien, G.S. Smith, *Journal of Organometallic Chemistry*, **2009**, 694, 3470. (b) N.P.E. Barry, M. Austeri, J. Lacour, B. Therrien, *Organometallics*, **2009**, 28, 4894. (c) O. Zava, J. Mattsson, B. Therrien, P.J. Dyson, *Chemistry: A European Journal*, **2010**, 16, 1428. (d) N.P.E. Barry, F. Edafe, B. Therrien, *Dalton Transactions*, **2011**, 40, 7172.

- [17]. (a) T.-T. Thai, B. Therrien, G. Süss-Fink, *Journal of Organometallic Chemistry*, **2009**, 694, 3973. (b) M. Auzias, J. Gueniat, B. Therrien, G. Süss-Fink, A.K. Renfrew, P.J. Dyson, *Journal of Organometallic Chemistry*, **2009**, 694, 855. (c) M. Gras, B. Therrien, G. Süss-Fink, A. Casini, F. Edafe, P.J. Dyson, *Journal of Organometallic Chemistry*, **2010**, 695, 1119.
- [18]. P. Govindaswamy, B. Therrien, G. Süss-Fink, P. Štěpnička, J. Ludvík, *Journal of Organometallic Chemistry*, **2007**, 692, 1661.
- [19]. M.A. Bennett, T.-N. Huang, T.W. Matheson, A.K. Smith, *Inorganic Syntheses*, **1982**, 21, 74.

SYNTHESIS OF NEW 5-(CHROMENE-3-YL)METHYLENE-2,4-THIAZOLIDINEDIONES

CRISTINA NASTASĂ^{a,*}, BRÎNDUŞA TIPERCIUC^a, LAURIAN VLASE^b,
ADRIAN PÎRNĂU^c, OVIDIU ONIGA^a

ABSTRACT. With the aim of developing new biologically active compounds, a series of new *N*-substituted 5-(chromene-3-yl)methylene-2,4-thiazolidinediones **3-12** has been synthesized. First step was the condensation of different chromone-3-carbaldehydes with 2,4-thiazolidinedione, followed by the reaction with various α -bromoalkylarylketones. The structures of all new compounds were confirmed by elemental analysis, mass spectra and ^1H NMR studies.

Keywords: chromone; thiazolidinedione; α -bromoalkylarylketones

INTRODUCTION

Microbial resistance represents, for more than decades, a real threat for the efficiency of current drug therapy [1-3]. For the patients at risk, this may involve prolonging the disease or even death. The main reasons for the increasing microbial resistance are: inappropriate use of antibiotics and the lack of compliance from patients, inappropriate prescribing [4], increasing number of immunocompromised patients, excessive use of antibiotics in the veterinary practice and decreased financial investments of big pharmaceutical companies in the research activities for discovering new potent antimicrobial drug. In 2014, WHO signalized the resistance of 9 bacterial strains to classic treatment. In the case of fungal infections, the increased resistance to azole drugs and the emergence of strains resistant to echinocandins, the newest class of antifungal agents, was reported [5].

^a "Iuliu Hațegianu" University of Medicine and Pharmacy, Faculty of Pharmacy, Department of Pharmaceutical Chemistry, 41 Victor Babeș street, Cluj-Napoca, Romania.

^b "Iuliu Hațegianu" University of Medicine and Pharmacy, Faculty of Pharmacy, Department of Pharmaceutical Technology and Biopharmaceutics, 41 Victor Babeș street, Cluj-Napoca, Romania.

^c National Institute for Research and Development of Isotopic and Molecular Technologies, 1 Donath street, Cluj-Napoca, Romania.

* Corresponding author: cmoldovan@umfcluj.ro

Nowadays, efforts are being made for the control of microbial resistance phenomenon, limiting the global spread and its effects. The research in this area is orientated towards the discovery of a new potent drug, with an original chemical structure and, why not, an original mechanism of action.

From the big family of heterocyclic compounds, the five-membered rings, containing two heteroatoms, receive special attention, due to their large spectrum of biological activities. A considerable amount of work has been done on the synthesis of thiazolidinedione derivatives as potent antibacterial and antifungal agents [6-10]. Chromones belong to the important class of oxygen-containing heterocyclic compounds and they are part of the flavonoid family. These compounds are widespread in nature and exhibit a wide range of pharmacological activity like antibacterial, antifungal [11-14], antitumor, antioxidant, anti-HIV, anti-inflammatory. Therefore, the vast range of biological effects associated with this scaffold has resulted in the chromone ring system being considered as a privileged structure in medicinal chemistry.

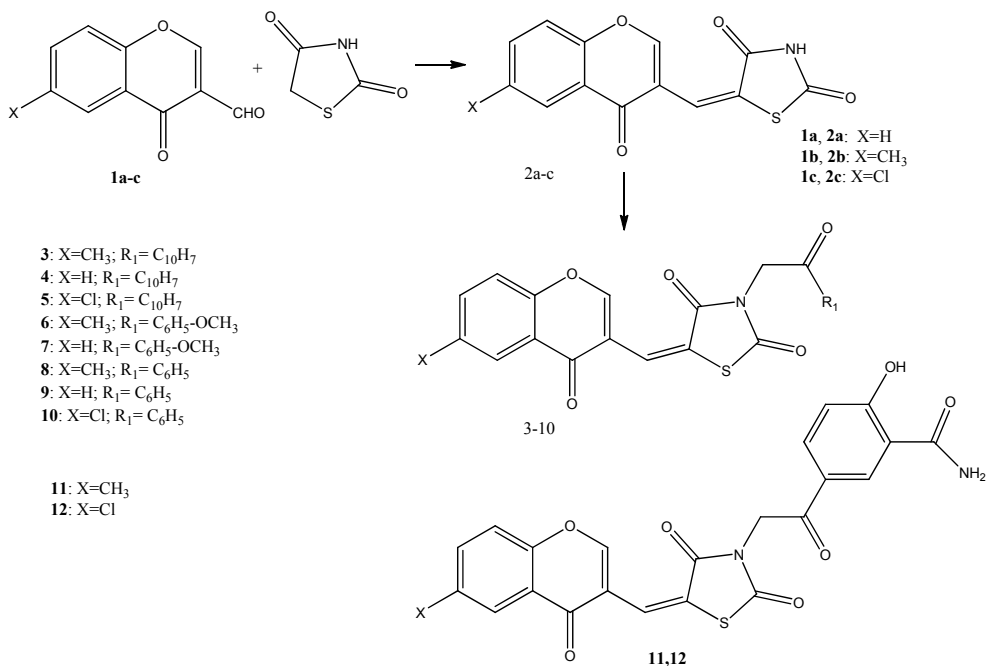
The association of two or more pharmacophores inside the same molecule may be associated with the increase of the biological effects. As a continuation of our work [15] and considering the facts presented above, we describe here, in this paper, the chemical synthesis of a new series of *N*-substituted 5-(chromene-3-yl)methylene-2,4-thiazolidinediones, which gather two important scaffolds in medicinal chemistry.

RESULTS AND DISCUSSION

Synthesis of new *N*-substituted 5-chromenyl-thiazolidinediones had two steps. First consisted in Knoevenagel condensation of 2,4-thiazolidinedione with 3-formyl-chromones **1a-c**, in acetic acid and in the presence of anhydrous sodium acetate (**Scheme 1**). Synthesis of compounds **2a** and **2b** was done according to literature data [16], and compound **2c** was obtained in our laboratory, following the same procedure [15]. The new derivatives were treated with various α -bromoalkylarylketones, in the presence of anhydrous potassium hydroxide and dimethylformamide (DMF), in order to obtain, in good yields, the new *N*-substituted molecules **3-12**.

The compounds were isolated, the melting points were registered and the purity was confirmed by thin layer chromatography (TLC). All new molecules were characterized by elemental analysis and spectroscopic data (NMR, MS), which were consistent with the assigned structures.

SYNTHESIS OF NEW 5-(CHROMENE-3-YL)METHYLENE-2,4-THIAZOLIDINEDIONES



Scheme 1. Synthesis of new *N*-substituted chromenyl-thiazolidinediones
i: anhydrous sodium acetate/acetic acid, 3h reflux; ii: α -bromoalkylarylketones, anhydrous potassium hydroxide, DMF, 30 minutes, stirring, room temperature

The ¹H NMR spectra showed characteristic singlets due to –CH= proton bound in position 5 of thiazolidinedione system, at δ 7.74–7.80 ppm, demonstrating the synthesis of 5-chromenyl-thiazolidinediones.

The disappearance, in the spectra, of the signal due to the H from –NH- in thiazolidinedione heterocycle and the appearance of signals specific for the phenyl protons, put in evidence the *N*-substitution and thus, the synthesis of the new derivatives.

CONCLUSIONS

The present work describes the synthesis of ten new *N*-substituted chromenyl-thiazolidinediones **3-12**. Compounds **2a** and **2b** were reproduced after the techniques presented in the literature and 5-chromenyl-thiazolidinedione **2c** was previously obtained in our research laboratory, using the same procedure. The structures of all new synthesized molecules were fully confirmed by physical data, elemental analyses and ¹H NMR spectroscopy in solution.

EXPERIMENTAL SECTION

General

Solvents were obtained from commercial sources. Analytical thin layer chromatography was carried out on precoated Silica Gel 60F₂₅₄ sheets using UV absorption for visualization. The melting points were taken with MPM-H1 Schorpp melting point meter, and are uncorrected. The ¹H NMR spectra were recorded at room temperature on a Bruker Avance NMR spectrometer operating at 500 MHz and were in accord with the assigned structures. Chemical shift values were reported relative to tetramethylsilane (TMS) as internal standard. The samples were prepared by dissolving the synthesized powder of the compounds in DMSO-d₆ ($\delta_H = 2.51$ ppm) as solvent. Mass spectra were recorded by Agilent 1100, type SL spectrometer (positive ionization) and with a Varian MAT CH-5 spectrometer (70 eV). Elemental analysis was registered with a Vario EI CHNS instrument.

Synthesis

General procedure

Synthesis of 5-chromenyl-2,4-thiazolidinedione (2a and 2b)

1 mmol of 4-oxo-4H-chromene-3-carbaldehyde **1a** or 6-methyl-4-oxo-4H-chromene-3-carbaldehyde **1b** was refluxed for 3 h with 1 mmol (0.117 g) of 1,3-thiazolidine-2,4-dione and 4 mmol (0.328 g) of anhydrous sodium acetate in 5 ml of acetic acid, according to the literature data [16]. The reaction mixture was cooled, and the crude product was filtered under reduced pressure, washed with water on the filter and purified by recrystallization from ethanol. Compound **2c** was obtained following the same procedure, starting from 6-chloro-4-oxo-4H-chromene-3-carbaldehyde **1c** [15].

Synthesis of N-substituted 5-chromenyl-2,4-thiazolidinedione (3-12)

For synthesis, 1 mmol of 5-chromenyl-2,4-thiazolidinedione **2a-c** was stirred for 30 minutes, at room temperature, with 1.1 mmol (0.062 g) of anhydrous potassium hydroxide, in 6 ml of DMF. After the potassium salt was formed, 1.1 mmol of α -bromoalkylarylketones were added. The crude product was filtered under reduced pressure, washed with water on the filter and purified by recrystallization from ethanol.

SYNTHESIS OF NEW 5-(CHROMENE-3-YL)METHYLENE-2,4-THIAZOLIDINEDIONES

5-((6-methyl-4-oxo-4H-chromen-3-yl)methylene)-3-(2-(naphthalen-2-yl)-2oxoethyl) thiazolidine-2,4-dione (3)

Yield 95 %. White powder, mp: 251 °C. ¹H NMR (DMSO-*d*₆, 500 MHz, ppm): δ 2.46 (s, 3H, -CH₃); 5.45 (s, 2H, -CH₂-); 7.66 (d, 1H, C₈-chromone-H); 7.68 (dd, 1H, C₇-chromone-H); 7.68-7.74 (m, 1H, naphtyl); 7.70 (dd, 1H, naphtyl); 7.75 (d, 1H, naphtyl); 7.78 (s, 1H, C=CH); 7.95 (s, 1H, C₅-chromone-H); 8.05 (d, 1H, naphtyl); 8.09 (d, 1H, naphtyl); 8.17 (d, 1H, naphtyl); 8.90 (s, 1H, naphtyl); 8.97 (s, 1H, C₂-chromone-H). Anal. Calcd. (%) for C₂₆H₁₇NO₅S (455.48): C, 68.56; H, 3.76; N, 3.08; S, 7.04. Found: C, 68.55; H, 3.76; N, 3.08; S, 7.04. MS (EI, 70 eV): *m/z* 456.5 [M+1].

3-(2-(naphthalen-2-yl)-2-oxoethyl)-5-((4-oxo-4H-chromen-3-yl)methylene) thiazolidine-2,4-dione (4)

Yield 85 %. White powder, mp: 264 °C. ¹H NMR (DMSO-*d*₆, 500 MHz, ppm): δ 5.41 (s, 2H, -CH₂-); 7.57 (d, 1H, C₆-chromone-H); 7.67 (d, 1H, C₈-chromone-H); 7.68 (dd, 1H, C₇-chromone-H); 7.69-7.73 (m, 1H, naphtyl); 7.70 (dd, 1H, naphtyl); 7.76 (d, 1H, naphtyl); 7.78 (s, 1H, C=CH); 7.94 (s, 1H, C₅-chromone-H); 8.04 (d, 1H, naphtyl); 8.09 (d, 1H, naphtyl); 8.16 (d, 1H, naphtyl); 8.91 (s, 1H, naphtyl); 8.96 (s, 1H, C₂-chromone-H). Anal. Calcd. (%) for C₂₅H₁₅NO₅S (441.46): C, 68.02; H, 3.42; N, 3.17; S, 7.26. Found: C, 68.03; H, 3.42; N, 3.15; S, 7.27. MS (EI, 70 eV): *m/z* 442.5 [M+1].

5-((6-chloro-4-oxo-4H-chromen-3-yl)methylene)-3-(2-(naphthalen-2-yl)-2oxoethyl) thiazolidine-2,4-dione (5)

Yield 83 %. Yellow powder, mp: 252 °C. ¹H NMR (DMSO-*d*₆, 500 MHz, ppm): 5.42 (s, 2H, -CH₂-); 7.61 (d, 1H, C₈-chromone-H); 7.67 (dd, 1H, C₇-chromone-H); 7.68-7.72 (m, 1H, naphtyl); 7.74 (dd, 1H, naphtyl); 7.76 (d, 1H, naphtyl); 7.80 (s, 1H, C=CH); 7.94 (s, 1H, C₅-chromone-H); 8.04 (d, 1H, naphtyl); 8.08 (d, 1H, naphtyl); 8.18 (d, 1H, naphtyl); 8.92 (s, 1H, naphtyl); 8.98 (s, 1H, C₂-chromone-H). Anal. Calcd. (%) for C₂₅H₁₄CINO₅S (475.9): C, 63.09; H, 2.97; N, 2.94; S, 6.74. Found: C, 63.10; H, 2.97; N, 2.93; S, 6.75. MS (EI, 70 eV): *m/z* 477 [M+1].

3-(2-(4-methoxyphenyl)-2-oxoethyl)-5-((6-methyl-4-oxo-4H-chromen-3-yl)methylene) thiazolidine-2,4-dione (6)

Yield 76 %. Yellow powder, mp: 238 °C. ¹H NMR (DMSO-*d*₆, 500 MHz, ppm): δ 3.03 (s, 3H, -CH₃); 3.06 (s, 3H, -CH₃); 5.23 (s, 2H, -CH₂-); 7.12 (d, 2H, phenyl); 7.65 (d, 1H, C₈-chromone-H); 7.71 (dd, 1H, C₇-chromone-H); 7.75 (s, 1H, C=CH); 7.94 (s, 1H, C₅-Chromone-H); 8.06 (d, 2H, phenyl); 8.95 (s, 1H, C₂-chromone-H). Anal. Calcd. (%) for C₂₃H₁₇NO₆S (435.45): C, 63.44; H, 3.94; N, 3.22; S, 7.36. Found: C, 63.43; H, 3.93; N, 3.21; S, 7.37. MS (EI, 70 eV): *m/z* 436.5 [M+1].

3-(2-(4-methoxyphenyl)-2-oxoethyl)-5-((4-oxo-4H-chromen-3-yl)methylene)thiazolidine-2,4-dione (7)

Yield 99 %. White powder, mp: 254 °C. ^1H NMR (DMSO- d_6 , 500 MHz, ppm): δ 2.46 (s, 3H, -CH₃); 5.20 (s, 2H, -CH₂-); 7.14 (d, 2H, phenyl); 7.56 (d, 1H, C₆-chromone-H); 7.62 (d, 1H, C₈-chromone-H); 7.70 (dd, 1H, C₇-chromone-H); 7.74 (s, 1H, C=CH); 7.98 (s, 1H, C₅-Chromone-H); 8.04 (d, 2H, phenyl); 8.98 (s, 1H, C₂-chromone-H). Anal. Calcd. (%) for C₂₂H₁₅NO₆S (421.42): C, 62.70; H, 3.59; N, 3.32; S, 7.61. Found: C, 62.71; H, 3.59; N, 3.32; S, 7.62. MS (EI, 70 eV): *m/z* 422.5 [M+1].

5-((6-methyl-4-oxo-4H-chromen-3-yl)methylene)-3-(2-oxo-2-phenylethyl)thiazolidine-2,4-dione (8)

Yield 78%. Light brown powder, mp: 228 °C. ^1H NMR (DMSO- d_6 , 500 MHz, ppm): δ 2.45 (s, 3H, -CH₃); 5.30 (s, 2H, -CH₂-); 7.61 (t, 2H, phenyl); 7.65 (d, 1H, C₈-chromone-H); 7.70 (dd, 1H, C₇-chromone-H); 7.75 (t, 1H, phenyl); 7.76 (s, 1H, C=CH); 7.94 (s, 1H, C₅-Chromone-H); 8.09 (d, 2H, phenyl); 8.95 (s, 1H, C₂-chromone-H). Anal. Calcd. (%) for C₂₂H₁₅NO₅S (405.42): C, 65.18; H, 3.73; N, 3.45; S, 7.91. Found: C, 65.19; H, 3.72; N, 3.45; S, 7.92. MS (EI, 70 eV): *m/z* 406.5 [M+1].

3-(2-oxo-2-phenylethyl)-5-((4-oxo-4H-chromen-3-yl)methylene)thiazolidine-2,4-dione (9)

Yield 93 %. Light yellow powder, mp: 252 °C. ^1H NMR (DMSO- d_6 , 500 MHz, ppm): δ 5.32 (s, 2H, -CH₂-); 7.58 (d, 1H, C₆-chromone-H); 7.63 (t, 2H, phenyl); 7.67 (d, 1H, C₈-chromone-H); 7.70 (dd, 1H, C₇-chromone-H); 7.72 (t, 1H, phenyl); 7.76 (s, 1H, C=CH); 7.91 (s, 1H, C₅-Chromone-H); 8.08 (d, 2H, phenyl); 8.90 (s, 1H, C₂-chromone-H). Anal. Calcd. (%) for C₂₁H₁₃NO₅S (391.40): C, 64.44; H, 3.35; N, 3.58; S, 8.19. Found: C, 64.45; H, 3.35; N, 3.58; S, 8.20. MS (EI, 70 eV): *m/z* 392.5 [M+1].

5-((6-chloro-4-oxo-4H-chromen-3-yl)methylene)-3-(2-oxo-2-phenylethyl)thiazolidine-2,4-dione (10)

Yield 84 %. Yellow powder, mp: 243 °C. ^1H NMR (DMSO- d_6 , 500 MHz, ppm): δ 5.28 (s, 2H, -CH₂-); 7.64 (t, 2H, phenyl); 7.66 (d, 1H, C₈-chromone-H); 7.72 (dd, 1H, C₇-chromone-H); 7.75 (t, 1H, phenyl); 7.77 (s, 1H, C=CH); 7.92 (s, 1H, C₅-Chromone-H); 8.10 (d, 2H, phenyl); 8.90 (s, 1H, C₂-chromone-H). Anal. Calcd. (%) for C₂₁H₁₂ClNO₅S (425.84): C, 59.23; H, 2.84; N, 3.29; S, 7.53. Found: C, 59.22; H, 2.83; N, 3.28; S, 7.54. MS (EI, 70 eV): *m/z* 427 [M+1].

SYNTHESIS OF NEW 5-(CHROMENE-3-YL)METHYLENE-2,4-THIAZOLIDINEDIONES

2-hydroxy-5-(2-(5-((6-methyl-4-oxo-4H-chromen-3-yl)methylene)-2,4-dioxothiazolidin-3-yl)acetyl)benzamide (11)

Yield 30 %. Light brown powder, mp: 303 °C. ^1H NMR (DMSO- d_6 , 500 MHz, ppm): δ 2.51 (s, 3H, -CH₃); 5.29 (s, 2H, -CH₂-); 7.08 (d, 1H, phenyl); 7.42 (d, 1H, phenyl); 7.66 (d, 1H, C₈-chromone-H); 7.72 (dd, 1H, C₇-chromone-H); 7.77 (s, 1H, C=CH); 7.95 (s, 1H, C₅-Chromone-H); 7.98 (br, 1H, -CO-NH₂); 8.12 (dd, 1H, phenyl); 8.43 (br, 1H, -CO-NH₂); 8.96 (s, 1H, C₂-chromone-H); 13.97 (s, 1H, Ar-OH). Anal. Calcd. (%) for C₂₃H₁₆N₂O₇S (464.45): C, 59.48; H, 3.47; N, 6.03; S, 6.90. Found: C, 59.49; H, 3.47; N, 6.01; S, 6.90. MS (EI, 70 eV): m/z 465.5 [M+1].

5-(2-(5-((6-chloro-4-oxo-4H-chromen-3-yl)methylene)-2,4-dioxothiazolidin-3-yl) acetyl)-2-hydroxybenzamide (12)

Yield 30 %. Light yellow powder, mp: 303 °C. ^1H NMR (DMSO- d_6 , 500 MHz, ppm): δ 5.28 (s, 2H, -CH₂-); 7.09 (d, 1H, phenyl); 7.44 (d, 1H, phenyl); 7.66 (d, 1H, C₈-chromone-H); 7.71 (dd, 1H, C₇-chromone-H); 7.78 (s, 1H, C=CH); 7.97 (s, 1H, C₅-Chromone-H); 7.98 (br, 1H, -CO-NH₂); 8.10 (dd, 1H, phenyl); 8.42 (br, 1H, -CO-NH₂); 8.94 (s, 1H, C₂-chromone-H); 13.92 (s, 1H, Ar-OH). Anal. Calcd. (%) for C₂₂H₁₃ClN₂O₇S (484.87): C, 54.50; H, 2.70; N, 5.78; S, 6.61. Found: C, 54.49; H, 2.70; N, 5.79; S, 6.60. MS (EI, 70 eV): m/z 486 [M+1].

ACKNOWLEDGMENTS

The research was (partially) funded by POSDRU grant no. 159/1.5/S/136893 grant with title: "Parteneriat strategic pentru creșterea calității cercetării științifice din universitățile medicale prin acordarea de burse doctorale și postdoctorale – DocMed.Net_2.0" and within the research contract no. 1494/5/28.01.2014 financed by "Iuliu Hațieganu" University of Medicine and Pharmacy Cluj-Napoca, Romania.

REFERENCES

- [1]. S.S. Tang, A. Apisarnthanarak, L. Yang Hsu, *Adv Drug Deliver Rev*, **2014**, 78, 3.
- [2]. G. Na, W. Zhang, S. Zhou, H. Gao, Z. Lu, X. Wu, R. Li, L. Qiu, Y. Cai, Z. Yao, *Mar Pollut Bull*, **2014**, 84, 70.
- [3]. D.O. Ogbolu, M. A. Webber, *Int J Antimicrob Ag*, **2014**, 43, 412.
- [4]. L.Y. Hsu, T.Y. Tan, V.H. Tam, A. Kwa, D.A. Fisher, T.H. Koh, *Antimicrob Agents Chemother*, **2010**, 54(3), 1173.

- [5]. WHO Library Cataloguing-in-Publication Data. Antimicrobial resistance: global report on surveillance. WHO Press, World Health Organization, 20 Avenue Appia, 1211 Geneva 27, Switzerland.
- [6]. F.L. Gouveia, R.M.B. de Oliveira, T.B. de Oliveira, I.M. da Silva, S.C. do Nascimento, K.X.F.R. de Sena, J.F.C. de Albuquerque, *Eur J Med Chem*, **2009**, 44(5), 2038.
- [7]. D.A. Heerdind, L.T. Christmann, T.J. Clark, D.J. Holmes, S. F. Rittenhouse, D.T. Takata, J.W. Venslavsky, *Bioorg Med Chem Lett*, **2003**, 13, 3771.
- [8]. V.V. Mulwad, A.A. Mir, H.T. Parmar, *Ind J Chem*, **2009**, 48B, 137.
- [9]. K.R. Alagawadi, S.G. Alegaon, *Arab J Chem*, **2011**, 4(4), 465.
- [10]. X.F. Liu, C.J. Zheng, L.P. Sun, X.K. Liu, H.R. Piao. *Eur J Med Chem*, **2011**, 46(8), 3469.
- [11]. K. Hatzade, V. Taile, P. Gaidhane, V. Ingle *Turk J Chem*, **2010**, 34, 241.
- [12]. T.E. Ali, M.A. Ibrahim, *J Brazil Chem Soc*, **2010**, 21, 1007.
- [13]. C.N. Khobragade, R. Bodade, M.S. Shinde, D. Jaju, R.B. Bhosle, B.S. Dawane, *J Enzym Inhib Med Ch*, **2008**, 23, 341.
- [14]. S.B. Kale, B.K. Karale, *J Het Chem*, **2007**, 44, 289.
- [15]. C. Nastasă, M. Duma, C. Marie, D. Scherman, B. Tiperciuc, O. Oniga, *Dig J Nanomater Bios*, **2013**, 8(3), 1079.
- [16]. O. Bozdağ-Dündar, B. Evranos, N. Daş-Evcimen, M. Sarıkaya, R. Ertan, *Eur J Med Chem*, **2008**, 43(11), 2412.

DEVELOPMENT OF AN UPLC METHOD FOR SIMULTANEOUS DETERMINATION OF TARTRAZINE, CONGO RED AND METHYL ORANGE

ANAMARIA NEGRULESCU^{a,b}, VIORICA PATRULEA^{a,b},
MANUELA MINCEA^b, CRISTINA MORARU^{a,b}, VASILE OSTAFE^{a,b*}

ABSTRACT. An UPLC method was developed to determine the concentrations of tartrazine (TAR), Congo red (CR), and methyl orange (MO) in aqueous mixtures. The chromatographic method was optimized considering the temperature of the column, the composition of mobile phases and the gradient program. The chosen method has allowed the separation and identification of TAR, CR, and MO from aqueous samples in 2 min. The calibration plots ($R^2 > 0.991$) were linear over the ranges 0.5 – 50 µg/mL. Accuracy of the method was investigated, by applying recovery tests, with average recovery higher than 99%. The precision analysis included an intra-day variation, for which RSD (%) had values lower than 0.94, and an inter-day variation with RSD (%) values lower than 1.07. The developed method was successfully tested on water samples collected from a river nearby a textile industry plant.

Keywords: azo dyes; Congo red; methyl orange; tartrazine; UPLC.

INTRODUCTION

Industries such as textiles, paper, leather, rubber, cosmetics, plastics, automotive and other consumer goods discharge large amounts of colored wastewater containing various dyes [1], some of which influence food chains, aquatic ecosystems and are even mutagenic and carcinogenic to humans [2, 3]. Contamination of water with dyes is especially objectionable because of their acute toxicity. However, color in aqueous environments is also unacceptable due to the limitation of the reoxygenation capacity of the affected water [4, 5],

^a Department of Biology – Chemistry, Faculty of Chemistry, Biology, Geography, West University of Timisoara, 16 Street Pestalozzi, Timisoara 300115, Romania.

^b Advanced Research Environmental Laboratories, Multidisciplinary Research Platform “Nicholas Georgescu - Roegen”, 4 Street Oituz, Timisoara 300086, Romania.

* Corresponding author: vasile.ostafe@e-uvt.ro

reduction of sunlight penetration and not in the least because of natural aesthetic reasons. Therefore, the removal of color from process or waste effluents becomes environmentally important.

Tartrazine, Congo red, and methyl orange (Figure 1) are azo dyes used commercially in foods, textiles, paper and drugs in order to make them more attractive for consumers. Congo red, 3,3'-(1,1'-diphenyl)-4,4'-diylbis(azo)] bis-(4-amino-1-naphthalene acid) disodium salt, is a potentially toxic dye, if orally ingested due to the fact that it can be metabolized to benzidine, a highly carcinogenic compound. Additionally, it can decrease the concentration of proteins in serum and cause thrombocytopenia, platelet aggregation, and disseminated microembolism [6, 7]. CR mainly occurs in the effluents discharged from textile, paper, printing, leather industries etc. During dyeing operations, up to 15% of CR can end up in wastewaters [8].

Tartrazine, trisodium 5-hydroxy-1-(4-sulfonatophenyl)-4-(4-sulfonato-phenylazo)-H-pyrazol-3-carboxylate, is one of the most frequently used food additives. It is being used abundantly in cosmetics, foodstuffs, medicines and textile materials [9]. Out of all the azo dyes, tartrazine appears to cause the most allergic and/or intolerance reactions, asthmatics and aspirin intolerant persons being particularly affected by tartrazine. Tartrazine sensitivity is mainly manifested by urticaria, but common symptoms can also include migraines, itching and blurred vision [10, 11].

Methyl orange, sodium $[(p\text{-dimethylamino})\text{phenyl}]\text{-azo}$ benzene sulphonate, is a water-soluble azo dye, which is widely used in textile, printing, paper manufacturing, pharmaceutical, food industries and in research laboratories as an acid base indicator. MO can inadvertently enter the body through oral ingestion and metabolize into aromatic amines, which can ultimately lead to intestinal cancer [12]. The toxic nature of the dye has not been yet properly quantified, but its presence in living organisms can prove to be harmful [13].

Ultra performance liquid chromatography (UPLC) is a chromatographic separation technique in which the use of high operating pressures (up to 1000 bar as opposed to the 400 bar maximum of HPLC) enables columns packed with particles having a diameter under 2 μm to be operated at high linear velocities. UPLC means that high peak capacities and high resolving powers can be generated along with short separation times [14]. The UPLC method is an accurate and rapid method used increasingly frequently [15, 16, 17] for the quantification of the amount of many compounds, including azo dyes [18, 19].

The objective of this work was to develop a simple, accurate, sensitive, economical, reproducible, and rapid UPLC method for the analysis of ternary mixtures of azo-dyes. The desired method should be suitable for routine quality control of wastewaters from the textile industry, and therefore it would be used successfully on river samples acquired from nearby a textile producing plant.

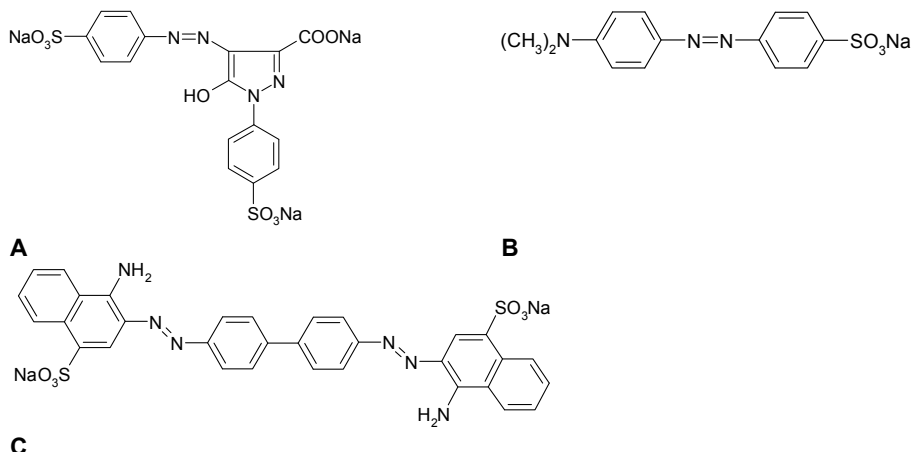


Figure 1. The chemical structures of industrial dyes:
(a) tartrazine; (b) methyl orange; (c) Congo red.

RESULTS AND DISCUSSION

Chromatographic Method Development

Different mobile phases containing various proportions of methanol and formic acid, as well as a few different buffer solutions (pH between 5 and 7) introduced in mobile phase B, were examined (data not shown). Finally, 10 % methanol in acetate buffer, $\text{pH} = 5.6$ was selected, as appropriate resolution was achieved. The optimum run time was 2 min. The MaxPlot chromatogram obtained from a mixed standard solution of TAR, CR, and MO is shown in Figure 2. At a flow rate of 0.3 mL/min, the retention time was 0.417 min for TAR, 0.903 min for CR, and 1.11 min for MO.

The left part of Figure 3 presents the spectra of the dyes recorded in the range 210 – 500 nm. In the right part, the extracted chromatograms at the wavelength, where the maximum absorption occurs, are presented for each dye. These chromatograms were used, in comparison with MaxPlot chromatograms for quantification of the analytes. As there were no significant differences between the two sets of results, quantification based on MaxPlots was used further. As each dye has two maximum absorptions in the recorded spectra range, the extracted chromatograms at these maximum absorption wavelengths were also used for confirmation that a peak belonged to a certain dye. The specificity of the method was tested for solutions containing only one dye at a time and the mixture of all three dyes, and no interferences were noticed when the detection was checked at two maximum absorption wavelengths. These results were also corroborated with the results obtained by *Peak Purity Check* and *Library Match* subroutines.

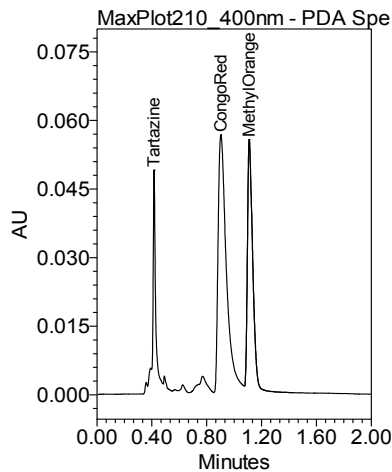


Figure 2. UPLC chromatogram of the separation of TAR, CR and MO using gradient elution program.

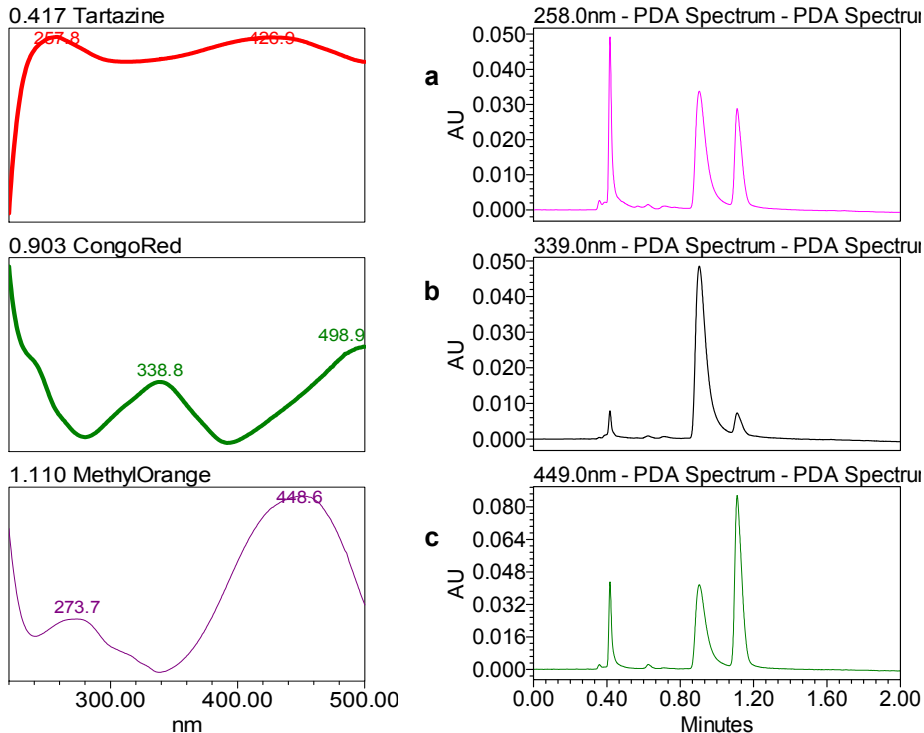


Figure 3. DAD-UV-Vis spectra and chromatograms corresponding to mixtures of the three dyes at different wavelengths (a) 258 nm, (b) 339 nm and (c) 449 nm.

The calculated parameters corresponding to the standard curves, as well as a few statistical parameters are shown in Table 1. The regression equation coefficients were higher than 0.991. At the MaxPlot, the calibration equations gave good linearity and successful results for TAR, CR, and MO.

Method Validation

Standard calibration plots were linear over the range 0.5 – 50 µg/mL, with regression coefficients higher than 0.991, obtained for all three dyes. The LOD and LOQ were 0.06 and 0.3 µg/mL for TAR, 0.12 and 0.9 µg/mL for CR, and 0.05 and 0.3 µg/mL for MO, respectively. The validation data are summarized in Table 1.

Table 1. Calculated standard curve parameters, LOD, and LOQ values

Compound	Standard curve equation	R ²	LOD (µg/mL)	LOQ (µg/mL)
Tartrazine	$2.49 \times 10^4x + 3.40 \times 10^4$	0.993	0.06	0.3
Congo red	$4.16 \times 10^4x + 9.96 \times 10^4$	0.991	0.12	0.9
Methyl orange	$1.10 \times 10^4x + 1.18 \times 10^4$	0.994	0.05	0.3

Note: R²: regression coefficient; LOD: limit of detection; LOQ: limit of quantification

To study the accuracy and precision of the method, recovery was determined for three different mixtures containing known concentrations of dyes. Results from recovery studies, as well as linear regression analysis and other statistical results based on the relationship between added and measured concentrations are reported in Table 2.

Table 2. Recovery results obtained by applying the proposed method to the synthetic mixtures of dyes

TAR	Added (µg/mL)		Recovery (%)		
	CR	MO	TAR	CR	MO
15	45	15	97.3	98.8	101.6
9	27	9	101.2	99.4	101.3
3	9	3	98.4	98.7	100.1
Average			99.0	99.0	101.0
RSD			2.03	0.38	0.79

Note: RSD: Relative standard deviation between the recovery percentages obtained for each dye

The precision of the method was also evaluated by assay of dye mixture samples containing TAR, CR, and MO. Six replicate analyses were performed on the same day on accurately weighed amounts of the dyes and the experiments were repeated on three different days. Intra-day precision RSD

($n = 6$) was 0.94% for TAR, 0.48% for CR, and 0.63% for MO, respectively. For inter-day precision experiments, the calculated RSD ($n = 3$) was 1.07% for TAR, 0.55% for CR, and 0.81% for MO, respectively.

Chromatographic method application

The previously developed method was applied to river samples, acquired from downstream a textile producing plant. In order to assure the applicability of the developed method, river samples were spiked with reference standard solutions of TAR (3 $\mu\text{g/mL}$), CR (9 $\mu\text{g/mL}$) and MO (3 $\mu\text{g/mL}$), proving that the method is suitable for real wastewater samples. Based on the two chromatograms presented in Figure 4 the following concentrations were quantified in the river sample: 6.08 $\mu\text{g/mL}$ TAR, 15.05 $\mu\text{g/mL}$ CR, and 4.17 $\mu\text{g/mL}$ MO.

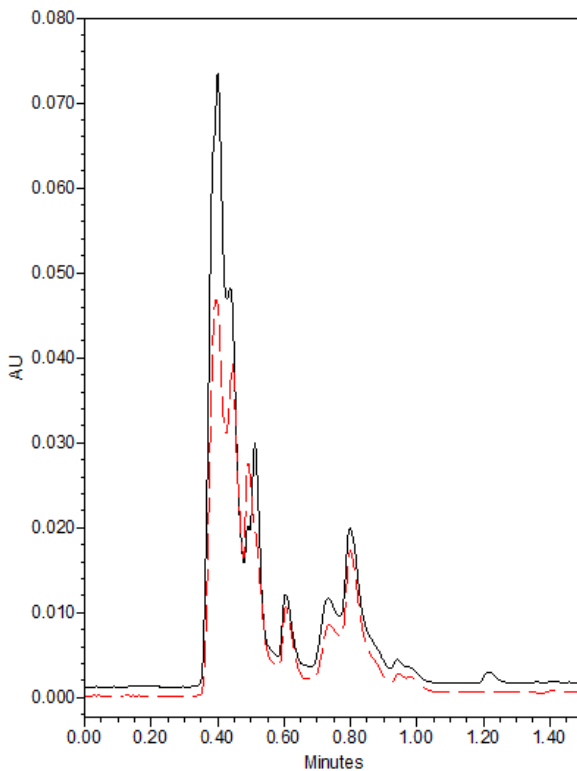


Figure 4. Comparative chromatograms of an aqueous mixture of standard solutions (dashed red line) and a downstream river sample spiked with reference standard solutions (solid black line).

CONCLUSIONS

The validated UPLC method proved to be simple, fast, accurate, precise, and robust and could, thus, be used for routine analysis of TAR, CR, and MO in combined dye samples. The UPLC method developed proved to be efficient in the separation of the three dyes in less than 2 min.

The method was validated, by studying its accuracy and specificity. Accuracy was investigated, using recovery and precision tests. The average recovery value was higher than 99%. The intra-day and inter-day precision assessments had values of RSD (%) lower than 0.94 and 1.07, respectively. Good correlation ($R^2 > 0.991$) of individual plots of all three dyes, using data obtained by applying the UPLC method, demonstrated that the developed method was efficient for the separation of TAR, CR, and MO.

EXPERIMENTAL SECTION

Materials and methods

TAR, CR, MO, sodium chloride, acetic acid and sodium hydroxide were purchased from Sigma Aldrich Chemie GmbH (Germany). Standards were analytical-reagent grade. Methanol was bought from Carl Roth (Switzerland) HPLC grade. All other chemicals were of analytical grade. Mobile phases and all injected samples were filtered on 0.2 μm filter before use.

Stock standard solutions of TAR (1004.8 $\mu\text{g}/\text{mL}$), CR (1008 $\mu\text{g}/\text{mL}$), and MO (1001 $\mu\text{g}/\text{mL}$) were made in 0.1 M NaCl solution. Diluted standard solutions were prepared from stock solutions with ultrapure water by serial dilutions.

Chromatographic Conditions

The UPLC system (Milford, USA) consisted of Acquity Binary Solvent Manager, Acquity Sample Manager and Acquity PDA Detector. The detector was set to collect data between 210 and 500 nm. The UPLC column was Acquity UPLC BEH C18 2.1 mm x 50 mm (1.7 μm particle diameter). Column temperature was kept at 30 °C. The autosampler temperature was set at 4 °C. The injection volume was varied between 2 and 10 μL (partial loop method) depending on standard or sample concentration. UV signal was detected as spectra in the range 210 – 500 nm (sampling rate: 20 pts/s).

The gradient elution (0.3 mL/min) program was prepared with 100% MeOH as mobile phase A and 0.1 M acetate buffer in 10% MeOH as mobile phase B. The integration was performed with Empower software, using the

MaxPlot extracted chromatogram (a special chromatogram that plots the maximum spectral absorbance measured at each time point in the data file). The subroutine Peak Purity Check was used for the evaluation of the purity of the eluted peaks and the subroutine Library Match for the identification of the eluted peaks based on comparison of their spectra with the spectra of standards stored in the spectra library [20].

Procedure for Analysis of Dye Mixtures

Different volumes of TAR, CR, and MO stock solutions were mixed in vials and afterwards diluted with ultrapure water. Previous to the injection, the solutions were filtered on 0.2 µm cellulose Millipore syringe filters and 10 µL of the filtrate was injected in the UPLC system. After the chromatographic run, quantification was performed either using MaxPlot subroutine or at channels extracted at the wavelength where each dye had its maximum absorption in the range of the recorded spectra, e.g. 258, 339 and 449 nm, for TAR, CR, and MO, respectively. The amount of each dye in every mixture was determined based on the respective calibration plot.

Preparation of Calibration Plots

Six diluted standard solutions of all three dyes in the concentration range 0.5 – 50 µg/mL were injected in the UPLC system, under the conditions described above. Each amount was analyzed five times and peak areas were recorded.

Method Validation

From the calibration plot of each dye, the Limits of Detection (LOD) and Quantification (LOQ) parameters were calculated from the regression equation of TAR, CR, and MO, using Equation (1) and Equation (2), respectively:

$$LOD = 3.3 \frac{\sigma}{S} \quad (1)$$

$$LOQ = 10 \frac{\sigma}{S} \quad (2)$$

where σ is the standard deviation of the response and S is the slope of the calibration plot.

Accuracy of the assay was determined in relation to repeatability (intra-day) and intermediate precision (inter-day). In order to estimate the repeatability of the experiments, for the same concentration of each dye six

samples were analyzed during the same day. To study inter-day variation, an analysis of three mixed standard solutions of the same concentration was performed on three different days [21]. To confirm the specificity of the method, solutions of each single dye and a mixture of all three dyes, having the same concentrations, were injected into the UPLC system and the concentrations of individual dye and of the mixture were compared.

Recovery Studies

To check the accuracy of the method, recovery studies were conducted after addition of standard dye solution for three different mixtures containing known concentrations of dyes, at three different levels on the linear part of the standard curves. Three samples were prepared for each recovery level. The solutions were analyzed and the percentage of recoveries was calculated from the calibration curves.

Method application

In order to prove that the developed method is relevant for real samples, river water samples (the spiking experiment was done in triplicate) were obtained from downstream a textile plant in Hunedoara county (Romania). Prior to the analysis, the river water samples were filtered on 0.2 µm filter and kept well sealed, at 4 °C. For the spiked samples, standard dyes solutions mixture was added to downstream river samples (3 µg/mL TAR, 9 µg/mL CR, and 3 µg/mL MO).

ACKNOWLEDGMENTS

This work was supported by the project 464 RoS-NET financed by the EU Instrument for Pre-Accession (IPA) funds, under the framework of the Romania – Republic of Serbia IPA Cross-border Cooperation Programme.

REFERENCES

1. D. Căilean, G. Barjoveanu, C.P. Musteret, N. Sulitanu, L.R. Manea, C. Teodosiu, *Environmental Engineering and Management Journal*, **2009**, 8(3), 503.
2. M. Ali, T.R. Sreekrishnan, *Advances in Environmental Research*, **2001**, 5, 175.
3. G. Crini, *Progress in Polymer Science*, **2005**, 30, 38.
4. A. Mittal, L. Kurup, J. Mittal, *Journal of Hazardous Materials*, **2007**, 146, 243.
5. G. Crini, P.M. Badot, *Progress in Polymer Science*, **2008**, 33, 399.
6. T.B. Tschopp, H.R. Baumgartner, A. Studer, *Thrombosis et Diathesis Haemorrhagica*, **1971**, 26(3), 488.

7. M. Giger, H.R. Baumgartner, G. Zbinden, *Agents and Actions*, **1974**, 4(3), 173.
8. S. Chatterjee, M.W. Lee, S.H. Woo, *Bioresource Technology*, **2010**, 101(6), 1800.
9. E. Dinc, A. Hakan Akyas, D. Baleanu, O. Ustundag, *Journal of Food and Drug Analysis*, **2006**, 14(3), 284.
10. C. Collins-Williams, *Journal of Asthma*, **1985**, 22, 139.
11. D.J. Baumgardner, *Postgraduate Medicine*, **1989**, 85, 265.
12. K.T. Chung, J.S.E. Stevens, C.E. Cerniglia, *Critical Reviews in Microbiology*, **1992**, 18(3), 175.
13. A. Mittal, A. Malviya, D. Kaur, J. Mittal, L. Kurup, *Journal of Hazardous Materials*, **2007**, 148(1-2), 229.
14. S.A.C. Wren, P. Tchelitcheff, *Journal of Pharmaceutical and Biomedical Analysis*, **2006**, 40(3), 571.
15. A. Bratan, M. Mincea, I. R. Lupsa, M.G. Pirtea, V. Ostafe, *Studia UBB Chemia*, **2014**, LIX(1), 47.
16. E. Preda, M.M. Mincea, C. Ionascu, A.V. Botez, V. Ostafe, *Studia UBB Chemia*, **2013**, LVIII, 167.
17. C. Ionascu, V. Ostafe, *Studia UBB Chemia*, LIX, **2014**, 4, 17
18. C. Li, T. Yang, Y. Zhang, Y. L. Wu, *Chromatographia*, **2009**, 70, 319.
19. A. Negrulescu, V. Patrulea, M. Mincea, C. Moraru, V. Ostafe, *Digest Journal of Nanomaterials and Biostructures*, **2014**, 9(1), 45
20. M. Mincea, I. Lupsa, I. Talpoş, V. Ostafe, *Acta Chromatographica*, **2009**, 21(4), 591.
21. ICH Harmonised Tripartite Guideline, “Validation of Analytical Procedures: Text and Methodology Q2(R1)”, International Conference on Harmonization, Chicago, **2005**, online at:
http://www.ich.org/fileadmin/Public_Web_Site/ICH_Products/Guidelines/Quality/Q2_R1/Step4/Q2_R1__Guideline.pdf

COMPARATIVE HPLC-MS ANALYSIS OF PHENOLICS FROM ACHILLEA DISTANS AND ACHILLEA MILLEFOLIUM AND THEIR BIOACTIVITY

DANIELA BENEDEC^a, IULIA-ELENA POPICA^a,
ILIOARA ONIGA^a, DANIELA HANGANU^a, MIHAELA DUMA^b,
RADU SILAGHI-DUMITRESCU^c, CRISTINA BISCHIN^{c,*},
LAURIAN VLASE^a

ABSTRACT. The purpose of this study was to characterize the polyphenolic composition of *Achillea distans* and *Achillea millefolium* and to evaluate their antioxidant and antimicrobial activities. The total polyphenolic content was determined spectrophotometrically. The phenolic compounds were identified and quantified by HPLC-MS. The extracts were screened for antioxidant activities using two *in vitro* assay models: DPPH radical scavenging assay and hemoglobin ascorbate peroxidase activity inhibition (HAPX) assay. A method based on electron paramagnetic resonance (EPR) polyphenolic radicals' detection was also described. The antimicrobial activity was determined using the disc diffusion method. For the species of *Achillea*, the phenolic profile showed the presence of two phenolic acid derivatives (chlorogenic and *p*-coumaric acids), four flavonoid glycosides (hyperoside, isoquercitrin, rutin and quercitrin) and four free flavonoids (quercetin, patuletin, luteolin and apigenin), in different concentrations. The evaluation of antioxidant activity indicated that *A. millefolium* extract has more antioxidant than *A. distans*, related with the polyphenolic total content. Both extracts showed activity against all tested bacterial species. These results suggest that the two native species of *Achillea* can be used as a potential source of polyphenolic compounds with bioactive properties for cosmetic and medicinal applications.

Keywords: *Achillea*, phenolics, HPLC-MS, antioxidant and antimicrobial activities.

^a Iuliu Hatieganu University of Medicine and Pharmacy, Faculty of Pharmacy, 8, Victor Babes Street, Cluj-Napoca, Romania.

^b State Veterinary Laboratory for Animal Health and Safety, 1 Piata Marasti Street, Cluj-Napoca, Romania.

^c Babes-Bolyai University, 11 A. Janos Street, Cluj-Napoca, Romania.

* Corresponding author: cbischin@chem.ubbcluj.ro

INTRODUCTION

The *Achillea* genus (within the Asteraceae family), commonly referred to as yarrow, contains ~ 130 flowering plants throughout the world [1-3] - most commonly in arid and semi-arid subtropical and lower-temperate regions. *Achillea* flowers contain sesquiterpene lactones, essential oil (azulene), flavonoids, phenolic acids determined by different chromatographic and spectroscopic methods: GC-MS, GCQ, HPTLC, RP-HPLC, HPLC-MS, NMR[4-13]. Several species of this genus have for a long time been used to treat wounds, bleedings, inflammation, respiratory infections, skin conditions, spasmody diseases and dyspepsia, and are at present times employed in the medicinal and cosmetic industry, especially as they are also useful sources of metabolites, which known to display tonic, anti-inflammatory, anti-spasmodic, cytotoxic, diuretic or antimicrobial effects [1,3,10,12,14-16]. Phenolic acids such as present in these species are known for their potential protective role against oxidative damage diseases (coronary heart disease, stroke, and cancers) [17]. In Romania, there are 23 *Achillea* species and 10 varieties or subspecies [2]. *Achillea distans* Waldst. & Kit. ex Willd. (Alps yarrow) an alpino-carpatho-balkan type is often found alongside with the medicinal and officinal species *Achillea millefolium* (yarrow) with natural pink flowers. It causes the hybridization phenomenon's of the officinal species or the adulteration of the vegetal product (*Millefoliflos*). Thus, a broader knowledge of the chemical composition of the species becomes an important aim. So far, studies have shown that the essential oil of *A. distans* has a poor quality. This is why the evaluation of the polyphenolic profile that may become a favorable argument for the medicinal use of *A. distans*.

The aim of this work was to analyze the phenolic compounds from two Romanian *Achillea* species and to investigate their antioxidant and antimicrobial properties, for a better chemical characterization and exploitation of these medicinal plants.

RESULTS AND DISCUSSION

HPLC Analysis of Polyphenolics

HPLC coupled with MS allows a simultaneous analysis of different classes of polyphenolics by a single pass column (the separation of all examined compounds was carried out in 35 min). The concentrations of identified polyphenolic compounds in the analyzed samples are presented in Table 1. The HPLC chromatograms of the *A. distans* and *A. millefolium* samples are presented in Figures 1 and 2, respectively.

Chlorogenic acid was found in *Achillea distans* and *Achillea millefolium* extracts in similar amounts (cca. 230 mg/100 g). Four flavonoid glycosides, hyperoside, isoquercitrin, rutin and quercitrin were identified and quantified (Table 1). Hyperoside and isoquercitrin were identified in both extracts, but they were in too low concentration to be quantified (< 0.02). *A. distans* was distinctly the richer species in rutin and quercitrin (with 31.43 mg/100 g and 18.313 mg/100 g, respectively). Four flavonoid aglycones (quercetin, patuletin, luteolin and apigenin) were found in these two extracts, but in varying amounts. Thus, *A. millefolium* contained larger quantities of quercetin, luteolin and apigenin than *A. distans*, while patuletin was quantified only in *A. distans* (0.21 mg/100 g). Concerning the phenolic compounds identification, the results obtained in the present study are in agreement with previously published data on the two species from other areas [7-811-12].

Considering the 19 standard compounds used in this study, some other peaks were not identified.

Therefore can be concluded that these two *Achillea* species can be considered important sources of chlorogenicacid.

Table 1. Phenolic compounds in *Achillea* species
(mg/100 g plant material)

Polyphenolic compounds	m/z value	tR ± SD (min)	<i>A. distans</i>	<i>A. millefolium</i>
Chlorogenic acid	353	6.43 ± 0.05	233.75 ± 6.24	231.71 ± 8.28
p-Coumaric acid	163	9.48 ± 0.08	<0.02	0.50± 0.09
Hyperoside	463	19.32 ± 0.12	<0.02	<0.02
Isoquercitrin	463	20.29 ± 0.10	<0.02	<0.02
Rutin	609	20.76 ± 0.15	31.43 ± 3.53	3.52 ± 0.67
Quercitrin	447	23.64 ± 0.13	18.31 ± 0.68	8.21± 1.78
Quercetin	301	27.55 ± 0.15	1.38 ± 0.61	1.60 ± 0.19
Patuletin	331	29.41 ± 0.12	0.21 ± 0.08	<0.02
Luteolin	285	29.64 ± 0.19	50.24 ± 4.75	54.67 ± 3.32
Apigenin	279	39.45 ± 0.15	13.22 ± 1.75	25.96 ± 1.03

Note: NF - not found, below limit of detection. Values are the mean ± SD (n = 3).

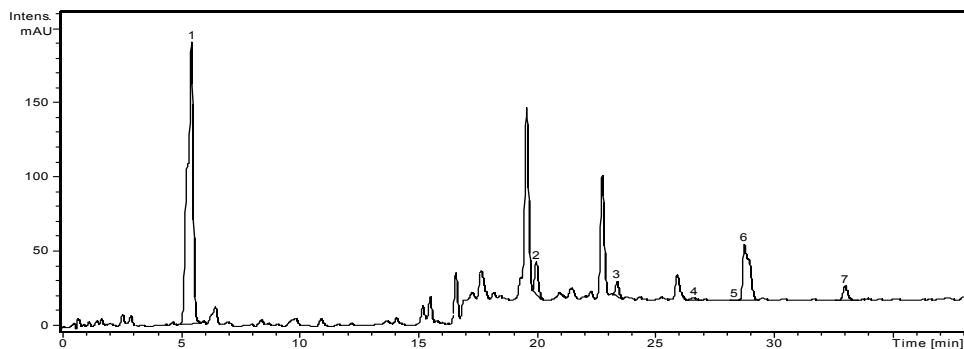


Figure 1. HPLC chromatogram of *A. distans*

Notes: The identified compounds: 1, chlorogenic acid; 2, rutin; 3, quercitrin; 4, quercetin; 5, patuletin; 6, luteolin; 7, apigenin.

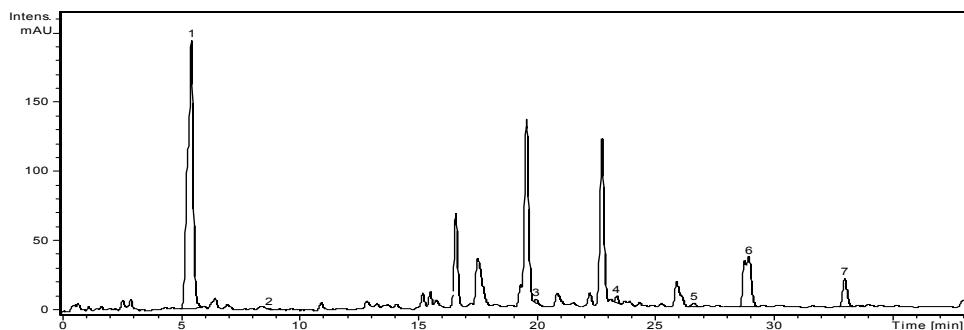


Figure 2. HPLC chromatogram of *A. millefolium*

Notes: The identified compounds: 1, chlorogenic acid; 2, *p*-coumaric acid; 3, rutin; 4, quercitrin; 5, quercetin; 6, luteolin; 7, apigenin.

Polyphenolic content and the antioxidant activity

The *A. millefolium* ethanolic extract contained a higher amount of polyphenols and flavonoids (38.12 and 22.21 mg/g, respectively) than the *A. distans* counterpart (32.56 and 19.47 mg/g, respectively), as illustrated in Table 2. Comparing the phenolic content, these species was poorer than the Italian same species [7].

The ethanolic extracts were also screened for their antioxidant activities using two *in vitro* assay models: DPPH bleaching method and hemoglobin ascorbate peroxidase activity inhibition (HAPX).

Table 2. The content of polyphenols (TPC, flavonoid) and the results of antioxidant activity for *Achillea* extracts

Samples	TPC (mg GAE/g)	Flavonoids (mg RE/g)	DPPH IC ₅₀ (µg/mL)	HAPX (mg RE/g)
<i>A. distans</i>	32.56 ± 1.42	19.47 ± 1.53	150.30 ± 7.69	0
<i>A. millefolium</i>	38.12 ± 2.00	22.21 ± 1.96	102.84 ± 1.15	724 ± 143
Quercetin	-	-	5.47 ± 0.16	-

Each value is the mean ± SD of three independent measurements. GAE: Gallic acid equivalents; RE: rutin equivalents.

Judging on the lower the IC₅₀ value (i.e., more powerful antioxidant capacity [18]). *A. millefolium* (IC₅₀ = 102.84 µg/mL), showed a slightly higher radical scavenging activity than *A. distans* (IC₅₀ = 150.30 µg/mL). The results are in line with the phenolic contents listed in Table 2. Compared to the methanolic extract of *A. millefolium* from Turkey, the ethanol extracts of Romanian *A. millefolium* showed lower antioxidant capacity [4].

The HAPX assay monitors the ability of the antioxidants present in the extracts to inhibit the oxidation of hemoglobin by hydrogen peroxide. This reaction occurs normally in the body and can be accelerated under certain stress conditions generating a high valent iron species – ferryl. The method was proposed to be more physiologically relevant for the evaluation of antioxidant capacity, compared to chemical-based methods (ABTS, DPPH, TBARS, etc) [19]. The *A. millefolium* extract exhibits an important capacity to quench the free radical generated in hemoglobin after exposure to hydrogen peroxide, while *A. distans* does not have any effect. This is despite the relatively similar TPC, ABTS and DPPH values, and suggests that certain *A. distans* components may act as prooxidants when confronted with a real-world protein reaction, offsetting the inherent antioxidant effects of the already demonstrated polyphenols and flavonoids.

Direct detection of free radical

Treatment of natural polyphenolic-rich extracts with alkali in presence of molecular oxygen is known to generate semiquinone anion radicals via autoxidation – allowing for a possible fingerprinting of the extracts as well as for correlation of the intensity of the signal with other chemical parameters, such as concentration of the EPR-activated antioxidants [19]. The EPR spectra recorded 2 min after alkali treatment of the *Achillea* extracts display a hyperfine structure at the room temperature and show the same line shape for both extracts, with a pattern very similar to quercetin and other polyphenols as chlorogenic acid, isoquercitrin, quercytrin and hyperoside (data not shown).

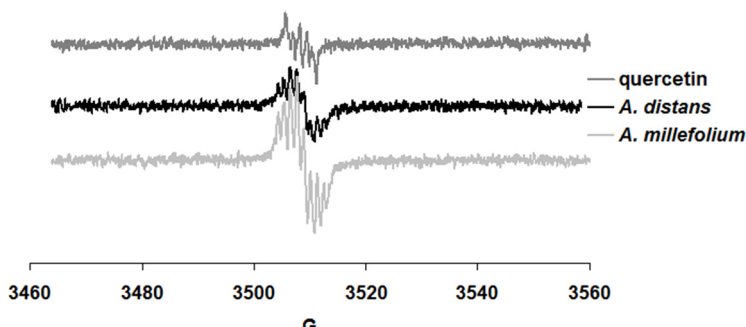


Figure 3. The EPR spectra of quercetin (2 mM) and *Achillea* extracts diluted 10 times and treated with NaOH, in ethanol 90%.

In vitro antimicrobial activity

The ethanolic extracts of *A. distans* and *A. millefolium* were investigated for their *in vitro* antimicrobial properties against four bacteria species and one fungus (Table 3).

Table 3. Antimicrobial activity of *Achillea* extracts

Samples	Inhibition zone diameter (mm)				
	<i>S. aureus</i>	<i>L. monocytogenes</i>	<i>E. coli</i>	<i>S. typhimurium</i>	<i>C. albicans</i>
<i>A. distans</i>	12	14	11	11	6
<i>A. millefolium</i>	12	12	10	10	6
Gentamicin	19	18	22	18	-
Fluconazole	-	-	-	-	25

Gentamicin (10 µg/well) and Fluconazole (25 µg/well) were used as positive control.

The two extracts were found to be active against the gram-positive bacteria and inactive on the *C. albicans*. Both studied samples showed a low antibacterial action against all bacterial strains tested. However, *A. distans* extract was slightly more active against *L. monocytogenes*, *E. coli* and *S. typhimurium*. Our findings are in agreement with those of other authors [3,4,12,14].

CONCLUSIONS

The phenolic content, antioxidant and antimicrobial activities of *Achillea millefolium* and *Achillea distans* are reported, thus complementing the scientific information concerning the bioactivity and polyphenolic composition of *Achillea* species. This study shows that the phenolic profiles of the both *Achillea* were

generally similar, varying only in the amounts found. The results of the antioxidant assays as well as the phenolic contents indicate that *A. millefolium* extract is clearly more antioxidant than *A. distans* extract. The antimicrobial assays reveal that *Achillea* extracts were effective against tested bacteria. Accordingly, these two indigenous species of *Achillea* may be considered important sources of polyphenols with bioactive properties, justifying their pharmaceutical use.

EXPERIMENTAL SECTION

Plant material and extraction procedure

The flowers of *A. millefolium* (Voucher No. 952) and *A. distans* (Voucher No. 951) were collected in 2013 from the spontaneous flora in Cluj and Maramures counties, in the blossom period. Voucher specimens were deposited in the Herbarium of the Department of Pharmacognosy of the Faculty of Pharmacy, Cluj-Napoca, Romania.

The plant material was reduced to a proper degree of fineness. 5.0 g of the material was extracted with 50 mL of 70% ethanol (Merck, Darmstadt, Germany), for 30 min on a water bath, at 60 °C. The samples were then cooled down and centrifuged at 4,500 rpm for 15 min, and the supernatant was recovered [12,18,20-21].

HPLC-MS analysis

HPLC-MS analysis was performed on an Agilent 1100 HPLC Series system (Agilent, USA) using the chromatographic conditions previously described [12,18,20]. Quantitative determinations were performed using an external standard method; retention times were determined with a standard deviation ranging from 0.04 to 0.19 min. For all compounds, the accuracy was between 94.1.3% and 105.3%. Accuracy was checked by spiking samples with a solution containing each standard compound in a 10 µg/mL concentration. In all analyzed samples the compounds were identified by comparison of their retention times and recorded electrospray mass spectra with those of standards in the same chromatographic conditions. Calibration curves in the 0.5-50 mg/mL range with good linearity ($R^2 > 0.999$) for a five points plot were used to determine the concentration of polyphenolics in plant samples.

Determination of phenolic compounds content

The total polyphenolic content (TPC) of the extracts were determined using the Folin-Ciocalteu method, with a calibration curve of gallic acid ($R^2 = 0.999$), the absorbance being measured at 760 nm [12,21,22,23]. The spectrophotometric aluminum chloride method was used for flavonoid determination

and the absorbance was measured at 430 nm [21]. Total flavonoid content values, expressed as rutin equivalent (RE), were determined using a calibration curve based on rutin ($R^2 = 0.999$).

DPPH bleaching assay

For the DPPH assay, 2.0 ml of methanolic DPPH solution (0.25 mM) were added to 2.0 ml of extract solution (or standard) in ethanol at different concentrations (12.5-100 μ g/mL). After 30 minutes of incubation at 40°C in a thermostatic bath, the decrease in the absorbance was measured at 517 nm. The percent DPPH scavenging ability was calculated as: DPPH scavenging ability = $(A_{\text{control}} - A_{\text{sample}})/A_{\text{control}} \times 100$, where Abs_{control} is the absorbance of DPPH radical and methanol (containing all reagents except the sample) and Abs_{sample} is the absorbance of DPPH radical and sample extract. Afterwards, a curve of % DPPH scavenging capacity *versus* concentration was plotted and IC₅₀ values were calculated. IC₅₀ denotes the concentration of sample required to scavenge 50% of DPPH free radicals. Quercetin was used as positive control [12,18,20,23].

HAPX (hemoglobin/ascorbate peroxidase activity inhibition) assay

The hemoglobin ascorbate peroxidase activity assay (HAPX) was described in detail in [19,24]. The reaction was monitored at 405 nm, where all the changes are due to the hemoglobin transformation. Met hemoglobin (6 μ M) was added to a mixture of ascorbate (120 μ M), peroxide (700 μ M) and extracts (5 μ l), in acetate buffer, pH 5.5 to start the reaction. An increase in the inhibition time denotes a good antioxidant capacity of the tested extract which acts in competition with the ascorbate. The percentage of the inhibition time for each case was converted to rutin equivalents using a calibration curve ($R = 0.98$) with rutin standard solutions of 0-1.5 mM.

Free radical generation experiment

For the EPR experiment the extracts were diluted 10 times in 90% ethanol, followed by the treatment with 5 mM NaOH (yielding a pH of 11.7). A low quantity (100 μ l) of sample was rapidly transferred to a glass capillary EPR tube. The capillary was placed in the holder of a Bruker ELEXSYS E-580 spectrometer with continuous wave at X band (~ 9.4 GHz). The spectra were measured at room temperature with the following parameters: modulation frequency 100 kHz, microwave power 9.6 mW, modulation amplitude 0.5 G, center field 3514 and sweep field 100 G [19].

Determination of antimicrobial activity

The disc-diffusion assay was employed on the ethanolic extracts of *A. distans* and *A. millefolium* against a panel of microorganisms including gram-positive and gram-negative bacteria: *Listeria monocytogenes* (ATCC 13076), *Salmonella typhimurium* (ATCC 14028), *Escherichia coli* (ATCC 25922), *Staphylococcus aureus* (ATCC 49444), and *Candida albicans* (ATCC 10231). All microorganism strains were distributed by MicroBioLogics®. Each microorganism was suspended in Mueller Hinton (MH) broth and diluted approximately to 10^6 colony forming unit (cfu)/mL. They were “flood-inoculated” onto the surface of MH agar and MH Dextrose Agar (MDA) and then dried. Six millimetres diameter wells were cut from the agar using a sterile cork-borer and 15 µL of each extract were delivered into the wells. The plates were incubated at 37° C and the diameters of the growth inhibition zones were measured after 18 h. Gentamicin and Fluconazole were used as standard drugs. The controls were performed with only sterile broth and with only overnight culture and 10 µL of 70% ethanol. The clear halos greater than 10 mm were considered as positive results [18,25].

ACKNOWLEDGMENTS

We would like to thank “Iuliu Hatieganu”University of Medicine and Pharmacy of Cluj-Napoca (B.D. grant 1494/6/28.01.2014, I.-E.P. 1493/11/2014) for financial support of these projects. C.B. thanks for the financial support of the Sectoral Operational Programme for Human Resources Development 2007-2013, co-financed by the European Social Fund, under the project POSDRU/159/1.5/S/132400 - “Young successful researchers – professional development in an international and interdisciplinary environment”.

REFERENCES

- [1]. S. Saeidnia, A. Gohari, N. Mokhber-Dezfuli, F. Kiuchi, *Daru*, **2011**, 19, 173.
- [2]. V. Ciocarlan, "Illustrated Flora of Romania. Pteridophyta et Spermatophyta", Ceres Publishing House: Bucharest, Romania, **2009**.
- [3]. W.L. Applequist, D.E. Moerman, *Economic Botany*, **2011**, 65, 209.
- [4]. F. Candan, M. Unlu, B. Tepe, D. Daferera, M. Polissiou, A. Sökmen, H.A. Akpulat, *Journal of Ethnopharmacology*, **2003**, 87, 215.
- [5]. R. Paduch, G. Matysik, M. Nowak-Kryska, P. Niedziela, M. Kandefer-Szerszeń, *Journal of Pre-Clinical and Clinical Research*, **2008**, 2, 49.
- [6]. A. Konakchiev, M. Todorova, B. Mikhova, A. Vitkova, H. Najdenski, *Natural Product Communications*, **2011**, 6, 905.

- [7]. S. Vitalini, G. Beretta, M. Iriti, S. Orsenigo, N. Basilico, S. Dall'Acqua, M. Iorizzi, G. Fico, *Acta Biochimica Polonica*, **2011**, 58, 203.
- [8]. R. Benetis, J. Radusiene, V. Jakstas, V. Janulis, G. Puodziuniene, A. Milasius, *Pharmaceutical Chemistry Journal*, **2008**, 42, 153.
- [9]. L. Georgieva, A. Gadjalova, D. Mihaylova, A. Pavlov, *InternationalFood Research Journal*, **2015**, 22, 1347.
- [10]. A. Smelcerovic, M. Lamshoeft, N. Radulovic, D. Ilic, R. Palic, *Chromatographia*, **2010**, 71, 113.
- [11]. M. Popovici, L. Vlase, I. Oniga, M. Tamas, *Farmacia*, **2007**, 3, 353.
- [12]. D. Benedec, L. Vlase, I. Oniga, A. C. Mot, G. Damian, D. Hangany, M. Duma, R. Silaghi-Dumitrescu, *Molecules*, **2013**, 18, 8725.
- [13]. M.N. Todorova, B. Mikhova, A. Trendafilova, A. VitkovaDuddeck, H, *Biochemical Systematics and Ecology*, **2007**, 12,852.
- [14]. G. Stojanovic, N. Radulovic, T. Hashimoto, R. Palic, *Journal of Ethnopharmacology*, **2005**, 101, 185.
- [15]. M. Popovici, A.E. Pârvu, I. Oniga, A. Toiu, M. Tamas, D. Benedec, *Farmacia*, **2008**, 1, 15.
- [16]. B. Haroon Mohi-ud-din, B. Khursheed Ahmad, P. Shashi, H. Abid, *Journal of Academia and Industrial Research*, **2014**, 2, 487.
- [17]. W.Y. Huang, Y.Z. Cai, Y. Zhang, *Nutrition and Cancer*, **2010**, 62, 1.
- [18]. M. Mureşan, D. Benedec, L. Vlase, R. Oprean, A. Toiu, I. Oniga, *Studia UBB Chemia*, **2015**, LX, 127.
- [19]. A.C. Mot, C. Bischin, G. Damian, R. Silaghi-Dumitrescu, *Methods in Molecular Biology*, **2015**, 1208, 247.
- [20]. L. Vlase, D. Benedec, D. Hangany, G. Damian, I. Csillag, B. Sevastre, A.C. Mot, R. Silaghi-Dumitrescu, I. Tilea, *Molecules*, **2014**, 19, 5490.
- [21]. Romanian PharmacopoeiaXth Edition, Medical Publishing House Bucharest, Romania, **1993**.
- [22]. European Pharmacopoeia, 7th Edition, European Directorate for Quality Medicines, Strasbourg, **2010**.
- [23]. V.L. Singleton, R. Orthofer, R.M. Lamuela-Raventos, *Method Enzymology*, **1999**, 299, 152.
- [24]. C.E. Cooper, R. Silaghi-Dumitrescu, M. Rukengwa, A. Alayash, P. Buehler, *Biochimica et Biophysica Acta*, **2008**, 1784, 1415.
- [25]. D.S. Mi Reeves, L.O. White, "Principles of methods of assaying antibiotics. In *Pharmaceutical Microbiology*", 3rd Edition, Blackwell Scientific Publication, **1983**.

SOLVATOCHROMISM OF ASYMMETRICAL SUBSTITUTED 3,7-DIAMINOPHENOTHIAZINIUM DYE

CAMELIA CIOBOTARIU^a, LUCIAN CORNEL POP^a, DAN PORUMB^{a*}

ABSTRACT. A convenient procedure for the synthesis of 3-diethylamino-7-phenylaminophenothiazin-5-iium iodide was developed and the solvatochromism of this blue dye was examined by means of UV-Vis spectroscopy. The maximum of the absorption wavelength was detected in the range 550-665 nm, the asymmetrical phenothiazinium dye exhibiting a large red shift upon variation of the solvent structure from aprotic dipolar (THF, DMF) to protic solvents (water, methanol, acetic acid).

Keywords: *phenothiazin-5-iium, cationic dye; UV-Vis absorption, solvatochromism*

INTRODUCTION

The phenothiazine based dyes are some of the oldest synthetic compounds developed for applications in textile industry. Large scale production of the thionine (3,7-diaminophenazathionium chloride) and methylene blue (3,7-*bis*-dimethylaminophenazathionium chloride) (figure 1) was based on coupling of primary aromatic amines (aniline, or *p*-diamethylaminoaniline) under oxidative conditions, followed by ring closure in the presence of thiosulfate. Methylene blue found more important medicinal and biological applications due to antimicrobial, cytology, cytopathology, and haematological staining properties and recently became a lead compound of phenothiazine-based photosensitisers [1]. Methylene blue analogous containing symmetrical or non-symmetrical dialkylamine functionality in the auxochromic C-3 and C-7 positions of the phenothiazin-5-iium chromophore were prepared and investigated for potential applications in the fields of photodynamic therapy and photodynamic antimicrobial chemotherapy.

An alternative step-wise synthetic route to 3,7-*bis*(dialkylamino) phenothiazin-5-iium salts involves in the first step the generation of a phenothiazin-5-iium cationic salt by oxidation of phenothiazine, followed by the addition of dialkylamine nucleophile. [2] The oxidation of phenothiazine to phenothiazin-5-

^a Babeș-Bolyai University, Faculty of Chemistry and Chemical Engineering, 11 Arany Janos str., RO-400028, Cluj-Napoca, Romania.

* Corresponding author: pdan@chem.ubbcluj.ro

ium tetraiodide hydrate was thoroughly investigated by a systematic variation of the reaction solvent (chloroform, dichloromethane, *t*-butylmethylether), time and temperature as well as iodine addition manner (in solution or portion-wise solid); crude product was obtained in excellent to quantitative reaction yields. [3] The access to asymmetric analogs was reached by adding different amines in sequence. [4] Symmetrical methylene blue analogous containing longer alkyl chains (C_2-C_6) [5,6] as well as some asymmetric derivatives exhibiting varying degrees of polar and spatial asymmetry have been reported [7-9]. Figure 1 summarizes the variation of auxochromic substituents in methylene blue analogues. Phenothiazinium iodides thus prepared can be transformed to chlorides by using a resin exchange column [10].

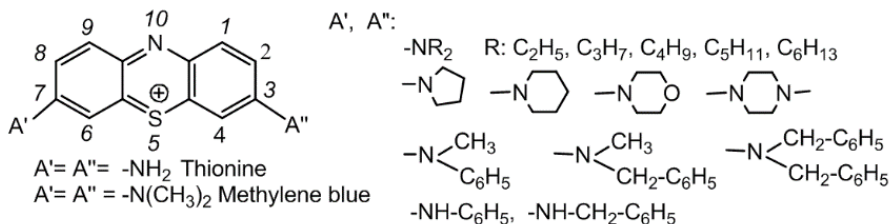


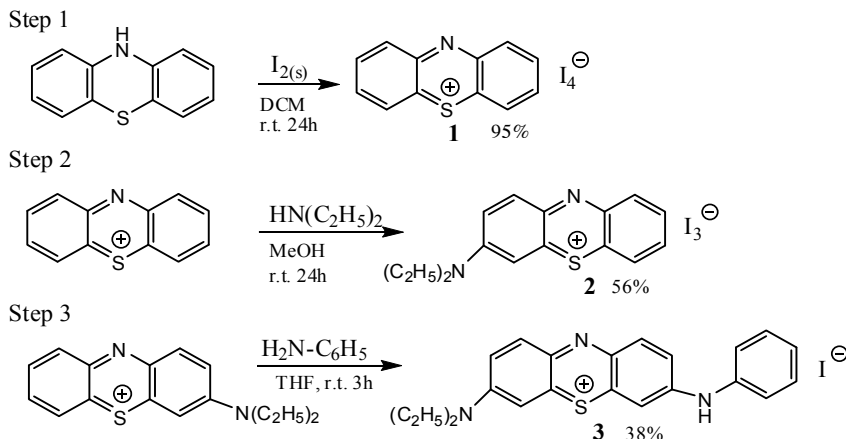
Figure 1. Auxochromic substituents on phenothiazin-5-ium cation

The target 3-diethylamino-7-phenylamino-phenothiazin-5-ium iodide was previously reported among several 3-dialkylamino-7-arylamino-phenothiazinium iodides susceptible for singlet oxygen generation [4], but in this work we described a modified synthetic procedure and we report for the first time the solvatochromism examined by UV-Vis spectroscopy. The change in color from purple ($\lambda_{\max}=550$ nm in THF) to deep blue ($\lambda_{\max}=665$ nm in water), also visible by naked eye, imply a great potential in developing new moisture sensors for hygroscopic materials as well as methachromatic staining of biological tissues.

RESULTS AND DISCUSSION

In this work the stepwise procedure based on the oxidation of the phenothiazine substrate followed by successive nucleophilic substitution of the phenothiazin-5-ium cationic salt with diethylamine and aniline was revisited and we described a modified procedure resulted after a careful selection of the reaction conditions for each step (scheme 1). The reaction conditions are smooth, requiring ambient temperature and pressure and also tolerant to the presence of air. Different solvents were selected for each step of the procedure in order to allow the reaction to proceed in homogeneous conditions and easily collect the insoluble product by filtration. In step 1 the phenothiazin-5-ium cationic salt **1** was prepared in DCM solution by portion-wise addition of solid iodine in order

to handle reduced volumes of solvent [3]. The intermediate 3-diethylamino-phenotheniazin-5-iium triiodide **2** precipitated in the second step from the methanol solution was further employed in the third step without purification only by dissolution in THF. The crude 3-diethylamino-7-phenylamino-phenotheniazin-5-iium iodide **3** was purified by column chromatography for analytical purposes.



The recorded high resolution $^1\text{H-NMR}$ spectra unambiguously confirmed the molecular structure of the cationic dye **3**. In figure 2 is presented the first order $^1\text{H-NMR}$ spectrum depicting the coupling patterns of the aromatic protons in the fenazathionium cation ($\text{H}_{1,2,4,6,8,9}$) and the pending phenyl unit ($\text{H}_{\text{A,M,X}}$).

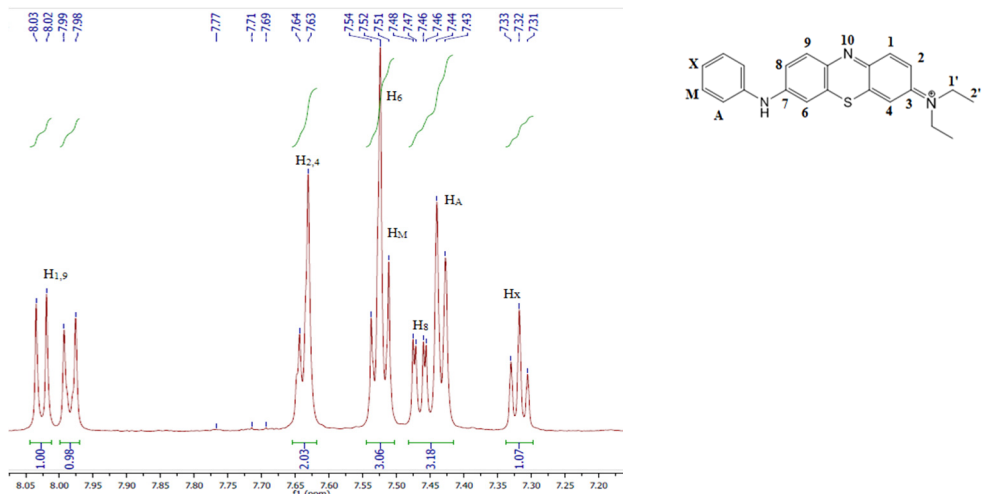


Figure 2. 600 MHz $^1\text{H-NMR}$ spectrum of **3** in DMSO-d_6 (detail aromatic region)

The optical properties of **3** were estimated by UV-Vis spectroscopy. The dye is characterized by a strong absorption band situated in the 550-660 nm region with an important shift of the absorption maximum (λ_{\max}) according to the nature of the solvent employed. In Table 1 are presented the solvatochromic effects recorded in upon variation of the solvent polarity from less polar DCM to polar DMF solvent.

A very small red shift of the absorption maxima occurred upon variation of the polarity among protic solvents (methanol, water \approx 10 nm), but a considerable large red shift (\approx 100 nm) can be observed upon variation of the solvent structure from aprotic dipolar (THF, DMF) to protic solvents (water, methanol, acetic acid) as depicted in figure 3.

Table 1. Position of the visible absorption maxima of **3** in aprotic and protic dipolar solvents

Solvent	Dipole moment [D]	λ_{\max} [nm]	ϵ [$\text{L mol}^{-1}\text{cm}^{-1}$]
Dimethylformamide	3.82	560	28000
Water	1.85	665	83000
Acetic acid	1.74	660	48000
Methanol	1.70	655	40000
Tetrahydrofurane	1.63	550	53000
Dicloromethane	1.14	655	48000

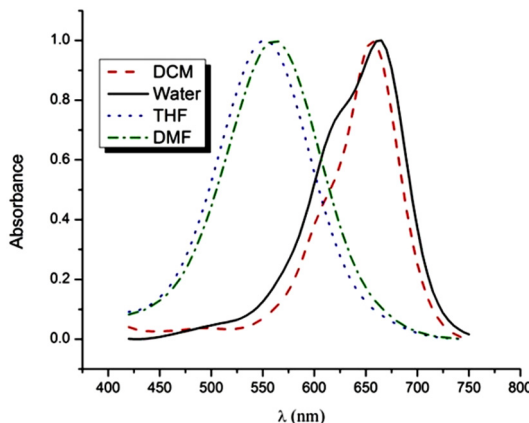


Figure 3. Normalized absorbance of **3** in aprotic and protic dipolar solvents

Assuming that the absorption bands in UV-Vis spectra of **3** arise from vertical electronic transitions between frontier molecular orbitals with relative energies affected by the interaction with the solvent (especially hydrogen bond associations with protic solvents), we employed the Spartan 04 software package [11] for modeling the optimized geometry and the electronic distribution in the

frontier molecular orbitals. From figure 4 one can notice that the atomic orbitals of the three N and S atoms considerably participate to LUMO, thus generating an excited state more susceptible to interaction with polar solvents.

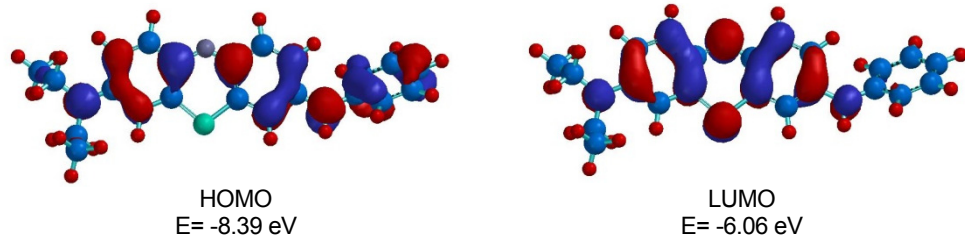


Figure 4. Frontier molecular orbitals plots and energy values modeled using the Spartan 04 software package.

The red shift of the Vis absorption maxima observed in protic solvents can be sustained by a possible stabilization of the excited state (modeled by the LUMO) by multiple hydrogen bond associations which may considerably reduce the HOMO-LUMO energy gap.

CONCLUSIONS

A convenient synthetic procedure was developed for the synthesis of the asymmetric methylene blue analogue 3-diethylamino-7-phenylamino-phenothiazin-5-i um iodide.

The large solvatochromism of the dye was explained in terms of stabilization of the excited state modeled by the LUMO by multiple hydrogen bond associations in protic solvents, which may considerably reduce the HOMO-LUMO energy gap.

EXPERIMENTAL

Phenothiazin-5-i um tetraiodide 1

10H-Phenothiazine (2 g, 10 mmol) was dissolved in 50 ml DCM at room temperature. Iodine (8 g, 31 mmol) was added portion wise during 20 min and then the mixture was stirred for 5h at room temperature. The resulting dark brown solid was filtered, washed free of iodine with DCM and dried. Crude product M.p.170°C (dec). yield 6.7g, 95%.

3-Diethylaminophenothiazinium triiodide 2

Phenothiazinium tetraiodide (2.15 g, 3 mmol) was dissolved in methanol (20 ml) at room temperature and a solution of diethylamine (0.8 ml, 7.6 mmol) in methanol (20 ml) was added dropwise over 20 min. The reaction mixture was

stirred at room temperature for 3h and then allowed to stand overnight. The dark blue solid accumulated upon standing was filtered off, washed with cold methanol and dried. Crude product yield 1.3 g, 56%

3-Diethylamino-7-phenylaminophenothenothiazinium iodide 3

To a solution of **2** (0.5 g 6.5 mmol) in THF (10 ml), a solution of aniline (1.2 ml, 13 mmol) in THF (10 ml) was added dropwise and the mixture was stirred at room temperature for 2h. The blue solid accumulated upon standing was filtered off and thoroughly washed with diethyl ether. The product was purified by column chromatography on silica gel using gradient elution in dichloromethane/methanol. Yield 0.13 g, 38%. ¹H-NMR (600 MHz, DMSO-d₆): δ (ppm) 1.34 (t, J=6Hz, 6H), 3.78 (q, J=6Hz, 4H), 7.32 (t, J=6Hz, 1H), 7.44 (d, J=6Hz, 2H), 7.46 (d, J=6Hz, 1H), 7.51 (m, 3H), 7.63 (m, 2H), 7.99 (d, J=6Hz, 2H), 8.02 (d, J=6Hz, 2H).

REFERENCES

- [1]. M. Wainwright, H. Mohr, W.H. Walker, *Journal of Photochemistry and Photobiology B: Biology*, **2007**, 86, 45.
- [2]. L. Strekowski, D. Hou, R.L. Wydra, R.F. Schinazi, *Journal of Heterocyclic Chemistry* **1993**, 30, 1693.
- [3]. J.A. Cody, C.S. Larabee, M.D. Clark, S. Hlynchuk, J.A. Tatum, *Tetrahedron Letters*, **2012**, 53, 4896.
- [4]. M. Wainwright, K. Meegan, C. Loughran, R.M. Giddens, *Dyes Pigments*, **2009**, 82, 387.
- [5]. K.J. Mellish, R.D. Cox, D.I. Vernon, J. Griffiths, S.B. Brown, *Photochemistry and Photobiology*, **2002**, 75 392.
- [6]. N. Leventis, M. Chen, C. Sotiriou-Leventis, *Tetrahedron* **1997**, 53 10083.
- [7]. A. Gorman, A.L. Bell, J. Griffiths, D. Roberts, S.B. Brown, *Dyes and Pigments* **2006**, 71, 153.
- [8]. M. Wainwright, S.D. Brandt, A. Smith, A. Styles, K. Meegan, C. Loughran *Journal of Photochemistry and Photobiology B: Biology*, **2010** 99, 74
- [9]. B. Wilson, M-J. Fernandez, A. Lorente, K.B. Grant, *Tetrahedron*, **2008**, 64 3429.
- [10]. Y-T Lu, C. Arai, J-F. Ge, W-S. Ren, M. Kaiser, S. Wittlin, R. Brun, J-M. Lu, M. Ihara, *Dyes and Pigments*, **2011**, 89, 44.
- [11]. Spartan'04 Wavefunction, Inc. Irvine, CA Except for molecular mechanics and semi-empirical models, the calculation methods used in Spartan'04 have been documented in: J. Kong, C.A. White, A.I. Krylov, C.D. Sherrill, R.D. Adamson, T.R. Furlani, M.S. Lee, A.M. Lee, S.R. Gwaltney, T.R. Adams, C. Ochsenfeld, A.T.B. Gilbert, G.S. Kedziora, V.A. Rassolov, D.R. Maurice, N. Nair, Y. Shao, N.A. Besley, P.E. Maslen, J.P. Dombroski, H. Daschel, W. Zhang, P.P. Korambath, J. Baker, E.F.C. Byrd, T. Van Voorhis, M. Oumi, S. Hirata, C.-P. Hsu, N. Ishikawa, J. Florian, A. Warshel, B.G. Johnson, P.M.W. Gill, M. Head-Gordon and J.A. Pople, *J. Computational Chem.*, **2000**, 21, 1532. A discussion and assessment of commonly-used calculation methods is found in: W.J. Hehre, A Guide to Molecular Mechanics and Quantum Chemical Calculations, Wavefunction, Irvine, **2003**.

THE EFFECT OF USING PYROLYSIS OILS FROM POLYETHYLENE AND DIESEL ON THE POLLUTANT EMISSIONS FROM A SINGLE CYLINDER DIESEL ENGINE

GEORGE LIVIU POPESCU^a, NICOLAE FILIP^a,
ANDREIA MOLEA^b, VIOLETA POPESCU^{b,*}

ABSTRACT. The paper presents data related to the results obtaining following the testing of a commercial diesel fuel and a fuel obtained by chemical recycling of polymers waste based on polyethylene in a single cylinder diesel engine. The concentrations of CO, CO₂, hydrocarbons, NO_x and smoke have been determined in the exhausted gases. The experimental results showed that using synthesized polyethylene-based fuel, the emission of pollutants was smaller compared to the emissions when using commercial diesel fuel, except the concentration of hydrocarbons which was higher.

Keywords: recycling, pyrolysis, polymers waste, fuel, pollutants, diesel engine.

INTRODUCTION

The Directive 2008/98/EC on waste, provides a framework for the environmentally sound management of waste, including the preferred hierarchy of waste management options. Waste management strategies should focus both on reducing the amount of produced waste and its hazardousness [1]. The amount of used plastic materials (PM) continues to increase every year. Using and producing more PM involves the producing of higher quantities of waste. Because waste generation can not be avoided, waste should be reused as much as possible.

Quantitative targets for the recycling and recovery of packaging waste were set for 31 December 2008 (55 - 70 % recycling, 60 - 75 % recovery), but Romania is far from reaching this target. Directive 94/62/EC regulates the Packaging and Packaging Waste in European Union, while Government Decision

^a Technical University of Cluj-Napoca, Faculty of Mechanical Engineering, 103-105, Muncii Avenue, RO-400641, Cluj-Napoca, Romania

^b Technical University of Cluj-Napoca, Faculty of Materials and Environmental Engineering, 103-105 Muncii Avenue, RO-400641, Cluj-Napoca, Romania

* Corresponding author: Violeta.Popescu@chem.utcluj.ro

no. 349/2002 revised and amended in 2004 (899/2004) is applied in Romania, resulting an imperative necessity for identification of an appropriate method for recycling of each type of waste, because new European regulators are setting increasingly stringent standards to reduce the impact of PM waste in the environment.

Current statistics for Western Europe estimate the annual consumption of plastic products at almost 100 kg/person for a total of over 39.1 million tons [2, 3]. Over 78 wt % of this total corresponds to thermoplastics (low and high density polyethylene LDPE-HDPE, polypropylene PP, polyvinyl chloride PVC and polyethylene terephthalate PET) and the remaining 22 wt % to thermosets (mainly epoxy resins and polyurethane) [2]. This generates a vast waste stream, estimated at around 21.5 million tons, that needs to be effectively managed. Today 61 wt % of all the waste plastics generated in Europe are still disposed of to landfill, a management alternative that generates serious environmental problems due to their low density, resistance to biological degradation and combustible nature.

Even though in European Union collection and recycling of waste is already a current practice; plastic materials recycling represents nevertheless an important objective of European and Romanian researches, in order to elaborate the most efficient technologies from economical and environmental point of view. In the Sectorial Operation Programs (POS) of Romania, the first priority is „The development of regional systems for water and waste management” [4].

One of the potential options for polyolefin waste management is chemical recycling for fuel production.

Plastic pyrolysis is a method for plastic materials recycling that can be applied to a variety of polymers. A wide range on degradation products can be obtained. The composition of degradation products depends on many factors such as: polymer type, temperature, catalysts.

Pyrolysis technology has reached by now a state of development that opens more favorable possibilities for waste disposal than some of the traditional techniques. Special complex waste materials which contain plastic, such as contaminated materials, can now be properly recycled by pyrolytic treatment.

Pyrolysis, also termed thermolysis, is a process of chemical and thermal decomposition of polyolefins, generally, leading to smaller molecules. In most pyrolysis processes, air is excluded, for reasons of safety, product quality and yield. Pyrolysis can be conducted at various temperature levels, reaction times, pressures and in the presence or absence of reactive gases or liquids, and/or catalysts. PE pyrolysis proceeds at low (<400°C), medium (400–600°C) or high temperature (>600°C). The pressure is generally atmospheric. The thermal decomposition of PE yields gases, distillates and char, albeit in widely variable relative amounts. These can be applied as fuels or petrochemicals.

Polyolefin resins contain only carbon, hydrogen and additives, such as antioxidants and UV stabilizers. Depending on the polymers or polymer mixtures fed and the operating conditions used, yields can vary widely. Both gaseous

and liquid products are mixtures of numerous different compounds. The problem of fractionating these effluents and upgrading to commercial specifications, while separating undesirable impurities must be investigated on a case-by-case basis, but until than, the developing of appropriate methods for using the pyrolysis product as is, can be of high interest.

By thermal degradation of HDPE and XLDPE, a significant quantity of waxes is formed, and the quantity of liquid products is smaller when using LDPE and LLDPE. This suggests that PE which contain lateral chains (such as LDPE and LLDPE, respectively), by pyrolysis process a higher quantity is transformed in to liquid products, comparing with HDPE and XLDPE (with linear chains). The use of catalyst leads to the increase of liquid and gaseous degradation products.

Catalytic degradation of LDPE, in controlled conditions, leads to the obtaining of valuable aromatic products (namely: benzene, toluene, xylene and feedstock for petrochemicals [5-7]). By pyrolysis of LDPE from plastic bags results a mixture of compounds, whose concentration differs depending on pyrolysis conditions (temperature, catalysts) resembling the composition of commercial gasoline [6].

Even if the studies regarding chemical recycling of plastic waste were systematically done, a few studies regarding the impact of using plastic fuels derived in engines are presented in the literature [8-14].

Moriya et al [13] shown that cracked PE (polyethylene) can be used for engine as a 30-40 % blended fuels with Diesel fuel. Other studies involved a thermal recycling system of plastic wastes. In this case, the plastic waste is melted and mixed with heavy oil resulting a fuel for Diesel engine generator systems [12,14].

Santaweesuk and Janyalertadun used for their study a 4-Stroke, compression ignition, water cooled, single cylinder engine. By changing the engine speed they concluded that compression ignition engine is able to run with distilled waste plastic oil, because physical characteristics of distilled waste plastic oil (DWPO) is similar to diesel oil. Engine fueled with distilled waste plastic oil exhibits lower brake thermal efficiency but increase average when setting nozzle pressure and results are higher than average in brake specific fuel consumption for distilled waste plastic oil (DWPO) but lower average when setting nozzle pressure. Exhaust gas emission increase average when setting nozzle pressure in distilled waste plastic oil (DWPO) compared to diesel operation and results are that the nozzle setting pressure can help reduce better the emissions [15].

Jani, Patel, Rathod also used a 4-Stroke, water-cooled diesel engine of 5 HP rated power and established that using the synthesized fuel, the best results have been obtained in CI engine with blends containing 30 % pyrolysis product regarding both performance and emission of diesel engine [16].

The novelty of our researches consists in the study of a fuel obtained from polyolefin in our laboratory and testing of synthesized fuel in diesel engine air-cooled, without any modification, without blending with commercial diesel fuel. Our team conducted both studies regarding fuel production and testing.

RESULTS AND DISCUSSION

The yield in liquid degradation products of interest was up to 93 %, [17]. The composition of the liquid fuel resulted following the pyrolysis process has been determined using gas chromatography and reveled that the fuel contains both saturated and unsaturated compounds [18, 19]. The main difference between pyrolysis product and commercial products consists on the small quantities of light fraction (C_3-C_5) up to 4 %, and heavy fraction ($C_{23}-C_{35}$) up to 12 % [17].

The formation of the above presented hydrocarbons in the pyrolysis product can be explained by the mechanism of thermal cracking of PE.

Polyethylene is formed from $-(CH_2-CH_2)_n-$ monomer units (mers), containing also a small number of terminal methyl ($-CH_3$) groups. Thermal cracking of PE leads to saturated and α unsaturated hydrocarbons due to scissions of PE long chains following a multistep radical chain reaction with all the general features of such reaction mechanisms: initiation, propagation, branching, and termination steps [18].

Random chain scission takes places in the initiation stage, conducting to the formation of free radicals [18].



where: P_n is a polymer containing n mers; $\cdot R_r$ and $\cdot R_{n-r}$ are radicals containing r and respectively $(n-r)$ mers.

In the propagation stage the chain suffer other scission reactions due to intramolecular or intermolecular H transfer and unzipping depolymerization resulting new radicals, saturated and unsaturated (P_m , P_{n-j} , P_1) hydrocarbons.



Intramolecular H transfer reaction involves the transfer of a hydrogen atom within a single polymer chain forming an unsaturated (P_m) polymer and a new terminal radical (R_{r-m}).

Intermolecular H transfer involves the transfer of one H atom from a inner carbon atom (not a terminal one), between neighbors polymer chains forming a new saturated polymer (P_r) and a new inner located radical that breaks up into an unsaturated polymer (P_{n-j}) and a new radical.

The last propagation mechanism (unzipping depolymerization) that involve the depolymerization with the formation of monomers and smaller chain polymers has no important impact in the specific case of polyethylene since the yield in liquid fraction is so high, being specific for polymers with functional groups such as polystyrene and polymethyl methacrylate [19] that suffer depolymerization reactions conducting to monomers with a high yield.

The termination stage occurs due to recombination of monomers or to disproportionation. While in the case of recombination two radicals react forming a new polymer, in the case of disproportionation one of the radicals donate a hydrogen atom, forming an unsaturated hydrocarbon (P_n), while the other radical accept the hydrogen atom forming a saturated hydrocarbon (P_s).



The mechanism of polyethylene degradation is not so simple since the unsaturated hydrocarbons can participate to polymerization reactions conducting to the formation of higher molecular weight hydrocarbons in tar or coke [20, 21].

For the limitation of the re-polymerization reactions, the gaseous product resulted following the pyrolysis was rapidly cooled using a Low Temperature Ethylene Glycol/Water Recirculation System. The rapid cooling conducted to the increasing of the yield of liquid pyrolysis product reducing the quantity of solid residue.

One can conclude that thermal cracking of polyethylene occurs by random chain scissions conducting to a broad spectrum of saturated and unsaturated hydrocarbons.

Both breaking and re-polymerization takes places due to free radicalic reactions [22].

For the investigation of thermal degradation of PE, FT-IR spectra for polyethylene and the pyrolysis product were recorded (fig. 1).

In polyethylene spectrum one can observe only vibrations due to methylene groups [23].

The absorption band centered at 2916 cm^{-1} can be assigned to C-H asymmetric stretch, while the one from 2848 cm^{-1} to C-H symmetric stretch from methylene groups. Around 1467 cm^{-1} can be observed a doublet due C-H bends for methylene groups.

In the spectrum of the fuel the asymmetric/symmetric C-H stretch due to methylene groups are shifted towards higher wavenumbers 2922 cm^{-1} (compared to 2916 cm^{-1}) and 2853 cm^{-1} (compared to 2848 cm^{-1}) respectively, while C-H bends can be observed at 1460 cm^{-1} . The presence of methyl groups can be clearly observed at 2957 cm^{-1} (C-H asymmetric stretch) and 2873 cm^{-1} (C-H symmetric stretch), 1379 cm^{-1} (C-H symmetric bend), proving the formation of new CH_3 terminal groups. The presence of unsaturated compounds can be observed due to the presence of alkenyl absorption band (C=C stretch at 1643 cm^{-1}), vinyl terminal stretch at 3075 cm^{-1} , vinyl C-H out of plane bend at 989 and 908 cm^{-1} and vinylidene C-H out of plane bend.

No oxidation processes took places since the C=O absorption band is missing (around 1700 cm^{-1}).

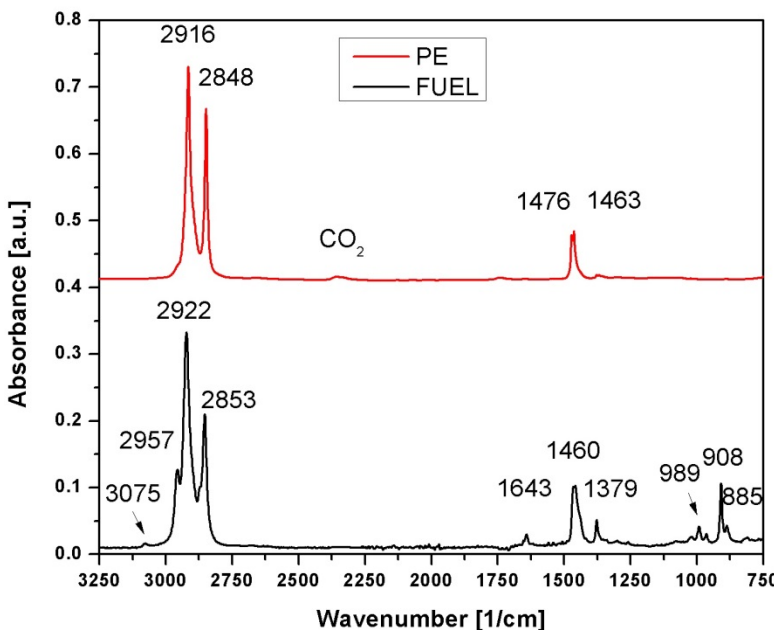
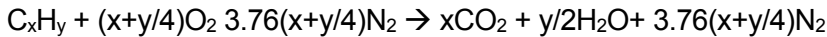


Figure 1. FT-IR spectra of PE and PE derived fuel

Other properties of the fuels, determined according to ISO 3104 and ASTM D445, revealed the similarity of the pyrolysis product properties with the property of commercial fuel [24] and the similar dependence of density, kinematic and dynamic viscosity on the temperature [25].

The reactions for the formation of unburned hydrocarbons (UBHC), CO_2 , CO, NO_x following fuel burning in internal combustion engine are briefly presented subsequently [26].

General exothermal reaction of fuel burning in the presence of oxygen from air leads to the formation of CO_2 :



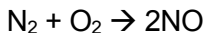
The presence of unburned hydrocarbons (UBHC) in the exhausted gas can be explained by the incomplete burning reaction. The temperature in the cylinder is not uniform, since the temperature at the time of combustion is 2500–3000°C, while the walls of cylinder are around 200°C. The exhaust starts at 1000 °C, but cools quickly after leaving cylinder and UBHC are formed in the quench zone.

The formation of CO can be explained both by the incomplete burning of hydrocarbon and the combustion in the condition of deficit of oxygen. Even if there is sufficient oxygen for total combustion of fuel, the formation of CO is possible because of the fact that fuel injected in later part of the injection does

not find enough oxygen due to local depletion in certain parts of the combustion chamber. More than that, when the temperature reaches certain values the dissociation of CO₂ can occur:

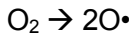


Nitrogen oxides are formed due to the presence of nitrogen from the air and nitrogen compounds from some fuels. Generally the used fuels have small concentration of nitrogen compounds. NO forms when fuel combustion takes places at high temperatures leading to the oxidation of nitrogen molecules following the general reaction:

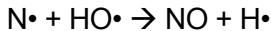


This reaction is strongly endothermic, having the free enthalpy of ΔH=90,4 KJ/mol. The quantity of the formed NO markedly decreases with the decrease of the combustion temperature.

The reaction is much more complex taking places due to the formation of free radical of oxygen in the flame by the dissociation of oxygen molecules. The following reaction takes places initiated by a radicalic mechanism, as described by Yakov Borisovich Zeldovich:



An important role is played by the reaction with hydroxyl radicals (HO·) that can be formed at high temperatures from combustion chamber:



The smoke is a direct product of burning process while it forms as a pollutant in the process of burning propagation and quantitatively intensify on the path of gases evacuation.

Engine tests

One concludes that the properties of the oil obtained by thermal degradation of PE are close enough (in accordance with EN 590 regulation) with the properties of commercial diesel fuel [25], leading to the conclusion that the synthesized fuel can be used as it is or as mixtures with commercial diesel fuels, in diesel engines. During tests, the hourly fuel consumption and the concentration of pollutants from exhausted gasses were determined as a function of engine's speed.

Hourly fuel consumption

The determination of hourly consumption (figure 2) has been made by weighting the quantity of consumed fuel in an establish time period and a specific speed rate. The test was timed, obtaining the time for fuel consumption, and in the final, the hourly consumption (c_h) has been calculated with the relation:

$$c_h = \frac{\tau \cdot m_\tau}{3600} \quad [g/h]$$

where: τ is the time, in seconds, during which m_τ fuel has been consumed; m_τ - the mass, in grams, of the fuel consumed in the time interval τ .

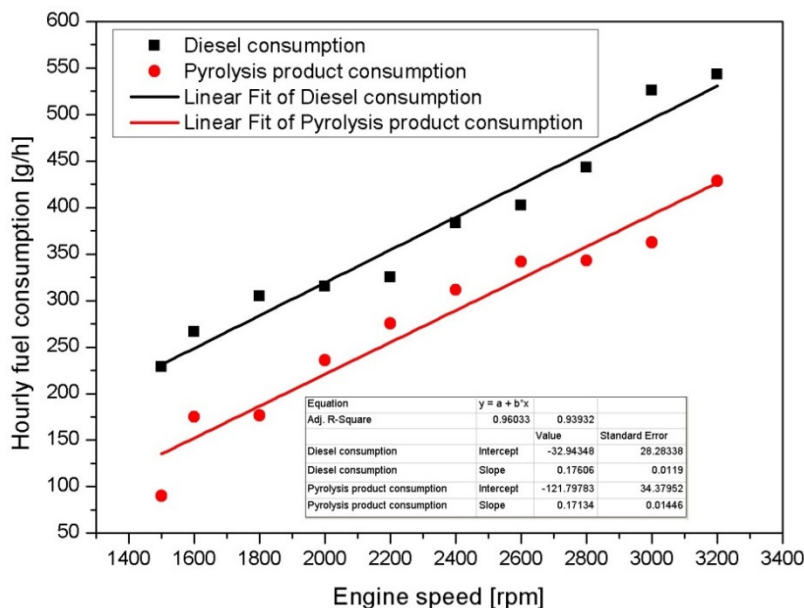


Figure 2. Comparison between the hourly consumptions of the two fuels

From the figure 2 it can be seen that at all engine speeds the hourly fuel consumption achieved from polyethylene-based fuel is significantly lower than of diesel.

Carbon monoxide emissions

Carbon monoxide forms when the fuel burnig process is incomplete and it is considerate a toxic gas due to his capacity to react with hemoglobin from the blood. The reduction of CO from exhausted gases is important both for human and environment protection.

Figure 3 presents the concentration of CO measured from the exhausted gases as a function of engine speed. The plot contains the values obtained following the measurements and the curve obtained applying second order polynomial regression. As can be seen from the figure 3, for engine speed smaller than 2400 rpm, the concentration of carbon monoxide is almost the same for experimental PE-based fuel and the commercial fuel.

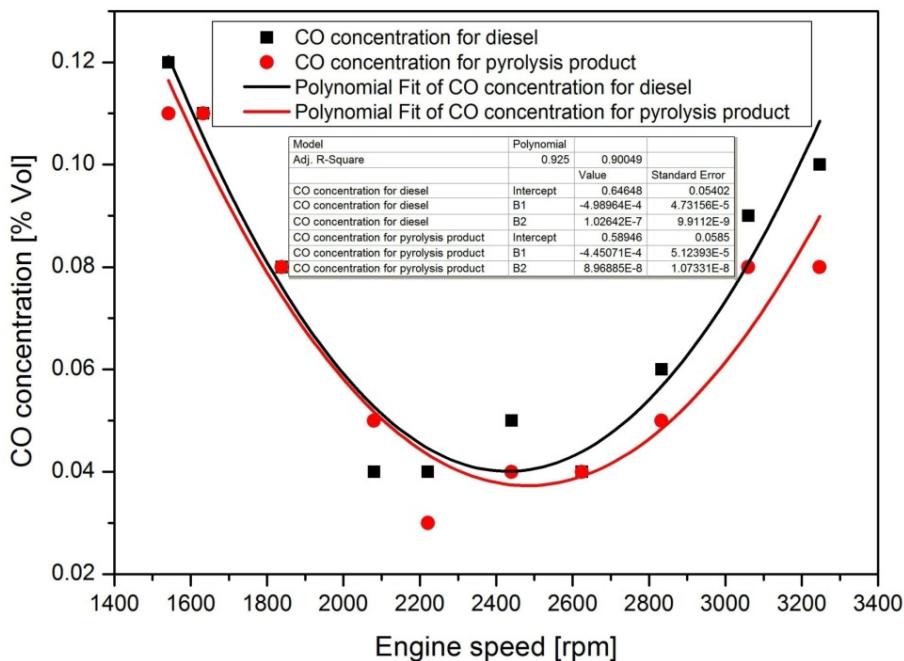


Figure 3. The concentration of CO from the exhausted gas as a function of engine speed

Increasing the speed engine, the concentration of CO resulted when pyrolysis product was used as fuel suffered a slightly reduction comparing with the concentration of CO resulted when commercial diesel fuel was used. The reduction of CO emissions when plastic derived fuels was used in a four stroke, compression ignition, water cooled, single cylinder, change speed diesel engine has been observed also by Santaweesuk Chumsunti, and Adun Janyalertadun [15]. In our experiment, the smallest CO emissions can be observed for both fuels when the engine speed is about 2400 rpm. The highest CO concentration was attained for engine speed of 1400 rpm. The increasing of engine speed at values higher than 2400 rpm leads to an increase of CO emission concentration.

Carbon dioxide emissions

Carbon dioxide forms when the combustion of fuels is complete. When the speed rate of the engine is smaller than 2200 rpm, the difference between the emissions of CO₂ is insignificant for the two fuels.

The increasing of engine speed determined the increase of the concentration of CO₂ for both fuels, but the concentration was higher when commercial diesel fuel was used. One can conclude that a positive effect on the concentration of CO₂ in the exhausted gases can be observed in the case of pyrolysis product (figure 4).

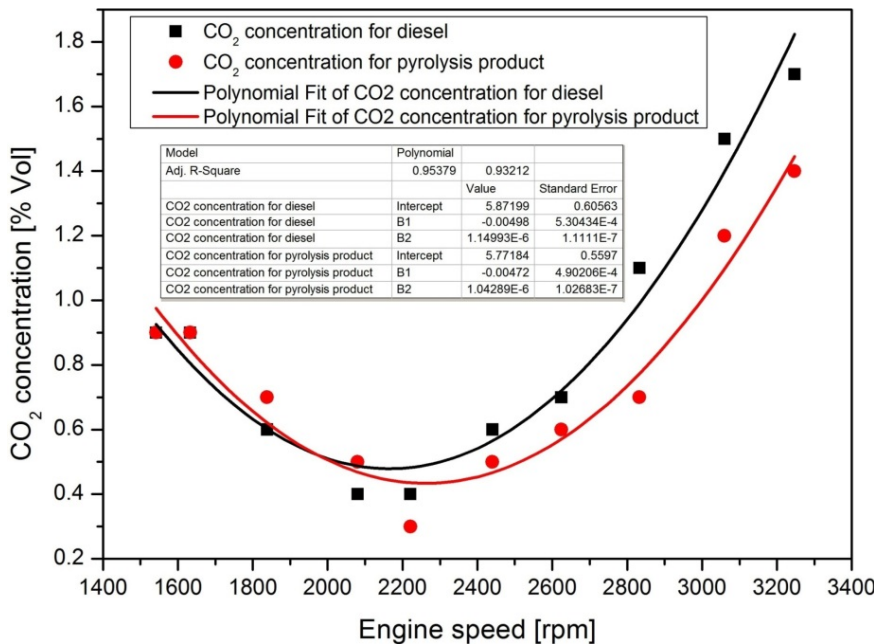


Figure 4. The concentration of CO₂ from the exhausted gas as a function of engine speed

Smoke's opacity emissions

The formation of smoke in the exhaust gases of the engine is related to the incomplete burn of the fuel, when particles of unburned carbon are present into the gases.

The smoke's opacity resulted following the combustion suffered an important decrease when the PE-based fuel was used (figure 5), for all speed rates. The reduction of the smoke concentration can be explained by the composition of the plastic derived oil, that contains only hydrocarbons with C and H, and the combustion took places in better conditions.

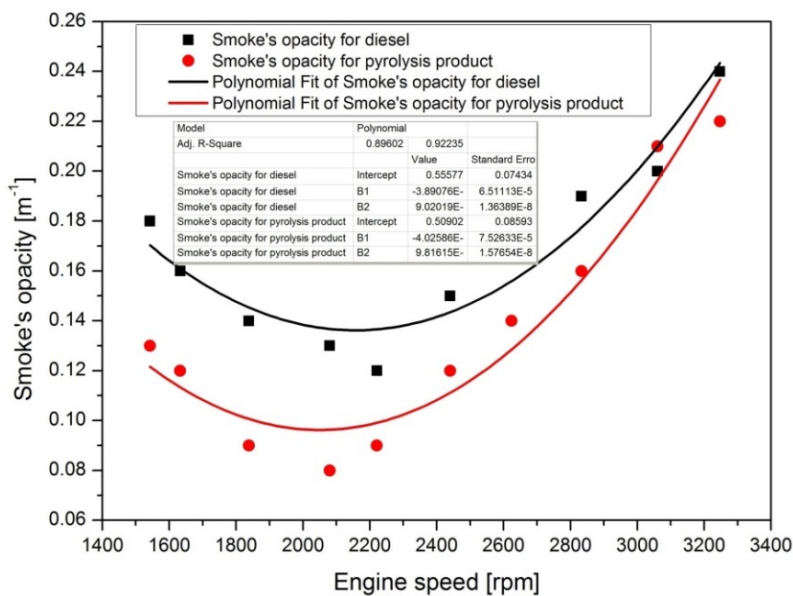


Figure 5. The smoke's opacity from the exhausted gas as a function of engine speed

Unburned hydrocarbons emissions

The pyrolysis product contains a fraction of hydrocarbons (HC) with high molecular weight, higher than the heavy fraction from the commercial fuel.

The existence of the high molecular pyrolysis products conducted to the increased of UBHC concentration in the exhausted gases compared to the concentration resulted when commercial diesel fuel was used (figure 6). Probable, heavy chains of pyrolysis product can not be broken in the engine combustion process.

Nitrogen oxides emissions

The results obtained for nitrogen oxides (NO_x) emissions are presented in figure 7. It can be seen that, when the engine is powered with fuel obtained by pyrolysis, the concentration of NO_x suffered a significant decrease comparing to the concentration resulted by burning the commercial diesel fuel.

One can explain this situation through the composition of pyrolysis product that is formed only by saturated and unsaturated hydrocarbons, without nitrogen products, compounds that can suffer proper combustion reactions inside the internal combustion engine.

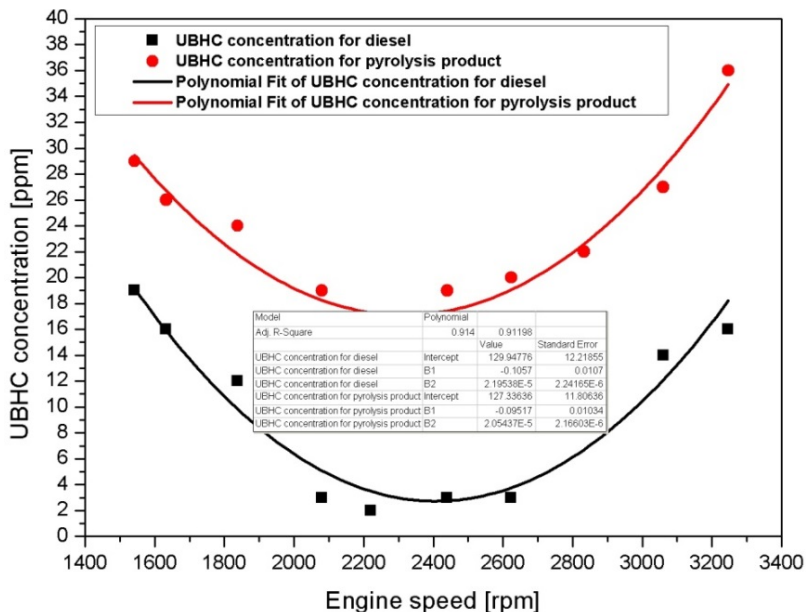


Figure 6. The concentration of HC from the exhausted gas as a function of engine speed

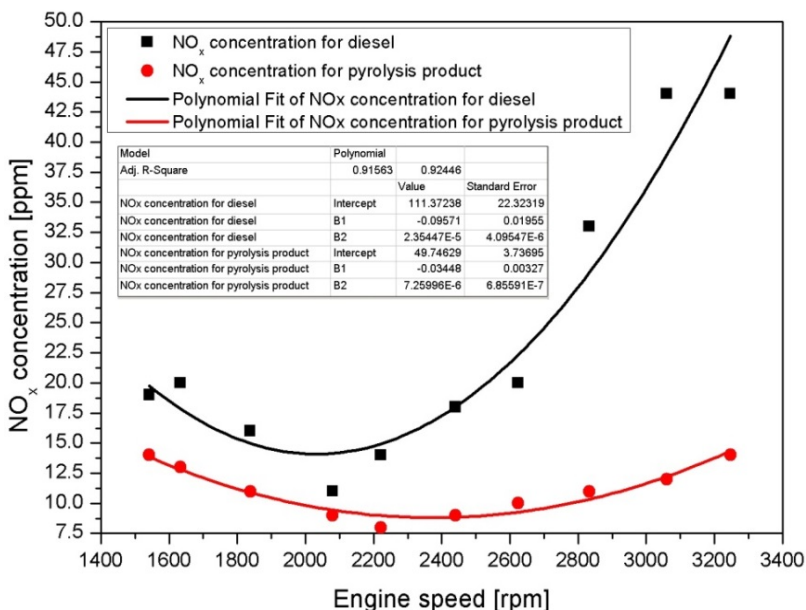


Figure 7. The concentration of NO_x from the exhausted gas as a function of engine speed

CONCLUSIONS

A comparative study regarding the emissions of CO, CO₂, smoke's opacity, hydrocarbons and NO_x in the exhausted gases, when a commercial diesel fuel and an experimental fuel obtained from polyethylene by pyrolysis, was made.

One concluded that pollutant emissions with the exception of hydrocarbons is smaller when the experimental PE-based fuel was used, leading to the conclusion that PE plastic waste can be successfully converted into a fuel with good properties for using as an alternative fuel in diesel engines with no other additives or blending with commercial diesel fuel.

At all engine speeds the hourly fuel consumption achieved from polyethylene-based fuel is significantly lower than of diesel.

For engine speed smaller than 2400 rpm, the concentration of carbon monoxide is almost the same for experimental PE-based and the commercial fuels, respectively. Increasing the speed engine, the concentration of CO resulted when pyrolysis product was used as fuel suffered a slightly reduction comparing with the concentration of CO resulted when commercial diesel fuel was used.

The increasing of engine speed determined the increase of the concentration of CO₂ for both fuels, but the concentration was higher when commercial diesel fuel was used.

The smoke's opacity resulted following the combustion suffered an important decrease when the PE-based fuel was used, for all speed rates.

The high molecular pyrolysis products from PE-based fuel conducted to the increased of the unburned HC concentration in the exhausted gases from the engine.

The concentration of NO_x suffered a significant decrease in the case of pyrolysis product comparing to the concentration resulted from commercial diesel fuel.

Another important advantage of the experimental fuel is the reduced hourly consumption comparing to the consumption of diesel commercial fuel.

Large scale application of chemical recycling of PE for fuel production can be a good alternative for solving the problems related to the impact of plastic waste on environment, leading to fossil fuel saving in conditions of proper engine efficiency, due to the high quality of pyrolysis product regarding combustion behavior.

EXPERIMENTAL SECTION

The obtaining of the fuel

A bench scale installation has been used for the obtaining of fuel starting from PE. Details regarding the pyrolysis process applied for fuel production were presented in our previous studies [17, 24, 25, 27, 28].

IR spectra of polyethylene and pyrolysis product were recorded with a Spectrum BX II FT-IR spectrophotometer provided with an Attenuated Total Reflectance (ATR) accessory.

For fuel testing, a single cylinder diesel engine model Kipor KM 186FAG, has been used. The main specifications and technical data for the diesel engine are presented in table 1. All tests were conducted on the engine running without load.

A gas analyzer AGS 688 Brain Bee was used to determine the concentration of different pollutants gases. For the determination of the opacity from the exhaust gases, a DSS 2 opacimeter from the diagnosis equipment SMP 4000 was used.

Following the experiments the concentration of pollutants from exhausted gasses was determined as a function of the engine speed.

Table 1. Technical specification of the diesel engine used for tests

Item	Technical specifications and data
Model	KM186FA
Type	In line, 4-stroke, single cylinder, air-cooled, direct injection, diesel engine
Cylinder bore x stroke (mm)	86 x 72
Displacement (cc)	418
Rated speed (rpm)	3000
Rated power kW	5.7
Compression ratio	19:1
Starting system	Recoil and electric starter
Rotating direction (viewed from flywheel)	Clockwise

ACKNOWLEDGMENTS

This paper was supported by the Post-Doctoral Programme POSDRU/159/1.5/S/137516, project co-funded from European Social Fund through the Human Resources Sectorial Operational Program 2007-2013.

REFERENCES

- [1]. Defra (Department for Environment, Food and Rural Affairs). "Energy from Waste, a Guide to the Debate." February 2014 (revised edition), Defra, https://www.gov.uk/government/uploads/system/uploads/attachment_data/file/284612/pb14130-energy-waste-201402.pdf (Accessed June 06, 2015).
- [2]. J. Aguado, D. P. Serrano, G. San Miguel, *Global Nest Journal*, **2007**, 9, 12.

- [3]. Association of Plastic Manufacturers in Europe (APME), An analysis of plastics consumption and recovery in Europe, Brussels (Belgium) 2004, Accessed june 06, 2015, <http://www.plasticseurope.org/Document/plastics-in-europe--an-analysis-of-plastics-consumption-and-recovery-in-europe-2002-2003.aspx>
- [4]. Hotărârea nr. 870 din 06/11/2013, Monitorul Oficial, Partea I nr. 750 din 04/12/2013
- [5]. M.A. Uddin, K. Koizumi, K. Murata, Y. Sakata, *Polymer degradation and stability*, **1997**, 56, 37.
- [6]. D.S. Achillas, C. Roupakias, P. Megalokonomos, A.A. Lappas, A.E. Antonakou, *Journal of Hazardous Materials*, **2007**, 149, 536.
- [7]. K. Gobin, G. Manos, *Polymer Degradation and Stability*, **2004**, 83, 267.
- [8]. M. Mani, G. Nagarajan, *Energy*, **1999**, 34, 1617.
- [9]. M. Mani, S. Nagarajan, S. Sampath, *Fuel*, **2010**, 89, 1826.
- [10]. M. Mani, C. Subash, G. Nagarajan, *Applied Thermal Engineering*, **2009**, 29, 2738.
- [11]. M. Mani, G. Nagarajan, S. Sampath, *Energy*, **2011**, 36, 212.
- [12]. Y. Mitsuhasha, V.A. Soloiu, Y. A. Nakanishi, Y. Yoshihara, K. Nishiwaki, M. Hiraoka, *Transactions of the Japan Society of Mechanical Engineers. B*, **2001**, 67, 2618.
- [13]. S. Moriya, H. Watanabe, R. Yaginuma, T. Matsumoto, M. Nakajima, M. Tsukada, N. Isshiki, *Energy Conversion Engineering Conference and Exhibit*, 2000 (IECEC) 35th Intersociety (Vol. 1, pp. 510-515). IEEE.
- [14]. Y. Nakanishi, Y. Yoshihara, M. Hiraoka, K. Nishiwaki, V.A. Soloiu, Y. Mitsuhasha, *Nippon Kikai Gakkai, Jidosha Gijutsukai Nainen Kikan Shinpojumu Koen Ronbunshu*, **2000**, 16, 461.
- [15]. C. Santaweesuk, A. Janyalertadun, *International Journal of Environmental Science and Development*, **2013**, 4, 316.
- [16]. A. Jani, T. Patel, G. Rathod, *IOSR Journal of Mechanical and Civil Engineering*, **2015**, 12, 37.
- [17]. G.L. Popescu, N. Filip, V. Popescu, *SMAT 2014 - SIAR Congress 3rd International Congress Science and Management of Automotive and Transportation Engineering* 23rd - 25th of October, 2014 Craiova, Romania, 271.
- [18]. C.L. Beyler, M.M. Hirschler, "Thermal decomposition of polymers" in SFPE handbook of fire protection engineering", 2002, chapter 7, http://ewp.rpi.edu/hartford/~ernesto/F2012/EP/MaterialsforStudents/Patel/Beyler_Hirschler_SFPE_Handbook_3.pdf (Accessed November 27, 2015).
- [19]. V. Popescu, C. Vasile, M. Brebu, G.L. Popescu, M. Moldovan, C. Prejmerean, C. Trișcă-Rusu, I. Cojocaru, *Journal of Alloys and Compounds*, **2009**, 483, 432.
- [20]. J. Scheirs, W. Kaminsky (Eds.) "Feedstock recycling and pyrolysis of waste plastics. Converting Waste Plastics into Diesel and Other Fuels". John Wiley & Sons, **2006**.
- [21]. I. Çit, A. Sınağ, T. Yumak, S. Uçar, S., Z. Mısırlıoğlu, M. Canel, *Polymer bulletin*, **2010**, 64, 817.
- [22]. P.E. Savage, *Journal of Analytical and Applied Pyrolysis*, **2000**, 54, 109.
- [23]. J. Coates, "Interpretation of infrared spectra, a practical approach." Encyclopedia of Analytical Chemistry. R.A. Meyers (Ed.), John Wiley & Sons, **2006**.
- [24]. G.L. Popescu, N. Filip, V. Popescu, *INMATEH-Agricultural Engineering*, **2015**, 45, 141.

- [25]. G.L. Popescu, N. Filip, V. Popescu, *Aktualni Zadaci Mehanizacije Poljoprivrede*, **2011**, 39, 39.
- [26]. R.C. Flagan, J.H. Seinfeld, "Fundamentals of air pollution engineering", Prentice-Hall, Inc. A Division of Simon&Schuster Englewood Cliffs, New Jersey 07632, **1988**, chapter 3 and 4.
- [27]. G.L. Popescu, *Acta Technica Napocensis-Series: Applied Mathematics, Mechanics, and Engineering*, **2012**, 55, 897.
- [28]. G.L. Popescu, *INMATEH-Agricultural Engineering*, **2012**, 37, 79.

CRYSTAL VIOLET DYE BIOSORPTION AND PHYTOEXTRACTION USING LIVING *SALVINIA NATANS* AND *SALVINIA NATANS* POWDER: A COMPARATIVE STUDY

CARMEN MÂNZATU^a, BOLDIZSÁR NAGY^a, ANAMARIA TÖRÖK^a,
LUMINIȚA SILAGHI-DUMITRESCU^a and MAJDIK CORNELIA^{a*}

ABSTRACT. The main focus of this work was to investigate the biosorption behavior of living and powder *Salvinia natans* on Crystal violet (CV) removal. The effects of process parameters were studied in order to determine the optimum phytoremediation conditions. Adsorption isotherm and kinetic models for both processes were used to analyze the equilibrium data. It was found that Langmuir isotherm and pseudo-second-order kinetics models describe better the CV removal process. Thermodynamic parameters showed that the biosorption and phytoextraction process is endothermic. From the obtained results it can be concluded that *S. natans* powder showed higher bisorption capacity on CV removal compared to the living one.

Key words: *Salvinia natans*, *Crystal violet*, *biosorption*, *phytoextraction*, *surface characteristic*

INTRODUCTION

Wastewater discharge containing hazardous dyes poses an important and increasing environmental danger [1]. Dyes remains one of the major constituents of the wastewater produced by many industries, such as textile, paint, varnishes, ink, plastics, pulp and paper, cosmetics, tannery and the dye-producing ones [2, 3, 4]. The discharge of extremely small amounts of dyes even at minimum concentrations can be toxic and difficult to degrade and remove due to their complex stable structure [5, 6, 7]. Among various dyes, Crystal violet (CV), also known as Basic Violet 3, belongs to the triphenylmethane dyes class. It is a cationic dye used for various purposes among which include: biological stain, dermatological agent, veterinary medicine, poultry feed additive to

^a Babeș-Bolyai University, Faculty of Chemistry and Chemical Engineering, 11 Arany János str., RO-400028, Cluj Napoca, Romania

* Corresponding author: majdik@chem.ubbcluj.ro

inhibit propagation of mould, intestinal parasites and fungus etc. The presence of CV in the aqueous water system is considered risky to human health [8]. Because it is carcinogenic and non-biodegradable it can persist in a variety of environments. Therefore, CV it has been classified as a recalcitrant molecule since it is poorly metabolized by microbes [7, 9, 10].

Most of the technologies employed for dyes removal from wastewaters are based on physicochemical processes such as dilution, adsorption, coagulation and flocculation, chemical precipitation, oxidation, ion-exchange, reverse osmosis and ultra-filtration [11].

Bioremediation receives a considerable amount of attention as an alternative process to traditional methods in dyes and heavy metal removal from contaminated waters [12]. Bioremediation is a natural process which relies on bacteria, fungi and plants to alter contaminants, as these organisms carry out their normal life functions [13].

Therefore, many researchers use agricultural by-products such as olive tree pruning waste [14], sawdust [15], fir cone [16], olive-stone, olive mill solid, cocoa shells [17], grape stalks [18], in the removal of textile dye effluents [19].

Phytoremediation represents the use of green plants to remove or degrade contamination from soils and surface waters. It has been proposed as a cheap, sustainable, effective, and environment-friendly alternative to conventional remediation technologies. Plants use solar energy (through photosynthesis) to extract chemicals from the soil and to deposit them in the above-ground part of their bodies or to convert them to a less toxic form [20, 21]. Aquatic plant biomass, irrespective whether living or dead represents an abundant, cost-effective biological resource that possesses an immense capacity to accumulate organic dyes [22, 23] and hence is exploited worldwide for developing environment-friendly wastewater treatment technologies. Phytoremediation is often referred as botanical bioremediation or green remediation [24] and defined as the use of green plants to remove pollutants from the environment or to render them harmless. It is considered a new highly-promising technology for the remediation of polluted sites [25] and is currently divided into areas, being one of as phytoextraction.

Plant assays are highly sensitive to many environmental pollutants, including dyes [26] but few cases have been reported in which it is proven that plants have the potential capacity to degrade textile dyes [27]. The potential of some aquatic plants to accumulate dyes has been well demonstrated, supporting their possible use in the phytoextraction of contaminated water. These include: *Nymphaea violacea* [28], *Eleocharis dulcis* [29], *Ceratophyllum demersum* [30], *Myriophyllum spicatum* [31], *Lemna gibba* [32] and *Lemna minor* [33].

Salvinia natans is an ideal testing system that can be used in the water quality studies to monitor aquatic pollutants [34]. Besides the aquatic floating macrophytes, *S. natans* floating fern is a fast growing free-floating aquatic

weed and was found to be particularly efficient in metal and pesticide removal from wastewaters [35]. Nevertheless, the use of powders obtained from plants, such as *S. natans* for organic dyes removal could be more advantageous than the use of living plants.

The aim of the present study was to compare the removal capacity and efficiency of Crystal violet dye using the aquatic plant *S. natans*, in both living and powder form. This research focuses on the removal of CV, from a comparative perspective, as well on the characterization of the plant's systems for the biosorption and accumulation capacities and morphological changes for the two processes.

RESULTS AND DISCUSSION

SEM analysis

The SEM micrograph of the adsorbent (after the phytoremediation experiments), *S. natans* and dye loaded adsorbent is presented in Fig. 1a, b. The analysis of the images showed the heterogeneous surface within *S. natans* powder particle where adsorption could occur. The micrographs show that the dye had densely and homogeneous adheres to the surface of carrier, as a result of either natural entrapment into the pores [36], due to physical adsorption by electrostatic force or due to covalent binding between the dye molecules and adsorbent.

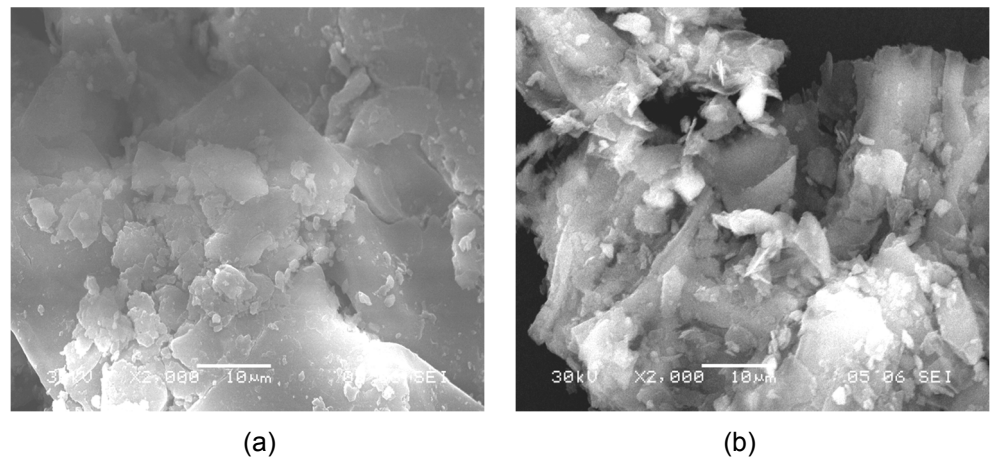


Fig. 1. SEM micrographs of *S. natans*
a) control plant and b) after the phytoremediation process.

Effects of the initial CV concentration

The biosorption of CV was carried out at different initial dye concentrations ranging from 20 to 90 mg/L contacting 0.4 g *S. natans* powder obtained from 5 g fresh biomass, pH initial = 5.4, 150 rpm stirring rate at room temperature 23°C, with 240 min of contact time (until equilibrium was reached). Experiments with living biomass were carried out at the same initial dye concentrations ranging from 20 to 90 mg/L containing 5g fresh biomass, at room temperature 23°C, pH_{initial} = 5.4 and 200 mL synthetic dye solution.

The results are presented in (Fig. 2). In both cases, the biosorption capacity augments with the increasing of the initial concentration. The increase in biosorption capacity occurs due to the higher adsorption rate and the utilization of all the available active sites for biosorption at higher CV concentration.

According to the obtained results, it was concluded that the aquatic plants' highest removal efficiency was attained at the smallest initial concentration and that the removal capacity of aquatic plants depended strongly on the initial dye concentrations. Also the plant phytoextraction capacity is influenced by the plant's surface active sites and by the plant's uptake abilities and saturation.

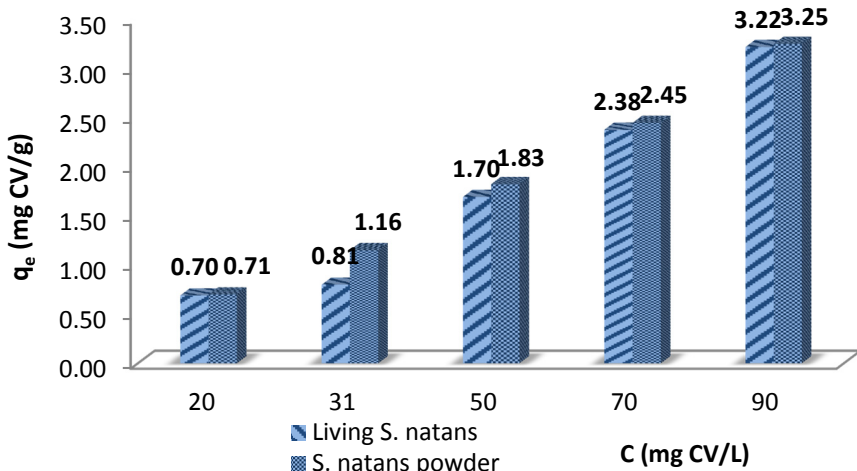


Fig. 2. Influence of the initial dye concentration over the biosorption capacity for CV phytoextraction and biosorption; $C_i = 20\text{-}90 \text{ mg/L}$, 0.4 g biomass, 23°C, pH 5.4, 150 rpm (biosorption).

The effect of pH

The pH has been identified as one of the most important parameter, that effect on dye biosorption. The pH of the aqueous medium is an important factor, which affects directly the living system's biological and

biochemical functions and it is directly related to the competition between protons and dye ions to active sites on the biosorbent surface. The effect of the solution pH onto CV biosorption and phytoextraction was studied within the range of pH 3.0 - 10. The highest removal efficiency for both processes was determined at the initial pH value of 5.4 and can be observed in (Fig. 3). At lower pH, the H⁺ ions compete effectively with dye cations, showing a decrease in the dye removal efficiency. At higher pH, the plants surface becomes negatively charged, and this can intensify electrostatic force of attraction of the CV cations, increasing the phytoremediation efficiency.

The aquatic plants can tolerate a wide range of initial pH from acidic to alkaline. Their dye removal efficiency was notable in various cases and the hydrophytes possess characteristic properties to equilibrate the pH, which may present the plants responses to the induced water stress. These results can be explained by the plants metabolic reactions involving consumption, production or transfer of protons during the processes [37].

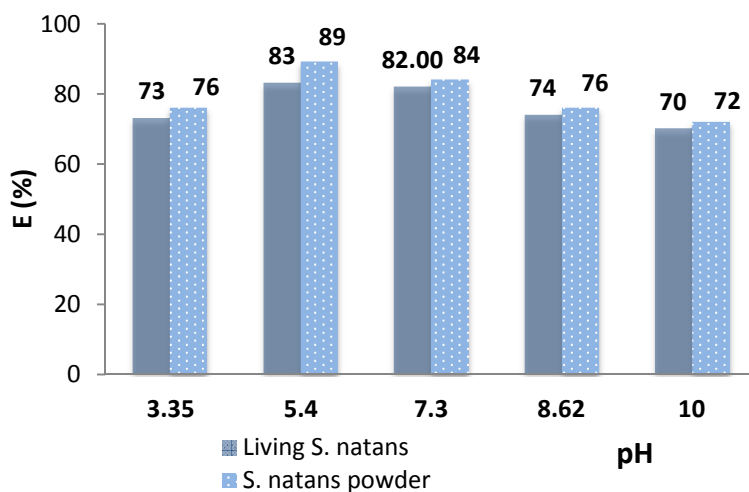


Fig. 3. The effect of initial pH values on the removal efficiency for CV phytoextraction and biosorption; $C_i = 50 \text{ mg/L}$, 0.4 g biomass, 23°C, 150 rpm (biosorption).

The effect of temperature

During the biosorption processes, temperature has a major effect on the plants' biochemical processes affecting the enzyme activity, the translocation of nutrients and photosynthesis [38]. The effect of temperature on the phytoremediation (for phytoextraction and biosorption, respectively) efficiency of CV dye was tested at the range of 10 - 35°C. Results showed that the removal efficiency of dye CV increases with an increase in temperature from 10 to 35°C

(Fig. 4), for both processes. The observed increase in biosorption of CV with rise in temperature is indicative of the fact that the biosorption process is endothermic in nature. The increase in the temperature of the system affects the solubility and particularly the chemical potential of the dye, which is known to be a controlling factor in the process of adsorption. A temperature increase minimizes the solubility of dye, hence adsorption accentuates. An increasing number of molecules may acquire sufficient energy to undergo an interaction with the active site at the surface [37].

The results indicated that the two types of phytoremediation processes have the ability to remove CV dye from the aqueous solutions.

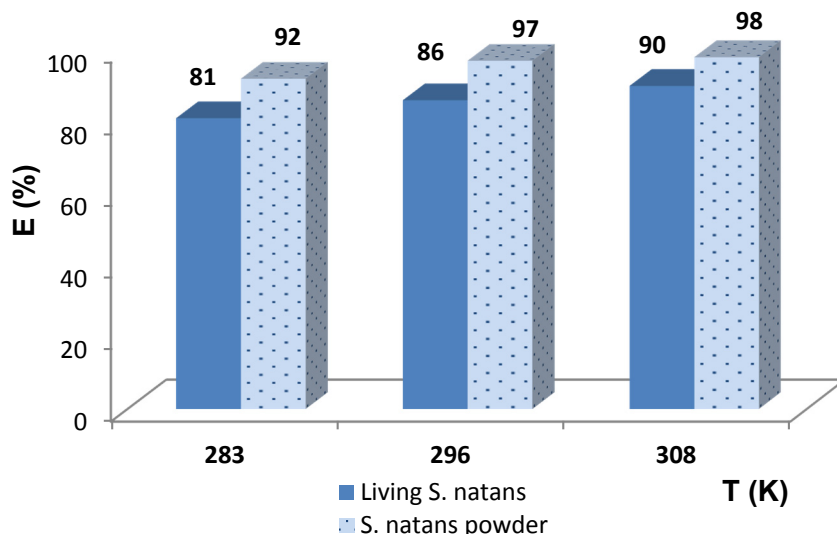


Fig. 4. Temperature influence over the removal efficiency of CV on living *S. natans* and *S. natans* powder; $C_i = 50 \text{ mg/L}$, 0.4 g biomass, pH 5.4, 150 rpm (biosorption).

Biosorption and phytoextraction kinetics

The prediction of the biosorption rates gives important information for designing batch biosorption systems. Lagergren's pseudo-first-order and Ho's pseudo-second-order model, were applied on the experimental data to clarify the biosorption and phytoextraction kinetics of CV onto *S. natans* biomass [39,40]. The linear form of the pseudo-first-order (1) and pseudo-second-order (2) rate equation is given as:

$$\ln(q_e - q_t) = \ln q_e - k_1 t \quad (1)$$

and

$$\frac{dq_t}{dt} = k_2 (q_e - q_t)^2 \quad (2)$$

where q_t and q_e (mg/g) are the amounts of the adsorbed dye ions at equilibrium time (mg/g) and t (min), respectively and k_1 and k_2 is the rate constant (min^{-1}).

The R^2 and $q_{e,\text{exp}}$ values presented in (Table 1) indicated that the biosorption mechanisms and the phytoextraction process of CV onto *S. natans* biomass does not follow the pseudo-first-order kinetic model. It can be also seen that the experimental biosorption capacities are not in good agreement with the calculated ones. Therefore, the pseudo-first-order model is not suitable for modelling the CV biosorption and phytoextraction processes onto *S. natans*.

The rate constant for the pseudo-second-order model (k_2), R^2 and q_e values are given in (Table 2). The R^2 values are found very high (in range of 0.992-0.999 for CV biosorption and 0.9838-0.992 for phytoextraction, respectively). In addition, the theoretical $q_{e,\text{cal}}$ values were closer to the experimental $q_{e,\text{exp}}$ values. In view of these results, it can be said that the pseudo-second-order kinetic model provided a good correlation for the biosorption and phytoextraction of CV onto *S. natans* in contrast to the pseudo-first-order model [41].

Table 1. Pseudo-first-order and pseudo-second-order rate constants, calculated and experimental q_e values for CV removal using living *S. natans* and *S. natans* powder at different initial concentrations; $C_i = 20\text{-}90 \text{ mg/L}$, 0.4 g (biosorption)/5 g (phytoextraction) biomass, 23°C, pH 5.4

C (mg/L)	q_e (exp) (mg/g)	Pseudo-first-order			Pseudo-second-order		
		k_1 (1/min)	q_e (calc) (mg/g)	R^2	k_2 (g/mg·min)	q_e (calc) (mg/g)	R^2
Living <i>Salvinia natans</i>							
20	0.70	5.96×10^{-2}	0.65	0.986	1.06×10^{-2}	0.81	0.994
31	0.81	2.25×10^{-2}	0.54	0.886	8.88×10^{-2}	1.87	0.972
50	1.70	5.76×10^{-2}	1.14	0.859	1.18×10^{-2}	1.81	0.983
70	2.39	6.22×10^{-2}	2.18	0.931	2.57×10^{-2}	2.82	0.985
90	3.22	6.96×10^{-2}	3.32	0.978	2.60×10^{-2}	3.69	0.991
<i>Salvinia natans</i> powder							
20	0.71	1.02×10^{-3}	0.87	0.905	4.29×10^{-2}	0.71	0.990
31	1.16	0.06×10^{-3}	0.42	0.609	1.03×10^{-2}	1.09	0.988
50	1.83	1.29×10^{-2}	0.68	0.853	0.07×10^{-3}	1.83	0.997
70	2.45	1.70×10^{-2}	1.39	0.910	0.02×10^{-3}	2.59	0.999
90	3.25	1.38×10^{-2}	2.90	0.943	0.06×10^{-4}	3.74	0.983

Biosorption and phytoextraction isotherm models

Equilibrium adsorption isotherms have fundamental importance for the adsorption process design since they indicate how dyes are partitioned between the adsorbent surface and liquid phases at equilibrium as a function of

the dye concentration [42]. In this study, the biosorption and the phytoextraction experimental data were investigated using four equilibrium models, namely the Langmuir, Freundlich Temkin and Dubinin–Radushkevich (D–R) [43–46].

The Langmuir model assumes that a monomolecular layer is formed when biosorption and phytoextraction takes place without any interaction between the adsorbed molecules.

The Langmuir isotherm linear equation is expressed as follows:

$$\frac{1}{q_e} = \frac{1}{q_m b} \times \frac{1}{C_e} + \frac{1}{q_m} \quad (3)$$

where q_e is the solid-phase adsorbate concentration at equilibrium (mg/g), q_{max} is the maximum adsorption capacity corresponding to the monolayer adsorption capacity (mg/g), C_e is the concentration of CV solution at equilibrium (mg/L), and b is the adsorption equilibrium constant that is related to the apparent energy of adsorption.

Freundlich isotherm is an empirical equation based on a heterogeneous adsorption due to the diversity of adsorption sites or diverse nature of the adsorbed metal ions and dyes, free or hydrolysed species. The Freundlich isotherm linear equation is expressed as:

$$\log q_e = \log K_F + \frac{1}{n} \times \log C_e \quad (4)$$

where k is related to adsorption capacity and n is related to intensity of adsorption. The $\ln q_e$ versus $\ln C_e$ plot allows the determination of the Freundlich constants.

The monolayer saturation capacity of CV q_m was calculated to be 12.74 mg/g, while the Langmuir constant, which is related to adsorption energy, was determined to be 0.226 mg/L. Freundlich isotherm constants were also calculated (Table 2). The linearity of the two plots, expressed by R^2 , can give information about the fitting between the experimental data and the isotherm model. The one closest to linearity could be considered as describing better the adsorption equilibrium in a certain system.

When comparing the determination coefficient for these two models it can be concluded that the experimental data were most decided by Langmuir model $R^2 = 0.972$ for biosorption and $R^2 = 0.958$ for phytoextraction.

The Dubinin–Radushkevich isotherm model was also applied to the equilibrium data, in order to determine the nature of the biosorption processes as physical or chemical. The D–R sorption isotherm is more general than the Langmuir isotherm as its derivation is not based on ideal assumptions such as equipotent of the sorption sites, absence of stoic hindrance between sorbed and incoming particles and surface homogeneity on microscopic level.

$$\ln q_e = \ln q_m - \beta \varepsilon^2 \quad (5)$$

where, q_e is the mole amount of metal ions adsorbed on per unit weight of biomass (mol/g), q_m is the maximum biosorption capacity (mol/g), β is the activity coefficient related to biosorption mean free energy (mol²/J²) and ε is the Polanyi potential, where, R is the universal gas constant (8.314 J/mol K) and T is the absolute temperature (K).

Free energy E per molecule, of adsorbate, which helps to distinguish between the physical and chemical adsorption of metal ions is given below:

$$E = \frac{1}{\sqrt{-2\beta}} \quad (6)$$

The isotherm constants q_m and β were obtained from the intercept and the slope of the plot $\ln q_e$ vs. ε^2 . If E values are between 8 and 16 kJ mol⁻¹, the biosorption process is chemical and if $E < 8$ mol⁻¹ the biosorption process is physical [47]. The Dubinin-Radushkevich isotherm expresses the adsorption mechanism with a Gaussian energy distribution onto a heterogeneous surface. The Dubinin-Radushkevich isotherm parameters are shown in the (Table 2). In our case, the value of the mean free energy for both processes was 5 mol⁻¹ indicating a physisorption process.

Temkin isotherm equation contains a factor that takes into account the adsorbent-adsorbate interactions. It is based on the fact that the heat of adsorption of all the molecules in the layer decreases linearly with the coverage of molecules due to the adsorbate-adsorbent repulsions and the adsorption of cadmium ions uniformly realised on the surface. In addition, it also assumes that the fall in the heat of adsorption is linear rather than logarithmic, as implied in the Freundlich isotherm. The equation of this model is given below:

$$Q_e = B \ln \times A_T + B \ln \times C_e \quad (7)$$

$$B = \frac{RT}{bT} \quad (8)$$

where A_T is the Temkin isotherm equilibrium constant (g/L), b_T is Temkin isotherm constant and B is a constant related to the heat of adsorption (J/mol). From the q_e vs. $\ln C_e$ plot, A_T and B constants were determined. Taking into consideration the calculated value of the constant related to heat of sorption, which has a value smaller than 20 kJ mol⁻¹, we concluded that according to this isotherm, the sorption process takes place as physisorption (Table 2).

Table 2. Langmuir, Freundlich, Dubinin-Radushkevich and Temkin calculated coefficients using linear regression analysis for CV removal using living *S. natans* and *S. natans* powder; $C_i = 20\text{-}90 \text{ mg/L}$, 0.4 g (biosorption)/ 5 g (phytoextraction) biomass, 296 K , 23°C , pH 5.4

	Langmuir			Freundlich			Dubinin-Radushkevich			Temkin		
	K_L (L/mg)	q_{max} (mg/g)	R^2	n	K_f (mg ^(1/n) L ^{1/n} /g)	R^2	β (mol ² /kJ ²)	E (kJ/mol)	R^2	A_T (L/g)	B (J/mol)	R^2
Living <i>S. natans</i>	0.417	2.07	0.958	1.15	3.04	0.930	2×10^{-6}	5	0.914	2.50	3×10^{-6}	0.886
S. natans powder	0.226	12.74	0.972	1.03	3.13	0.967	2×10^{-6}	5	0.870	2.50	4×10^{-6}	0.862

The biosorption and phytoextraction thermodynamics

The thermodynamic parameters, the change in free energy change (ΔG°), enthalpy (ΔH°) and entropy (ΔS°) of the biosorption process –were evaluated for the biosorption of CV onto *S. natans* powder at different temperatures $10\text{--}35^\circ\text{C}$.

Thermodynamic parameters were calculated using the following equations [48]:

$$\ln K_d = \frac{\Delta H^\circ}{RT} + \frac{\Delta S^\circ}{R} \quad (9)$$

$$\Delta G^\circ = RT \ln K_d \quad (10)$$

where ΔH° , ΔS° , ΔG° , and T are the enthalpy, entropy, Gibbs free energy, and absolute temperature and R the universal gas constant. The ΔH° and ΔS° parameters were found from the slope and intercept of the plots of $\ln K_D$ against $1/T$. Experimental results were used to calculate the thermodynamic parameters which are presented in (Table 3).

The negative values of ΔG° indicated the feasibility and spontaneity of CV biosorption and phytoextraction using *S. natans*. The decrease in ΔG° values shows a decline in the feasibility of biosorption as temperature is increased. The negative ΔS° value means a decrease in the randomness at the solid/solution interface during the biosorption process. The positive value of ΔH° indicated the endothermic nature of the biosorption of CV onto *S. natans* [49]. The endothermic process shows that the diffusion from bulk solution to adsorbent surface may require energy to overcome interaction of dissolved ions with solvation molecules [15].

Table 3. Termodynamic parameters for the removal of CV dye on living *S. natans* and *S. natans* powder at various temperatures; $C_i = 50 \text{ mg/L}$, 0.4 g (biosorption)/ 5 g (phytoextraction) biomass, pH 5.4

	ΔS°	ΔH°	$\Delta G^\circ, (\text{kJ/mol})$		
	(kJ/K·mol)	(kJ/mol)	283 K	296 K	308 K
Living <i>S. natans</i>	-0.12×10^{-2}	0.012	-3.29	-3.45	-3.58
<i>S. natans</i> powder	-0.09×10^{-2}	0.010	-2.81	-2.94	-3.06

CONCLUSIONS

In this study, the use of *S. natans*, in both living and powder form, was tested for the removal of CV from aqueous solutions. The removal capacity depends on the initial dye concentration, biomass quantity, initial pH and temperature. Findings suggest similarities between the two processes for *S. natans*, in both living and powder form. Our results demonstrate that for both processes the sorption on the plant surface is determinant. Equilibrium models (Langmuir and Freundlich isotherm), kinetics (pseudo-first- and pseudo-second-order) and thermodynamics of the considered biosorption process were discussed in detail. According to the Dubinin-Radushkevich and Temkin, the adsorption of CV on living *S. natans* and *S. natans* powder was physical in nature. Equilibrium was best described by the Langmuir isotherm, while the kinetic of the process was best described by the pseudo-second-order model for both. Thermodynamic parameters showed that the CV biosorption and phytoextraction processes on *S. natans* are endothermic.

Using the plant in powder form had some advantages. One of them was that no large quantity solutions were required. The other one would be related to the fact that no living plants were necessary.

EXPERIMENTAL SECTION

Living Salvinia natans

S. natans L. (family of *Salviniaeae*) a free-floating aquatic fern, was the plant chosen for the phytoextraction process. *S. natans* was growth in a hydroponic greenhouse system (at University of Agricultural Sciences and Veterinary Medicine in Cluj-Napoca, Romania), with an addition of fertilizer (Complex 3, 0.5 %). The plants that aged 30 days were selected for the phytoremediation experiments.

***Salvinia natans* powder**

Prior to its utilization, *S. natans* was washed several times with deionized water and dried at 80°C for 48 hours. The dried samples were grinded and sieved, 200 and 400 µm mesh size were further used in all experiments. The biomass was washed again with 0.01 M HCl to remove any soluble biomolecules that might have caused interference, and then cleaned with sterile distilled water. The samples were filtered and dried at 80°C for 48 h.

Chemicals

The CV was used as pollutant in the phytoremediation experiments. The cationic CV dye (Tris (4-(dimethylamino) phenyl) methylum chloride, chemical formula = $C_{25}N_3H_{30}Cl$, molecular weight = 407.9788 g/mol. Wavelength maximum (λ_{max} = 590 nm). All chemicals and reagents used in the study were of analytical grade (purity \geq 99 %) and supplied by Merck (Germany).

Phytoextraction experiments with living *Salvinia natans*

The phytoremediation experiments were carried out in controlled conditions (at room temperature 21-23°C, illuminated with a lamp with the 14/10 h light/dark photoperiod), in 250 mL glass beakers containing 200 mL synthetic wastewater and 5 g fresh aquatic plants along with the macro- and micronutrients [50]. Before experiments, the plants were kept in laboratory conditions for an acclimatization period of 4 days in a modified Hoagland nutrient solution with the following chemical composition: 1 mM KNO_3 ; 1 mM $Ca(NO_3)_2 \cdot 4H_2O$; 1 mM $NH_4H_2PO_4$; 1 mM $MgSO_4 \times 7H_2O$; 25 mM KCl ; 12.5 mM H_3BO_3 ; 1 mM $MnSO_4 \times H_2O$; 1 mM $ZnSO_4 \times 7H_2O$; 0.25 mM $CuSO_4 \times 5H_2O$; 0.25 mM H_2MoO_4 (85% MoO_3) with Fe(III) citrate.

Biosorption experiments with *Salvinia natans* powder

The biosorption experiments were performed in batch condition, contacting 0.4 g powder obtained from 5 g fresh plant with 200 mL of CV at different initial concentrations (20 - 90 mg/L), under stirring (150 rpm), at room temperature $23^\circ C \pm 2^\circ C$ (296 ± 2 K). In order to establish the evolution of the removal process, samples of 500 µL were collected at different time intervals up to 240 min. The collected samples at predetermined time intervals were centrifuged (10 min) and the dye concentration in the aqueous phase was determined on a daily basis. The concentrations were determined using the double beam UV-visible spectrophotometer (GBC Cintra 202, Australia).

Characterizations of the process

For both processes, phytoextraction and biosorption, the same parameters and conditions were studied: a) effect of plant quantity: $m_{plant} = 1-5$ g b) effect of initial concentration of CV: $C_i = 20 - 90$ mg/L, c) effect of initial pH = 3.0-10; d) effect of temperature: $t_1 = 10^\circ C$, $t_2 = 23^\circ C$, $t_3 = 35^\circ C$ (283-308 K).

The pH of the solution was initially adjusted by adding a small amount of 0.1 M HCl or 0.1 M NaOH solutions and then measured using a pH meter.

In order to evaluate the amount of CV retained per unit mass of biomass, the biosorption and phytoextraction capacity were calculated using the following equations [51]:

$$E, (\%) = \frac{C_i - C_f}{C_i} \times 100 \quad (11)$$

$$q_{\max} (\text{mg/g}) = \frac{(C_i - C_f)V}{m} \quad (12)$$

where E, (%) represents the removal efficiency, C_i and C_f the initial and final concentrations of CV (mg/L) in the aqueous solution, q_{\max} (mg/g) represents the amount of CV retained onto unit weight of plant, V (L) means the volume of dye aqueous solution and m (g) the plant quantity. The experiments were conducted simultaneously both for living and powder-form plant, following the same parameters.

Scanning electron microscopy (SEM)

Scanning electron microscopy was utilized for characterizing surface microstructures, and fundamental physical properties of different adsorbents. The surface morphology of *S. natans* was determined using a scanning electron microscope JEOL JSM 5510 LV (Japan).

ACKNOWLEDGEMENTS

This work was possible due to the financial support of the Sectorial Operational Program for Human Resources Development 2007-2013, co-financed by the European Social Fund, under the project number POSDRU/159/1.5/S/132400 with the title „Young successful researchers – professional development in an international and interdisciplinary environment”.

REFERENCES

1. H.A. Mekkawy, M.O. Ali, and A.M. El-Zawahry, *Toxicol Lett*, **1998**, 95, 155–161.
2. E.A. Clarke and R. Anliker, Organic dyes and pigments, New York, **2005**, p 181–215.
3. G. Mishra and M.A. Tripathy, *Colourage*, **1993**, 40, 35–38.
4. A.O. Akeem, and G. Mustafa, *Toxicol Environ Chem*, **2014**, 96, 837-848.
5. N.M Mahmoodi, *J. Chem. Eng. Data*, **2011**, 56, 2802–2811.
- A. Arunagiri, P. Prabisha, and R. Kalaichelvi, *J Thermodynam Article ID*, **2014**, 670186.

6. J. Mittal, A. Malviya, A.D. Kaur, and V.K.Gupta, *J Colloid Interface Sci*, **2010**, 343, 463–473.
7. C. Chen, J.T. Kuo, H.A. Yang, and Y.C. Chung, *Chemosphere*, **2013**, 92, 695–701.
8. R. Ahmad, *J Hazard Mater*, **2009**, 171, 767–773.
9. S. Khan, A. Arunarani, and P. Chandran, *Clean – Soil Air Water*, **2015**, 43, 67–72.
10. I.M. Banat, P. Nigam, D. Singh, and R. Marchant, *Bioresour Techno*, **1996**, 58, 217–227.
11. S. Ahluwalia and D. Goyal, *Bioresour Technol*, **2007**, 98, 2243–2257.
12. D. Sud, G. Mahajan, and M.P. Kaur, *Bioresour Technol*, **2008**, 99, 6017–6027.
13. G. Blazques, L. Martin, T. Guadalupe and M. Calero, *Chem Eng J*, **2011**, 170–177.
14. B. Nagy, A. Maicaneanu, C. Indolean, S. Burca, L. Silaghi-Dumitrescu, and C. Majdik, *Acta Chim Slov*, **2013**, 60, 263–273.
15. M. Momcilovic, M. Purenovic, A. Bojic, A. Zarubica, and M. Randelovic, *Desalination*, **2011**, 276, 53–59.
16. N. Meunier, J. Laroulandie, J.F. Blais, and R.D. Tyagi *Bioresour Technol*, **2003**, 90, 255–263.
17. B.H. Hameed, and M.I. El-Khaiary *J Hazard Mater*, **2008**, 162, 305–311.
18. E.G. Mueller, *Mol Biology*, **1996**, 7, 1805–1813
- I. Raskin, and D. Ensley, New York, “Phytoremediation of toxic metals”, **2000** p.12-33.
19. P.L. Gratão, M.N.V. Prasad, P.F. Cardoso, P.J. Lea, and R.A. Azevedo, *J Plant Physiol*, **2005**, 175, 53–64.
- A. Marques, O. Anto’Nio, S. Rangel, and M.L. Paula, *Environ Sci Techno.I*, **2009**, 39, 622–654.
20. R.A. Usman, R. Alkredaa, and M.I. Al-Wabel, *Ecotox Environ Safe*. **2014**, 97, 263–270.
21. R.L. Chaney, K.M. Malik, Y.M. Li, S.L. Brown, E.P. Brewer, and J.S. Angle *Curr Opin Biotechnol*, **1997**, 8, 279–284.
22. D.E. Salt and U. Kramer, Phytoremediation of Toxic Metals, Berlin, **1999** p. 231–246.
23. W.C. Wang and Km. Freemark, *Ecotox Environ Saf*, **1995**, 30, 289–301.
24. S. Aubert and J.P. Schwitzguebel *Wat Res*, **2004**, 381, 3569–3575.
25. H.B.L. Pettersson, H.A. Johnston, and A.S. Murray, *J Environ Radioac*, **1993**, 19, 85–108.
26. R.A. Overall and D.L. Parry, *Environ Pollut*, **2004**, 132, 307–320.
27. U.N. Rai, S. Sinha, R.D. Tripathi, and P. Chandra, *Ecol Eng*, **1995**, 5, 5–12.
28. O. Keskinan, *Asian J Chem*, **2005**, 17, 1507–1515.
29. M. Mkandawire and E.G. Dudel, *Sci Total Environ*, **2005**, 336, 81–90.
- A. Török, E. Buta, L. Silaghi-Dumitrescu, C. Indolean, C. Majdik, and S. Tonk, *Acta Chim Slov*, **2015**, 62, 452–461.
30. S. Radic, D. Stipanicev, P. Cvjetko, R.M. Marijanovic’, S. Sirac, B. Pevalek, and M. Pavlica, *Ecotox Environ Saf*, **2011**, 74, 182–187.
31. G. Sánchez-Galván, O. Monroy, G. Gómez, and E.J. Olguín, *Water Air and Soil Pollu*, **2008**, 194, 77–90.
32. G. Annadurai, L.Y. Ling, and J.F. Lee, *J Hazard Mater*, **2008**, 152, 337–346.
33. D. Zhao, K.R. Reddy, V.G. Kakani, and V.R. Reddy, *Eur J Agron*, **2005**, 22, 391–403.

34. R. Bligny, E. Gout, W. Kaiser, U. Heber, and D. Walker, R. Douce, *Biochim Biophys Acta (BBA) – Bioenergetics*, **1997**, *1320*, 142-152.
35. B. Nagy, C. Mânzatu, A. Török, C. Indolean, A. Măicăneanu, S. Tonk, and C. Majdik, *Rev Roum Chim*, **2015**, *60*, 257-264.
36. Y.S. Ho and G. McKay, *Process Biochem*, **1999**, *34*, 451–465.
37. Ho YS, McKay G, and Wase DAJ, *Ads Sci Technol*, **2000**, *18*, 639–650.
38. M.E. Argun, S.C. Dursun, and M. Ozdemir Karata, *J Hazard Mater*, **2007**, *141*, 77-85.
- I. Langmuir, *J Am Chem Soc*, **1918**, *40*, pp 1361-1367.
39. H.M.F. Freundlich, Über die Adsorption in Lösungen, **1906**, pp 385-470.
40. M.J. Temkin and V. Pyzhev, *Acta Physiochim*, **1940**, *12*, 217-222.
41. M.M. Dubinin, E.D. Zaverina, and L.V. Radushkevich, *Zhurnal Fizicheskoi Khimii*, **1947**, *21*, 1351–1362.
42. E. Gilca, A. Maicaneanu, P. Ilea, *Cent. Eur J. Chem*, **2014**, *12*, 821-828.
43. A.U. Itodo, and H.U. Itodo, *J Life Sci*, **2010**, *7*, 31–39.
44. L.K. Fraji, D.M. Hayer, and T.C. Werner, *J Chem Educ*, **1992**, *69*, 424–427.
45. E. Eren, O. Cubuk, H. Ciftci, B. Eren, and B. Caglar, *Desalination*, **2010**, *252*, 88-96.
46. L. Taiz and E. Zeiger, *Plant Physiology*, **2002**, *35*, 68-72.
47. T. Akar, S. Celik, and S.T. Akar, *Chem Eng J*, **2010**, *160*, 466–472.